Early Cretaceous
Shoal Water Carbonates from the Central Apennines
–
Sedimentology, Chemostratigraphy and Sclerochemistry

Von der Naturwissenschaftlichen Fakultät der
Gottfried Wilhelm Leibniz Universität Hannover

zur Erlangung des Grades
Doktorin der Naturwissenschaften (Dr. rer. nat.)

genehmigte Dissertation
von
Katharina Elena Schmitt, Diplom - Geologin

[2019]

Referent: Prof. Dr. Ulrich Heimhofer
Korefferent: Prof. Dr. Adrian Immenhauser
Tag der Promotion: 04.06.2019

Table of Contents

Table of Contents I

Abstract V

Zusammenfassung VI

List of Abbreviations VIII

1. Introduction 1

1.1 The Cretaceous: A Period of Extremes 1

1.2 Carbonate Platforms: A Shallow-Water Ecosystem 3

1.3 Rudists: Main Producers of Shallow Marine Carbonate Platforms during the Cretaceous 5

1.4 The Apennine Carbonate Platform: A Natural Laboratory 7

1.5 Aims and Objectives 9

1.6 Synopsis 11

1.7 References 12

2. Methodology 18

2.1 Field Work and Thin Section Microscopy 18

2.2 Isotope-ratio Mass Spectrometry (Gasbench) 19

2.3 Trace Element Analysis and Strontium Isotope Analysis (SIS) 20

2.4 µX-ray Fluorescence 21

2.5 Cathodoluminescence (CL) 22

2.6 References 22

3. Deciphering the Fragmentary Nature of Cretaceous Shallow-water Limestone Archives: A Case Study from the Subtropical Apennine Carbonate Platform 25

Abstract 25

3.1 Introduction 26

3.2 Geological setting 27

3.3 Field approaches and laboratory methods 28

3.3.1 Field work and thin section microscopy 28

3.3.2 Carbon and oxygen isotope analysis 30

3.3.3 Element and strontium isotope analysis of low-Mg calcite shells 30

3.4 Lithostratigraphy and carbonate microfacies 32

3.5 Biostratigraphy 37

3.6 Geochemical results 40

3.6.1 Bulk carbonate carbon- and oxygen isotope stratigraphy 40

3.6.2 Trace element and strontium isotope results 41

3.7 Discussion 41

3.7.1 Significance of bulk carbonate and bivalve shell chemostratigraphic patterns 41

3.7.2 Integrated bio- and chemostratigraphic dating 44

3.7.3 Time lost in discontinuity surfaces 48

3.8 Conclusions 50

Acknowledgements 51

3.9 References 51

4. Platform-wide Shift to Microbial Carbonate Production during the Late Aptian cold snap 57

Abstract 57

4.1 Introduction 57

4.2 Geological setting 58

4.3 Methods 59

4.4 Results 60

4.5 Discussion 61

4.5.1 Platform-wide expansion of microbial carbonate production 61

4.5.2 Implications for mid-Cretaceous *Lithocodium-Bacinella* mass occurrences 62

Acknowledgements 64

4.6 References 64

5. Radiolitid Rudists: An Underestimated Archive for Climate Reconstruction? 67

Abstract 67

5.1 Introduction 67

5.2 Material 69

5.3 Methods 71

5.4 Results 73

5.4.1 Shell micro- and macrostructures (sclerochronology *sensu stricto*) 73

5.4.2 Elemental and isotope compositions ... 79

5.5 Discussion ... 84

5.5.1 Preservation state ... 84

5.5.1.1 Elemental dataset ... 84

5.5.1.2 Isotopic dataset ... 85

5.5.2 Growth variations ... 86

5.5.3 Palaeoenvironmental implications ... 87

5.6 Conclusions ... 88

5.7 References ... 89

6. Summary and Outlook ... 93

7. Author contributions ... 95

8. Appendices ... 96

Acknowledgements ... 165

Curriculum Vitae ... 166

Abstract

During the Cretaceous (145.0 to 66.0 Myr) elevated atmospheric CO_2 levels resulted in Oceanic Anoxic Event (OAE) causing widely spread "black shales" and an abrupt increase in temperature. The climate of this period was disturbed by a few short-lived but prominent cooling events, interrupting the prevailing greenhouse conditions. An outstanding high global sea level, the submergence of several continental plates, and the evolution of large shelf areas favoured the development of isolated shallow marine carbonate platforms. The latter were exceptionally widespread, particularly in and around the Tethyan realm. There they built large and complex sedimentary systems, which have been repeatedly devastated by fast-changing environmental conditions. Rudists, an order of gregarious, sediment dwelling, heterodont, bizarrely shaped, sessile bivalves were the main carbonate producers.

Shallow marine carbonate platforms are a valuable archive for the reconstruction of deep-time environmental and climatic conditions due to their quick reaction to environmental changes. Their often-low resolution of biostratigraphic schemes makes a precise chronostratigraphic classification difficult, resulting in a fragmentary record.

In order to reconstruct palaeoenvironmental conditions, a precise chronostratigraphic framework was established. Two sections, the platform marginal Monte La Costa and the inner lagoonal Santa Lucia sections, located on the Apennine carbonate platform, were analysed in great detail, using an integrated bio- (calcareous algae and benthic foraminifera) and chemostratigraphic (C-, O- and Sr-isotope analysis) approach. Furthermore, both sections were correlated with well-dated pelagic reference curves and with each other. Several exposure surfaces and their related temporal gaps were detected at both sections and dated precisely.

A microbial episode appearing on the Apennine Carbonate Platform was detected in both sections. Its coeval onset was dated, using the aforementioned framework, to the OAE1b, between the Jacob and Kilian black-shale level especially. The main phase of bacinelloid growth can be linked to the subsequent temperature rise after the Late Aptian cold snap as well as an increase in sea level.

In order to use low-Mg calcite radiolitid shells as a palaeoenvironmental archive, a first approach of high-resolution sampling, using isotopic and elemental data, was applied. Shells were selected using literature based thresholds. Sclerochronological profiles were created and various shell structures (compact and porous) described. The results of selected shells are promising: The smooth, sine functional $\delta^{18}O$ pattern in the compact left valve may be used for palaeotemperature and palaeosalinity reconstructions. In the right valves two microstructure types were classified: Shells, where compact and non-compact parts alternating, might be used for palaeoenvironmental reconstructions, while those that contain a celluloprismatic structure, can be used only for habitat reconstructions, as the isotopic and elemental dataset shows the impact of diagenetic alteration.

Keywords: Shallow marine carbonate platform; Cretaceous; Rudist

Zusammenfassung

Gase aus vulkanischen und/oder methanogenen Quellen erhöhten während der Kreidezeit (145,0 bis 66,0 Ma) den atmosphärischen CO_2-Gehalt, was zu Ozeanischen Anoxischen Events (OAE) und den damit weit verbreiteten "Schwarzschiefern" führte. Das Klima dieser Zeit wurde durch einige kurzlebige aber markante Abkühlungen geprägt, welche die ansonsten vorherrschenden Treibhausbedingungen unterbrachen. Ein außergewöhnlich hoher globaler Meeresspiegel, die Überflutung mehrerer Kontinentalplatten und die Entwicklung großer Schelfgebiete begünstigten die Entwicklung isolierter, flach-mariner Karbonatplattformen. Letztere waren, insbesondere in und um den Bereich der Tethys, weit verbreitet. Dort wurden große und komplexe Sedimentsysteme ausgebildet, die durch schnell ändernde Umweltbedingungen immer wieder zerstört wurden. Rudisten, eine Ordnung von sedimentbewachsenden, heterodontalen, bizarr geformten, festsitzenden Muscheln, waren die Hauptkarbonatproduzenten.

Flach marine Karbonatplattformen sind wegen ihrer schnellen Reaktion auf Umweltveränderungen ein wertvolles Archiv für die Rekonstruktion von Umwelt- und Klimabedingungen. Dennoch sind sie aufgrund der geringen biostratigraphischen Auflösung und der damit verbundenen erschwerten chronostratigraphischen Klassifizierung oft schwer zu entschlüsseln. Zusätzlich wird eine zeitliche Einordnung oft durch Lücken erschwert, die durch Expositionsoberflächen verursacht werden, sodass die Sedimentation oft als fragmentarisch erscheint.

Um die paläoökologischen Bedingungen zu rekonstruieren, wurde ein präziser chronostratigraphischer Rahmen geschaffen. Zwei Abschnitte auf der apenninischen Karbonatplattform, der am Plattformrand gelegene Monte La Costa und der im inneren der Lagune gelegene Santa-Lucia Aufschluss, wurden mit einem integrierten bio- (Kalkalgen und benthische Foraminiferen) und chemostratigraphischen (C-, O- und Sr-Isotopenanalyse) Ansatz analysiert. Darüber hinaus wurden beide Abschnitte mit gut datierten pelagischen Referenzkurven und untereinander korreliert. Mehrere Expositionsflächen und die damit verbundenen Zeitverluste wurden bei beiden Aufschlüssen erfasst und präzise datiert.

Eine mikrobielle Blüte, die auf der Apenninkarbonatplattform auftritt, wurde in beiden Abschnitten nachgewiesen. Ihr zeitgleicher Beginn wurde unter Verwendung des oben genannten Rahmens auf das OAE1b datiert, auf das Intervall zwischen dem Jacob- und Kilian-Schwarzschieferevent. Die Hauptphase des bacinelloiden Wachstums ist mit dem Temperaturanstieg korreliert, der auf den Late Aptian ‚Cold Snap‘ folgt, sowie mit einem Meeresspiegelanstieg.

Um Radiolitidenschalen aus Tief-Mg Calcit als Paläoumweltarchiv zu nutzen, wurde ein erster Versuch unternommen, Isotopen- und Elementdaten hochauflösend zu messen. Die Auswahl der Schalen erfolgte anhand von literaturbasierten Grenzwerten. Es wurden sklerochronologische Profile erstellt und verschiedene Schalenstrukturen (kompakt und porös) beschrieben. Die Ergebnisse ausgewählter Schalen sind vielversprechend: Das zyklische, sinusförmige $\delta^{18}O$-Muster in der kompakten, linken Klappe kann für Paläotemperatur- und Paläosalinitätsrekonstruktionen verwendet werden. In den rechten Klappen wurden zwei Mikrostrukturtypen klassifiziert: Schalen, bei denen kompakte und nicht-kompakte Teile abwechselnd zu finden sind, können für paläoökologische Rekonstruktionen verwendet werden, während solche, die eine celluloprismatische Struktur enthalten, nur für die Rekonstruktion des Lebensraums verwendet werden können, da der isotopische - und elementare Datensatz die Auswirkungen diagenetischer Veränderungen zeigt.

Stichworte: Flach marine Karbonatplattformen; Kreide; Rudisten

List of Abbreviations

%	Per cent, parts per hundred
‰	Per mill, parts per thousand
°C	degree Celsius
ACP	Apennine Carbonate Platform
bx	Bauxite
CAP	Central Apennine Platform
cf.	(Latin) confer: "compare"
CIE	Carbon isotope excursion
CL	Cathodoluminescence
CO_2	Carbon dioxide
e.g.	(Latin) exempli gratia; “for example”
Fe	Iron
FO	First occurrence
h	Hour
ICP-AES	Inductively Coupled Plasma - Atomic Emission Spectrometry
ICP-OES	Inductively Coupled Plasma - Optical Emission Spectrometry
IRMS	Isotope-ratio Mass Spectrometry
i.e.	(Latin) id est; “meaning”
kV	Kilovolt
LIP	Large Igneous Province
LO	Last occurrence
LV	Left valve
m	Metre
Mg	Magnesium
MLC	Monte La Costa section

mm	Millimetre
Mn	Manganese
Myr	Million years
OAE	Oceanic Anoxic Event
OJP-LIP	Ontong Java Plateau large igneous province
ppl	plane polarised light
ppm	Parts per million
RUB	Ruhr-University Bochum
RV	Right valve
SIS	Strontium isotope stratigraphy
SL	Santa Lucia section
Sr	Strontium
SST	Sea Surface Temperature
VPDB	Vienna-Pee Dee Formation belemnite
δ	Delta-Notation
µg	Microgram
µm	Micrometre
σ / s.d.	Standard deviation

1. Introduction

1.1 The Cretaceous: A Period of Extremes

The Cretaceous, ranging from 145.9 to 66.0 Myr is subdivided into 12 stages based on chemo-, magneto-, cyclo- and biostratigraphy (Gradstein et al., 2012). The latter is based on ammonite ranges (Birkelund et al., 1984; Kennedy, 1984) supported by calcareous nannofossil data (Gradstein et al., 2012). The Cretaceous period includes the zenith of the dinosaurs, the rise of land flowering plants (angiosperms), the first occurrence of birds and the massive bloom of coccolithophores forming large chalk deposits, which gave the Cretaceous its name. It was terminated by a major mass-extinction at the K/Paleogene boundary (Gradstein et al., 2012; Skelton et al., 2003).

During the Cretaceous several extraordinary events occurred: The breakup of the supercontinent Pangaea, into Laurasia in the north and Gondwana in the south, has already advanced creating equatorial new sea passages, namely the east-west orientated Tethys at low latitudes and the narrow Central Atlantic (Skelton et al., 2003).

The global sea level rose to its maximum during the Late Cretaceous (dark blue curves in Fig. 1.1). This was triggered by the growth of new mid-ocean ridge systems and by an increased production of oceanic crust that caused the displacement of water from oceanic basins (Skelton et al., 2003). The increasing sea level caused the submergence of several continental plates while other continents were surrounded by large shelf areas (Hennhöfer, 2013). Thus, conditions were in favour of the development of isolated shallow marine carbonate platforms, shallow seas, and barrier reefs (Frakes et al., 1992; Skelton et al., 2003).

The Cretaceous climate is classified as a greenhouse world interrupted by short-lived but prominent cooling events (cold snaps; green squares in Fig. 1.1) during the Berriasian-Valanginian, earliest Late Valanginian, earliest Aptian and Late Aptian (Weissert, 1991; Hochuli et al., 1999; Miller et al., 1999; Pucéat et al., 2003; Skelton et al., 2003; Steuber et al., 2005; Bornemann et al., 2008; Mutterlose et al., 2009). Amongst other factors, cooling is evidenced by dropstones and glendonites found at higher latitudes in the marine realm (Mutterlose et al., 2009). Using foraminifera and belemnite oxygen isotope ratios and TEX_{86} data, a temperature maximum of 37 °C was reconstructed (light blue curve in Fig. 1.1; Huber et al., 1995; Bornemann et al, 2008; Mutterlose et al., 2009; Skelton et al., 2003; Huber et al., 2011; Bodin et al., 2015; Friedrich et al., 2012; McAnena et al., 2013). Polar forests reaching up to 82°N support this hypothesis. These polar forests were habitats for plants (conifer needles), shells, fish, crocodiles and turtles as well as herbivore and carnivore dinosaurs (Francis and Frakes, 1993; Frakes et al, 1992; Skelton et al., 2003; Huber, 1998). The low equator to pole temperature gradient was responsible for a weak atmospheric and oceanic circulation (Frakes et al., 1992).

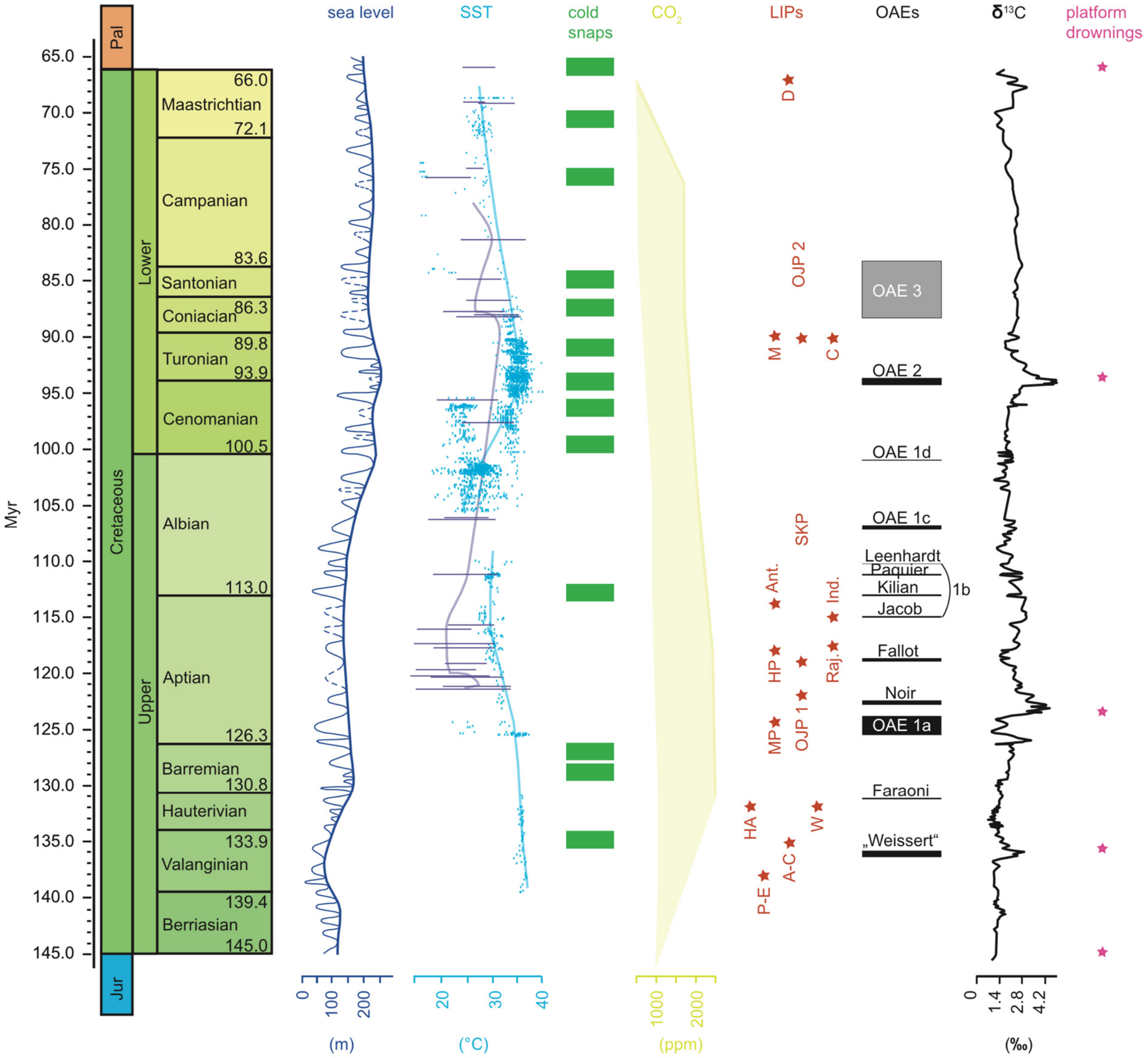

Fig. 1.1: Compilation of major environmental changes during the Cretaceous including sea level changes in dark blue (Haq et al., 2014); SST (sea surface temperature) changes using TEX_{86} (light blue) for low palaeolatitude after O'Brien et al. (2017) and rudist ranges (purple) after Steuber (2005), possible cold snaps (green) after Hu et al. (2012), the reconstructed range of palaeo-CO_2 (yellow) after Wang et al. (2014) with the minimum values of Berner (1994) and maximum values of Ekart et al. (1999); LIPs (large igneous provinces: A-C: Caribbean Columbian Province; Ant.: Antarctic Lamprophyre; D: Deccan Traps; HA: High Arctic Large Igneous Province; HP: Hikurangi Plateau; Ind.: Indian Lamprophyre; M: Madagascar; MP: Manihiki Plateau; OJP 1: Ontong Java Plateau Event 1; OJP 2: Ontong Java Plateau Event 2; P-E: Paraná–Etendeka traps; Raj.: Rajmahal Traps; SKP: Southern Kerguelen Plateau; W: Whitsunday) compiled after Bryan et al. (2012), Bottini et al. (2015) and Gradstein et al. (2012), OAEs (oceanic anoxic events) from Locklair et al. (2011) and Wagreich (2012), $\delta^{13}C$ values in black in Gradstein et al. (2012) and platform drowning events (pink) after Skelton et al. (2003). All data are adapted to the GTS 2012 (Gradstein et al., 2012).

In addition, it is assumed that the high sea levels were caused by the temporary absence of polar ice caps (Skelton et al., 2003). Transgression as well as temperature maxima were reached during the Turonian (Skelton et al., 2003; Haq et al., 1987; Sahagian et al., 1996; Kominz et al., 2008) with a sea level 200 m higher than today (Haq et al., 1987; Skelton et al., 2003) and thus the highest level recorded throughout the Phanerozoic (Miller et al., 2005). The transgression was caused by high sea floor spreading rates (Skelton et al., 2003) triggered by an increased productivity of oceanic crust (Larson, 1991). This enhanced oceanic crust production resulted in an elevated atmospheric CO_2 level (Jones and Jenkyns, 2001) that was at least three times higher than today (Bice et al., 2006; Caldeira and Rampino, 1991) (yellow curve in Fig. 1.1). Additionally, the atmosphere was affected by volcanic gases emitted from large igneous provinces (LIPs) or methanogenic sources (Jenkyns, 2010) (red asterisks in Fig. 1.1). This rapid emission of vast amounts of CO_2 resulted in an abrupt increase in temperature (Jenkyns, 2010) that most likely caused the formation of widely spread “black shales”: organic-rich lithologies in which a large quantity of organic carbon was buried (Arthur et al., 1987; Arthur et al., 1990). These globally important organic-carbon burials, termed Oceanic Anoxic Event (OAE) (Arthur et al., 1990), are related to global short-lived major perturbations in the carbon cycle. OAEs are marked as positive anomalies in several carbon isotope records (Scholle and Arthur, 1980) of pelagic deposits and occasionally in shallow marine carbonate platform limestones (black curve in Fig. 1.1). An advantage of pelagic deposits is their continuous record which allows global and local correlations. However, shallow marine carbonate platforms react fast to environmental changes but contain often a fragmentary record. Therefore, they pose a high potential as well as one of the greatest challenges to the research of palaeoenvironmental reconstruction.

1.2 Carbonate Platforms: A Shallow-Water Ecosystem

The distribution of landmasses combined with high sea levels provided excellent conditions for an accumulation of shallow marine limestones in low latitudes (Fig. 1.2). These carbonate platforms were exceptionally widespread, particularly in and around the Tethyan realm, where they built large and complex sedimentary systems with regional variations (Skelton et al., 2003).

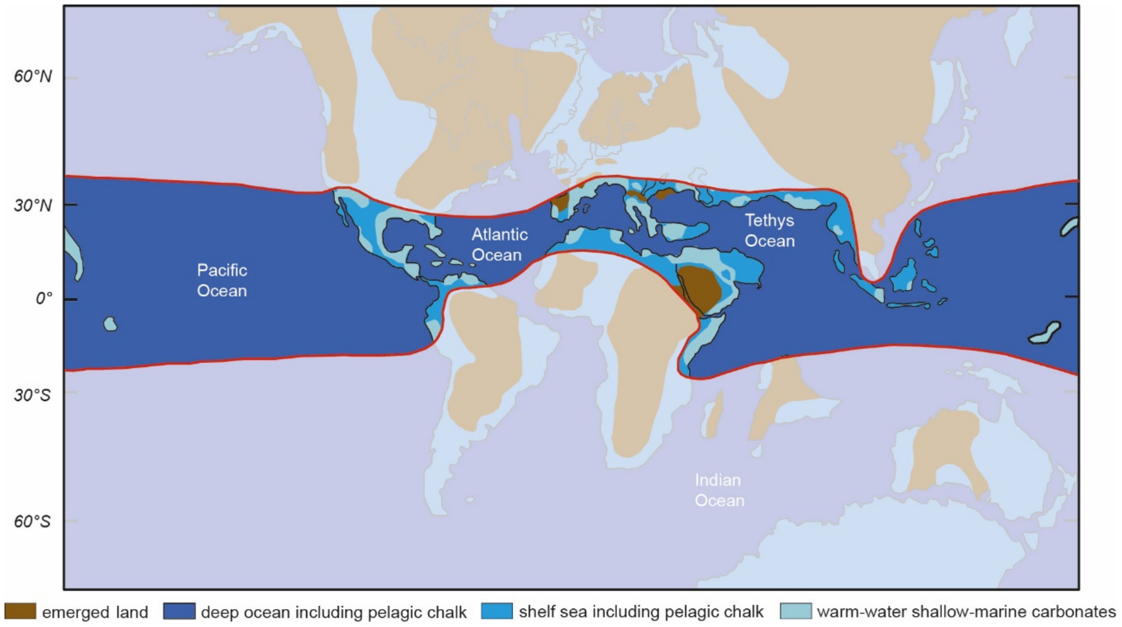
60°N
30°N
0°
30°S
60°S
Pacific Ocean
Atlantic Ocean
Tethys Ocean
Indian Ocean
emerged land
deep ocean including pelagic chalk
shelf sea including pelagic chalk
warm-water shallow-marine carbonates

Fig. 1.2: Palaeogeographic reconstruction of shallow marine carbonate platforms (light blue) in low latitudes during the Late Cretaceous (98 Ma) modified after Skelton et al. (2003).

Cretaceous carbonate platforms were composed of algae with calcareous skeletons, gastropods, scleractinian corals, benthic foraminifera and a distinct shelly benthos, mainly rudists. The latter were the main carbonate producers building extensive meadows spread across low relief sediment (Skelton et al., 2003).

Due to sea level oscillations and tectonic activity, two settings alternated in the Cretaceous: The exceptional rapid growth and expansion of platforms, which was interrupted by short but global episodes of their demise (Fig. 1.3). Particularly outstanding declines can be recognized during the Mid Valanginian, the Early and Mid Aptian, the Cenomanian/Turonian and finally in the Late Maastrichtian. Those drownings or collapses of the carbonate producing systems (Masse and Philip, 1986; Ross and Skelton, 1993) were caused by processes like a sea level rise/drop or the infiltration by microencrusting species, e.g. *Lithocodium aggregatum* Elliott (1956) and *Bacinella irregularis* Radoičic (1959) that replaced the previously dominant shelly biota (Immenhauser et al., 2005).

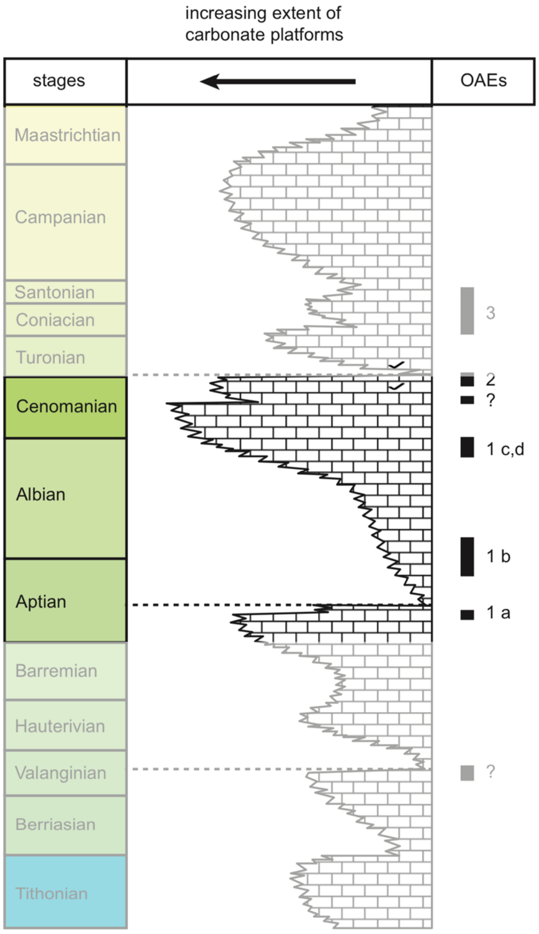

Fig. 1.3: Major crises that are often correlated to OAEs, interrupting the carbonate platform evolution during the Cretaceous in the Tethyan/Atlantic oceanic realm modified after Skelton et al. (2003). Aptian to Cenomanian period are highlighted to show studys' focus.

Although it is often difficult to decipher them, shallow-water carbonate platform sections are a valuable archive for the reconstruction of deep-time environmental and climatic conditions due to their quick response to environmental changes. But the low resolution of biostratigraphic schemes often hampers their precise chronostratigraphic classification and the fragmentary record. This is caused by diagenetic alteration and exposure surfaces. However, it is possible to date such sections using integrated bio- and chemostratigraphy. As a start, biostratigraphy is used for an initial age assessment. Then, carbon isotopes values are measured and utilized to correlate shallow marine sections with well-dated pelagic sections. In addition, carbon and oxygen isotope analyses are valuable tools to identify exposure surfaces (negative values) and to exclude samples that were altered by meteoric diagenesis. The latter is often indicated by a correlation between $\delta^{18}O$ and $\delta^{13}C$ values or increasingly negative $\delta^{13}C$ values with constant $\delta^{18}O$ values (Gradstein et al., 2012). This process is then followed by strontium isotope stratigraphy (SIS). In order to exclude diagenetic altered samples, suitable low-Mg calcite shells with high Sr and Mg but low Mn and Fe concentration needs to be identified by Inductively Coupled Plasma-Optical Emission Spectrometry (ICP-OES) (Steuber, 1999). This elemental analysis allows for the identification of the best-preserved and best-suited material.

1.3 Rudists: Main Producers of Shallow Marine Carbonate Platforms during the Cretaceous

Rudists (superfamily Hippuritoidea), an order of gregarious, sediment dwelling, heterodont, bizarrely shaped sessile bivalves, evolved during the Late Jurassic (Skelton and Smith, 2000) and were extinct at the K/Paleogene boundary (Skelton et al., 2003; Skelton, 1978). During the Early Aptian the abundance and spreading of rudist species increases (Fig. 1.4; Steuber and Löser, 2000). Colonizing an entire platform (from low energy inner platform settings to high energy shelf marginal settings), carbonate ramps and seamounts (Rauch, 2005), they dominated the carbonate platforms in the Tethyan ocean and were the main carbonate producers with a carbonate production rate of 2.2 to 35.7 kg $CaCO_3$ $m^{-2}year^{-1}$ (Skelton et al., 2003).

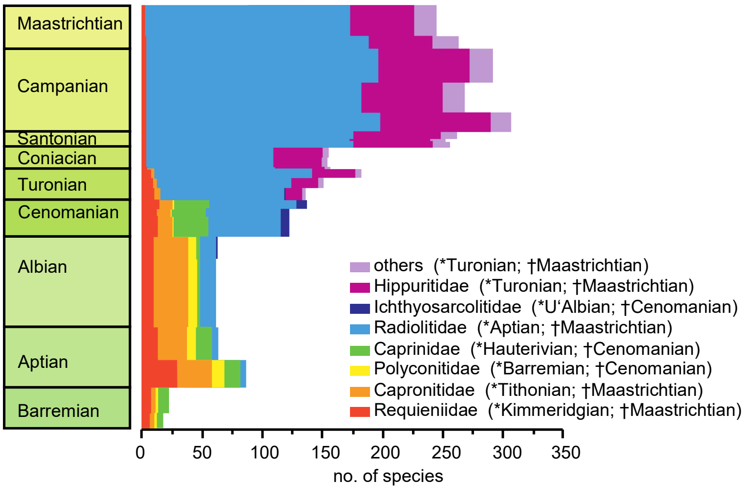

Fig. 1.4: Number of species recorded in the Mediterranean and Middle East region from the Barremian to the Maastrichtian including the global ranges of the families modified after Steuber and Löser (2000).

Although they are often described as reef biota, they did not built reefs but “meadows” (Skelton et al., 2003). While growing in bouquets (few specimens attached to each other), clusters (dozens together) or thickets (> 100 rudists) (Philip, 1972; Hennhöfer, 2013). Rudists developed several different growth forms and morphotypes in order to adapt to and occupy various habitats (Fig. 1.5):

1. Recumbents (Fig. 1.5 A) lay prone but unattached on mobile lime sand or shelly rubble substrate in a current-swept environment, where no significant sediment accumulation occurred during their lifespan (Ross and Skelton, 1993). Due to a platform drowning event in the Late Cenomanian (Fig. 1.3), all recumbents that thrived in the outermost platform environment went extinct.
2. Clingers (Fig. 1.5 B) consisted of an attached valve with a large basal surface (horizontal growth) and an “unattached” one (growth inclination of 45°). They grew on stable substrate and tolerated occasional sediment influx and currents.
3. Elevators (Fig. 1.5 C) formed an elongated attached valve that was stabilized by surrounding sediment or by an attachment to the neighbouring rudist (clustering). Due to their need of surrounding sediment, they implanted in an accumulating sediment environment (Skelton and Gili, 1991, Skelton et al., 2003).

All rudist species formed their shell following the same structural design: with two inner aragonitic layers and an outer low-Mg calcite layer. Due to the chemical composition, the outer layer is very stable against diagenetic alteration and hence a valuable archive for recording environmental conditions that prevailed while the shell was secreted. Since rudists are building growth increments, they are considered suitable for sclerochronological analysis. In past studies, they have therefore been used for dating (SIS), the reconstruction of seasonal variations in ocean chemistry (Mg/Ca) and climate reconstruction, which utilize the periodic oscillations of oxygen ($\delta^{18}O$) and carbon ($\delta^{13}C$) isotope values in the shell carbonate (Steuber, 2000; Steuber, 2003; Steuber, 1999; Steuber, 1996; Immenhauser et al., 2005; Rauch, 2005).

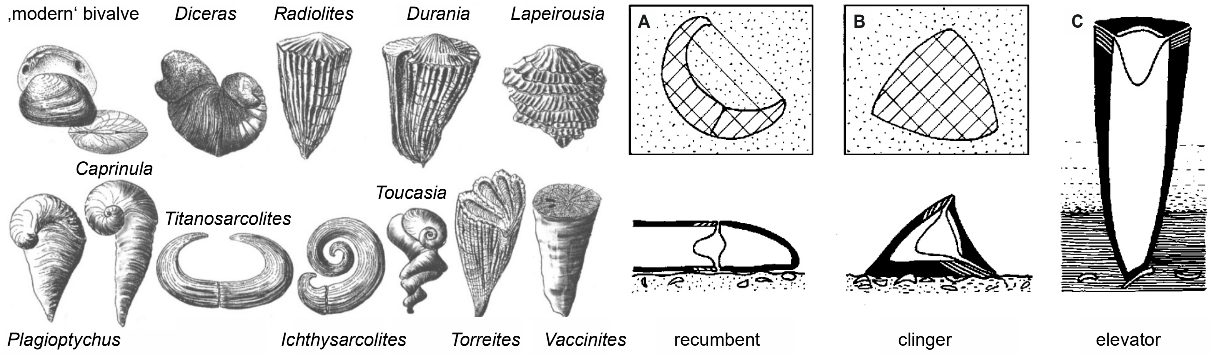

Fig. 1.5: Various morphologies of rudist shells (left half of the figure; Schumann and Steuber, 1997) and their three morphotypes after Skelton and Gili (1991). Right half of the figure: A. Recumbent; B: clinger, C: elevator. A and B show above in plain view (with contact area and basal support) and profile below.

1.4 The Apennine Carbonate Platform: A Natural Laboratory

The Apennine Carbonate Platform (ACP) is one of only a few isolated carbonate platforms at the south-west margin of the Tethys (around 15°N; Fig. 1.6 A) that recorded a nearly continuous shallow-water carbonate sedimentation (Skelton et al., 2003; D'Argenio et al., 1973; Frijia et al., 2015) and shows an extremely diverse and abundant rudist assemblage (Frijia et al., 2015).

The ACP contains shallow tropical water carbonate successions and is interpreted as a part of a more or less articulated system of carbonate platforms (including the following units: Capri-Bulgheria, Alburno-Cervati and Monti della Maddalena; Simbruini-Matese; Western Marsica-Meta) (Pattaca and Scandone 2007). They are separated by deep water basins and deep water tongues linking the Umbria domain and the Lagonegro-Molise Basin (D'Argenio, 1973; Patacca and Scandone, 2007) (Fig. 1.6 B). The ACP was part of a palaeo-tectonic domain called Adria or Apulia. For further specification of domain name, please refer to Schettino and Turco (2011). It is alternatively interpreted as the promontory of the African continent or as an independent continental block separated from Africa by an oceanic corridor (Decourt et al., 1986; Bosellini, 2002; Schettino and Turco, 2011; Frijia et al., 2015).

During the Mid Triassic, continental rifting created two carbonate platforms: The Apennine and the Apulian platforms, which were separated by the Lagonegro basin (Di Lucia et al., 2012). Shallow-water carbonate sedimentation of the ACP started in the Late Triassic (Cosentino et al., 2010) and stopped at the end of the Cretaceous, when the platform emerged. The sedimentation process continued locally during the Paleogene and the Early Miocene but was finally terminated in the Middle Miocene, when the platform drowned below the photic zone (Frijia et al., 2015) and siliciclastic deep water deposits accumulated (Sgrosso, 1998; Patacca and Scandone, 2007). However, several subaerial exposure surfaces are recorded, containing gaps of various durations. These emersion phases are shown for exmple by the occurrence of discontinuous lenses of bauxite (Carannante et al., 1988; Ruberti et al., 2013) or brecciated intervals. They were possibly caused by starvation in carbonate production, sea level changes and/or through tectonic uplift (Selli, 1957; 1962).

The ACP contains a 4-5 km-thick sequence of limestones, of which 1-1.2 km were deposited during the Cretaceous (Sartoni and Crescenti, 1962; D'Argenio and Alvarez, 1980; Frijia et al., 2005; Di Lucia et al., 2012). The depositional system of the platform changed over time: from a flat-topped Bahamian-type carbonate platform dominated by chloralgal and chlorozoan associations (D'Argenio et al., 1975) to a ramp-like open shelf setting, dominated by a foramol-type assemblage (Carannante et al., 1997). Due to the continuous sedimentation processes, various bio events (e.g. microbial episodes; *A. reicheli*-Level; *S. dinarica* acme; several Orbitolina levels) were recorded and can be used as platform-wide correlation levels.

The outcrops studied in this thesis are located in the southern Apennines in Italy (Fig. 1.6 C) and are located along a SE-NW proximal-to-distal transect across the ACP. The 597 m-thick Santa Lucia

(SL) section, which belongs to the Lazio-Abruzzi carbonate platform, is located along the road cut which connects Villa Santa Lucia and Terelle (41°31'00.6"N 13°46'40.0"E to 41°31'02.0"N 13°47'02.8"E). This succession represents an open lagoon setting, dominated by mudstones alternating with grainstones. Special feature of this outcrop is the bauxitic layer (bx1). The 470 m-thick Monte La Costa (MLC) section, which is part of the Simbruini-Matese unit, is a small mountain range in the Matese Mountains (41°28'12.4"N 14°29'50.0"E) and is interpreted as a platform marginal setting. Grainstones are the dominant facies, alternating with pack- and framestones. In both sections, a bacinelloid-bearing interval of ~ 150 m was recognized.

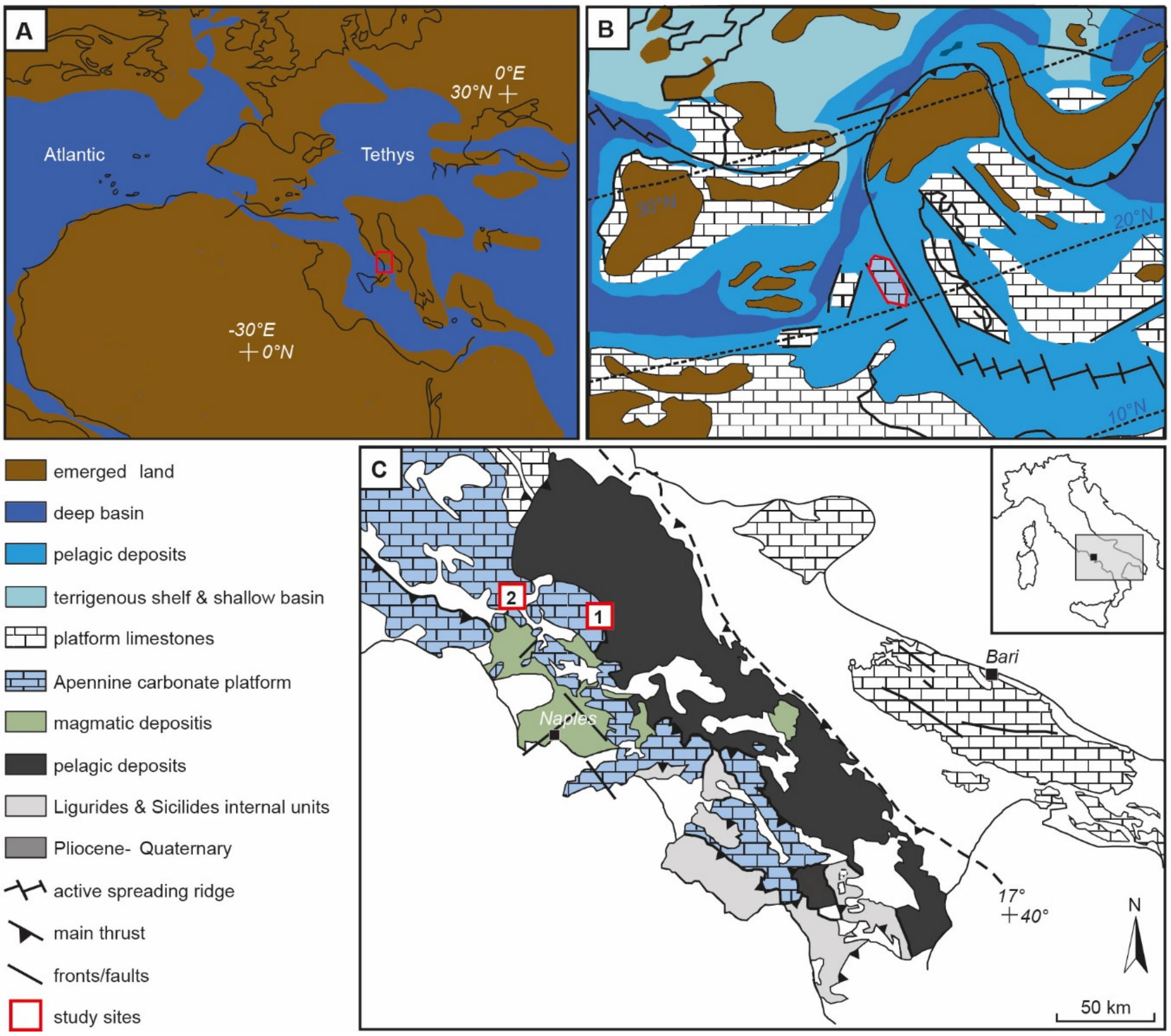
A
0°E
30°N
Atlantic
Tethys
-30°E
0°N
B
30°N
20°N
10°N
C
2
1
Bari
Naples
17°
40°
N
50 km
emerged land
deep basin
pelagic deposits
terrigenous shelf & shallow basin
platform limestones
Apennine carbonate platform
magmatic depositis
pelagic deposits
Ligurides & Sicilides internal units
Pliocene- Quaternary
active spreading ridge
main thrust
fronts/faults
study sites

Fig. 1.6: (A) Palaeogeographic map of the Upper Cretaceous with the Apennine Carbonate Platform (red square) in the Tethyan realm. (B) Detailed view of the Apennine carbonate platform (red outline) with surrounded carbonate platforms. (C) Schematic geological map of the Central and Southern Apennines (Italy) with the location of the study sections. 1 - Monte La Costa, 2 - Santa Lucia. Modified after Parente et al. (2007).

1.5 Aims and Objectives

The focus of this thesis is to date and reconstruct major events of the shallow marine Apennine Carbonate Platform (ACP) as well as the reconstruction of mid-Cretaceous palaeoenvironmental parameters using the ACPs' main carbonate producers. Due to a fast reaction to environmental changes, these platforms are valuable archives for the reconstruction of deep-time environmental and climatic conditions (e.g. Di Lucia et al., 2012). Therefore, the ACP was analysed in-depth using various methods to decipher the depositional setting.

Although the ACP is determined as having a more or less continuous sedimentation (Skelton et al., 2003; Frijia et al., 2015), several exposure surfaces (e.g. bauxite, breccias) and related temporal gaps have been reported in several studies. Until now these platforms have solely been dated by means of biostratigraphy, with the result that the chronostratigraphic age of platform successions and/or their possible fragmentary record were solely defined through biozones (e.g. Chiocchini et al., 1989; Mondillo et al., 2011; D'Argenio and Mindszenty, 1995; D'Argenio et al., 2011). Traditionally, biostratigraphy based on benthic foraminifera and calcareous algae was primarily used (e.g. De Castro, 1991; Carannante et al., 2000; Mancinelli and Chiocchini, 2006; Chiocchini et al., 2008), although this approach was limited by the low resolution of shallow-water biozones. However, in recent years more precise chronostratigraphic frameworks have been established using integrated bio- and chemostratigraphy (e.g. Frijia et al., 2015; Parente et al., 2007; Frijia and Parente, 2008).

In order to allow environmental reconstructions of the ACP, a precise chronostratigraphic framework, containing the duration of possible hiatuses, has to be established. To achieve this, the degree of fragmentation needs to be determined as a prerequisite for the framework. Therefore, the first question of this thesis is:

(1) To what extent can a continuous sedimentation of the ACP be confirmed?

Biostratigraphy (foraminifera and algae) was combined with high-resolution carbon isotope stratigraphy and (rudist and chondrodont shell) strontium isotope stratigraphy at the Monte La Costa (MLC) and the Santa Lucia (SL) sections. Both sections were chosen due to their position on the ACP, an open lagoon and a platform marginal setting, in order to create a SE-NW proximal-to-distal transect across the ACP. Through this approach, the sedimentation processes and its continuity can be reconstructed and a very precise chronostratigraphic framework can be established.

During fieldwork, a mass-occurrence of microencrusting organisms was noted in both analysed sections. Their appearance was reported in numerous publications (e.g. Raspini, 2012; Graziano and Raspini, 2015; Mancinelli and Chiocchini, 2006). However, the description of their occurrence differ greatly. Ruberti et al. (2013) describe large *Bacinella/Lithocodium* oncoids and lumps in rock forming abundance from the Upper Aptian portion of the Serra Sbregavitelli section (13 km SW of the MLC section), assuming that these intercalated oncoid-rich beds are caused by storm events. Di Lucia et al. (2012) mention *Lithocodium-Bacinella* nodules in five sections across the ACP (Mt. Croce, Mt. Raggeto, Mt. Tobenna, Mt. Motola, and Mt. Coccovello). Both the interval thickness and stratigraphic distribution vary (Lower Aptian to Upper Aptian).

To reconstruct the environmental parameters during the appearance of microbial encrusters the newly established timeframe was used. The following question guided the inquiry:

(2) When was the onset of the microbial episode in each analysed section and what environmental conditions can be reconstructed for this period?

Based on the scheme of Rameil et al. (2010), morphotypes of the bacinelloidics were defined. Furthermore, the appearance of bacinelloid containing intervals, recorded in the MLC and the SL sections, was tied to the GTS 2012 (Gradstein et al., 2012) and the spatial and temporal expansion of the microencrusters in both sections was compared. Palaeotemperature was determined using Tex_{86}. Sea level reconstruction is based on the biostratigraphic data, SIS and cyclostratigraphy (Maurer et al., 2013).

Both analysed sections contained rudist shells, with the MLC showing a high degree of accumulation. Bivalve shells in general are used for palaeoenvironmental reconstructions like temperature or salinity (e.g. Butler et al., 2013; Wanamaker et al., 2011; Schöne et al., 2005). During the Cretaceous, rudist bivalves were generally abundant and are therefore a valid opportunity to reconstruct environmental conditions of that time (e.g. Steuber, 1999; Steuber et al., 2005). They can furthermore be used for strontium isotope stratigraphy, in order to determine their precise chronostratigraphic age (Huck and Heimhofer, 2015). This is due to their low-Mg calcite shell, which is resistant against diagenetic alteration and records palaeoenvironmental conditions (e.g. Steuber, 1999; Regidor-Higuera et al., 2007). Nevertheless, certain rudist genera are preferred for palaeoenvironmental reconstructions due to their compact shell structure.

Interestingly, radiolitids (a family of the order rudists) are mostly excluded from geochemical analyses because of their porous, often cement-filled outer shell layer. Nevertheless, since radiolitids are the primary genus found in the MLC, their abundance poses a significant potential for comprehensive environmental reconstruction. To gain further insights into the usability of radiolitids for environmental reconstructions, the following question arose:

(3) To what extent are radiolitids a viable basis for environmental reconstruction, especially temperature, salinity and habitat?

In order to test if it is possible to decipher palaeoenvironmental signals, selected shells are sampled for isotopic record, elemental composition and sclerochronological properties.

1.6 Synopsis

The work detailed in this thesis lays a focus on the Apennine shallow marine carbonate platform (ACP) located in Italy, represented by the Monte Cairo Massif (Santa Lucia section; SL) and the Matese Mountains (Monte La Costa section; MLC). It is divided into six chapters, with chapter two stating used methods, chapters three to five addressing the questions stated above (see 1.6) and chapter six giving a conclusive summary of the collected results.

The **second chapter** outlines briefly the sampling and applied methods. Field work and thin section microscopy, isotope-ratio mass spectrometry (Gasbench), Trace Element Analysis and Strontium Isotope Analysis (SIS), µX-ray Fluorescence and Cathodoluminescence (CL) are described.

The **third chapter** addresses question (1), see p. 9. It is comprised of the lithological description and chemostratigraphic analysis of the MLC and SL sections. Both sections were sampled, logged and are described in detail. Using integrated bio- and chemostratigraphy the sections were dated from Barremian to Cenomanian (SL) and from Aptian to Albian (MLC) and a high-resolution framework was established. It was used to determine a fragmentary record of the ACP, including the identification of several exposure surfaces and their resulting variable time losses. Furthermore, sections of the ACP dated previously by biostratigraphy can be inserted in the new chronostratigraphic framework to improve their temporal classification.

Question 2, see p. 10, is the focus of **chapter four**. As both sections are dated using integrated bio- and chemostratigraphy, it appears that the onset of the pervasive bacinelloid microencrusters was coeval in the MLC and SL successions. Its begin is stratigraphically positioned between the Jacob and Kilian black-shale levels of the Late Aptian OAE1b multi-event. The microencrusters appeared during the upper part of a prolonged positive carbon isotope excursion in both carbon isotope records and can subsequently be linked to an increase in both sea surface temperatures and sea level.

In **chapter five** radiolitid rudist shells were evaluated for their ability to serve as a palaeoenvironmental archive, as stated in question (3), see p. 10. In order to test the suitability of these shells, sclerochronological analysis was combined with high-resolution geochemical sampling methods. Two right valves, a left valve plus its articulated right valve and a left valve were analysed. The left valve was shown to be a promising basis for palaeoenvironmental reconstructions, with regard to temperature and salinity. While the right valve is a suitable archive for habitat reconstructions.

Chapter six summerises the most important findings of this thesis and provides an outlook into future research.

1.7 References

Arthur, M.A., Jenkyns, H.C., Brumsack, H.-J., Schlanger, S.O., 1990. Stratigraphy, geochemistry, and paleoceanography of organic-carbon-rich Cretaceous sequences, in Cretaceous Resources, Events and Rhythms, NATO ASI Ser. 304, edited by R. N. Ginsburg and B. Beaudoin, 75–119.

Arthur, M.A., Zachos, J.C., Jones, D.S., 1987. Primary productivity and the Cretaceous/Tertiary boundary event in the oceans. Cretaceous Research 8, 43-54.

Berner, R.A., 1994. GEOCARB II: A revised model of atmospheric CO_2 over phanerozoic time. American Journal of Science (United States) 294.

Bice, K.L., Birgel, D., Meyers, P.A., Dahl, K.A., Hinrichs, K.U., Norris, R.D., 2006. A multiple proxy and model study of Cretaceous upper ocean temperatures and atmospheric CO_2 concentrations. Paleoceanography, 21.

Birkelund, T., 1984. Cretaceous stage boundaries-proposals. Bull. Geol. Soc. Denmark, 33, 3-20.

Bodin, S., Meissner, P., Janssen, N.M., Steuber, T., Mutterlose, J., 2015. Large igneous provinces and organic carbon burial: Controls on global temperature and continental weathering during the Early Cretaceous. Global and Planetary Change, 133, 238-253.

Bornemann, A., Norris, R.D., Friedrich, O., Beckmann, B., Schouten, S., Damsté, J.S. S., Vogel, J., Hofmann, P., Wagner, T., 2008. Isotopic evidence for glaciation during the Cretaceous supergreenhouse. Science, 319, 189-192.

Bosellini, A., 2002. Dinosaurs "re-write" the geodynamics of the eastern Mediterranean and the paleogeography of the Apulia Platform. Earth-Science Reviews 59, 211-234.

Bottini, C., Erba, E., Tiraboschi, D., Jenkyns, H.C., Schouten, S., Sinninghe Damsté, J.S., 2015. Climate variability and ocean fertility during the Aptian Stage. Climate of the Past 11, 383-402.

Bryan, S.E., Cook, A., Allen, C.M., Siegel, C., Purdy, D., Greentree, J., Uysal, T., 2012. Early-mid Cretaceous tectonic evolution of eastern Gondwana: from silicic LIP magmatism to continental rupture. Episodes 35, 142-152.

Butler, P.G., Wanamaker Jr, A.D., Scourse, J.D., Richardson, C.A., Reynolds, D.J., 2013. Variability of marine climate on the North Icelandic Shelf in a 1357-year proxy archive based on growth increments in the bivalve Arctica islandica. Palaeogeography, Palaeoclimatology, Palaeoecology 373, 141-151.

Caldeira, K., Rampino, M.R., 1991. The mid-Cretaceous super plume, carbon dioxide, and global warming. Geophysical Research Letters, 18, 987-990.

Carannante, G., Esteban, M., Milliman, J.D., Simone, L., 1988. Carbonate lithofacies as paleolatitude indicators: problems and limitations. Sedimentary Geology 60, 333-346.

Carannante, G., Graziano, R., Ruberti, D., Simone, L., 1997. Upper Cretaceous temperate-type open shelves from northern (Sardinia) and southern (Apennines-Apulia) Mesozoic Tethyan margins. In James N.P. and Clarke J. Eds., «Cool water carbonates», Spec. Publ. Soc. Econ. Paleont. Mineral., 56, 309-325.

Carannante, G., Ruberti, D., Sirna, M., 2000. Upper Cretaceous ramp limestones from the Sorrento Peninsula (southern Apennines, Italy): micro-and macrofossil associations and their significance in the depositional sequences. Sedimentary geology 132, 89-123.

Chiocchini, M., Mancinelli, A., Romano, A., 1989. The gaps in the Middle-Upper Cretaceous carbonate series of the southern Apennines (Abruzzi and Campania regions). Geobios 22, 133-149.

Chiocchini, M., Chiocchini, R.A., Didaskalou, P., Potetti, M., 2008. Microbiostratigrafia del Triassico superiore, Giurassico e Cretacico in facies di piattaforma carbonatica del Lazio centro-meridionale e Abruzzo: revisione finale. Mem. Descr. Carta Geol. d'It. 84, 5-170.

Cosentino D., Cipollari, P., Marsili, P., Scrocca, D., 2010. Geology of the central Apennines: a regional review. Journal of the Virtual Explorer, Electronic Edition 36, paper 11.

D'Argenio, B., Mindszenty, A., 1995. Bauxites and related paleokarst: Tectonic and climatic event markers at regional unconformities. Eclogae Geologicae Helvetiae 88, 453-499.

D'Argenio, B., Ferreri, V., Amodio, S., 2011. Eustatic cycles and tectonics in the Cretaceous shallow Tethys, Central-Southern Apennines. Italian journal of geosciences 130, 119-127.

D'Argenio, B., Pescatore, T., Scandone, P., 1973. Schema geologico dell'Appennino meridionale (Campania e Lucania). Accademia Nazionale dei Lincei 182, 49-72.

D'Argenio, B., Alvarez, W., 1980. Stratigraphic evidence for crustal thickness changes on the southern Tethyan margin during the Alpine cycle. Geological Society of America Bulletin 91, 681-689.

D'Argenio, B., De Castro, P., Emiliani, C., Simone, L., 1975. Bahamian and Apenninic Limestones of Identical Lithofacies and Age: Geological Notes. AAPG Bulletin 59, 524-530.

De Castro, P., 1985. Sellialveolina vialii COLA-LONGO, 1963.- In Schroeder.R. Neumann, M. (eds.): Les grands Foraminifères du Crétacé moyen de la région méditerranéenne. Geobios, Mem. Spec 7, 88-97.

Delcourt, P.A., Delcourt, H.R., Cridlebaugh, P.A., Chapman, J., 1986. Holocene ethnobotanical and paleoecological record of human impact on vegetation in the Little Tennessee River Valley, Tennessee. Quaternary Research 25, 330-349.

Di Lucia, M., Trecalli, A., Mutti, M., Parente, M., 2012. Bio-chemostratigraphy of the Barremian-Aptian shallow-water carbonates of the southern Apennines (Italy): pinpointing the OAE1a in a Tethyan carbonate platform. Solid Earth 3, 1–28.

Ekart, D.D., Cerling, T.E., Montanez, I.P., Tabor, N.J., 1999. A 400 million year carbon isotope record of pedogenic carbonate: implications for paleoatmospheric carbon dioxide. American Journal of Science 299, 805-827.

Elliott, G.F., 1956. Further records of fossil calcareous algae from the Middle East. Micropaleontology 2, 327-334.

Frakes, L.A., Francis, J.E., Syktus, J.I., 1992. Climate modes of the Phanerozoic. Cambridge University Press, pp. 274.

Francis, J.E., Frakes, L.A., 1993. Cretaceous climates. Sedimentology Review, 1, 17-30.

Friedrich, O., Norris, R. D., Erbacher, J., 2012. Evolution of middle to Late Cretaceous oceans—a 55 my record of Earth's temperature and carbon cycle. Geology, 40, 107-110.

Frijia, G., Parente, M., 2008. Strontium isotope stratigraphy in the upper Cenomanian shallow-water carbonates of the southern Apennines: Short-term perturbations of marine $^{87}Sr/^{86}Sr$ during the oceanic anoxic event 2. Palaeogeography, Palaeoclimatology, Palaeoecology 261, 15–29.

Frijia, G., Parente, M., Di Lucia, M., Mutti, M., 2015. Carbon and strontium isotope stratigraphy of the Upper Cretaceous (Cenomanian-Campanian) shallow-water carbonates of southern Italy: Chronostratigraphic calibration of larger foraminifera biostratigraphy, Cretaceous Res. 53, 110–139.

Frijia, G., Parente, M., Iannace, A., 2005. Thermal maturity of the southern Apenninic platform unit (southern Italy): constraints from rock-eval pyrolysis T_{max} data. Atti Ticinensi di Scienze della Terra 10, 95-98.

Gradstein, F.M., Ogg, J.G., Schmitz, M.D., Ogg, G. 2012. The Geologic Time Scale 2012. Elsevier, Amsterdam, pp. 1139.

Graziano, R., Raspini, A., 2015. Long-and short-term hydroclimatic variabilities in the Aptian Tethys: Clues from the orbital chronostratigraphy of evaporite-rich beds in the Apennine carbonate platform (Mt. Faito, southern Italy). Palaeogeography, Palaeoclimatology, Palaeoecology 418, 319-343.

Haq, B.U., 2014. Cretaceous eustasy revisited. Global and Planetary Change 113, 44-58.

Haq, B.U., Hardenbol, J., Vail, P.R., 1987. Chronology of fluctuating sea levels since the Triassic. Science, 235, 1156-1167.

Hennhöfer, D.K., 2013. Palaeoecology and palaeobiology of rudist communities from the Tethyan and Caribbean realm: a new approach using grinding tomography and 3D reconstructions. Doctoral dissertation, PhD thesis, 148 pp., Universität Heidelberg, Heidelberg, Germany.

Hochuli, P.A., Menegatti, A.P., Weissert, H., Riva, A., Erba, E., Silva, I.P., 1999. Episodes of high productivity and cooling in the early Aptian Alpine Tethys. Geology 27, 657-660.

Hu, X., Wagreich, M., Yilmaz, I.O., 2012. Marine rapid environmental/climatic change in the Cretaceous greenhouse world. Cretaceous Research 38, 1-6.

Huber, B. T., 1998. Tropical paradise at the Cretaceous poles? Science 282, 2199-2200.

Huber, B.T., Hodell, D.A., Hamilton, C.P., 1995. Middle–Late Cretaceous climate of the southern high latitudes: stable isotopic evidence for minimal equator-to-pole thermal gradients. Geological Society of America Bulletin, 107, 1164-1191.

Huber, B.T., Leckie, R.M., 2011. Planktic foraminiferal species turnover across deep-sea Aptian/Albian boundary sections. The Journal of Foraminiferal Research, 41, 53-95.

Huck S., Heimhofer, U., 2015. Improving shallow-water carbonate chemostratigraphy by means of rudist bivalve sclerochemistry. Geochem. Geophys. Geosyst. 16, 3111–3128.

Immenhauser, A., Hillgärtner, H., Van Bentum, E., 2005. Microbial-foraminiferal episodes in the Early Aptian of the southern Tethyan margin: ecological significance and possible relation to oceanic anoxic event 1a. Sedimentology 52, 77-99.

Jenkyns, H. C., 2010. Geochemistry of oceanic anoxic events. Geochemistry, Geophysics, Geosystems 11.

Jones, C. E., Jenkyns, H. C., 2001. Seawater strontium isotopes, oceanic anoxic events, and seafloor hydrothermal activity in the Jurassic and Cretaceous. American Journal of Science, 301, 112-149.

Kennedy, W.J., 1984. Ammonite faunas and the ‘standard zones’ of the Cenomanian to Maastrichtian Stages in their type areas, with some proposals for the definition of the stage boundaries by ammonites. Bulletin of the geological Society of Denmark, 33, 147-163.

Kominz, M.A., Browning, J.V., Miller, K.G., Sugarman, P.J., Mizintseva, S., Scotese, C. R., 2008. Late Cretaceous to Miocene sea-level estimates from the New Jersey and Delaware coastal plain coreholes: an error analysis. Basin Research, 20, 211-226.

Larson, R.L., 1991. Latest pulse of Earth: Evidence for a mid-Cretaceous superplume. Geology 19, 547-550.

Locklair, R., Sageman, B., Lerman, A., 2011. Marine carbon burial flux and the carbon isotope record of Late Cretaceous (Coniacian–Santonian) Oceanic Anoxic Event III. Sedimentary Geology 235, 38-49.

Mancinelli, A., Chiocchini, M., 2006. Cretaceous benthic foraminifers and calcareous algae from Monte Cairo (southern Latium, Italy). Bollettino della Società Paleontologica Italiana 45, 91-113.

Masse, J.P., Philip, J., 1986. L’évolution des rudistes au regard des principaux événements géologiques du Crétacé. Bulletin du Centre de Recherches Elf Exploration Production 10, 437-456.

Maurer, F., Van Buchem, F.S., Eberli, G.P., Pierson, B.J., Raven, M.J., Larsen, P.H., Vincent, B., 2013. Late Aptian long-lived glacio-eustatic lowstand recorded on the Arabian Plate. Terra Nova 25, 87-94.

McAnena, A., Flögel, S., Hofmann, P., Herrle, J.O., Griesand, A., Pross, J., Talbot, H.M., Retemeyer, J., Wallmann, K., Wagner, T., 2013. Atlantic cooling associated with a marine biotic crisis during the mid-Cretaceous period. Nature Geoscience 6, 558-651.

Miller, K.G., Barrera, E., Olsson, R.K., Sugarman, P.J., Savin, S.M., 1999. Does ice drive early Maastrichtian eustasy?. Geology, 27, 783-786.

Miller, K.G., Kominz, M.A., Browning, J.V., Wright, J.D., Mountain, G.S., Katz, M.E., Sugarman, P.J., Cramer, B.S., Christie-Blick, N., Pekar, S.F., 2005. The Phanerozoic record of global sea-level change. science, 310, 1293-1298.

Mondillo, N., Balassone, G., Boni, M., Rollinson, G., 2011. Karst bauxites in the Campania Apennines (southern Italy): a new approach. Periodico di Mineralogia 80, 407-432.

Mutterlose, J., Bornemann, A., Herrle, J., 2009. The Aptian–Albian cold snap: Evidence for. Neues Jahrbuch für Geologie und Paläontologie-Abhandlungen 252, 217-225.

O'Brien, C.L., Robinson, S.A., Pancost, R.D., Damsté, J.S.S., Schouten, S., Lunt, D.J., Alsenz, H., Bornemann, A., Bottini, C., Brassell, S.C., Farnsworth, A., Forster, A., Huber, B.T., Inglis, G.N., Jenkyns, H., C., Linnert, C., Littler, K., Markwick, P., McAnena, A., Mutterlose, J., Naafs, B., D., A., Püttmann, W., Sluijs, A., Helmond, N., A., G., M. van, Vellekoop, J., Wagner, T., Wrobel, N., E., 2017. Cretaceous sea-surface temperature evolution: Constraints from TEX_{86} and planktonic foraminiferal oxygen isotopes. Earth-science reviews 172, 224-247.

Parente, M., Frijia, G., Di Lucia, M., 2007. Carbon-isotope stratigraphy of Cenomanian-Turonian platform carbonates from southern Apennines (Italy): a chemostratigraphic approach to the problem of correlation between shallow water and deep-water successions. Journal of the Geological Society of London 164, 609-620.

Patacca, E., Scandone, P., 2007. Geology of the Southern Apennines. In: Mazzotti, A., Patacca, E., Scandone, P. (Eds.), CROP-04, Bollettino Societa Geologica italiana (Ital. J. Geosci.), Special Issue, 7, 75-119.

Philip, J., 1972. Paléoécologie des formations à rudistes du Crétacé supérieur - l'exemple du sud-est de la France. Palaeogeography, Palaeoclimatology, Palaeoecology 12, 205-222.

Pucéat, E., Lécuyer, C., Sheppard, S.M., Dromart, G., Reboulet, S., Grandjean, P., 2003. Thermal evolution of Cretaceous Tethyan marine waters inferred from oxygen isotope composition of fish tooth enamels. Paleoceanography, 18, 1433-1458.

Radoičić, R., 1959. Some problematic microfossils from the Dinarian Cretaceous. Bull. Serv. geol. Yougosl. 17, 87-92.

Rameil, N., Immenhauser, A., Warrlich, G., Hillgaertner, H., Droste, H.J., 2010. Morphological patterns of Aptian *Lithocodium–Bacinella* geobodies: relation to environment and scale. Sedimentology 57, 883-911.

Raspini, A., 2012. Shallow water carbonate platforms (Late Aptian-Early Albian, Southern Apennines) in the context of supraregional to global changes: re-appraisal of palaeoecological events as reflectors of carbonate factory response. Solid Earth 3, 225-249.

Rauch, M., 2005.Geochemie von Rudistenschalen-Beiträge zur Meerwasserchemie (Sr/Ca, Mg/Ca, $\delta^{13}C$) und Paläoklima der Kreide. Doctoral dissertation, PhD thesis, 198 pp., Ruhr-Univ. Bochum, Bochum, Germany.

Regidor-Higuera, I., García-Garmilla, F., Skelton, P.W., 2007. Sclerochronology and diagenesis of Late Cretaceous radiolitids (Bivalvia, Hippuritoidea), Spain. Cretaceous Rudists and Carbonate Platforms: Environmental Feedback, SEPM Special Publication 87, 115-140.

Ross, D.J., Skelton, P.W., 1993. Rudist formations of the Cretaceous: a palaeoecological, sedimentological and stratigraphical review. Sedimentology review 1, 73-91.

Ruberti, D., Bravi, S., Carannante, G., Vigorito, M., Simone, L., 2013. Decline and recovery of the Aptian carbonate factory in the southern Apennine carbonate shelves (southern Italy): climatic/oceanographic vs. local tectonic controls. Cretaceous Research 39, 112-132.

Sahagian, D., Pinous, O., Olferiev, A., Zakharov, V., 1996. Eustatic curve for the Middle Jurassic--Cretaceous based on Russian platform and Siberian stratigraphy: Zonal resolution. AAPG bulletin 80, 1433-1458.

Sartoni, S., Crescenti, U., 1962. Ricerche biostratigrafiche nel Mesozoico dell'Appennino meridionale. Giornale di Geologia 29, 161-293.

Schettino, A., Turco, E., 2011. Tectonic history of the western Tethys since the Late Triassic. Bulletin 123, 89-105.

Scholle, P.A., Arthur, M.A., 1980. Carbon isotope fluctuations in Cretaceous pelagic limestones: potential stratigraphic and petroleum exploration tool. AAPG Bulletin 64, 67-87.

Schöne, B.R., Giere, O., 2005. Growth increments and stable isotope variation in shells of the deep-sea hydrothermal vent bivalve mollusk Bathymodiolus brevior from the North Fiji Basin, Pacific Ocean. Deep Sea Research Part I: Oceanographic Research Papers 52, 1896-1910.

Schumann, D., Steuber, T., 1997. Rudisten. Erfolgreiche Siedler und Riffbauer der Kreidezeit. Städte unter Wasser-2 Milliarden Jahre. Kleine Senckenberg-Reihe 24, 117-122.

Selli, R., 1957. Sulla trasgressione del Miocene nell'Italia meridionale. Giornale di Geologia 2, 1-54.

Selli, R., 1962. Il Paleogene nel quadro della Geologia dell'Italia Centro-Meridionale. Memorie della Societ_a Geologica Italiana 3, 737-789.

Sgrosso, I., 1998. Possibile evoluzione cinematica miocenica nell'orogene centro-sud appenninico. Bollettino della Società geologica italiana 117, 679-724.

Skelton, P.W., 1978. The evolution of functional design in rudists (Hippuritacea) and its taxonomic implications. Phil. Trans. R. Soc. Lond. B 284, 305-318.

Skelton, P.W., Gili, E., 1991. Palaeoecological classification of rudist morphotypes. In First International Conference on Rudists, Proccedings, Serbian Geological Society, Belgrade, 71-86.

Skelton, P.W., Smith, A.B., 2000. A preliminary phylogeny for rudist bivalves: sifting clades from grades. Geological Society, London, Special Publications 177, 97-127.

Skelton, P.W., Spicer, R.A., Kelley, S.P., Gilmour, I., 2003. The cretaceous world. The Cretaceous World, by Peter W. Skelton and Robert A. Spicer and Simon P. Kelley and Iain Gilmour. Cambridge, UK. Cambridge University Press, July 2003, 360.

Steuber, T., 1996. Stable isotope sclerochronology of rudist bivalves: growth rates and Late Cretaceous seasonality. Geology 24, 315-318.

Steuber, T., 1999. Isotopic and chemical intra-shell variations in low-Mg calcite of rudist bivalves (Mollusca-Hippuritacea): disequilibrium fractionations and late Cretaceous seasonality. Int Journ Earth Sciences 88, 551–570.

Steuber, T., 2000. Skeletal growth rates of Upper Cretaceous rudist bivalves: Implications for carbonate production and organism-environment feedbacks. Geological Society, London, Special Publications 178, 21-32.

Steuber, T., 2003. Strontium isotope stratigraphy of Cretaceous hippuritid rudist bivalves: rates of morphological change and heterochronic evolution. Palaeogeography, Palaeoclimatology, Palaeoecology 200, 221-243.

Steuber, T., Löser, H., 2000. Species richness and abundance patterns of Tethyan Cretaceous rudist bivalves (Mollusca: Hippuritacea) in the central-eastern Mediterranean and Middle East, analysed from a palaeontological database. Palaeogeography, Palaeoclimatology, Palaeoecology 162, 75-104.

Steuber, T., Rauch, M., Masse, J. P., Graaf, J., Malkoč, M., 2005. Low-latitude seasonality of Cretaceous temperatures in warm and cold episodes. Nature, 437, 1341-1344.

Wagreich, M., 2012. "OAE 3"-regional Atlantic organic carbon burial during the Coniacian-Santonian. Climate of the Past 8, 1447.

Wanamaker Jr, A.D., Hetzinger, S., Halfar, J., 2011. Reconstructing mid-to high-latitude marine climate and ocean variability using bivalves, coralline algae, and marine sediment cores from the Northern Hemisphere. Palaeogeography, Palaeoclimatology, Palaeoecology 302, 1-9.

Wang, Y., Huang, C., Sun, B., Quan, C., Wu, J., Lin, Z., 2014. Paleo-CO2 variation trends and the Cretaceous greenhouse climate. Earth-Science Reviews 129, 136-147.

Weissert, H., 1991. Ice age interludes during the time of Cretaceous greenhouse climate?. In: Controversies in Modern Geology, edited by D. W. Mueller et al., 173–191.

2. Methodology

In the following chapter, the applied methodologies of this thesis are briefly presented, including fieldwork procedure, sample preparation and laboratory work. Furthermore, the usability of the analysed elements as tools for palaeoenvironmental reconstructions and their use as indicator for diagenetic alteration is described.

2.1 Field Work and Thin Section Microscopy

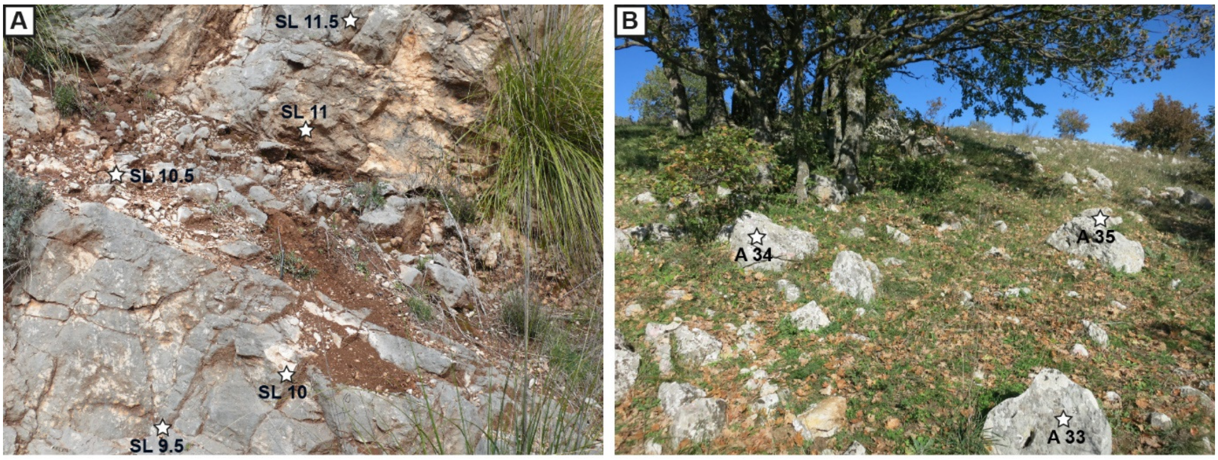

Fig. 2.1: Digital images of outcrop sites studied in this thesis: (A) Stars mark five samples (SL-9.5 to SL-11.5) taken with an average spacing of 0.5 m at the SL section. (B) Due to hampered outcrop conditions, the average sample spacing (A 33 to A 35) needed to be expanded to 1 m (stars).

During two field campaigns in November 2015 and March 2017, the 597 m-thick Santa Lucia (SL) section and the 469 m-thick Monte La Costa (MLC) section were logged and studied in detail. The carbonate classification scheme of Dunham (1962), modified by Embry and Klovan (1971) was applied for an outcrop-based carbonate facies description supported by petrographic analysis of polished slabs and thin sections. The fossil content of the samples was described, giving a particular focus to pristine rudist and chondrodont shells, non-skeletal components, subaerial exposure surfaces and karstic features. Samples for geochemical and petrographic investigations were taken at an average spacing of 0.5 m (Fig. 2.1 A). Across facies boundaries and discontinuity surfaces, a higher sample density was applied (spacing 0.1 m). Partially weathered outcrop conditions and accessibility obstructed the identification of bedding planes and other sedimentary features and sample spacing had to be widened to 1 m where necessary (Fig. 2.1 B).

Lithological and sedimentological analyses were supported by thin section analysis. A total of 131 thin sections of the SL section and 180 thin sections of the MLC section were prepared and analysed under a binocular. In addition, emphasis was laid on the identification and classification of microencrusting organisms (*Lithocodium-Bacinella*).

For bulk isotope analysis, all collected samples were cut, cleaned with distilled water and dried for 24 h at 40 °C. Rock specimens were screened with a magnifying glass to identify the most fine-grained portions, which were sampled with a hand-held micro-drill equipped with tungsten drill bits.

2.2 Isotope-ratio Mass Spectrometry (Gasbench)

The ratios of isotopes in open seawater equilibrate in a relatively short amount of time. Hence, long-term variations are interpreted as a global signal and are subsequently suitable for global and local correlations (Skelton et al., 2003). An added application lies in revealing the development of Earth's climate (hot and cold house episodes), the evolution of biota and the existence of diagenesis (Gradstein et al., 2012).

The carbon isotope record is based on the partitioning between organic carbonate and carbonate carbon reservoirs (e.g. Shackleton and Hall, 1984; Kump and Arthur, 1999; Sundquist and Visser, 2004) and is thus connected to the biosphere (Gradstein et al., 2012). Further processes that influence the carbon cycle are e.g. volcanic emission (Ridgwell and Edwards, 2007), the dissociation of methane clathrates (Dickens, 1995), continental weathering, upwelling, OAEs (Gradstein et al., 2012) or deep burial of carbon-rich rocks like carbonates or organic-rich mudstones (Skelton et al., 2003). Carbon isotope ratios are mostly used to correlate sediments (carbon isotope stratigraphy) (Weissert, 1989).

Variations in the oxygen cycle are mainly caused by climate changes, which make this isotope ratio, derived from calcite shells or from phosphatic fish skeletons, a valuable tool for its reconstruction: Lighter oxygen (^{16}O) reacts faster than heavy oxygen (^{18}O). During evaporation processes or the formation of ice, lighter oxygen escapes more easily and the residual water is enriched in heavy oxygen (^{18}O), which increases its $\delta^{18}O$ ratio.

An enrichment or depletion is expressed in the delta notation after Epstein (1951) that normalizes the isotope ratio to a selected standard:

$$\delta\ (‰) = \left(\frac{R_{sample}}{R_{standard}} - 1\right) * 1000 \tag{1}$$

with R_{sample} and $R_{standard}$ being the ratios of the sample and the standard reference material.

For this study, $\delta^{13}C$ curves were primarily used to correlate shallow marine carbonate sections with pelagic sections and additionally to link various sections of the ACP. The analysed $\delta^{18}O$ values, derived from the low-Mg calcite shells, were used for palaeotemperature reconstructions. Their combination (cross-plot) marked the influence of diagenetic alteration, which is applied to the highly fragmentary record of shallow marine sections and their included subaerial exposure surfaces of great importance. In total, $\delta^{18}O$ and $\delta^{13}C$ values of 1647 bulk and 502 shell samples were analysed using a Thermo Fisher Scientific Gasbench II carbonate device connected to a Thermo Fisher Scientific Delta 5 Advantage isotope ratio mass spectrometer at the stable isotope laboratory of the Institute of Geology, Leibniz University Hannover, Germany. The gas bench uses viscous water-free (98 g mol^{-1}) orthophosphoric acid at 72°C to release CO_2 of the calcitic sample material 1 h before the measurement is started. Repeated analyses of certified carbonate standards (NBS 19, IAEA CO-1, NBS 18 and Carrara Marble) show an external reproducibility of $\leq$ 0.06 ‰ for $\delta^{13}C$ and 0.08 ‰ for $\delta^{18}O$. Values are expressed in conventional delta notation relative to the Vienna-Pee Dee Formation belemnite (VPDB) international standard, in parts per thousand (‰).

2.3 Trace Element Analysis and Strontium Isotope Analysis (SIS)

The $^{87}Sr/^{86}Sr$ ratio is used for a numerical age determination (McArthur, 2004) to elucidate the duration of gaps (Miller et al., 1988), to define biozones (McArthur et al., 1993) and stages (Weedon and Jenkyns, 1999) or to track changes in sedimentation rate (McArthur, 2007). It is assumed that the world's oceans are homogenous, which means that the residence time of Sr in the ocean (10^6 a) is higher than oceans mixing time (10^3 a). The variations in the $^{87}Sr/^{86}Sr$ ratio of oceans are caused by the fact that continental rocks contain more ^{87}Sr (relative to ^{86}Sr) than rocks derived from the mantle. Consequently, if continental weathering increases and/or oceanic volcanism decreases the $^{87}Sr/^{86}Sr$ ratio of the ambient ocean water will increase. Previous studies have shown that the outer low-Mg calcite layer of Cretaceous rudist and chondrodont shells are suitable archives for the strontium isotope composition of contemporaneous ocean waters (Steuber et al., 2005; Frijia and Parente, 2008; Frijia et al., 2015; Huck and Heimhofer, 2015), enabling accurate age assignments of shallow marine strata by comparison with the global marine strontium isotope record (Howarth and McArthur, 1997; McArthur et al., 2001).

All found shells were cleaned, cut and dried like the bulk samples and afterwards selected by means of the following criteria:

1. well visible growth increments
2. fibrous microstructure of the compact outer shell layer
3. negligible impact of bioerosion and fracturing

Well preserved shells, classified as such by fullfulling aforementioned criteria, were used for further analysis. Their stable isotope ratios were measured as described above at the Institute of Geology, Leibniz University Hannover, Germany. For further analysis, powdered samples (1.35 to 1.65 mg) of 56 shells were analysed for their elemental composition (Ca, Mg, Sr, Fe and Mn) using inductively coupled plasma-atomic emission spectrometry (ICP-AES) at the isotope laboratory of the Institute of Geology, Mineralogy and Geophysics at Ruhr-University Bochum (RUB), Germany. Element concentration is used as proxy for evaluating the impact and degree of diagenetic alteration (Brand and Veizer, 1980). Re-equilibration processes with diagenetic fluids typically result in elevated Fe and Mn concentrations paired with low Sr concentrations (Brand and Veizer, 1980; Veizer, 1983; Al-Aasm and Veizer 1986; Steuber et al., 2005). A further indicator for diagenesis in rudist shells is a parallel decrease in Mg concentration and $\delta^{18}O$ values (Rauch, 2005; Marshall, 1992). 39 shells with < 100 ppm Mn and Fe concentrations (Steuber, 1999) and strontium concentrations > 800 ppm for rudists and > 500 ppm for chondrodonts (Steuber, 1999; Damas Mollá et al., 2006) were analysed at RUB for their strontium isotope ratios using a thermal ionisation mass-spectrometer (Finnigan MAT 262) in dynamic mode. Corrections of measured ratios to USGS EN-1 (rather than to NIST SRM987) were done following the procedure of Howarth and McArthur (1997).

2.4 µX-ray Fluorescence

To analyse the preservation of shells, the µXRF scanning method was applied. This non-destructive method is used to characterize the abundance of different elements in the shell. A sample is radiated with an X-ray source and various elements are detected due to their emitted fluorescence. The measurements were performed at the research group Analytical, Environmental and Geochemistry of the Vrije Universiteit (Brussel) using a Tornado M4 micro X-ray fluorescence (µXRF) scanner (Bruker Nano GmbH, Berlin, Germany). The µXRF scanner is equipped with a Rhodium source and two X Flash 430 Silicon Drift detectors. µXRF maps were created to allow a semi-quantitative analysis of the shell and an assessment of major and trace elements. Therefore, the entire polished shell surface was scanned using a short acquisition time of 1 ms per pixel. Quantitative point-by-point µXRF line scans were applied to each of the analysed shells, perpendicular to growth lamellae and following the growth direction (starting at the umbonal area). The average sampling space accounted 100 µm. The X-ray beam dwelled on each point for 60 s at maximized energy settings (50 kV, 600 µA, no source filter). Due to the growth form (morphology), various line scans were compiled to cover the entire shell. For further details, refer to de Winter and Claeys (2016) and de Winter et al. (2017). A total of 28 elements (Fig. 2.2) have been detected. This study focuses only on strontium (Sr), manganese (Mn), magnesium (Mg) and iron (Fe), which are the most important elements for the determination of diagenetic alteration (Steuber et al., 1999).

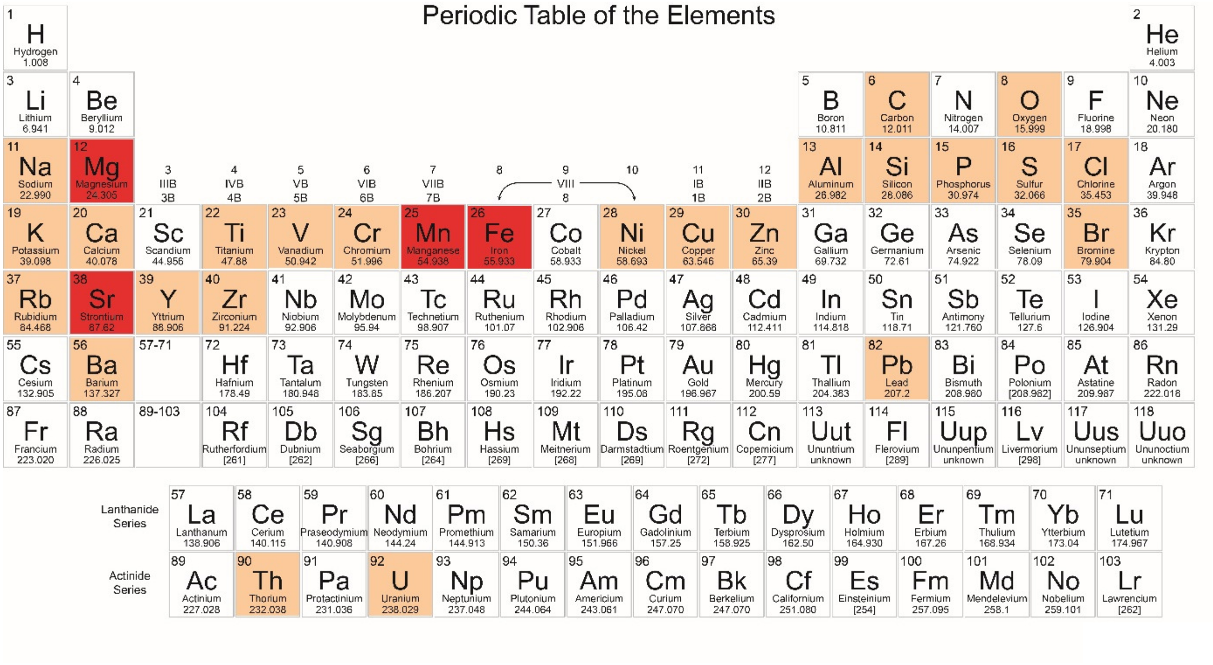
Periodic Table of the Elements
1 H Hydrogen 1.008
2 He Helium 4.003
3 Li Lithium 6.941
4 Be Beryllium 9.012
5 B Boron 10.811
6 C Carbon 12.011
7 N Nitrogen 14.007
8 O Oxygen 15.999
9 F Fluorine 18.998
10 Ne Neon 20.180
11 Na Sodium 22.990
12 Mg Magnesium 24.305
3 IIIB 3B
4 IVB 4B
5 VB 5B
6 VIB 6B
7 VIIB 7B
8
9 VIII 8
10
11 IB 1B
12 IIB 2B
13 Al Aluminum 26.982
14 Si Silicon 28.086
15 P Phosphorus 30.974
16 S Sulfur 32.066
17 Cl Chlorine 35.453
18 Ar Argon 39.948
19 K Potassium 39.098
20 Ca Calcium 40.078
21 Sc Scandium 44.956
22 Ti Titanium 47.88
23 V Vanadium 50.942
24 Cr Chromium 51.996
25 Mn Manganese 54.938
26 Fe Iron 55.933
27 Co Cobalt 58.933
28 Ni Nickel 58.693
29 Cu Copper 63.546
30 Zn Zinc 65.39
31 Ga Gallium 69.732
32 Ge Germanium 72.61
33 As Arsenic 74.922
34 Se Selenium 78.09
35 Br Bromine 79.904
36 Kr Krypton 84.80
37 Rb Rubidium 84.468
38 Sr Strontium 87.62
39 Y Yttrium 88.906
40 Zr Zirconium 91.224
41 Nb Niobium 92.906
42 Mo Molybdenum 95.94
43 Tc Technetium 98.907
44 Ru Ruthenium 101.07
45 Rh Rhodium 102.906
46 Pd Palladium 106.42
47 Ag Silver 107.868
48 Cd Cadmium 112.411
49 In Indium 114.818
50 Sn Tin 118.71
51 Sb Antimony 121.760
52 Te Tellurium 127.6
53 I Iodine 126.904
54 Xe Xenon 131.29
55 Cs Cesium 132.905
56 Ba Barium 137.327
57-71
72 Hf Hafnium 178.49
73 Ta Tantalum 180.948
74 W Tungsten 183.85
75 Re Rhenium 186.207
76 Os Osmium 190.23
77 Ir Iridium 192.22
78 Pt Platinum 195.08
79 Au Gold 196.967
80 Hg Mercury 200.59
81 Tl Thallium 204.383
82 Pb Lead 207.2
83 Bi Bismuth 208.980
84 Po Polonium [208.982]
85 At Astatine 209.987
86 Rn Radon 222.018
87 Fr Francium 223.020
88 Ra Radium 226.025
89-103
104 Rf Rutherfordium [261]
105 Db Dubnium [262]
106 Sg Seaborgium [266]
107 Bh Bohrium [264]
108 Hs Hassium [269]
109 Mt Meitnerium [268]
110 Ds Darmstadtium [269]
111 Rg Roentgenium [272]
112 Cn Copernicium [277]
113 Uut Ununtrium unknown
114 Fl Flerovium [289]
115 Uup Ununpentium unknown
116 Lv Livermorium [298]
117 Uus Ununseptium unknown
118 Uuo Ununoctium unknown
Lanthanide Series
57 La Lanthanum 138.906
58 Ce Cerium 140.115
59 Pr Praseodymium 140.908
60 Nd Neodymium 144.24
61 Pm Promethium 144.913
62 Sm Samarium 150.36
63 Eu Europium 151.966
64 Gd Gadolinium 157.25
65 Tb Terbium 158.925
66 Dy Dysprosium 162.50
67 Ho Holmium 164.930
68 Er Erbium 167.26
69 Tm Thulium 168.934
70 Yb Ytterbium 173.04
71 Lu Lutetium 174.967
Actinide Series
89 Ac Actinium 227.028
90 Th Thorium 232.038
91 Pa Protactinium 231.036
92 U Uranium 238.029
93 Np Neptunium 237.048
94 Pu Plutonium 244.064
95 Am Americium 243.061
96 Cm Curium 247.070
97 Bk Berkelium 247.070
98 Cf Californium 251.080
99 Es Einsteinium [254]
100 Fm Fermium 257.095
101 Md Mendelevium 258.1
102 No Nobelium 259.101
103 Lr Lawrencium [262]

Fig. 2.2: Periodic table of elements with all the detected elements in the µXRF scans marked in orange. Elements considered in chapter 4 are marked in red (modified after Helmenstine, 2018).

2.5 Cathodoluminescence (CL)

To analyse the preservation state of a shell, cathodoluminescence (CL) microscopy was applied to polished thin sections and polished slabs. CL is a non-destructive tool to identify primary or diagenetic structures. In order to produce luminescence, the sample is bombarded with electrons. Main activators are Mn^{2+} and Pb^{2+} (orange-red luminescence), while Fe^{2+} acts as squeezer (no luminescence) (Flügel, 2010). CL was performed using a Reliontron (Relion, U.S.A) cold-cathode luminescence device hosted at the University of Texas in San Antonio (USA). The CL microscope is characterized by an acceleration voltage ranging from 10 to 15 kV and a current intensity ranging from 0.8 to 1.2 mA. The CL chamber was mounted on a Leica DM2700 microscope equipped with 2.5x, 4x, 10x and 20x magnification objectives.

2.6 References

Al-Aasm, I.S., Veizer, J., 1986. Diagenetic stabilization of aragonite and low-Mg calcite; I, Trace elements in rudists. Journal of Sedimentary Research 56, 138-152.

Brand, U., Veizer, J., 1980. Chemical diagenesis of a multicomponent carbonate system-1: Trace elements, Journal of Sedimentary Petrology, 50, 1219-1236.

Damas Mollá, L., Aranburu Artano, A., García Garmilla, F., 2006. Resistencia a la alteración diagenética de conchas de Chondrodonta sp en las calizas rojas del Aptiense–Albiense inferior de Ereño (Bizkaia). GeoGaceta 40, 195-198.

de Winter, N.J., Sinnesael, M., Makarona, C., Vansteenberge, S., Claeys, P., 2017. Trace element analyses of carbonates using portable and micro-X-ray fluorescence: performance and optimization of measurement parameters and strategies. Journal of Analytical Atomic Spectrometry 32, 1211-1223.

de Winter, N.J., Snoeck, C., Claeys, P., 2016. Seasonal cyclicity in trace elements and stable isotopes of modern horse enamel. PloS one 11.

Dickens, G.R., O'Neil, J.R., Rea, D.K., Owen, R.M., 1995. Dissociation of oceanic methane hydrate as a cause of the carbon isotope excursion at the end of the Paleocene. Paleoceanography 10, 965-971.

Dunham, R.J., 1962. Classification of carbonate rocks according to depositional textures. In: Harn, W.E., ed., Classification of carbonate rocks: Am. Assoc. Petroleum Geologists Mem. 1, 108-121.

Embry, A.F., III, Klovan, J.E. 1971. A Late Devonian reef tract on Northeastern Banks Island, NWT. Bulletin of Canadian Petroleum Geology 19, 730-781.

Epstein, S., Buchsbaum, R., Lowenstam, H., Urey, H.C., 1951. Carbonate-water isotopic temperature scale. Geological Society of America Bulletin 62, 417-426.

Flügel, E. 2010. Microfacies analysis of limestones. Analysis, Interpretation and Application. Springer –Verlag, Berlin-Heidelberg, pp. 984.

Frijia, G., Parente, M., 2008. Strontium isotope stratigraphy in the upper Cenomanian shallow-water carbonates of the southern Apennines: Short-term perturbations of marine ^{87}Sr/^{86}Sr during the oceanic anoxic event 2. Palaeogeography, Palaeoclimatology, Palaeoecology 261, 15–29.

Frijia, G., Parente, M., Di Lucia, M., Mutti, M., 2015. Carbon and strontium isotope stratigraphy of the Upper Cretaceous (Cenomanian-Campanian) shallow-water carbonates of southern Italy: Chronostratigraphic calibration of larger foraminifera biostratigraphy, Cretaceous Res. 53, 110–139.

Gradstein, F.M., Ogg, J.G., Schmitz, M.D., Ogg, G. 2012. The Geologic Time Scale 2012. Elsevier, Amsterdam, pp. 1139.

Helmenstine, T., 2018. Periodic Table with 118 Elements - Black and White. Accessed: 6. January, 2019, from https://sciencenotes.org/periodic-table-2017-edition-black-white/.

Howarth, R., McArthur, J., 1997. Statistics for strontium isotope stratigraphy: A robust LOWESS fit to the marine Sr-isotope curve for 0 to 206 Ma, with Look-Up Table for derivation of numeric age. The Journal of Geology 105, 441-456.

Huck S., Heimhofer, U., 2015. Improving shallow-water carbonate chemostratigraphy by means of rudist bivalve sclerochemistry. Geochem. Geophys. Geosyst. 16, 3111–3128.

Kump, L.R., Arthur, M.A., 1999. Interpreting carbon-isotope excursions: carbonates and organic matter. Chemical Geology 161, 181-198.

Marshall, J.D., 1992. Climatic and oceanographic isotopic signals from the carbonate rock record and their preservation. Geological magazine 129, 143-160.

McArthur, J.M., Howarth, R.J., 2004. Strontium isotope stratigraphy. In: Gradstein, F., Ogg, J., Smith, A. (Eds.), A Geological Time Scale. Cambridge University Press, Cambridge, UK, 96-105.

McArthur, J.M., Howarth, R.J., Bailey, T.R., 2001. Strontium isotope Stratigraphy: LOWESS Version 3: Best Fit to the Marine Sr-Isotope Curve for 0–509 Ma and Accompanying Look-up Table for Deriving Numerical Age. The Journal of Geology 109, 155-70.

McArthur, J.M., Janssen, N.M.M., Reboulet, S., Leng, M.J., Thirlwall, M.F., van de Schootbrugge, B., 2007. Palaeotemperatures, polar ice-volume, and isotope stratigraphy (Mg/Ca, d^{18}O, d^{13}C, ^{87}Sr/^{86}Sr): The Early Cretaceous (Berriasian, Valanginian, Hauterivian). Palaeogeography, Palaeoclimatology, Palaeoecology 248, 391-430.

McArthur, J.M., Thirlwall, M.F., Chen, M., Gale, A.S., Kennedy, W.J., 1993. Strontium isotope stratigraphy in the late Cretaceous: Numerical calibration of the Sr isotope curve, and international correlation for the Campanian. Paleoceanography 8, 859-873.

Miller, K.G., Feigenson, M.D., Kent, D.V., Olson, R.K., 1988. Upper Eocene to Oligocene isotope (^{87}Sr/^{86}Sr, d18O, d13C) standard section, Deep Sea Drilling Project Site 522. Paleoceanography 3, 223-233.

Rauch, M., 2005.Geochemie von Rudistenschalen-Beiträge zur Meerwasserchemie (Sr/Ca, Mg/Ca, δ^{13}C) und Paläoklima der Kreide. Doctoral dissertation, PhD thesis, 198 pp., Ruhr-Univ. Bochum, Bochum, Germany.

Ridgwell, A., Edwards, U., 2007. Geological carbon sinks. Greenhouse gas sinks in Greenhouse Gas Sinks, edited by D. S. Reay et al., 74 – 97.

Shackleton, N.J., Hall, M.A., 1984. Carbon isotope data from Leg 74 sediments. Initial Reports of the Deep Sea Drilling Project 74.

Skelton, P.W., Spicer, R.A., Kelley, S.P., Gilmour, I., 2003. The cretaceous world. The Cretaceous World, by Peter W. Skelton and Robert A. Spicer and Simon P. Kelley and Iain Gilmour. Cambridge, UK. Cambridge University Press, July 2003, 360.

Steuber, T., 1999. Isotopic and chemical intra-shell variations in low-Mg calcite of rudist bivalves (Mollusca-Hippuritacea): disequilibrium fractionations and late Cretaceous seasonality. Int. Journ. Earth Sciences 88, 551–570.

Steuber, T., Rauch, M., Masse, J. P., Graaf, J., Malkoč, M., 2005. Low-latitude seasonality of Cretaceous temperatures in warm and cold episodes. Nature, 437, 1341-1344.

Sundquist, E.T., Visser, K., 2004. The Geologic History of the Carbon Cycle. Treatise on Geochemistry 8, 425-472.

Veizer, J., 1983. Chemical diagenesis of carbonates: theory and application of trace element technique. In: Arthur, M.A., Anderson, T.F., Kaplan, I.R., Veizer, J., Land, L.S.Ž., Eds., Stable Isotopes in Sedimentary Geology 10, Society of Economic Paleontologists and Mineralogists Short Course Notes, 3.1–3.100.

Weedon, G.P., Jenkyns, H.C., 1999. Cyclostratigraphy and the Early Jurassic timescale: Data from the Belemnite Marls, southern England. Geological Society of America Bulletin 111, 1823-1840.

Weissert, H., 1989. C-isotope stratigraphy, a monitor of paleoenvironmental change: a case study from the Early Cretaceous. Surveys in Geophysics 10, 1-61.

3. Deciphering the Fragmentary Nature of Cretaceous Shallow-water Limestone Archives: A Case Study from the Subtropical Apennine Carbonate Platform

K. SCHMITT, U. HEIMHOFER, G. FRIJIA, M. DI LUCIA, S. HUCK

To be submitted to Newsletters on Stratigraphy.

Abstract

Shallow-water carbonate platform sections are valuable archives for the reconstruction of deep-time environmental and climatic conditions, but the low resolution of biostratigraphic schemes associated with frequent sedimentary hiatuses often hampers their precise chronostratigraphic assignment. Moreover, chemostratigraphic correlation of shallow-water sections with well-dated pelagic successions is notoriously difficult and afflicted with large uncertainties, as shallow-water bulk carbonate archives are particularly prone to the impact of diagenesis. This study examines central Tethyan mid-Cretaceous carbonate platform deposits exposed in the central Apennines (southern Italy) suffering several emersion phases, which cause sedimentary gaps of variable duration. The investigated sections (Santa Lucia, Monte La Costa) represent a transect through the Apennine Carbonate Platform, ranging from the lagoonal inner carbonate platform realm towards the platform margin. Although benthic foraminifera are at times scarce and the carbonates evidently suffered diagenetic alteration, high-resolution carbon isotope stratigraphy combined with (rudist and chondrodont shell) strontium isotope stratigraphy enables a correlation of the studied sections with pelagic composite reference curves. A detailed foraminiferal-algal biostratigraphic record of the studied shallow-water sections and their integration into high-resolution carbon and strontium isotope stratigraphy is presented. This approach allows precise estimates of the time lost in major sedimentary hiatuses, three of which were identified at the Santa Lucia locality. There, long-lasting (1 to 14 Ma) hiatuses cover parts of the Early Aptian (3.2 Myr), the Late Aptian (3.3 Myr) and the Late Albian to Cenomanian (14.3 Myr), the latter being associated with formation of karst-filling bauxite. The here presented documentation and dating of sedimentary hiatuses in the Apennine Carbonate Platform sector is essential to correlate emersion phases observed in the peri-mediterranean region, in particular with respect to the mechanisms of their origin.

Keywords: Apennine carbonate platform (ACP); Cretaceous; Integrated bio-and chemostratigraphy; Emersion Phases

3.1 Introduction

During the mid-Cretaceous, widespread neritic carbonate deposition occured in the Tethyan Ocean (Simo et al., 1993). Tropical carbonate factories formed large and complex sedimentary systems that document phases of extensive accumulation interrupted by growth crises related to environmental perturbations and/or tectonic activity (Skelton, 2003). Unfortunately, the assessment of shallow-water palaeoenvironmental variations on spatial and stratigraphic scales is often hampered by a limited resolution of applied biostratigraphic schemes and a lack of stratigraphic tie-points for correlation with well-dated pelagic successions (Frijia et al., 2015). The integration of chemostratigraphic (carbon and strontium isotopes) data into biostratigraphic frameworks significantly improves the temporal resolution of the Cretaceous shallow water rock record and furthermore helps to date and correlate strata on local and global scales, and across different depositional environments (Parente et al., 2007; Huck et al., 2013; Horikx et al., 2014; Frijia et al., 2015; Di Lucia et al., 2012; Raspini, 2012; Huck and Heimhofer, 2015). But even if shallow water carbonate archives may record secular and short-term carbon cycle changes of global extent, supra-regional chemostratigraphic correlation approaches are often hampered by strongly variable sedimentation rates and frequent subaerial exposure events, which produce significant stratigraphic gaps and thus, locally different carbon isotope patterns (Weissert et al., 2008; Di Lucia et al., 2012). Given the long residence time of strontium in the ocean, secular variations in $^{87}Sr/^{86}Sr$ ratios (McArthur et al., 2012) recorded in pristine low-Mg calcite shells enable to detect major sedimentary hiatuses (> 1 Myr) and to estimate the time lost in the corresponding hiatal surfaces (Huck and Heimhofer, 2015; Navidtalab et al., 2016).

This paper seeks to illustrate and quantify the fragmentary nature of Cretaceous shallow water limestone archives, using the example of the central Apennine Carbonate Platform (ACP) in southern Italy. Both tectonic movements and eustatic sea level oscillations affected periadriatic shallow water carbonate platform environments during the Middle to Late Cretaceous (Carannante et al., 2007), amongst others expressed by two major emersion phases and associated karst bauxite (bx) formation. Both the Middle Albian to Middle Cenomanian and the Middle-Late Cenomanian to Late Turonian platform exposure episodes (bx1/bx2) are assumed to be mainly driven by local tectonic processes (D'Argenio and Mindszenty, 1995; Mindszenty et al., 1995). Estimating the duration of hiatuses of variable order in the Apennine shallow-water record, however, is not an easy task and in particular complicated due to the locally different impact of tectonic processes on carbonate sedimentation and preservation (D’Argenio et al., 2011).

The aim of this study is therefore to establish a highly resolved integrated bio-chemostratigraphic framework for two expanded shallow water sections representing both lagoonal and platform margin settings of the Central ACP. Special attention was paid to the assessment of sedimentary and geochemical data documenting major emersion phases. Most importantly, this approach will allow estimating the time lost in major sedimentary gaps and identifying the (tectonic) processes causing platform exposure on a platform-wide scale.

3.2 Geological setting

The Apennines are a fold-and-thrust belt extended along the Italian Peninsula, composed in large parts of thick Mesozoic shallow-water limestones deposited in the Tethyan domain (Fig. 3.1 A; Di Bucci, et al., 2006; Parente et al., 2007; Ruberti et al., 2008). The formation of these carbonate rocks (parts of them forming the ACP) started in the Late Triassic (Cosentino et al., 2010). Orogenic uplift was initiated in the Late Cretaceous/Eocene with the northward movement of the Adriatic/Apulian foreland (belonging to the African plate), resulting in the subduction of the Tethyan Ocean and subsequent collision with the Corsican/Sardinian foreland (Eurasian plate) (Vezzani et al., 2010; Cosentino et al., 2010). Carbonate sedimentation continued in the ACP until the end of the Miocene with huge gaps in the sedimentary record caused by the starvation in carbonate production and/or subaerial exposure through the uplift of the whole platform (Selli, 1957; 1962). Neogene folding and thrusting created complex imbricated units through low- and high-angle faults, which form the nappes stack of the Central and Southern Apennines (Brandano et al., 2007; Cosentino et al., 2010; Boncio et al., 2016).

The modern geological structure of the Central and Southern Apennines is the result of Quaternary extensional tectonics with a horst structure being bordered by NE - SW dipping normal faults (Boncio et al., 2016). The ACP represents a system of partly connected open shallow-water carbonate platforms (incl. Capri-Bulgheria, Alburno-Cervati and Monti della Maddalena Unit; Simbruini-Matese Unit; Western Marsica-Meta Unit) that were separated by basins and deep water tongues linking the Umbria domain and the Lagonegro-Molise Basin (Patacca and Scandone, 2007; Fig. 3.1 A).

The studied sections (Fig. 3.1 B) are located along a SE-NW proximal-to-distal transect across the ACP and represent the transition from lagoon (Santa Lucia, SL) towards a platform margin setting (Monte La Costa, MLC). The SL section is situated in the Southern Apennines in the Monte Cairo Massif (Lazio region) and belongs to the so-called Lazio-Abruzzi carbonate platform (Brandano, 2007). The 600 m-thick section is accessible along a road cut between Villa Santa Lucia and Terelle at the southern slope of Monte Cairo (41°31'00.6"N 13°46'40.0"E to 41°31'02.0"N 13°47'02.8"E). Chiocchini et al. (2004) investigated, most probably, the same section but measured a total thickness of only 420 m, which complicates an integration of their data into the current study.

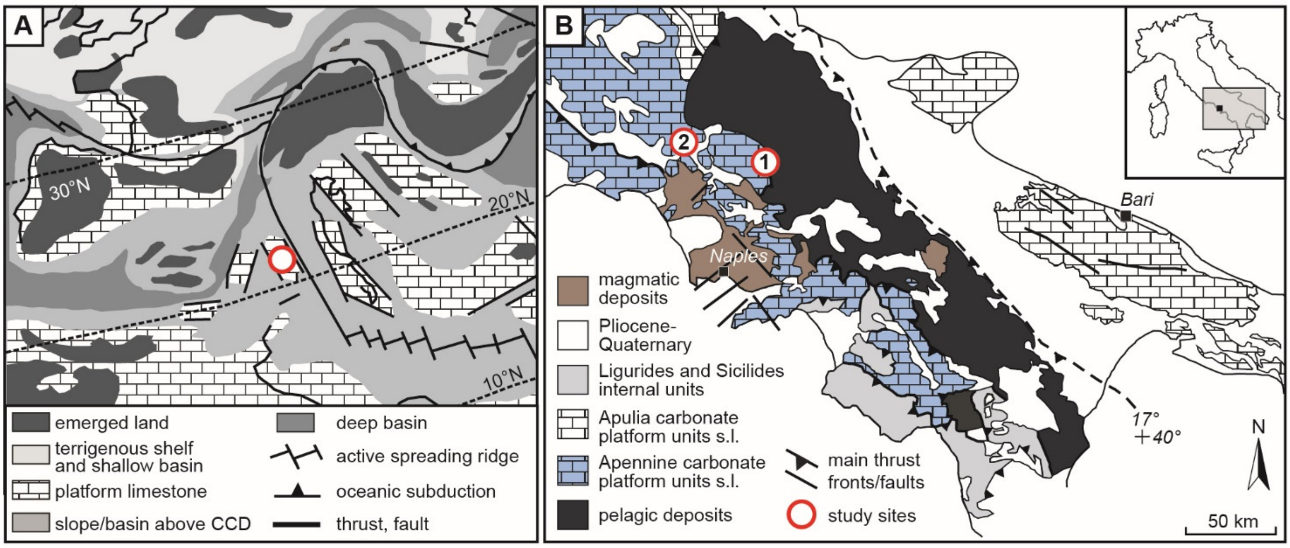
A
30°N
20°N
10°N
emerged land
terrigenous shelf and shallow basin
platform limestone
slope/basin above CCD
deep basin
active spreading ridge
oceanic subduction
thrust, fault
B
2
1
Naples
Bari
magmatic deposits
Pliocene-Quaternary
Ligurides and Sicilides internal units
Apulia carbonate platform units s.l.
Apennine carbonate platform units s.l.
pelagic deposits
main thrust fronts/faults
study sites
17°
+40°
N
50 km

Fig. 3.1: (A) Palaeogeographic map of the Upper Cretaceous showing the position of the study area of the Apennine Carbonate Platform (red circle). (B) Schematic geological map of the Central and Southern Apennines (Italy) with the location of the studied sections. 1 – Monte La Costa, 2 – Santa Lucia. Modified after Parente et al. (2007).

According to previous biostratigraphic observations based on benthic foraminifera and calcareous algae, the SL section covers the Hauterivian-Barremian to Upper Cenomanian interval (Chiocchini et al., 2004; Mancinelli and Chiocchini, 2006). The MLC section is located at the transition between the Central and Southern Apennines in the east-west oriented Matese Mountain Massif (Campania region). The 469 m-thick section (41°28'12.4"N 14°29'50.0"E) is located 1 km north of the village San Polo Matese. The section comprises platform margin shallow-water deposits of the Simbruini-Matese unit (Patacca and Scandone, 2007). Based on rudist and benthic foraminiferal biostratigraphy, the MLC succession has been attributed to the Barremian to Upper Cenomanian (Mainelli, 2000).

3.3 Field approaches and laboratory methods

3.3.1 Field work and thin section microscopy

During a second field campaign, the existing SL and MLC section logs (Schmitt et al., in preparation) have been extended. The sedimentological characterization involved an outcrop-based carbonate facies description supported by the analysis of 204 petrographic thin sections (Fig. 3.2). Strongly weathered outcrop conditions at MLC often hampered the identification of bedding planes and other sedimentary features. Therefore, lithological and sedimentological analysis of the MLC section is mainly based on thin section analysis. Samples for geochemical and petrographic investigations were taken at an average spacing of 0.5 m. Higher sample densities were applied across facies boundaries and discontinuity surfaces.

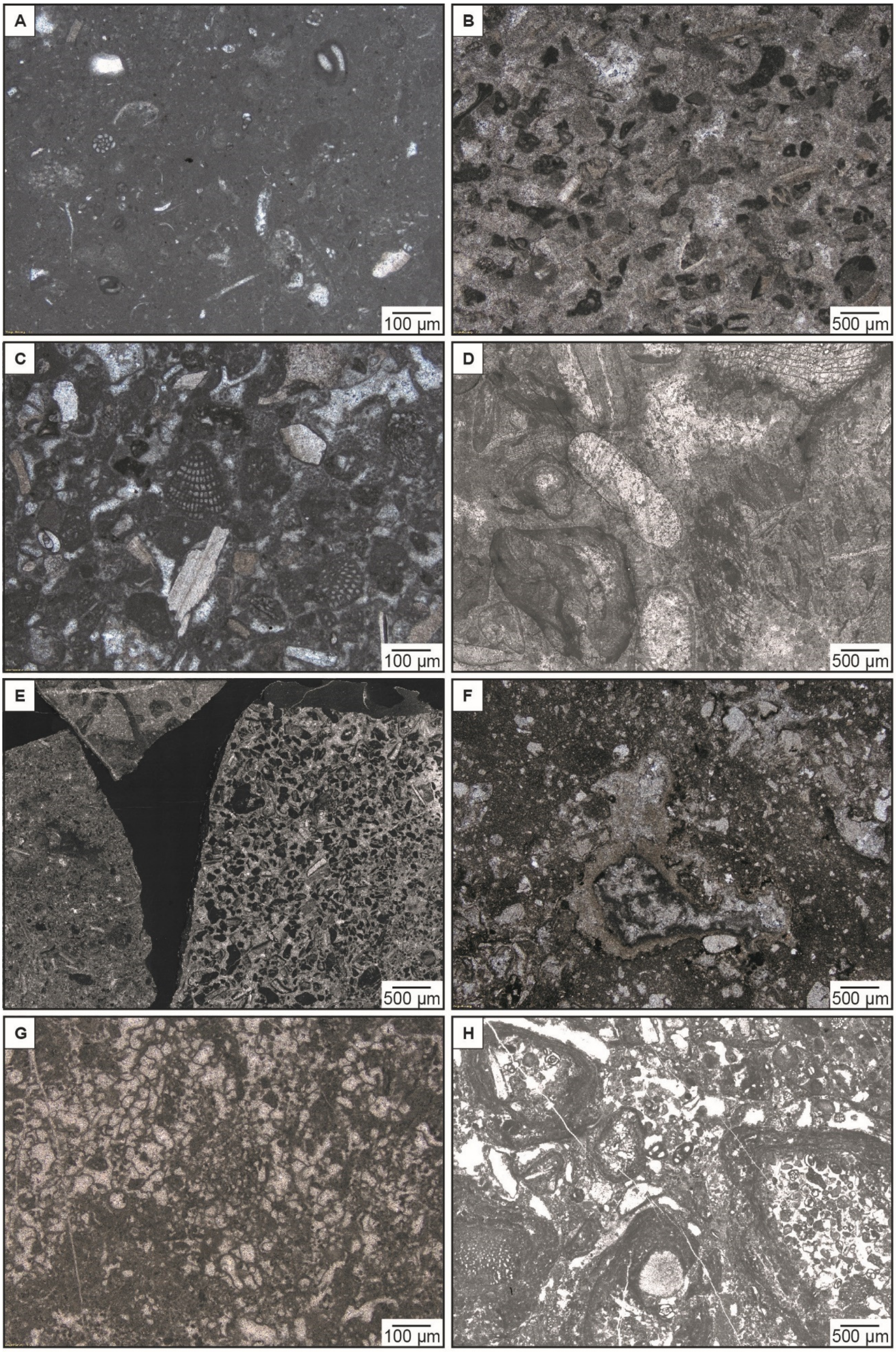
A
100 µm
B
500 µm
C
100 µm
D
500 µm
E
500 µm
F
500 µm
G
100 µm
H
500 µm

Fig. 3.2: Photomicrographs of representative microfacies types observed in the studied sections. (A) Mud-/wackestone with rare benthic foraminifera and fragments of molluscs (sample A-30; height 30 m; section MLC). (B) Bioclastic grainstone with rounded clasts (sample SL-298; height 298 m; section SL). (C) Pack-/grainstone with benthic foraminifera, mollusc debris and

micropeloids (sample A-146; height 146 m; section MLC). (D) Rudstone composed of reworked subangular to well-rounded bioclasts (sample SL-319; height 319 m; section SL). (E) Carbonate breccia composed of variable clasts surrounded by a greenish to brownish, argillaceous matrix (sample B-17; height 464 m; section MLC). (F) Details of bauxitic level (bx1) with bauxite-filled karst cavities (sample SL2.2-8; height 514 m; section SL). (G) Bacinelloid boundstone (sample A-80; height 80 m; section MLC). (H) Densely packed oncoidal rudstone with oncoids of variable size (sample SL-368; height 368 m; section SL).

3.3.2 Carbon and oxygen isotope analysis

Bulk carbonate stable isotope results presented in Schmitt et al. (in preparation) were complemented by 950 additional bulk rock samples derived from the SL (n=487) and MLC (n=463) localities. Carbon and oxygen isotope analysis were performed in the stable isotope laboratory of the Institute of Geology, Leibniz University Hannover, Germany. All rock samples were cut, cleaned with distilled water and dried for 24 h at 40 °C. Rock specimens were screened with a magnifier to identify the most fine-grained portions, which were sampled with the help of a hand-held micro-drill equipped with tungsten drill bits. Large bioclasts, sparry cements and diagenetic calcite veins were avoided from being sampled.

Stable isotope analyses were conducted using a Thermo Fisher Scientific Gasbench II carbonate device connected to a Thermo Fisher Scientific Delta 5 Advantage isotope ratio mass spectrometer. The gas bench uses viscous water-free (98 g mol^{-1}) orthophosphoric acid at 72°C to release CO_2 of the calcitic sample material 1 h before the measurement is started. Repeated analyses of certified carbonate standards (NBS 19, IAEA CO-1, NBS 18 and Carrara Marble) show an external reproducibility of ≤ 0.06 ‰ for $\delta^{13}C$ and 0.08 ‰ for $\delta^{18}O$. Values are expressed in conventional delta notation relative to the Vienna-Pee Dee Formation belemnite (VPDB) international standard, in parts per thousand (‰). To facilitate the correlation of the chemostratigraphic curves, a five-point moving average was calculated from all the measured carbon- and oxygen isotope values of each studied section.

3.3.3 Element and strontium isotope analysis of low-Mg calcite shells

Special attention was paid to the collection of well-preserved low-Mg bivalve shells (chondrodonts and rudists) for strontium isotope stratigraphy (SIS). Although the limited size (<4 cm) of the collected rudist fragments has hampered a precise taxonomic classification, the observed celluloprismatic shell microstructure indicates that the majority of analysed shells belong to the rudist family Radiolitidae. The best-preserved shells were selected by means of the following criteria: (1) visible growth increments, (2) compact fibrous microstructure of the outer shell layer and (3) negligible impact of bioerosion and fracturing. Powdered rudist (n=38) and chondrodont (n=18) samples (1.35 to 1.65 mg) were analysed for their elemental composition (Ca, Mg, Sr, Fe and Mn) using inductively coupled plasma-atomic emission spectrometry (ICP-AES) at the isotope laboratory of the Institute of Geology, Mineralogy and Geophysics at Ruhr-University Bochum (RUB), Germany.

Strontium, iron and manganese abundances in rudist shells are used as proxies for evaluating the impact and degree of diagenetic alteration (Brand and Veizer, 1980). Selected samples (n=39) with low Mn and Fe concentrations (threshold value of < 100 ppm) and high strontium concentrations (threshold value of > 800 ppm for rudists (Steuber et al., 1999) and > 500 ppm for chondrodonts (Damas Mollá et al., 2006)) were analysed at RUB for their strontium isotope ratios using a thermal ionisation mass-spectrometer (Finnigan MAT 262) in dynamic mode (SL: Tab. 2.1: MLC: Tab. 2.2). For more details on the analytical procedure, refer to Huck et al. (2011). Corrections of measured ratios to USGS EN-1 (rather than to NIST SRM987) were done following the procedure of Howarth and McArthur (1997).

Tab. 2.1: Elemental composition and Sr-isotope ratios of selected low-Mg rudist and chondrodont shells of the SL section. The grey dataset was already published (Schmitt et al., in preparation).

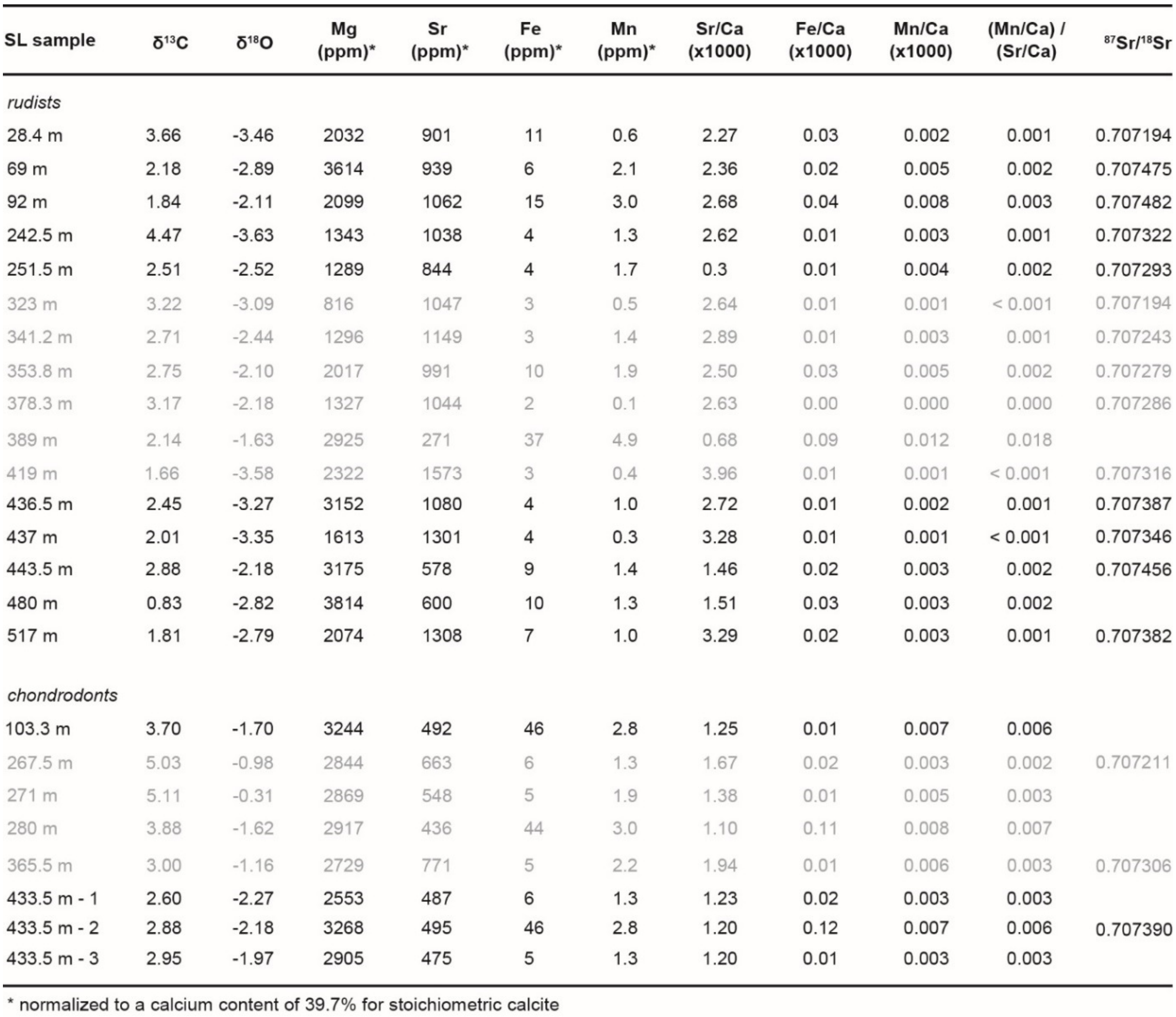

SL sample	**$\delta^{13}C$**	**$\delta^{18}O$**	**Mg (ppm)***	**Sr (ppm)***	**Fe (ppm)***	**Mn (ppm)***	**Sr/Ca (x1000)**	**Fe/Ca (x1000)**	**Mn/Ca (x1000)**	**(Mn/Ca) / (Sr/Ca)**	**$^{87}Sr/^{18}Sr$**
rudists											
28.4 m	3.66	-3.46	2032	901	11	0.6	2.27	0.03	0.002	0.001	0.707194
69 m	2.18	-2.89	3614	939	6	2.1	2.36	0.02	0.005	0.002	0.707475
92 m	1.84	-2.11	2099	1062	15	3.0	2.68	0.04	0.008	0.003	0.707482
242.5 m	4.47	-3.63	1343	1038	4	1.3	2.62	0.01	0.003	0.001	0.707322
251.5 m	2.51	-2.52	1289	844	4	1.7	0.3	0.01	0.004	0.002	0.707293
323 m	3.22	-3.09	816	1047	3	0.5	2.64	0.01	0.001	< 0.001	0.707194
341.2 m	2.71	-2.44	1296	1149	3	1.4	2.89	0.01	0.003	0.001	0.707243
353.8 m	2.75	-2.10	2017	991	10	1.9	2.50	0.03	0.005	0.002	0.707279
378.3 m	3.17	-2.18	1327	1044	2	0.1	2.63	0.00	0.000	0.000	0.707286
389 m	2.14	-1.63	2925	271	37	4.9	0.68	0.09	0.012	0.018	
419 m	1.66	-3.58	2322	1573	3	0.4	3.96	0.01	0.001	< 0.001	0.707316
436.5 m	2.45	-3.27	3152	1080	4	1.0	2.72	0.01	0.002	0.001	0.707387
437 m	2.01	-3.35	1613	1301	4	0.3	3.28	0.01	0.001	< 0.001	0.707346
443.5 m	2.88	-2.18	3175	578	9	1.4	1.46	0.02	0.003	0.002	0.707456
480 m	0.83	-2.82	3814	600	10	1.3	1.51	0.03	0.003	0.002	
517 m	1.81	-2.79	2074	1308	7	1.0	3.29	0.02	0.003	0.001	0.707382
chondrodonts											
103.3 m	3.70	-1.70	3244	492	46	2.8	1.25	0.01	0.007	0.006	
267.5 m	5.03	-0.98	2844	663	6	1.3	1.67	0.02	0.003	0.002	0.707211
271 m	5.11	-0.31	2869	548	5	1.9	1.38	0.01	0.005	0.003	
280 m	3.88	-1.62	2917	436	44	3.0	1.10	0.11	0.008	0.007	
365.5 m	3.00	-1.16	2729	771	5	2.2	1.94	0.01	0.006	0.003	0.707306
433.5 m - 1	2.60	-2.27	2553	487	6	1.3	1.23	0.02	0.003	0.003	
433.5 m - 2	2.88	-2.18	3268	495	46	2.8	1.20	0.12	0.007	0.006	0.707390
433.5 m - 3	2.95	-1.97	2905	475	5	1.3	1.20	0.01	0.003	0.003	

* normalized to a calcium content of 39.7% for stoichiometric calcite

Tab. 2.2: Elemental composition and Sr-isotope ratios of selected low-Mg rudist and chondrodont shells of the Monte La Costa section. The grey dataset was already published (Schmitt et al., in preparation).

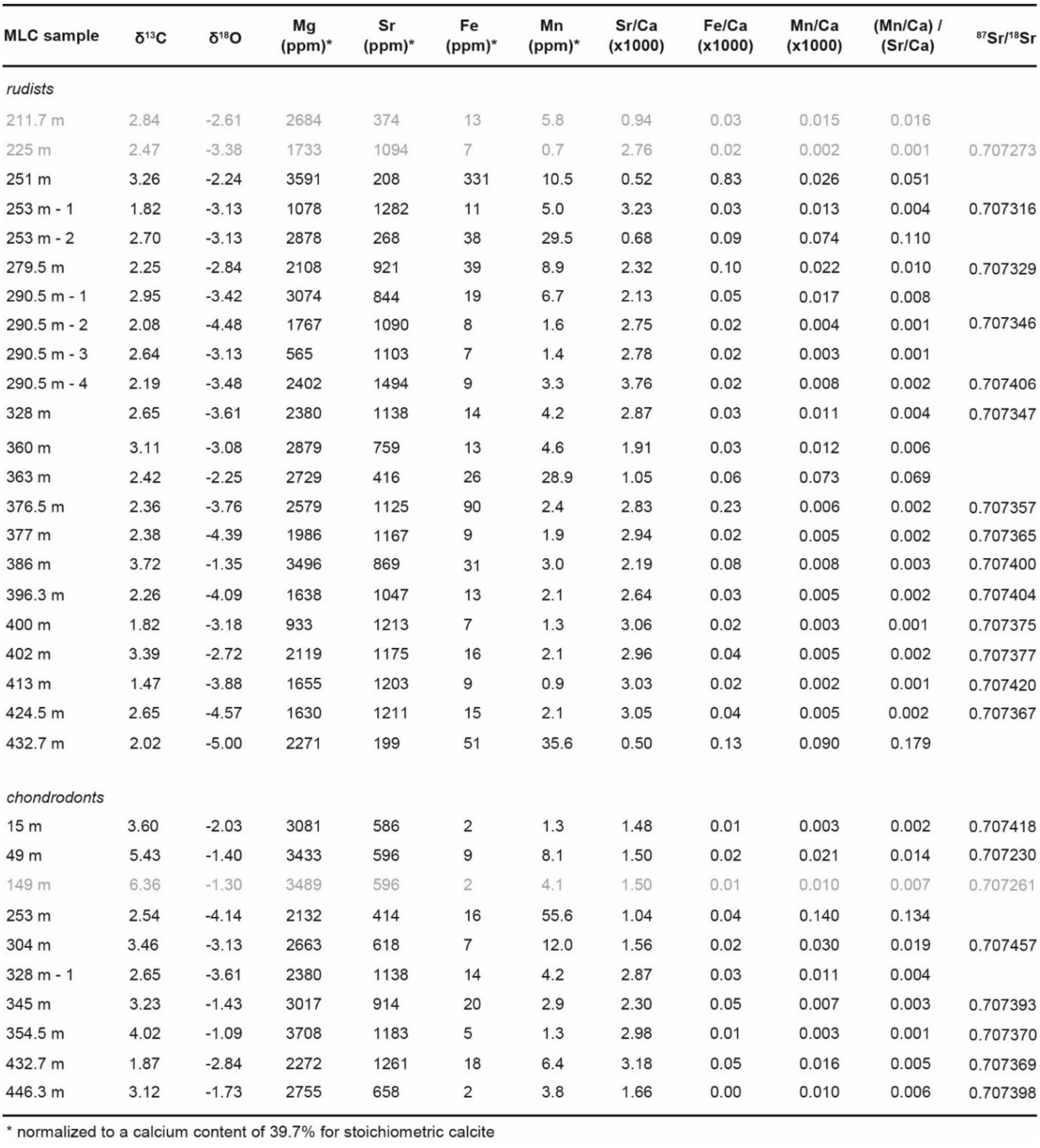

MLC sample	$\delta^{13}C$	$\delta^{18}O$	Mg (ppm)*	Sr (ppm)*	Fe (ppm)*	Mn (ppm)*	Sr/Ca (x1000)	Fe/Ca (x1000)	Mn/Ca (x1000)	(Mn/Ca) / (Sr/Ca)	$^{87}Sr/^{18}Sr$
rudists											
211.7 m	2.84	-2.61	2684	374	13	5.8	0.94	0.03	0.015	0.016	
225 m	2.47	-3.38	1733	1094	7	0.7	2.76	0.02	0.002	0.001	0.707273
251 m	3.26	-2.24	3591	208	331	10.5	0.52	0.83	0.026	0.051	
253 m - 1	1.82	-3.13	1078	1282	11	5.0	3.23	0.03	0.013	0.004	0.707316
253 m - 2	2.70	-3.13	2878	268	38	29.5	0.68	0.09	0.074	0.110	
279.5 m	2.25	-2.84	2108	921	39	8.9	2.32	0.10	0.022	0.010	0.707329
290.5 m - 1	2.95	-3.42	3074	844	19	6.7	2.13	0.05	0.017	0.008	
290.5 m - 2	2.08	-4.48	1767	1090	8	1.6	2.75	0.02	0.004	0.001	0.707346
290.5 m - 3	2.64	-3.13	565	1103	7	1.4	2.78	0.02	0.003	0.001	
290.5 m - 4	2.19	-3.48	2402	1494	9	3.3	3.76	0.02	0.008	0.002	0.707406
328 m	2.65	-3.61	2380	1138	14	4.2	2.87	0.03	0.011	0.004	0.707347
360 m	3.11	-3.08	2879	759	13	4.6	1.91	0.03	0.012	0.006	
363 m	2.42	-2.25	2729	416	26	28.9	1.05	0.06	0.073	0.069	
376.5 m	2.36	-3.76	2579	1125	90	2.4	2.83	0.23	0.006	0.002	0.707357
377 m	2.38	-4.39	1986	1167	9	1.9	2.94	0.02	0.005	0.002	0.707365
386 m	3.72	-1.35	3496	869	31	3.0	2.19	0.08	0.008	0.003	0.707400
396.3 m	2.26	-4.09	1638	1047	13	2.1	2.64	0.03	0.005	0.002	0.707404
400 m	1.82	-3.18	933	1213	7	1.3	3.06	0.02	0.003	0.001	0.707375
402 m	3.39	-2.72	2119	1175	16	2.1	2.96	0.04	0.005	0.002	0.707377
413 m	1.47	-3.88	1655	1203	9	0.9	3.03	0.02	0.002	0.001	0.707420
424.5 m	2.65	-4.57	1630	1211	15	2.1	3.05	0.04	0.005	0.002	0.707367
432.7 m	2.02	-5.00	2271	199	51	35.6	0.50	0.13	0.090	0.179	
chondrodonts											
15 m	3.60	-2.03	3081	586	2	1.3	1.48	0.01	0.003	0.002	0.707418
49 m	5.43	-1.40	3433	596	9	8.1	1.50	0.02	0.021	0.014	0.707230
149 m	6.36	-1.30	3489	596	2	4.1	1.50	0.01	0.010	0.007	0.707261
253 m	2.54	-4.14	2132	414	16	55.6	1.04	0.04	0.140	0.134	
304 m	3.46	-3.13	2663	618	7	12.0	1.56	0.02	0.030	0.019	0.707457
328 m - 1	2.65	-3.61	2380	1138	14	4.2	2.87	0.03	0.011	0.004	
345 m	3.23	-1.43	3017	914	20	2.9	2.30	0.05	0.007	0.003	0.707393
354.5 m	4.02	-1.09	3708	1183	5	1.3	2.98	0.01	0.003	0.001	0.707370
432.7 m	1.87	-2.84	2272	1261	18	6.4	3.18	0.05	0.016	0.005	0.707369
446.3 m	3.12	-1.73	2755	658	2	3.8	1.66	0.00	0.010	0.006	0.707398

* normalized to a calcium content of 39.7% for stoichiometric calcite

3.4 Lithostratigraphy and carbonate microfacies

Based on characteristic microfacies associations, key biota and discontinuity surfaces, the 597 m-thick SL section can be divided into 5 lithostratigraphic units (I-V; Fig. 3.3). The lowermost unit (I: 0-199 m) is characterised by the prevalence of thin bedded lime mud- and wackestones showing common fenestral fabrics, voids filled with green argillaceous sediment and subordinate laminations. These mud-dominated portions alternate with oolitic grainstones and pack- and grainstones characterised by laminoid fenestral fabrics (LF-BII type *sensu*; Flügel, 2010) and abundant calcimicrobes (hemispherical thalli of calcifying cyanobacteria) and/or algae (*Rivularia* sp., *Garwoodia* sp., *Hedstroemia/Cayeuxia* sp.; Mancinelli and Ferrandes, 2001). Lithostratigraphic marker levels include a dm-thick rudstone bed comprising densely packed large oncoids (at 123.5 m), reddish stylolites (161-173 m) and numerous cm- to dm-thick intra-formational karst-related breccias (48 m; 74 m, 93 m, 109-112 m, 115 m, 139 m, 142-145 m) characterised by angular clasts of limestone embedded in a greenish-brownish argillaceous matrix. The second unit (II: 199-236.5 m) is bound by brecciated levels and composed of mudstones (partly fenestral and laminated) containing sparse foraminifera and ostracods, and stratigraphically limited occurrences of calcimicrobes and dasycladacean algae (*Salpingoporella dinarica*). Reddish stylolites occur at two stratigraphic levels (200 m and 227.5 m). The unit III (236.5-332.5 m) is largely dominated by peloidal-bioclastic and foraminiferal grain- and rudstones bearing variable amounts of rudists (242-323 m), chondrodonts (271-280 m), nerineids (275 m), orbitolinids (286-312 m), solitary corals (313-324.5 m) and micritic oncoids (323.5-332 m) (Fig. 3.2 B and D). Mud-supported microfacies comprise (partly fenestral) miliolid-ostracod mudstones and wackestones and subordinate rudist floatstones (284-287 m). An interval characterised by the abundant occurrence (> 30% of the thin sections) of the dasycladacean green algae *S. dinarica* (248-265 m) is recorded beneath a well-exposed greenish karstic surface. Unit IV (333-516 m) is dominated by wacke- and floatstones containing common to abundant bacinelloid oncoids (Schmitt et al., in preparation) and gastropods that alternate with miliolid and bioclastic wackestones and subordinate grain- and floatstones bearing rudists (340-355 m, 419-436.5 m, 480 m, 513-515 m) and chondrodonts (370-387 m, 443.5 m). Densely packed oncoids of variable size (up to 5 cm in diameter) occur in rock-forming abundance at two stratigraphic levels (368-372.5 m, 392-394 m; Fig. 3.2 H). Further lithological marker levels include a reddish slightly brecciated palaeosoil (378.5-380 m) and a karst-related breccia characterised by angular mud-/wackestone clasts floating in a brownish-reddish slightly argillaceous matrix (443-443.5 m). Unit IV is bounded on top by a prominent brick-red bauxite level (514-516 m), which either occurs as massive layer or as complex system of multiple thin planar bauxite horizons and vertical bauxite-filled karst cavities (Fig. 3.2 F) that are interlocked with the rudist-bearing limestone host rock. In the uppermost part of the section (unit V: 516-597 m), two superordinate microfacies associations were differentiated. The first one comprises fenestral mudstones, which are frequently interrupted by coarser grained beds bearing variable amounts of oncoids and black pebbles. The second microfacies association is characterised by rapid facies changes, documented by alternations of thin mud-, wacke-, pack-, grain-, frame- and rudstone beds. The latter contain coral fragments, bacinelloid oncoids, green algae, gastropods, rudists and chondrodonts. Unfortunately, a comparably large part of unit V is covered by vegetation and weathering products (556-577 m). A calcareous karst breccia has been observed in the uppermost part of the section (586 m).

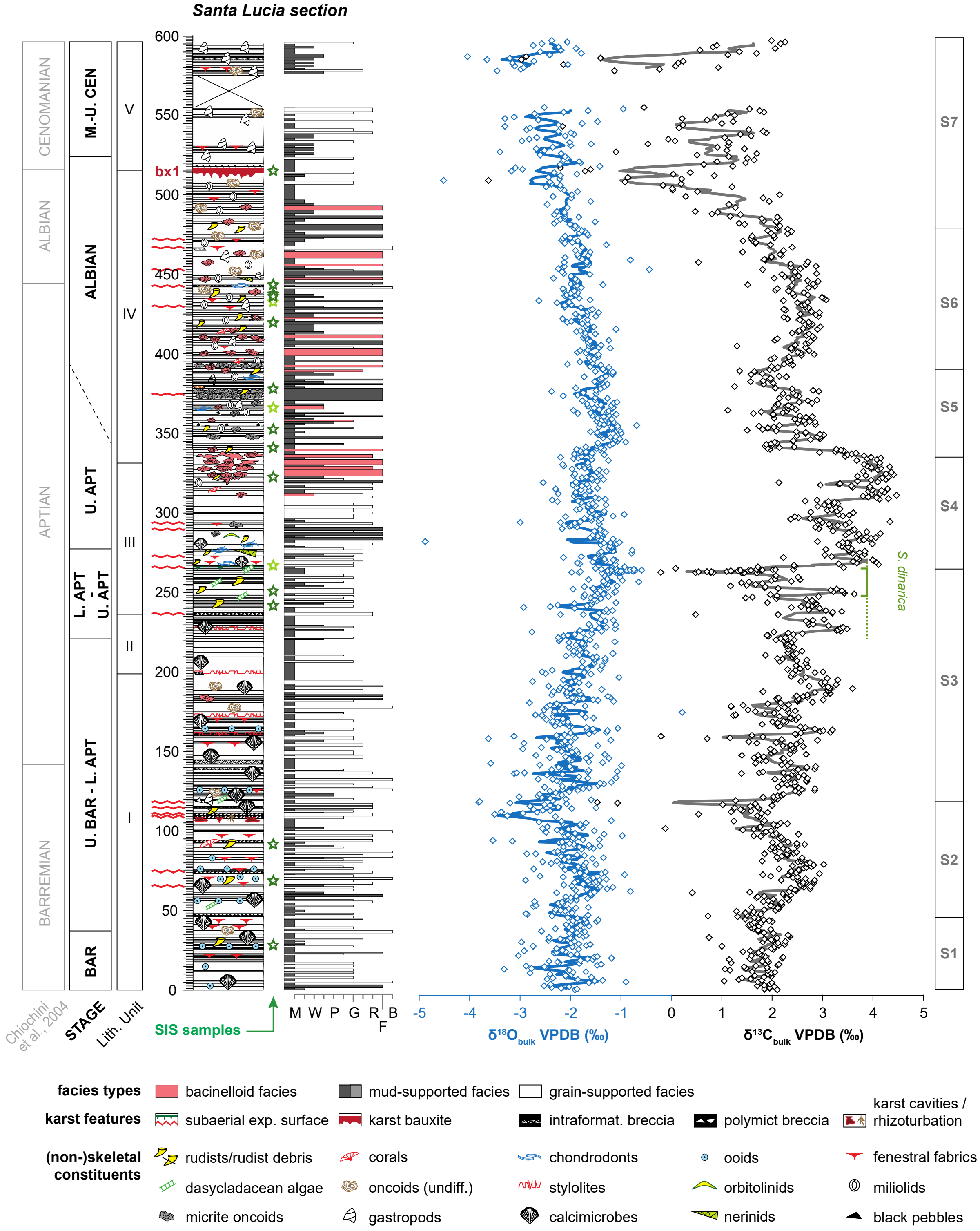

Fig. 3.3: Lithostratigraphy and high-resolution stable isotope stratigraphy of the Santa Lucia section. Chronostratigraphic calibration is based on the published data by Chiocchini et al. (2004). The therein mentioned bauxite level (bx1) is used as correltion point for the new findings of this work. The 597 m-thick profile can be divided into five lithostratigraphic units based on characteristic microfacies associations, key biota and discontinuity surfaces. A total of 16 samples were measured for SIS including 13 rudist (dark green asterisks) and three chondrodont (light green asterisks) shells. Classification of the rock samples follows Dunham (1962). Bold curves show the 5-point moving average of oxygen (blue) and carbon isotope (black) ratios with diamond symbols representing individual measured data points. Stratigraphic curves are subdivided into different segments (S1-S7) based on superimposed $\delta^{13}C$ trends.

The MLC section can be divided into four different units (Fig. 3.4; I-IV). The lowermost unit (I: 0-66 m) is composed of mud- and wackestones bearing variable amounts of fragmented rudists and chondrodonts, dasycladacean algae and orbitolinids (Fig. 3.2 A), as well as rare intercalations of bioclastic pack- and grainstones and bacinelloid floatstones. Lithostratigraphical marker levels include numerous cm- to dm-thick intra-formational karst-related breccias (angular limestone clasts embedded in a greenish-brownish argillaceous matrix) and stratigraphic levels documenting a change towards pelagic conditions (laminated mudstone, mud- to wackestone bearing planktic foraminifers). Unit II (66-190 m) documents a switch towards higher energy well-sorted deposits, represented by grainstones with variable amounts of black pebbles, orbitolinids and further benthic foraminifers, rudists, gastropods and chondrodonts (Fig. 3.2 C). A remarkable feature of this unit is the abundant presence of bacinelloid boundstones (> 90% of the rock composition) that occur at thin section level as massive microencrusting network (Fig. 3.2 G). Furthermore, a conspicuous horizon (166-168 m) characterised by karstification features (mm-to cm-sized elongated dissolution features filled with micro-brecciated material) is observed. Unit III (190-372 m) is dominated by coarse-grained and often cement-rich rud- and grainstones (cementstone *sensu* Fagerstrom, 1987), which are composed of reworked subangular to well-rounded bioclasts (mainly radiolitid rudists, orbitolinids and bacinelloid oncoids) (Fig. 3.2 D). Muddier interbeds include gastropod and bacinelloid wacke- and floatstones and subordinate mud- and pack-/grainstones characterised by laminoid fenestrae. Repeated episodes of subaerial exposure are indicated by pendant cements and extensive dissolution features (mm-to cm-sized karst fractures, spherical cavities), the latter being filled either with greenish to brownish slightly argillaceous micrite or brecciated limestone material. A thin mudstone layer containing globigerinid foraminifers marks the onset of unit IV (372-469 m). This unit comprises strongly reworked well-sorted rud- and grainstones bearing well-rounded rudist bioclasts, which show evidence for partial to complete recrystallization (crystallites *sensu* Dunham). Compared to unit III the thickness of single beds is increased. A karst-related brecciated limestone level occurs between 462 and 464 m. The breccia is reworked, whitish limestone clasts vary in diameter from 3 cm to 0.2 cm and comprise Late Cretaceous (*Marginotruncana sp.*, *M. pseudolinneiana* and other keeled forms) and Tertiary planktonic foraminifera. The clasts show a rather angular form and they are clearly separated from the greenish to brownish slightly argillaceous matrix by a fine (~ 0.1mm), dark brown to reddish rim (Fig. 3.2 E).

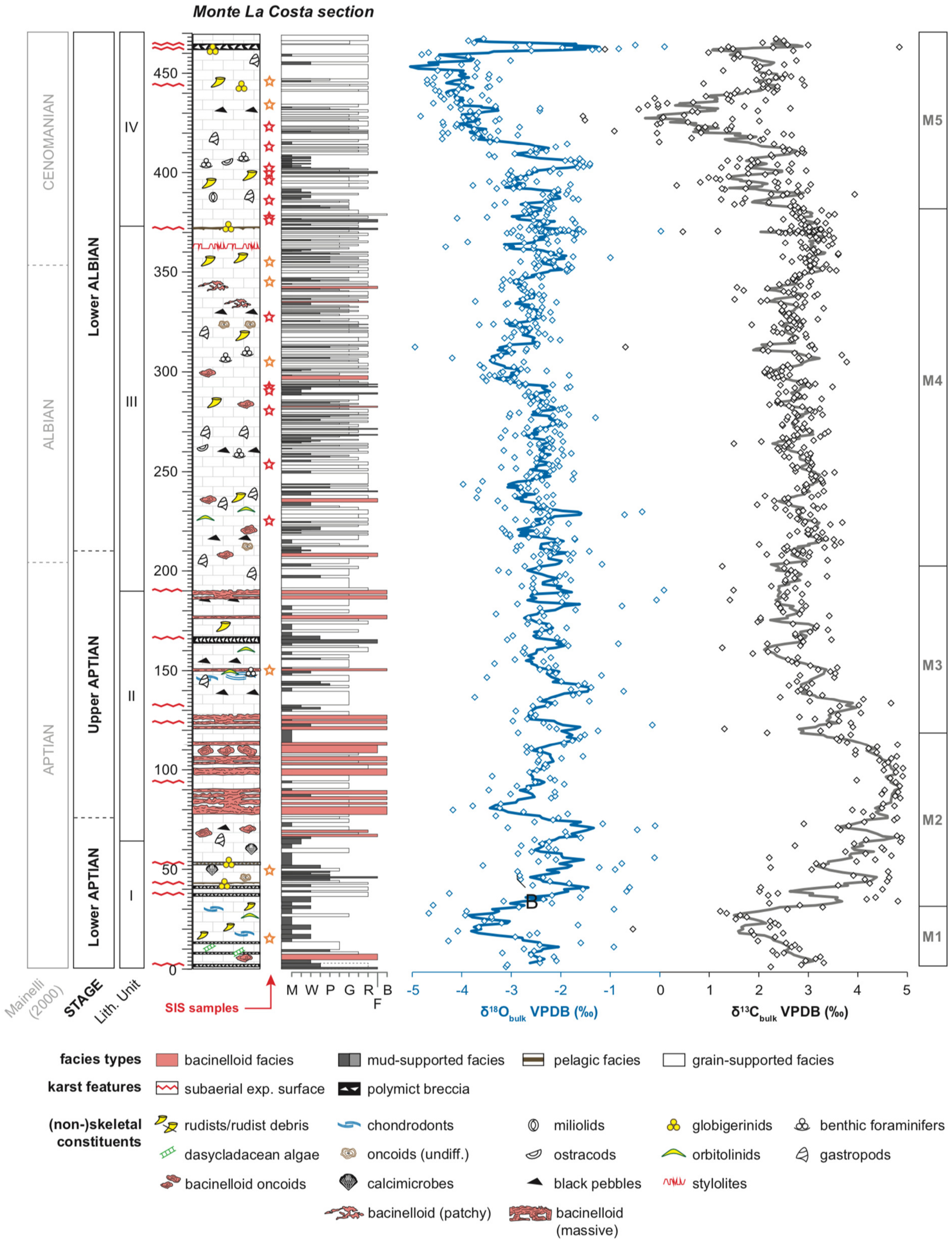

Fig. 3.4: Lithostratigraphy and high-resolution stable isotope stratigraphy of the Monte La Costa section. Chronostratigraphic calibration is based on the published data by Mainelli (2000) and new findings of this work. The 469 m-thick profile can be divided into four lithostratigraphic units based on characteristic microfacies associations, key biota and discontinuity surfaces. A total of 22 samples were measured for SIS including 14 rudist (red asterisks) and eight chondrodont (orange asterisks) shells. Classification of the rock samples follows Dunham (1962). Bold curves show the 5-point moving average of oxygen (blue) and carbon isotope (black) ratios with diamond symbols representing individual measured data points. Stratigraphic curves are subdivided into different segments (M1-M5) based on superimposed $\delta^{13}C$ trends.

3.5 Biostratigraphy

The stratigraphic range of identified benthic foraminifera and algae refer, among others, to widely used biostratigraphic schemes for the Central Apennine Platform (CAP) and the Adriatic Carbonate Platform (central Tethyan domain; Velic, 2007; Chiocchini et al., 2012; Di Lucia et al., 2012; Frijia et al., 2015). In Fig. 3.5, only those forms are plotted that are considered age-diagnostic.

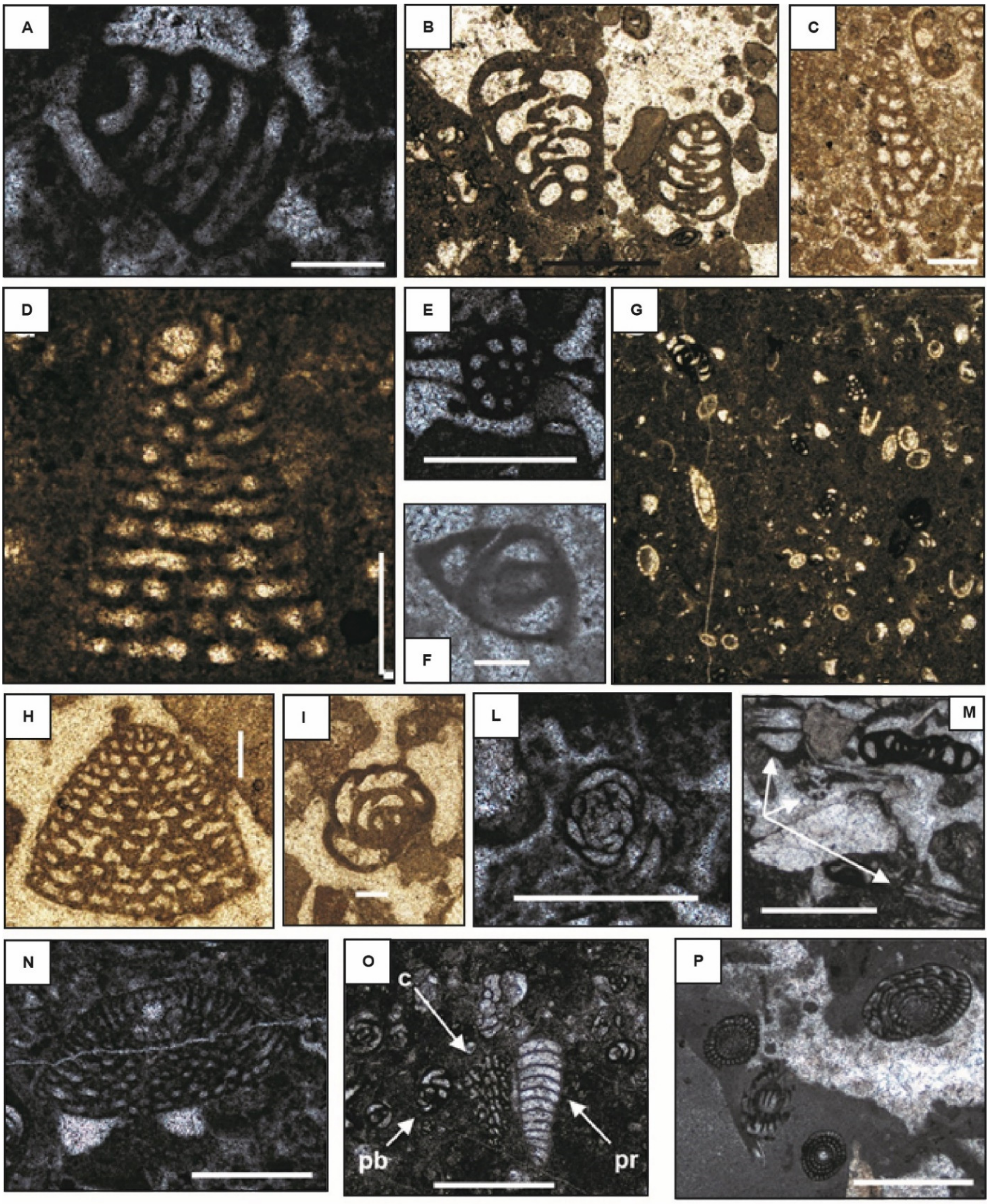

Fig. 3.5: Microphotographs of selected age diagnostic microfossils from the studied sections, (A) *Pseudolituonella conica* (sample A-50; height 50 m; section MLC). (B) *Praechrysalidina infracretacea* (sample SL-323.5; height 323.5 m; section SL).

(C) *Cuneolina cf. sliteri* (sample SA-52; height 260 m; section MLC). (D) *Cribellopsis arnaudae* (sample SL2-160; height 500 m; section SL). (E) cf. *Haplophragmoides globosus* (sample A-103; height 103 m; section MLC). (F) *Moesiloculina danubiana* (sample A-100; height 100 m; section MLC). (G) *Salpingoporella dinarica* (sample SL-254.5; height 254.5 m; section SL). (H) *Dictyoconus* cf. *algerianus* (sample SA-117.5; height 325.5 m; section MLC). (I) *Pseudonummoloculina aurigerica* (SA-117.5; height 325.5 m; section MLC). (L) *Glomospira urgoniana* (sample A-76; height 76 m; section MLC). (M) *Carphatoporella occidentalis* (arrows) (sample MLC-21; height 372 m; section MLC). (N) *Mesorbitolina parva* (sample A-76; height 76 m; section MLC). (O) *Pseudorhapydionina dubia* (pb); *Cuneolina pavonia parva* (c), *Pseudolituonella reicheli* (pr) (sample SL2.2-82; height 589 m; section SL). (P) Different cuts of *Sellialveolina viallii* (sample SL2.2-20; height 526 m; section SL). White scale bar represents 200 µm. Black scale bar represents 1 mm.

In unit I of the SL section (Fig. 3.3), the benthic foraminifera content is represented by *Cuneolina camposaurii*, *Praechrysalidina infracretacea*, cf. *Neotrocholina friburgensis* (*sensu* Guillaume and Reichel, 1957), *Mayncina* sp. and *Cuneolina scarsellai*. Based on the occurrence of the dasycladacean algae *Salpingoporella* cf. *muehlbergii* (37 m) accompanied by *Salpingoporella* sp., the lower portion of unit I is associated with the Barremian part of the *C. camposauri - C. scarsellai* biozone of Chiocchini et al. (2012). The lack of age-diagnostic taxa in the remainder of unit I and the lower part of unit II (37-220 m) hampers a precise biostratigraphic age assignment. Unit II records the first occurrence (FO) of the dasycladacean alga *Salpingoporella dinarica* (221 m). Subordinate microfossils found within this unit comprise *Haplophragmoides* sp., *P. infracretacea*, *Salpingoporella* sp., *Moesiloculina* sp. and *Cuneolina scarsellai*. An Early Aptian age is suggested for this unit, corresponding to the *S. dinarica* biozone of Chiocchini et al. (2012). Unit III bears benthic foraminifera such as *Orbitolina* (*Mesorbitolina*) sp., *Sabaudia minuta*, *Sabaudia* sp., *Moesiloculina* sp., *Debarina hahounerensis, P. infracretacea*, *Cuneolina scarsellai*, *C. camposauri*, *Nezzazzata* cf. *isabellae, Spiroloculina* sp. and *Haplophragmoides* cf. *globosus*. Dasycladacean algae such as *Clypeina* sp., *Salpingoporella* sp., and *S. dinarica* are also observed. The co-occurrence of *S. dinarica* and *D. hahounerensis* at 254 m either indicates a Lower (Chiocchini et al., 2012) or Lower to Upper Aptian age (Di Lucia et al., 2012). The last occurrence (LO) of *S. dinarica* at 272.5 m is followed by the FO of *Nezzazata* cf. *isabellae* at 276.5 m, which in the CAP is suggestive of an age not older than Late Aptian, biostratigraphically placed within the *Archeoalveolina reicheli* biozone of Chiocchini et al. (2012). Unit IV is characterised by the FO of high conical orbitolinids such as *Cribellopsis arnaudae* (343.5 m). Other observed benthic foraminifera include *P. infracretacea*, *P. aurigerica, C. pavonia*/*pavonia* var. *parva, C. laurenti*, *Nezzazzata* sp., *cf D. algerianus, Moesiloculina histri* and large planispiral, porcellanaceous (LPP) forms. This foraminiferal assemblage can be correlated to the uppermost Aptian to lowermost Albian portion of the *D. algerianus* biozone of Chiocchini et al. (2012). The FO of *Cribellopsis* cf. *arnaudae* at 393 m is indicative of an Early Albian age (Chiocchini, 1989). Unit V comprises ?*Pyrgo globulosa*, *Cisalveolina* cf. *lehneri, C. pavonia*/*pavonia* var. *parva*, *Nezzazzatinella* sp., *Pseudorhapydionina dubia, Pseudolituonella reicheli, Palaeosigmoilopsis apenninica*, *Sellialveolina viallii, Spiroloculina cenomana and Trochospira avnimelechi*. Whereas the occurrence of *S. vialli* at 523 m points to an intra-Lower (Chiocchini et al., 2012) to Middle Cenomanian (De Castro, 1985), an intra-Lower to intra-Upper Cenomanian is indicated by the sole occurrence of *Trochospira* *avnimelechi* at 537 m. The LO of *S. cenomana* and coeval FOs of *P. dubia* and *P. apenninica* at 555m suggest the Middle to Upper Cenomanian (Chiocchini et al., 2012). The stratigraphically youngest thin section sample (587 m) yields the sole occurrence of *P. reicheli*, a form that is indicative for the Upper Cenomanian. In light of the foraminiferal occurrences described above, unit V arguably ranges from the uppermost part of the Ostracoda and Miliolidae to the *C. gradata-P. reicheli* biozones (refer to Chiocchini et al., 2012).

Unit I (Fig. 3.4) of the Monte La Costa section comprises benthic foraminifera such as *H.* cf. *globosus, ?Earlandia conradi*, *Bulimina* sp.?, cf. *Dobrogelina ovidi*, *Quinqueloculina* sp., *Glomospira* sp., *Istriloculina elliptica, Orbitolina (cf. Mesorbitolina) sp.*, *Moesiloculina* cf. *danubiana, Nezzazzatinella* sp., *P. infracretacea, Pseudolituonella conica, Cuneolina* sp., *Spiroloculina* sp. and dasycladacean algae including *Triploporella marsicana.* Whereas *T. marsicana* (8-13 m) and *P. conica* (50 m) are reported from Lower Aptian shallow water deposits in the CAP, the occurrence of *Orbitolina* (*Mesorbitolina*) sp. at 5 m indicates an intra-Lower to Upper Aptian age, biostratigraphically positioned between the *S. dinarica* and the *A. reicheli* biozones of Chiocchini et al. (2012). Microfossils identified in unit II include *Glomospira urgoniana*, *Sabaudia* sp., *Cuneolina* sp., *Spiroloculina* sp., *Moesiloculina histri, Coptocampylodon fontis, Istriloculina* cf. *eliptica, Quinqueloculina* sp., cf *Moesiloculina danubiana, ?Nezzazzatinella* sp., *Cuneolina laurentii*, *Pseudolituonella conica, Trochamminoides cf. coronus*, *Nezzazata isabellae*, *Haplophragmoides* cf. *globosus, Orbitolina (cf. Mesorbitolina) sp.* and LPP forms. In the CAP, the FO of the 'incertae sedis' taxon *Carphatoporella occidentalis* (76 m) is indicative of an age not older than Late Aptian (*A. reicheli* biozone of Chiocchini et al., 2012). This age assignment is supported by the LO of *P. conica* at 150 m and the FO of *Nezzazata isabellae* at 188 m.

Unit III comprises benthic foraminifera such as *Cuneolina laurentii,* cf. *Glomospira* sp., *Orbitolina* (cf. *Mesorbitolina*) sp., *Istriloculina cf. elliptica, C. fontis, Cribellopsis cf. arnaudae, Cuneolina* cf. *sliteri, cf. Dictyoconus algerianus*, *Moesiloculina histri, Nezzazata isabellae*, *Pseudonummoloculina aurigerica, Sabaudia sp.*, *Cuneolina pavonia/pavonia* var. *parva, P. infracretacea,* LPP forms and the dasycladacean algae *Russoella radoicicae*. The association of *R. radoicicae* with *C. fontis*, *Orbitolina* (cf. *Mesorbitolina*) sp. and the FO of *P. aurigerica* at 210 m is indicative of an age not older than Early Albian in the CAP, biostratigraphically placed around the boundary between the *A. reicheli/D. algerianus* and Ostracoda and Miliolidae biozones of Chiocchini et al. (2012). A lower Albian age of the upper part of unit III is supported by the FO of *C. arnaudae* at 261 m and *D. algerianus* between 324 m and 371 m (Chiocchini, 1989; Chiocchini et al., 2012).

Benthic foraminifera identified in unit IV include *Cuneolina* sp., *C. pavonia/pavonia* var. *parva, Orbitolina (cf. Mesorbitolina) sp.*, *P. infracretacea*, cf. *Nummoloculina, P. aurigerica, Quinqueloculina sp., N. isabellae, C. fontis, Moesiloculina* sp. and LPP forms. This foraminiferal assemblage suggests an age not younger than Early Albian, biostratigraphically placed within the lower part of the Ostracoda and Miliolidae biozone of Chiocchini et al. (2012).

3.6 Geochemical results

3.6.1 Bulk carbonate carbon- and oxygen isotope stratigraphy

Bulk carbonate $\delta^{13}C$ values of samples derived from the SL section (Fig. 3.3) vary between -3.63 and 4.46 ‰ (mean: 2.2 ‰). Based on superimposed trends, the $\delta^{13}C$ record is divided into seven chemostratigraphic segments (S1-7). Segment S1 (0-46 m) exhibits $\delta^{13}C$ values fluctuating around a background value of about 2 ‰. Segment S2 (46-118 m) displays a well-expressed positive carbon isotope excursion (CIE) with an amplitude of about 1 ‰ that is terminated by a negative $\delta^{13}C$ spike. The following segment S3 (118-265 m) is composed of multiple negative and positive excursions that are superimposed on a trend towards more positive $\delta^{13}C$ values. Separated by a sharp negative $\delta^{13}C$ spike reaching $\delta^{13}C$ values of 0.1 ‰ (263 m), segment S4 (265-335 m) comprises rather strong $\delta^{13}C$ fluctuations that are superimposed on a stepwise positive shift reaching peak values of 4.3 ‰. A sharp negative carbon isotope spike marks the onset of segment S5 (335-390 m). This segment displays oscillating $\delta^{13}C$ values with average amplitudes of about 1 ‰, which are followed by an expanded moderately positive $\delta^{13}C$ bulge reaching 2.9 ‰ (S6: 390-480 m). The topmost segment S7 (480-596 m) appears as pronounced stepwise negative $\delta^{13}C$ shift, characterised by strongly fluctuating values and numerous negative spikes reaching values of -1.1 ‰.

Oxygen isotope values of bulk carbonates of the SL section range from -5.19 to 0.2 ‰ (mean: -1.9 ‰). The lowermost part of the $\delta^{18}O$ record (0-100 m) displays strongly variable values forming a plateau. A sharp negative shift marks the onset of the following chemostratigraphic segment that shows a stepwise trend towards more positive values (100-265 m). An expanded negative trend is observed in the remaining part of the $\delta^{18}O$ record (265-587 m), only interrupted by a short interlude (335-350 m) providing enhanced oxygen isotope values.

Bulk carbonate $\delta^{13}C$ values of the MLC section (Fig. 3.4) range between -1.51 and 4.86 ‰ (mean: 2.7 ‰). Superimposed $\delta^{13}C$ trends and inflection points enable distinguishing five chemostratigraphic segments (M1-5). Limestones of the lower part of the section (segment M1: 0-32 m) record a short negative $\delta^{13}C$ shift (as low as 1.22 ‰ at 30 m) followed by a long-term expanded positive $\delta^{13}C$ shift reaching values of up to 4.86 ‰ (M2: 32-118 m). Notably, the lower part of segment M2 is characterised by strong $\delta^{13}C$ fluctuations. A sharp negative carbon isotope spike at 118 m marks the onset of the following segment M3 (118-202 m). Carbonates representing this segment record a saw-tooth shaped $\delta^{13}C$ pattern with multiple fluctuations (amplitude: < 0.8 ‰) that are superimposed on a negative trend. The following chemostratigraphic segment M4 displays a carbon isotope plateau with strongly oscillating values (202-382 m). Limestones representing the uppermost part of the MLC section (M5: 382-469 m) record multiple negative $\delta^{13}C$ shifts that represent the lowest values of the $\delta^{13}C$ curve (-0.9 ‰ at 423 m).

Oxygen isotope values recorded by limestones of the MLC section vary between -4.94 and 0.1 ‰ (mean: -2.6 ‰). The lower part of the $\delta^{18}O$ curve (0-142 m) records alternating negative and positive excursions (amplitudes < 2 ‰) that are superimposed on a negative trend. Up-section, the oxygen isotope curve exhibits an expanded plateau interval characterised by values fluctuating around background values of about -2.4 ‰ (142-406 m). The uppermost part of the $\delta^{18}O$ curve (406-469 m) displays a very pronounced negative trend reaching minimum values of -5.04 ‰ at 455 m, which is followed by an abrupt positive $\delta^{18}O$ shift (0.1 ‰ at 465 m).

3.6.2 Trace element and strontium isotope results

Rudist shells derived from the Santa Lucia (Tab. 2.1; n=16) and Monte La Costa sections (Tab. 2.2; n=22) provide magnesium concentrations varying between 565 and 3814 ppm (mean: 2135 ppm; s.d.: 744 ppm), strontium concentrations varying between 199 and 1573 ppm (mean: 971 ppm; s.d.: 346 ppm), iron concentrations varying between 2 and 331 ppm (mean: 23 ppm; s.d.: 53 ppm) and manganese concentrations varying between 0.9 and 36 ppm (mean: 5 ppm; s.d.: 8 ppm). Analysed chondrodonts shells (Tab. 1: SL n=8; Tab. 2: MLC n=10) yield magnesium concentrations ranging from 2132 to 3708 ppm (mean: 2966 ppm; s.d.: 383 ppm), strontium concentrations ranging from 414 to 1183 ppm (mean: 650 ppm; s.d.: 208 ppm), iron concentrations ranging from 2 to 46 ppm (mean: 13 ppm; s.d.: 13 ppm) and manganese concentrations ranging from 1 to 56 ppm (mean: 7 ppm; s.d.: 12 ppm). Chondrodont and rudist shells selected for strontium isotope analysis (n=39) are characterised by average strontium abundances of 756 ppm (s.d.: 193 ppm) and 1138 ppm (s.d.: 161 ppm) and generally low iron (mean: 11 ppm; s.d.: 15) and manganese (mean: 3 ppm; s.d.: 3) abundances.

The SIS record of the SL section (including data presented in Schmitt et al, in preparation) is based on selected rudist (n=14) and chondrodont shells (n=3). The obtained SIS pattern mimics the overall Late Barremian to Early Albian evolution in marine strontium isotope ratios. During this interval, the $^{87}Sr/^{86}Sr$ ratio of marine carbonates is characterised by a long-term decreasing trend with minimum $^{87}Sr/^{86}Sr$ values during the latest Aptian and a subsequent positive trend towards the Albian-Cenomanian. Notably, a rudist shell located directly above a well-expressed karst breccia records the most radiogenic $^{87}Sr/^{86}Sr$ value (0.707482 ± 7*10-6). Rudist (n=14) and chondrodont (n=8) shells of the MLC section (including data presented in Schmitt et al., in preparation) record moderate $^{87}Sr/^{86}Sr$ fluctuations that are superimposed on an increasing trend towards more radiogenic values (0.707273 ± 7*10-6 to 0.707420 ± 5*10-6). Shells from the stratigraphically uppermost part of the section document a decline in $^{87}Sr/^{86}Sr$ ratios (0.707420 ± $5*10^{-6}$ to 0.707369 ± $5*10^{-6}$).

3.7 Discussion

3.7.1 Significance of bulk carbonate and bivalve shell chemostratigraphic patterns

High-resolution chemostratigraphy has become an indispensable tool for stratigraphic correlation of Mesozoic (hemi-) pelagic and shallow-water deposits (Weissert, 1989; Jenkyns et al., 1994; Menegatti et al., 1998; Godet et al., 2006; Parente et al., 2007; Weissert et al., 2008; Huck et al., 2011; Navidtalab et al., 2016). However, marine stable isotope signatures can be influenced by a multitude of environmental and post-depositional processes that will produce significant offsets from the global open marine primary signals (Hudson, 1977; Brand and Veizer, 1981; Allan and Matthews, 1982; Veizer, 1983; Lohmann, 1988; Immenhauser et al., 2008; Huck et al., 2017; Oehlert and Swart, 2014; Swart, 2015). Shallow-water carbonate platform settings are particularly prone to syn- and post-depositional alteration of stable isotope signatures due to (1) the high primary porosities of shallow-water bioclastic deposits and (2) the likeliness of subaerial exposure associated with sea level changes (Immenhauser et al., 2003; Strasser, 2015). Bulk carbonate oxygen isotope values often show evidence for diagenetic alteration, but can help to unravel the composition and temperature of involved diagenetic fluids (Brand and Veizer, 1981). Carbon isotope values, in contrast, are usually rock buffered and therefore more resilient (Moore, 1985).

Cross-plots of bulk carbonate $\delta^{13}C$ and $\delta^{18}O$ values (Fig. 3.6) document that the majority of analysed bulk carbonate isotope values (SL: 94%, MLC: 77%) overlap with the field of Barremian-Aptian low-latitude biotic calcite (Prokoph et al., 2008). The low covariance between carbon- and oxygen isotope values (SL: R^2= 0.19; MLC: R^2=0.11) suggests that most samples are well preserved. A moderately (SL section) to well expressed (MLC section) 'inverted J' stable isotope pattern, however, indicates a stratigraphically limited impact of meteoric diagenesis (Brand and Veizer, 1980; Allan and Matthews, 1982; Lohmann, 1988; Jones et al., 2015). Thin section inspection of samples derived from the stratigraphic levels SL: I: 100-120 m, II: 260-265 m, III > 500 m; MLC: i: > 416 m, ii: 14-30 m (Fig. 3.6) indeed reveal the occurrence of spar-filled fenestral fabrics, voids filled with green argillaceous micrite, vertical bauxite-filled karst cavities or karst-related intra-formational breccias – features typically associated with subaerial exposure episodes (Flügel, 2010; Raspini et al., 2012; Godet et al., 2016; Navidtalab et al., 2016).

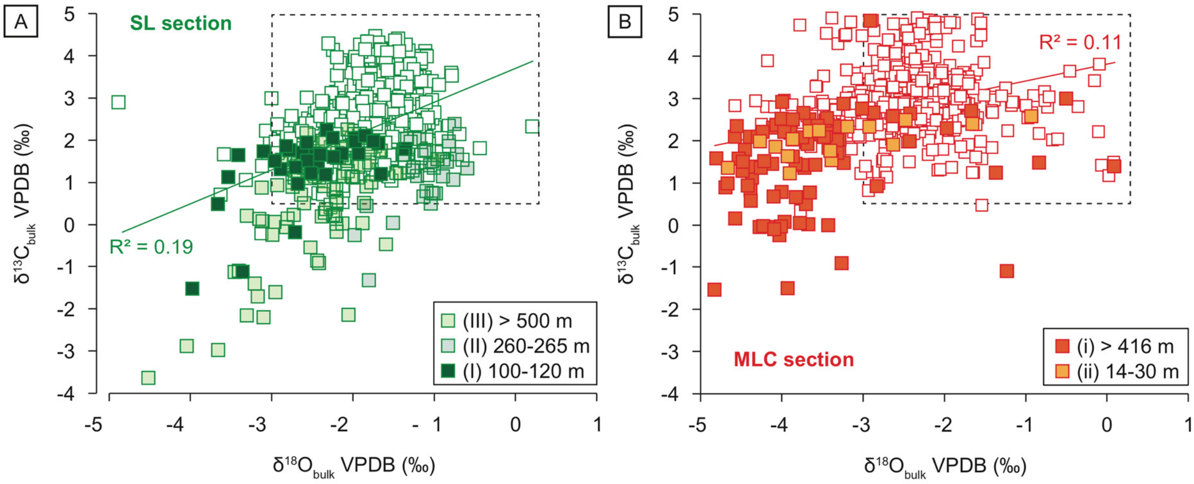

Fig. 3.6: Cross-plots of $\delta^{18}O$ and $\delta^{13}C$ values of bulk carbonate samples from the (A) Santa Lucia and (B) Monte La Costa sections. The grey square shows the average isotopic range of shallow marine tropical-subtropical carbonates compiled by the data of well-preserved biotic calcite from the Barremian-Aptian (modified after Di Lucia et al., 2012 from Prokoph et al.,

2008). Both diagramms show low covariance (SL: R^2= 0.19; MLC: R^2= 0.13). The isotopic compositions of some bulk carbonate samples, especially the ones below exposure surfaces (filled), provide evidence for diagenetic alteration under meteoric or shallow marine conditions.

Previous studies have demonstrated that the outer low-Mg calcite layer of Cretaceous rudist and oyster shells is a suitable archive for the strontium isotope composition of contemporaneous ocean waters (Steuber et al., 2005; Frijia and Parente, 2008; Burla et al., 2009; Schneider et al., 2009; Horikx et al., 2014; Frijia et al., 2015; Huck and Heimhofer, 2015), enabling accurate age assignments of shallow marine strata by SIS (Howarth and McArthur, 1997; McArthur et al., 2001; McArthur et al., 2012). Oysters typically inhabit coastal settings that are often characterised by radiogenic $^{87}Sr/^{86}Sr$ ratios associated with riverine siliciclastic input (Schneider et al., 2009). Thus, the interpretation of strontium isotope signals recorded by oyster-like chondrodont bivalves (Stanton, 1901; Ayoub-Hannaa and Fürsich, 2011) is not devoid of problems, in particular since comparably less is known about the palaeoecology and geochemistry of these extinct bivalves.

In general, both rudist and chondrodont shells show well-preserved growth increments at the macroscopic scale. Thin sections inspection, however, reveals that the microstructure of radiolitid rudists is, as expected, highly variable along shell sections, ranging from compact fibrous to celluloprismatic microstructures. In accordance with published elemental threshold values (Steuber et al., 2005; Frijia and Parente, 2008; Frijia et al., 2015), only compact rudist shell portions with Fe and Mn concentrations below 100 ppm and Sr concentrations exceeding 800 ppm are considered for SIS (Fig. 3.7 A). A cross-plot of Mg and Sr contents illustrates that values provided by selected pristine rudist shells plot closer to the regression line of biotic calcite than of abiotic calcite (Fig. 3.7 B; Carpenter and Lohmann, 1992; Steuber, 1999). Measured Mg (mean: 1919 ppm) and Sr contents (mean: 1138 ppm) largely overlap with those reported for compact fibrous shell portions of the radiolitid rudist *Gorjanovicia* cf. *costata*, but clearly deviate from those of the radiolitid rudist *Durania* aff. *mutabilis*, whose outer shell layer often comprises honeycomb-type structures filled with diagenetic low-Mg calcite (Fig. 3.7 B; Steuber 1999). Finally, a pristine preservation state of rudists is supported by $\delta^{13}C$ and $\delta^{18}O$ values, which show no correlation (Fig. 3.7 C; R^2= 0.004).

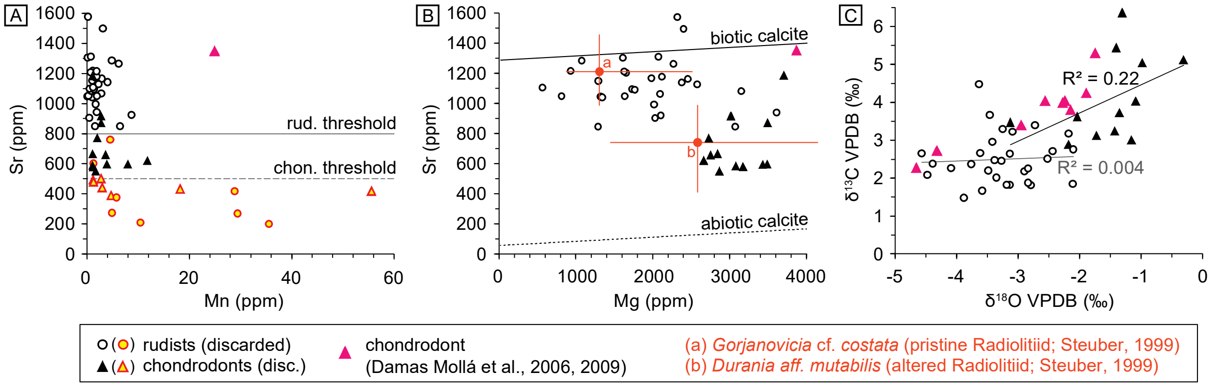

Fig. 3.7: Isotope and elemental compositions of bivalve shells derived from the SL and MLC sections (circle: rudist; triangle:

chondrodont). (A) The concentration of Sr and Mn is decisive for further analyses of the samples. Is the Sr concentration under a certain threshold (stippled line for rudists < 800 ppm; dashed line for chondrodonts < 500 ppm) the shell is excluded for further analyses (marked by a red frame and yellow filling). (B) Mg and Sr compositions of rudist and chondrodont shells compared with mean compositions of modern biotic (top line) and abiotic (bottom line) marine calcite (Carpenter and Lohmann 1992; Steuber 1999). For comparison published data derived from (a) an diagenetically unaltered radiolitid (*Gorjanovicia* cf. *costata*), (b) an altered *Durania* aff. *mutabilis* radiolotid (red; Steuber, 1999) were plotted. Red horizontal and vertical lines mark the ranges of these datasets (a: number of samples:19; b: number of samples: 24). Dataset of a chondrodont is indicated by a solid pink triangle (Damas Mollá, 2006; 2009) (C) Cross-plot of $\delta^{18}O$ and $\delta^{13}C$ values showing low covariance for rudists (R^2= 0.004) indicates the absence of strong diagenetic alteration of the isotopic signal. The chondrodonts show a high covariance (R^2=0.22) but compared to the dataset of Damas Mollà (2006; 2009) (pink triangles) they are plotting in a similar range.

According to a sclerochemical study of an Albian chondrodont shell from northern Spain, elemental compositions of chondrodonts are highly variable, with Sr contents of pristine portions of the shell ranging from 500 to 2000 ppm and Mn contents ranging from 10 to 250 ppm (Damas Mollá et al., 2006). Chondrodont shells with Sr concentrations below 500 ppm and Mn concentrations above 250 ppm are therefore not considered for SIS (Fig. 3.7 A). In line with the results obtained by Damas Mollá et al. (2006; 2009), most of the selected chondrodont shells reveal a low to moderate positive correlation of carbon and oxygen isotope ratios (Fig. 3.7 C; R^2=0.22).

3.7.2 Integrated bio- and chemostratigraphic dating

Age diagnostic benthic foraminifera and algae provide evidence that SL limestones are of Barremian to Late Cenomanian age. The MLC section is biostratigraphically attributed to the Late Aptian and Early Albian. In order to increase the stratigraphic precision of the identified foraminiferal-algal assemblages, a platform-wide carbon isotope based correlation of the studied sections is carried out, followed by SIS. The Aptian portions of both curves display a negative peak and a subsequent prominent positive excursion, which comprises the most positive carbon isotope values in both sections (Fig. 3.8: segments S4 and M2). The following interval is characterised by strongly variable but rather cyclic $\delta^{13}C$ changes that are superimposed on an overall negative trend (Fig. 3.8; segments S5 and M3). While the Albian portion of the SL section displays a low-amplitude positive carbon excursion (Fig. 3.8: S6), coeval sediments of the MLC section record fluctuating $\delta^{13}C$ values that are superimposed on a minor positive excursion (Fig. 3.8: segment M4). A strongly pronounced stepwise negative excursion characterises the uppermost portion of both sections (Fig. 3.8: segments S7 and M5).

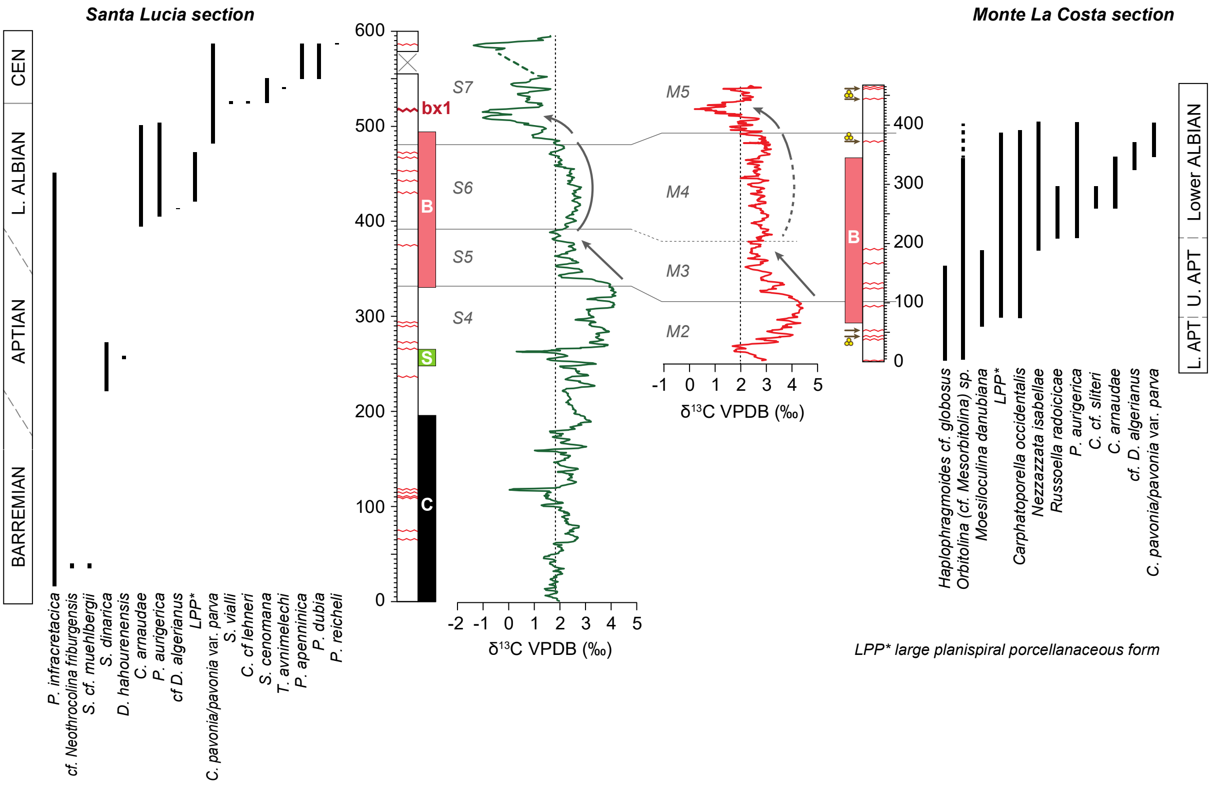

Fig. 3.8: Bio- and isotope stratigraphy of the SL (green) and the MLC (red) sections. Both δ^{13}C curves show a similar pattern with stratigraphic height. The appearance of calcimicrobes (C), *Salpingoporella dinarica* (S), bacinelloids (B), bauxite (bx1) and Globigerinids (⚘) are marked.

The carbon isotope pattern of both sections allows for a correlation with well-dated pelagic carbon isotope reference records. However, refinement of the biostratigraphic dating in the central and southern Apennines solely based on carbon isotope correlation is hampered by the occurrence of sedimentary hiatuses in the studied SL section. Carbon isotope stratigraphy is therefore improved and calibrated by means of SIS (McArthur et al., 2012) and subsequently compared with biostratigraphic data (Fig. 3.9). Due to the expanded stratigraphic range of the SL and MLC sections, two different pelagic carbon isotope reference records were compiled from literature (Fig. 3.9). The first composite record is based on δ^{13}C data derived from the Umbria Marche Basin in Italy (Sprovieri et al., 2006; Giorgioni et al., 2012; Bottini et al., 2015; Erba et al., 2015; Gambacorta et al., 2015), adjacent to the here studied ACP. The second composite carbon isotope record comprises data from the Vocontian Basin in southeastern France (Gale et al., 1996; Herrle et al., 2004; Godet et al., 2006; Gyawali et al., 2017). Notably, the hemipelagic deposits of the latter basin bear numerous belemnites providing a high-resolution strontium isotope stratigraphic framework (Bodin et al., 2009; Bodin et al., 2015). Both composite isotopic records were tied to the GTS2012 timescale (Gradstein et al., 2012) by integrating multiple stratigraphic information including ammonite and foraminiferal biostratigraphy, chemostratigraphy, sequence stratigraphy, magnetostratigraphy and lithostratigraphy (i.e., organic-rich levels associated with OAEs).

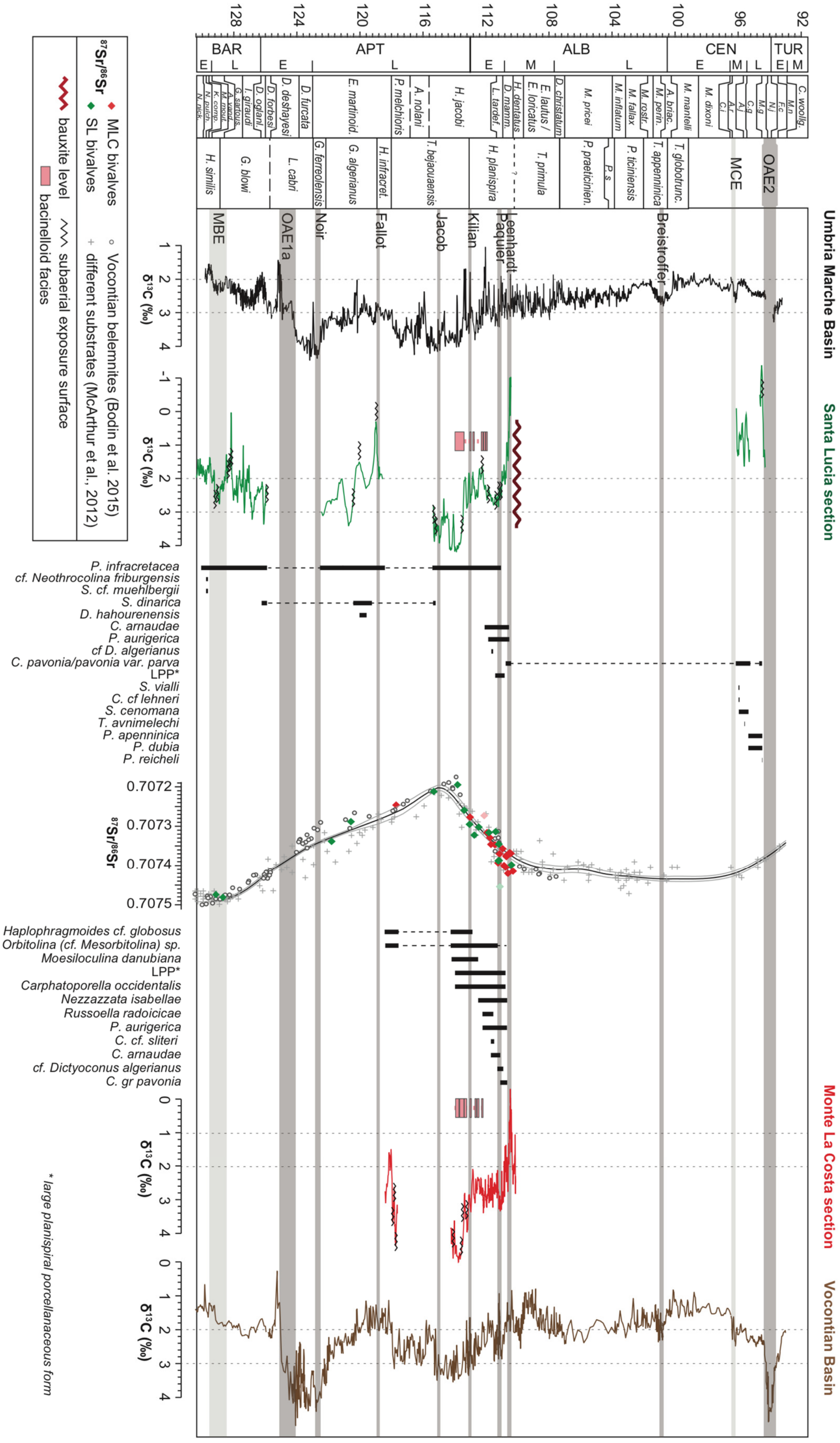

Fig. 3.9: Correlation of pelagic δ^{13}C reference curves with the shallow marine δ^{13}C record of Santa Lucia (green) and Monte La Costa (red). The pelagic δ^{13}C records were compiled using existing curves based on different profiles of the Umbria Marche

Basin (black; Sprovieri et al., 2006; Giorgioni et al., 2012; Bottini et al., 2015; Erba et al., 2015; Gambacorta et al., 2015) and the Vocontian Basin (brown; Gale et al., 1996; Herrle et al., 2004; Godet et al., 2006; Gyawali et al., 2017). The chronostratigraphic ages of the pelagic curves are based on foraminifera and ammonite data plotted against the GTS 2012 (Gradstein et al., 2012), while the SL and the MLC sections are correlated using biostratigraphic information combined with C- and Sr-isotope data. Global sea level changes after Haq 2014.

Strontium isotope values derived from the lower part of the SL section (mean: 0.707478; n=2) indicate an age not younger than early Late Barremian (McArthur et al., 2012). The corresponding stratigraphic interval (60-85 m) is characterised by a positive CIE that tentatively represents the mid-Barremian Event (MBE; Huck et al., 2013; Huck and Heimhofer, 2015). The following stepwise shift to more positive carbon isotope values is a typical Late Barremian-earliest Aptian feature of pelagic sections in the Umbria Marche (Gorgo a Cerbara: Sprovieri et al., 2006) and Vocontian basins (Angles: Godet et al., 2006). In line with previous shallow-water chemostratigraphic results from the Southern and Central Apennines (Di Lucia et al., 2012), the carbonate platform production at the SL locality came to a halt in the prelude of the Oceanic Anoxic Event (OAE) 1a. This is indicated by a dm-thick brecciated interval and the absence of the characteristic positive δ^{13}C excursion associated with OAE1a. Following biostratigraphic (*Salpingoporella dinarica*) and SIS evidence (^{87}Sr/^{86}Sr: 0.707293) recorded by SL limestones, the recovery of the carbonate platform factory (248-265 m) took place during the Late Aptian. Upsection another hiatus in the sedimentary record is indicated both by a prominent subaerial exposure surface and a rapid decline in ^{87}Sr/^{86}Sr ratios (see also Huck and Heimhofer, 2015) toward values typical for the latest Aptian (mean: 0.707194).

A prominent feature of both the SL and MLC carbon isotope curves is an interval with fluctuating but overall positive δ^{13}C values (SL: 160-385 m; MLC: 52-160 m) that is terminated by a sharp negative shift. Strontium isotope data derived from the SL section (0.707235 to 0.707194) clearly suggest that this chemostratigraphic segment correlates with the lower part of the OAE1b multi-event, stratigraphically positioned between the Jacob and Kilian levels (Schmitt et al., in preparation). Considering strontium isotope results, the δ^{13}C inflexion point marked by the most negative values at MLC corresponds to the Leenhardt episode of OAE1b. In the Vocontian and Umbria Marche carbon isotope records, the Kilian 'black-shale' interval is preceded by negative δ^{13}C spikes superimposed on a 1 ‰ negative CIE (Leckie et al., 2002; Erba et al., 2015; Herrle et al., 2004). As already documented by Schmitt et al. (in preparation), the coeval onset of pervasive bacinelloid microencruster growth in both the inner (SL) and marginal (MLC) carbonate platform domain during the upper part of the positive CIE (plateau phase) supports the abovementioned chemostratigraphic correlation.

A pronounced increase in ^{87}Sr/^{86}Sr ratios (0.707273 to 0.707420) is visible in bivalve calcite collected from post-Kilian limestones at SL and MLC. This pattern is a typical Early to Middle Albian feature of the global marine strontium isotope curve (McArthur et al., 2012). Unfortunately, sediments from above the bauxite level bx1 do not contain low-Mg calcite shell material suitable for SIS. The foraminiferal assemblage comprising *P. reicheli*, *P. dubia* and *P. apenninica*, however, clearly indicates a Middle to Late Cenomanian age for the uppermost part of the SL section.

3.7.3 Time lost in discontinuity surfaces

The fragmentary nature of marine sedimentary archives is a well-known phenomenon that is largely governed by a net loss of accommodation space and associated periods of mechanical erosion, condensation, non-deposition and/or chemical dissolution (Ager, 1973; Sadler, 1981; Strasser, 2015). Hiatuses in the depositional record of shallow sedimentary environments are particularly abundant and result from both short-term peritidal processes (e.g. scouring of tidal channels) and long-term sea level fluctuations, the latter being represented by major sequence boundaries (Strasser, 2015). Assessing the frequency and duration of shallow water sedimentary hiatuses is therefore almost impossible, although long-term carbonate platform emersion episodes (> 1 Myr) have the chance to be faithfully depicted by means of SIS (McArthur et al., 2001; Navidtalab et al., 2016).

The here presented integrated bio-chemostratigraphic framework of the central ACP Santa Lucia succession (Fig. 3.9) reveals that about 61% of the time (~ 20.7 Myr) is lost in three major hiatal surfaces incl. intervals of the Early Aptian (~ 3.2 Myr), Late Aptian (~ 3.3 Myr) and Middle Albian to uppermost Middle Cenomanian (~ 14.2 Myr). The Late Aptian hiatus is also recorded by the stratigraphically less expanded MLC section. Using the established stratigraphic framework, correlations and/or comparisons of several hiatuses across the platform are possible.

At the SL locality, large parts of the Early Aptian sedimentary record are missing. The corresponding hiatal surface (Fig. 3.3, 236 m), which is estimated to cover 3.2 Myr, appears as thin brecciated interval and is located at the transition from predominantly mud-supported (calcimicrobial) towards predominantly grain-supported (rudist-algal) facies types. An Early Aptian hiatus with a coeval onset but a 1 Myr longer duration has been reported from the Monte Croce section in the Aurunci Mountains (Fig. 3.10), located about 25 km southwest of Villa Santa Lucia (Di Lucia et al., 2012).

The second hiatus (3.3 Myr) appears as an exposure surface associated with incipient soil formation on top of fenestral limestones characterised by voids filled with greenish argillaceous micrite and a meteoric negative C-isotope spike (-0.2 ‰) recorded a few meters below the surface (Fig. 3.3). An abrupt decline of $^{87}Sr/^{86}Sr$ values (from 0.707293 towards 0.707211) clearly indicates that large parts of the Late Aptian are missing in the SL sedimentary record. Several sections across the ACP (e.g. Mt Croce, Serre Sbregavitelli and Monte Tobenna/Faito; Fig. 3.10) also provide evidence for an expanded Late Aptian emersion episode (D'Argenio et al., 2004; Raspini, 2012; Ruberti et al., 2013; Buccione et al., 2016).

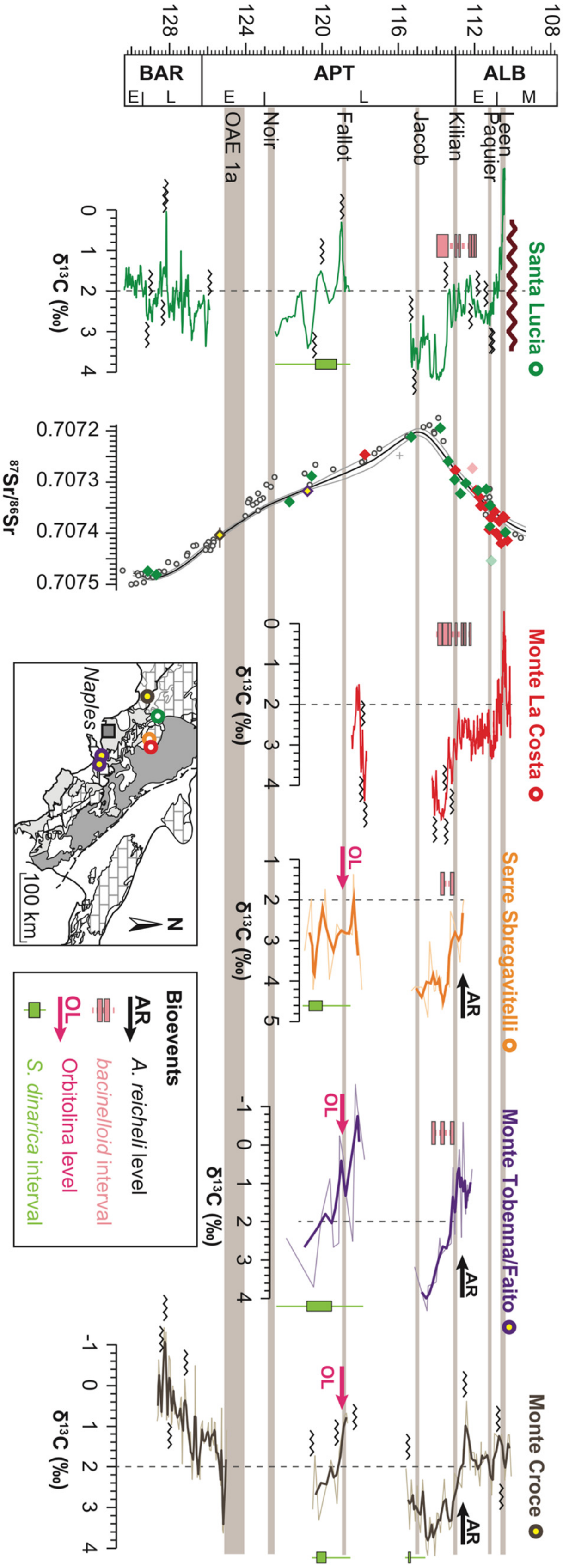

Fig. 3.10: Comparison of $\delta^{13}C$ trends of shallow marine succesions across the ACP including Monte Croce (Di Lucia et al., 2012), Serra Sbregavitelli (Ruberti et al., 2013; D'Argenio et al., 2004) and Monte Tobenna/Faito (Raspini, 2012; D'Argenio et al., 2004). Existing shallow water records were correlated to the here established chronostratographic framework of the MLC

and SL sections. Important bioevents used for stratigraphic correlation are marked. Note that not all bioevents are observed in all the different sections.

The youngest emersion phase (Middle Albian to uppermost Middle Cenomanian) at the SL locality is documented by a prominent 2-m-thick brick-red, karst-filling bauxite level (Fig. 3.3, 515 m) referred to as bx1 (Chiocchini et al., 2005), which is assumed to have formed from lateritic weathering of windblown volcanic ash (Bárdossy et al., 1977; Mondillo et al., 2011). This particular horizon is a well-documented feature of numerous Apennine and Apulian carbonate platform successions (Carannante et al, 2007; Mondillo et al., 2011). Considering chemostratigraphic and biostratigraphic evidence, the time lost in the bx1 level is in the order of about 14.3 Myr, a time span that is significantly longer than previously thought considering biostratigraphic data (1 to 10 Myr: Chiocchini et al., 1989; D'Argenio and Mindszenty, 1995; Chiocchini et al., 2005).

The widespread occurrence of the bx1 karst bauxite of the ACP area has been proposed to be the result of tectonically controlled exposure of vast carbonate platform areas under globally warm and humid climate conditions, combined with sufficient aeolian (volcanic) sediment supply (D'Argenio and Mindszenty, 1995). The long-lasting Cretaceous emersion phase of the ACP, which was required for bauxite formation, was probably caused by tectonic activity, induced either by (i) a lithospheric bulge during an early phase of the Alpine orogeny (D'Argenio and Mindszenty, 1995) or (ii) a Cretaceous to Cenozoic E-W oriented, left-lateral strike-slip fault (Schettino and Turco, 2011). This tectonic activity combined with the variable spatial distribution of windblown material caused the discontinuous formation of karst bauxite.

3.8 Conclusions

Integrated bio- and chemostratigraphy was used to establish a high-resolution chronostratigraphic age-model for the mid-Cretaceous (Barremian to Cenomanian) shallow marine successions of the Central ACP. Studied sections represent lagoonal (SL) and marginal platform settings (MLC). Both stratigraphic sections contain various exposure surfaces, which result in a fragmentary record of the successions. These exposure surfaces differ in terms of their sedimentological expression, geochemical signature and the amount of time covered by the corresponding hiatuses:

1. The SL section, ranging from the Barremian to the Cenomanian, contains three stratigraphic hiatuses. A first hiatus covers parts of the Early Aptian (~ 3.2 Myr), with a thin brecciated interval representing the hiatal surface. The second hiatus is dated to Late Aptian (~ 3.3 Myr) and associated with soil formation on top of a fenestral limestone that contains voids filled with greenish argillaceous micrite as well as a negative carbon isotope shift. The youngest hiatus ranges from Late Albian to Middle Cenomanian (~ 14.3 Myr) and is expressed in the field as a prominent 2-m-thick, red bauxite interval (bx1).

2. Similar to the SL section, the MLC section (Late Aptian to Early Albian) contains a Late Aptian hiatus (~ 3.3 Myr). In the field, this interval shows numerous cm- to dm-thick intra-formational karst-related breccia horizons (angular limestone clasts embedded in a greenish-brownish argillaceous matrix).
3. The Late Aptian hiatus is recorded in several shallow marine carbonate successions across the ACP (incl. Monte Croce, Serra Sbregavitelli, Monte Tobenna/Faito), which allows a platform-wide correlation of the sections and to integrate them into the here established stratigraphic framework.

Acknowledgements

We thank Christiane Wenske (LUH) for laboratory assistance and Fritz-Lukas Stoepke (LUH) for thin section preparation. Financial support from German Research Foundation (DFG) project HU 2258/2-1186 (SH) and HE 4467/8-1 is gratefully acknowledged.

3.9 References

Ager, D.V., 1973. The nature of the stratigraphical record. New York, John Wiley, pp.114

Allan, J.R., Matthews, R.K., 1982. Isotope signatures associated with early meteoric diagenesis. Sedimentology 29, 797-817.

Ayoub-Hannaa, W., Fürsich, F.T., 2011. Functional morphology and taphonomy of Cenomanian (Cretaceous) oysters from the eastern Sinai Peninsula, Egypt. Palaeobioldivers. Palaeoenviron. 91, 197–214.

Bárdossy, G., Jonas, K., Imre, A., Solymar, K., 1977. Interrelations of bauxite texture, micromorphology, mineral individualism, and heteromorphism. Economic Geology 72, 573-581.

Bodin, S., Fiet, N., Godet, A., Matera, V., Westermann, S., Clément, A., Janssen, N.M., M., Stille, P., Föllmi, K.B., 2009. Early Cretaceous (late Berriasian to early Aptian) palaeoceanographic change along the northwestern Tethyan margin (Vocontian Trough, southeastern France): $\delta^{13}C$, $\delta^{18}O$ and strontium isotope belemnite and whole-rock records. Cretaceous Research 30, 1247-1262.

Bodin, S., Meissner, P., Janssen, N.M., Steuber, T., Mutterlose, J., 2015. Large igneous provinces and organic carbon burial: Controls on global temperature and continental weathering during the Early Cretaceous. Global and Planetary Change 133, 238-253.

Boncio, P, Dichiarante, A.M., Auciello, E., Saroli, M., Stoppa, F., 2016. Normal faulting along the western side of the Matese Mountains: Implications for active tectonics in the Central Apennines (Italy). Journal of Structural Geology 82, 16-36.

Bottini, C., Erba, E., Tiraboschi, D., Jenkyns, H.C., Schouten, S., Sinninghe Damsté, J.S., 2015. Climate variability and ocean fertility during the Aptian Stage. Climate of the Past 11, 383-402.

Brand, U., Veizer, J., 1980. Chemical diagenesis of a multicomponent carbonate system-1: Trace elements, Journal of Sedimentary Petrology 50, 1219-1236.

Brand, U., Veizer, J., 1981. Chemical diagenesis of a multicomponent carbonate system-2: Stable isotopes, Journal of Sedimentary Petrology 51, 987-997.

Brandano, M., Giannini, E., Schiavinotto, F., Verrubbi, V., 2007. Miogypsina Globulina (Michelotti) from Lower Miocene Villa S. Lucia Section (Monte Cairo - Central Apennines). Geologica Romana 40, 119-127.

Buccione, R., Mongelli, G., Sinisi, R., Boni, M., 2016. Relationship between geometric parameters and compositional data: A new approach to karst bauxites exploration. Journal of Geochemical Exploration 169, 192–201.

Burla, S., Oberli, F., Heimhofer, U., Wiechert, U., Weissert, H., 2009. Improved time control on Cretaceous coastal deposits: New results from Sr isotope measurements using laser ablation. Terra Nova 21, 401–409.

Carannante, G., Ruberti, D., Simone, L., Vigliotti, M., 2007. Cenomanian Carbonate Depositional Setting: Case Histories from the Central-Southern Apennines (Italy). SEPM Special Publication 87, 11-25.

Carpenter, S.J., Lohmann, K.C., 1992. Sr-Mg ratios of modern marine calcite: Empirical indicators of ocean chemistry and precipitation rate. Geochimica et cosmochimica acta 56, 1837-1849.

Chiocchini M., Coccia, B., Mancinelli, A., Romano, A., Urgera, A., 2004. Microbiostratigrafia ed evoluzione paleogeografia del Mesozoico dell’area del Monte Cairo e di Vallerotonda (Lazio meridionale, Italia). Studi Geol. Camerti, Nuova Serie 2, 1-18.

Chiocchini M., Mancinelli, A., Romano, A., 2005. The gaps in the middle-upper Cretaceous Carbonate Series of the Southern Apennines (Abruzzi and Campania Regions). Geobios, memoire special 11, 133-149.

Chiocchini, M., Pampaloni, M.L., Pichezzi, R.M., 2012. Microfacies e microfossili delle successioni carbonatiche mesozoiche del Lazio e dell’Abruzzo (Italia centrale) - Cretacico. Mem. per Serv. Descr. della Carta Geol. d’It., ISPRA, Serv. Geol. d’It.- Dip. Dif. Suolo 17, pp. 269.

Cosentino D., Cipollari, P., Marsili, P., Scrocca, D., 2010. Geology of the central Apennines: a regional review. Journal of the Virtual Explorer, Electronic Edition 36, paper 11.

D’Argenio, B., Mindszenty, A., 1995. Bauxites and related paleokarst: Tectonic and climatic event markers at regional unconformities. Eclogae Geologicae Helvetiae 88, 453-499.

D'Argenio, B., Ferreri, V., Weissert, H., Amodio, S., Buonocunto, F.P., Wissler, L., 2004. A multidisciplinary approach to global correlation and geochronology. The Cretaceous shallow-water carbonates of southern Apennines, Italy. SEPM Special Publication 81, 103-122.

D’Argenio, B., Ferreri, V., Amodio, S., 2011. Eustatic cycles and tectonics in the Cretaceous shallow Tethys, Central-Southern Apennines. Italian journal of geosciences 130, 119-127.

Damas Mollá, L., Aranburu Artano, A., García Garmilla, F., 2009. Paleoclima y diagénesis en las calizas rojas de Ereño (Aptiense superior-Albiense inferior, Bizkaia).

Damas Mollá, L., Aranburu Artano, A., García Garmilla, F., 2006. Resistencia a la alteración diagenética de conchas de Chondrodonta sp en las calizas rojas del Aptiense–Albiense inferior de Ereño (Bizkaia). GeoGaceta 40, 195-198.

De Castro, P., 1985. Sellialveolina vialii COLA-LONGO, 1963.- In Schroeder.R. and Neumann, M. (eds.): Les grands Foraminifères du Crétacé moyen de la région méditerranéenne. Geobios, Mem. Spec 7, 88-97.

Di Bucci, D., Massa, B., Zuppetta, A., 2006. Relay ramps in active normal fault zones: A clue to the identification of seismogenic sources (1688 Sannio earthquake, Italy). GSA Bulletin 118, 430–448.

Di Lucia, M., Trecalli, A., Mutti, M., Parente, M., 2012. Bio-chemostratigraphy of the Barremian-Aptian shallow-water carbonates of the southern Apennines (Italy): pinpointing the OAE1a in a Tethyan carbonate platform. Solid Earth 3, 1–28.

Dunham, R.J., 1962. Classification of carbonate rocks according to depositional textures. In: Harn, W.E., ed., Classification of carbonate rocks: Am. Assoc. Petroleum Geologists Mem. 1, 108-121.

Erba, E., Duncan, R.A., Bottini, C., Tiraboschi, D., Weissert, H., Jenkyns, H. C., Malinverno, A., 2015. Environmental consequences of Ontong Java Plateau and Kerguelen Plateau volcanism. In: Neal, C.R., Sager, W.W, Sano, T., and Erba, E., eds., The Origin, Evolution, and Environmental Impact of Oceanic Large Igneous Provinces: Geological Society of America Special Paper 511, 271–303.

Fagerstrom, A.G., 1987. The Evolution of Reef Communities. Wiley, New York, NY, pp. 600.

Flügel, E. 2010. Microfacies analysis of limestones. Analysis, Interpretation and Application. Springer –Verlag, Berlin-Heidelberg, pp. 984.

Frijia, G., Parente, M., 2008. Strontium isotope stratigraphy in the upper Cenomanian shallow-water carbonates of the southern Apennines: Short-term perturbations of marine 87Sr/86Sr during the oceanic anoxic event 2. Palaeogeography, Palaeoclimatology, Palaeoecology 261, 15–29.

Frijia, G., Parente, M., Di Lucia, M., Mutti M., 2015. Carbon and strontium isotope stratigraphy of the Upper Cretaceous (Cenomanian-Campanian) shallow-water carbonates of southern Italy: Chronostratigraphic calibration of larger foraminifera biostratigraphy. Cretaceous Research 53, 110–139.

Gale, A.S., Kennedy, W.J., Burnett, J.A., Caron, M., Kidd, B.E., 1996. The Late Albian to Early Cenomanian succession at Mont Risou near Rosans (Drôme, SE France): an integrated study (ammonites, inoceramids, planktonic foraminifera, nannofossils, oxygen and carbon isotopes). Cretaceous Research 17, 515-606.

Gambacorta, G., Jenkyns, H.C., Russo, F., Tsikos, H., Wilson, P.A., Faucher, G., Erba, E., 2015. Carbon-and oxygen-isotope records of mid-Cretaceous Tethyan pelagic sequences from the Umbria–Marche and Belluno Basins (Italy). Newsletters on Stratigraphy 48, 299-323.

Giorgioni, M., Weissert, H., Bernasconi, S.M., Hochuli, P.A., Coccioni, R., Keller, C.E., 2012. Orbital control on carbon cycle and oceanography in the mid-Cretaceous greenhouse. Paleoceanography 27, 1-12.

Godet, A., Bodin, S., Föllmi, K.B., Vermeulen, J., Gardin, S., Fiet, N., Adatte, T., Stüben, D., Van de Schootbrugge, B., 2006. Evolution of the marine stable carbon-isotope record during the early Cretaceous: A focus on the late Hauterivian and Barremian in the Tethyan realm. Earth and Planetary Science Letters 242, 254-271.

Godet, A., Durlet, C., Spangenberg, J.E., Föllmi, K.B., 2016. Estimating the impact of early diagenesis on isotope records in shallow-marine carbonates: a case study from the Urgonian Platform in western Swiss Jura. Palaeogeography, palaeoclimatology, palaeoecology 454, 125-138.

Gradstein, F. M., Ogg, J.G., Schmitz, M.D., and Ogg, G.M. (Eds), 2012. The Geological Time Scale 2012, Amsterdam, Elsevier, pp. 1144.

Guillaume, H., Reichel, M., 1957. Neotrocholina friburgensis n. sp., foraminifere de l'Urgonien alpin. Eclogae Geologicae Helvetiae 50, 286-288.

Gyawali, B.R., Nishi, H., Takashima, R., Herrle, J.O., Takayanagia, H., Latild, J.-L., Iryua, Y., 2017. Upper Albian–upper Turonian calcareous nannofossil biostratigraphy and chemostratigraphy in the Vocontian Basin, southeastern France. Newsletters on Stratigraphy 50, 111-139.

Haq, B.U., 2014. Cretaceous eustasy revisited. Global and Planetary Change 113, 44-58.

Herrle, J.O., Kößler, P., Friedrich, O., Erlenkeuser, H., Hemleben, C., 2004. High-resolution carbon isotope records of the Aptian to Lower Albian from SE France and the Mazagan Plateau (DSDP Site 545): a stratigraphic tool for paleoceanographic and paleobiologic reconstruction. Earth and Planetary Science Letters 218, 149-161.

Horikx, M., Heimhofer, U., Dinis, J., Huck, S., 2014. Integrated stratigraphy of shallow marine Albian strata from the southern Lusitanian Basin of Portugal. Newsletters on Stratigraphy 47, 85-106.

Howarth, R., McArthur, J., 1997. Statistics for strontium isotope stratigraphy: A robust LOWESS fit to the marine Sr-isotope curve for 0 to 206 Ma, with Look-Up Table for derivation of numeric age. The Journal of Geology 105, 441-456.

Huck S., Heimhofer, U., 2015. Improving shallow-water carbonate chemostratigraphy by means of rudist bivalve sclerochemistry. Geochemistry, Geophysics, Geosystems 16, 3111–3128.

Huck, S., Heimhofer, U., Immenhauser, A., Weissert, H., 2013. Carbon-isotope stratigraphy of Early Cretaceous (Urgonian) shoal-water deposits: Diachronous changes in carbonate-platform production in the north-western Tethys. Sedimentary Geology 290, 157-174.

Huck, S., Heimhofer, U., Rameil, N., Bodin, S., Immenhauser, A., 2011. Strontium and carbon-isotope chronostratigraphy of Barremian-Aptian shoal-water carbonates: Northern Tethyan platform drowning predates OAE 1a. Earth Planetary Science Letters 304, 547-558.

Huck, S., Wohlwend, S., Coimbra, R., Christ, N., Weissert, H., 2017. Disentangling shallow-water bulk carbonate carbon isotope archives with evidence for multi-stage diagenesis: An in-depth component-specific petrographic and geochemical study from Oman (mid-Cretaceous). The Depositional Record 3, 233-257.

Hudson, J. D., 1977. Stable isotopes and limestone lithification. Journal of the Geological Society 133, 637-660.

Husinec, A., Jelaska, V., 2006. Relative sea-level changes recorded on an isolated carbonate platform: Tithonian to Cenomanian succession, southern Croatia. Journal of Sedimentary Research 76, 1120-1136.

Immenhauser, A., Della Porta, G., Kenter, J.A., Bahamonde, J.R. 2003. An alternative model for positive shifts in shallow-marine carbonate $\delta^{13}C$ and $\delta^{18}O$. Sedimentology 50, 953-959.

Immenhauser, A., Holmden, C., Patterson, W.P., 2008. Interpreting the Carbon- Isotope Record of Ancient Shallow Epeiric Seas: Lessons from the Recent. In: Pratt, B.R., Holmden, C. (Eds.), Dynamics of Epeiric Seas, Geological Association of Canada Special Publication, 48, 135-174.

Jenkyns, H.C., Gale, A.S., Corfield, R.M., 1994. Carbon-and oxygen-isotope stratigraphy of the English Chalk and Italian Scaglia and its palaeoclimatic significance. Geological Magazine 131, 1-34.

Jones, D.S., Creel, R.C., Rios, B., Ramos, D.P.S., 2015. Chemostratigraphy of an Ordovician–Silurian carbonate platform: $\delta^{13}C$ records below glacioeustatic exposure surfaces. Geology 43, 59-62.

Leckie, R.M., Bralower, T.J., Cashman, R., 2002. Oceanic anoxic events and plankton evolution: Biotic response to tectonic forcing during the mid-Cretaceous. Paleoceanography 17, 13-1.

Lohmann, K.C., 1988. Geochemical Patterns of Meteoric Diagenetic Systems and Their Application to Studies of Paleokarst. In: James, N.P., Choquette, P.W. (Eds.), Paleokarst. Springer- Verlag, New-York Berlin Heidelberg London Paris Tokyo, 58-80.

Mainelli, M., 2000. Monte la Costa Matese centro-settentrionale, Appunti di paleontologia. Arti grafiche La Regione.

Mancinelli, A., Ferrandes, D., 2001. Mesozoic cyanobacteria and calcareous? Algae of the Apennine platform (Latium and Abruzzi, Italy). Geobios 34, 533-546.

Mancinelli, A., Chiocchini, M., 2006. Cretaceous benthic foraminifers and calcareous algae from Monte Cairo (southern Latium, Italy). Bollettino della Società Paleontologica Italiana 45, 91-113.

McArthur, J.M., Howarth, R.J., Bailey, T.R., 2001. Strontium isotope Stratigraphy: LOWESS Version 3: Best Fit to the Marine Sr-Isotope Curve for 0–509 Ma and Accompanying Look-up Table for Deriving Numerical Age. The Journal of Geology 109, 155-70.

McArthur, J.M., Howarth, R.J., Shields, G.A., 2012. Strontium isotope stratigraphy. In: Gradstein, F.M., Ogg, J.G., Schmitz, M., Ogg, G. (Eds.), The Geologic Time Scale 2012. Elsevier Science Limited.

Menegatti, A.P., Weissert, H., Brown, R.S., Tyson, R.V., Farrimond, P., Strasser, A., Caron, M., 1998. High-resolution $\delta^{13}C$ stratigraphy through the early Aptian "Livello Selli" of the Alpine Tethys. Paleoceanography 13, 530-545.

Mindszenty, A., D'Argenio, B., Aiello, G., 1995. Lithospheric bulges recorded by regional unconformities. The case of Mesozoic-Tertiary Apulia. Tectonophysics 252, 137-161.

Mondillo, N., Balassone, G., Boni, M., Rollinson, G., 2011. Karst bauxites in the Campania Apennines (southern Italy): a new approach. Periodico di Mineralogia 80, 407-432.

Moore, C.H., 1985. Upper Jurassic subsurface cements: a case history. In: Carbonate Cements (Eds P.M. Hams and N. Schneidermann). SEPM Spec. Publ. 36, 291–308.

Navidtalab, A., Rahimpour-Bonab, H., Huck, S., Heimhofer, U., 2016. Elemental geochemistry and strontium-isotope stratigraphy of Cenomanian to Santonian neritic carbonates in the Zagros Basin, Iran. Sedimentary Geology, 346, 35-48.

Oehlert, A.M., Swart, P.K., 2014. Interpreting carbonate and organic carbon isotope covariance in the sedimentary record. Nature Communications 5, 4672.

Parente, M., Frijia, G., Di Lucia, M., 2007. Carbon-isotope stratigraphy of Cenomanian-Turonian platform carbonates from southern Apennines (Italy): a chemostratigraphic approach to the problem of correlation between shallow water and deep-water successions. Journal of the Geological Society of London 164, 609-620.

Patacca, E., Scandone, P., 2007. Geology of the Southern Apennines. In: Mazzotti, A., Patacca, E., Scandone, P. (Eds.), CROP-04, Bollettino Societa Geologica italiana (Ital.J.Geosci.), Special Issue 7, 75-119.

Prokoph, A., Shields, G.A., Veizer, J., 2008. Compilation and time-series analysis of a marine carbonate $\delta^{18}O$, $\delta^{13}C$, $^{87}Sr/^{86}Sr$ and $\delta^{34}S$ database through Earth history. Earth-Science Reviews 87, 113-133.

Raspini, A., 2012. Shallow water carbonate platforms (Late Aptian-Early Albian, Southern Apennines) in the context of supraregional to global changes: re-appraisal of palaeoecological events as reflectors of carbonate factory response. Solid Earth 3, 225-249.

Ruberti, D., Bravi, S., Carannante, G., Vigorito, M., Simone, L., 2013. Decline and recovery of the Aptian carbonate factory in the southern Apennine carbonate shelves (southern Italy): climatic/oceanographic vs. local tectonic controls. Cretaceous Research 39, 112-132.

Ruberti, D., Carannante, G., Simone, L., Mangiapia, R., Steuber, T., Vigliotti, M., 2008. Sedimentological and taphonomic characterization of rudist-dominated Senonian carbonate shelves (central-southerm Apennines). Rendiconti online della Societa Geologica Italiana 2, 169-172.

Sadler, P. M., 1981. Sedimentation rates and the completeness of stratigraphic sections. Journal of Geology 89, 569-584.

Schettino, A., Turco, E., 2011. Tectonic history of the western Tethys since the Late Triassic. Bulletin 123, 89-105.

Schmitt, K., Heimhofer, U., Frijia, G., Huck, S., 2019. Platform-wide shift to microbial carbonate production during the late Aptian cold snap. Manuscript in preparation.

Schneider, S., Fürisch, F.T., Werner, W., 2009. Sr-isotope stratigraphy, of the Upper Jurassic of central Portugal (Lusitanian Basin) based on oyster shells. International Journal of Earth Science 98(8), 1949–1970.

Selli, R., 1957. Sulla trasgressione del Miocene nell'Italia meridionale. Giornale di Geologia 2, 1-54.

Selli, R., 1962. Il Paleogene nel quadro della Geologia dell'Italia Centro-Meridionale. Memorie della Societ_a Geologica Italiana 3, 737-789.

Simo, J.A.T., Robert, S.W., Masse, J.P., 1993. Cretaceous carbonate platforms: an overview. In: Simo, J.A.T., Roberts, S.W. and Masse, J.P. (eds) Cretaceous Carbonate Platforms. American Association of Petroleum Geology, Memoirs, 56, 1–23.

Skelton, P.W., 2003. Changing Climate and biota in the marine record. In: Skelton, P.W. (Ed.), The Cretaceous World. Cambridge University Press, Cambridge, 163-184.

Sprovieri, M., Coccioni, R., Lirer, F., Pelosi, N., Lozar, F., 2006. Orbital tuning of a lower Cretaceous composite record (Maiolica Formation, central Italy). Paleoceanography 21, PA4212.

Stanton, T.W., 1901. *Chondrodonta*, a new genus of ostreiform mollusks from the Cretaceous, with descriptions of the genotype and a new species. U. S. Nat. Mus. Proc., 24, 301-307.

Steuber, T., Rauch, M., Masse, J.P., Graaf, J., Malkoč, M., 2005. Low-latitude seasonality of Cretaceous temperatures in warm and cold episodes. Nature 437, 1341-1344.

Steuber. T., 1999. Isotopic and chemical intra-shell variations in low-Mg calcite of rudist bivalves (Mollusca-Hippuritacea): disequilibrium fractionations and late Cretaceous seasonality. International Journal of Earth Sciences 88, 551–570.

Strasser, A., 2015. Hiatuses and condensation: an estimation of time lost on a shallow carbonate platform. The Depositional Record 1, 91–117.

Swart, P.K., 2015. The geochemistry of carbonate diagenesis: The past, present and future. Sedimentology 62, 1233-1304.

Veizer, J., 1983. Chemical diagenesis of carbonates: theory and application of trace element technique. In: Arthur, M.A., Anderson, T.F., Kaplan, I.R., Veizer, J., Land, L.S. ŽEds., Stable Isotopes in Sedimentary Geology 10, Society of Economic Paleontologists and Mineralogists Short Course Notes, 3.1–3.100.

Velić, I., 2007. Stratigraphy and Palaeobiogeography of Mesozoic Benthic Foraminifera of the Karst Dinarides (SE Europe)-PART 1. Geologia Croatica 60, 1-60.

Vezzani, L., Festa, A., Ghisetti, F.C., 2010. Geology and Tectonic Evolution of the Central-Southern Apennines, Italy. The Geological Society of America, Special Paper 469.

Weissert, H., 1989. C-isotope stratigraphy, a monitor of paleoenvironmental change: a case study from the Early Cretaceous. Surveys in Geophysics 10, 1-61.

Weissert, H., Joachimski, M., Sarnthein, M., 2008. Chemostratigraphy. Newsletters on Stratigraphy 42, 145-179.

4. Platform-wide Shift to Microbial Carbonate Production during the Late Aptian cold snap

K. SCHMITT, U. HEIMHOFER, G. FRIJIA, S. HUCK

To be submitted to Geology.

Abstract

Transient episodes of microbial carbonate resurgence in the aftermaths of Phanerozoic major extinction events have been linked to the dramatic decline of grazing metazoans leaving a wide range of ecological niches. Apart from the loss of metazoan competitors, the factors causing pervasive microbial carbonate production are not completely understood. Amongst others, outstanding warm temperatures coupled with low oxygenated waters were proposed as possible triggers. This study focuses on Late Aptian shallow marine carbonates deposited on the Apennine Carbonate Platform (ACP) in the central Tethys, where a platform-wide shift from a metazoan-dominated ecosystem to microbial 'bacinelloid' carbonate production is reported. By establishing an integrated high-resolution chemostratigraphic framework for two sections of the ACP, a coeval onset of pervasive bacinelloid growth is discovered. This initial phase coincides with the late stage of the so-called Late Aptian "cold snap" and the subsequent temperature increase, which was paralleled by a significant sea level rise. Our results contrast with observations from the Early Aptian Oceanic Anoxic Event 1a, where a similar shift towards microbial 'bacinelloid' carbonate production has been linked to exceptionally warm conditions and hypoxia.

4.1 Introduction

Most Phanerozoic reefal and carbonate platform ecosystems were composed of both microbial and skeletal organisms in a mutually beneficial relationship (Webb, 1996). In the aftermath of major biocrises, however, biodiverse metazoan-dominated reef ecosystems were often replaced by microbial carbonate-producing communities (e.g. Pomar and Hallock, 2008). Following the end-Permian mass extinction, for instance, the delayed recovery of metazoan grazers caused widespread microbialite formation in subtidal settings (Schubert and Bottjer, 1992). This reorganization of shallow water carbonate ecosystems is seen as a biological feedback to environmental pressure caused by Siberian Traps volcanism (Pietsch and Bottjer, 2014). It seems likely that the exclusive dominance of neritic microbialite production was fostered by exceptionally high sea-surface temperatures (SSTs) in combination with low dissolved oxygen levels and probably enhanced nutrient availability (e.g. Sun et al., 2011; Kershaw et al., 2012).

A similar set of environmental stressors may have acted on marine calcifying organisms during the mid-Cretaceous emplacement of the Ontong Java Plateau large igneous province (OJP-LIP; Erba et al., 2015). Biotic feedbacks to Early Aptian OJP-LIP related environmental perturbations include a crisis amongst calcareous nannoplankton (Erba et al., 2010), the demise and drowning of subtropical carbonate platforms (Föllmi et al., 1994), the widespread accumulation of organic matter (e.g. Jenkyns, 2010) during Oceanic Anoxic Event (OAE) 1a and the coeval proliferation of *Lithocodium-Bacinella* microencrusters in Tethyan shallow water carbonate platform habitats at the expense of coral-rudist platform communities (Immenhauser et al., 2005; Huck et al., 2010). The taxonomic position of *Lithocodium aggregatum*, *Bacinella irregularis* and 'lithocodoid' and 'bacinelloid' fabrics is still under debate, but it is widely accepted that these microproblematica should be attributed to encrusting algal and calcimicrobial communities (see discussion in Huck et al., 2012).

At this stage, it remains unclear whether shallow water *Lithocodium-Bacinella* episodes were mainly driven by short-lived global warming (hyperthermal) events, probably in combination with platform hypoxia that are superimposed on the long-term Early Aptian warming trend (Huck et al., 2012; Hüter et al., 2019). Indeed, isolated *Lithocodium* and/or *Bacinella* occurrences were reported from various Late Aptian and Early-Middle Albian shallow water settings (e.g. Neuweiler and Reitner, 1992; Greselle and Pittet, 2005; Waite et al., 2007; Di Lucia et al., 2012), but these microbial episodes often lack a precise stratigraphic assignment, which would allow them to be placed into a global context of environmental change.

The current study documents multiple pulses of pervasive bacinelloid microencruster growth in two Tethyan carbonate platform sections (Apennines, Italy) during the Aptian-Albian boundary interval. The overall aim is to chemostratigraphically (C, Sr) pin-point the onset of bacinelloid mass occurrences and to capture the spatial and temporal patterns of carbonate platform ecology change. The latter will be of importance for a better understanding of the palaeoecological impact of the Late Aptian 'cold snap' (Mutterlose et al., 2009; McAnena et al., 2013) and OAE1b-related environmental changes on shallow water carbonate platform communities.

4.2 Geological setting

During the mid-Cretaceous, the Apennine Carbonate Platform (ACP; Fig. 4.1 A) was one of several isolated central Tethyan carbonate platforms bordered by the Molise-Sannio-Lagonegro basin in the North (Fig. 4.1 B) at a palaeolatitude of about 15°N. The studied 153 m-thick Santa Lucia (SL; 41°31'00.6"N 13°46'40.0"E) and 166 m-thick Monte La Costa (MLC; 41°28'12.4"N 14°29'50.0"E) shallow water successions represent back-reef and shelf-margin settings of the ACP, respectively and are largely composed of thick-bedded peloidal-bioclastic and foraminiferal grain- and rudstones with mud-supported intercalations. The typical platform biota comprises radiolitid rudists, chondrodonts, gastropods, benthic foraminifers including orbitolinids, dasycladacean algae and solitary corals. A remarkable feature characterizing both the SL and MLC sections is the repeated pervasive growth of bacinelloid microencrusters. Biostratigraphically, the studied limestone deposits are assigned to the Aptian-Albian ‘Calcari con Requienie e Gasteropodi’ Formation’ (Di Stefano et al., 2011).

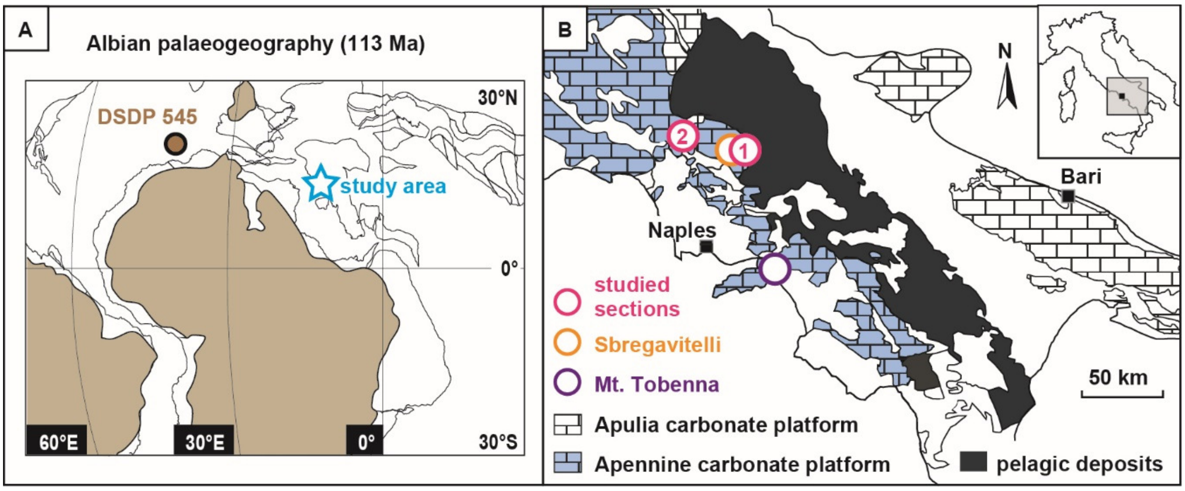

Fig. 4.1: (A) Palaeogeographic map of the Upper Cretaceous showing the location of the study area in the Tethys and North Atlantic deep-sea sections considered in the text (modified after Huber and Leckie, 2011). (B) Location of the studied sections (1: Santa Lucia; 2: Monte La Costa) in the Central and Southern Apennines, Italy (modified after Frijia and Parente, 2008).

4.3 Methods

Samples for microfacies and geochemical investigations were taken at a spacing of ~ 0.5 to 1 m. Bacinelloid microencrusters were studied and semi-quantitatively analyzed in 55 petrographic thin sections. The differentiation of bacinelloid morphotypes is based on the classification scheme of Rameil et al. (2010) and Huck et al. (2012).

The most fine-grained portion of 436 bulk carbonates was sampled with a hand-held micro-drill and measured for its carbon and oxygen isotope composition at the Institute of Geology at Leibniz University Hannover (LUH), Germany. Certified carbonate standards (NBS 19, NBS-18, IAEA, CO-1) produce an external reproducibility of 0.08 ‰ for $\delta^{18}O$ and 0.06 ‰ for $\delta^{13}C$. All isotope results are reported in ‰ relative to the Vienna-Pee Dee Formation belemnite (VPDB) standard in the conventional delta notation. For Sr-isotope analyses, the preservation state of outer shell layers of low-Mg calcite bivalve shells (rudists: n = 5; chondrodonts: n = 3) was examined by elemental compositions (Ca, Mg, Sr, Fe and Mn) provided by inductively coupled plasma-atomic emission spectrometry at the Institute of Geology, Mineralogy and Geophysics at Ruhr-University Bochum (RUB), Germany. In total, five rudist and three chondrodont shells were analyzed at RUB for $^{87}Sr/^{86}Sr$ ratios using a Finnigan MAT 262 thermal ionization mass-spectrometer in dynamic mode.

4.4 Results

Bacinelloid fabrics are characterized by differently sized and shaped sparite-filled vesicles or ‘cells’ (Schlagintweit et al., 2010) that either form (I) oncoids (Ø 250 µm to 5 cm), (II) irregular shaped cm-sized patches or (III) massive, laminar crusts. In the inner carbonate platform domain - covered by the SL section - the dominance of bacinelloid microencrusters is demonstrated by the intermittent occurrence of m-thick beds of float- and rudstones bearing bacinelloid morphotypes I and II (Fig. 4.2: 58–75 m; 124–148 m). The size and volumetric abundance of morphotype I is strongly variable, including stratigraphic levels comprising small-sized, dispersed or cm-sized amalgamated (condensed) and partly reworked oncoids. At the platform margin represented by the MLC section, massive bacinelloid boundstone facies types in rock-forming abundance (morphotype III) occur at several stratigraphic intervals (27–74 m; 124–140 m). In contrast to the SL locality, morphotypes I and II are rare or absent.

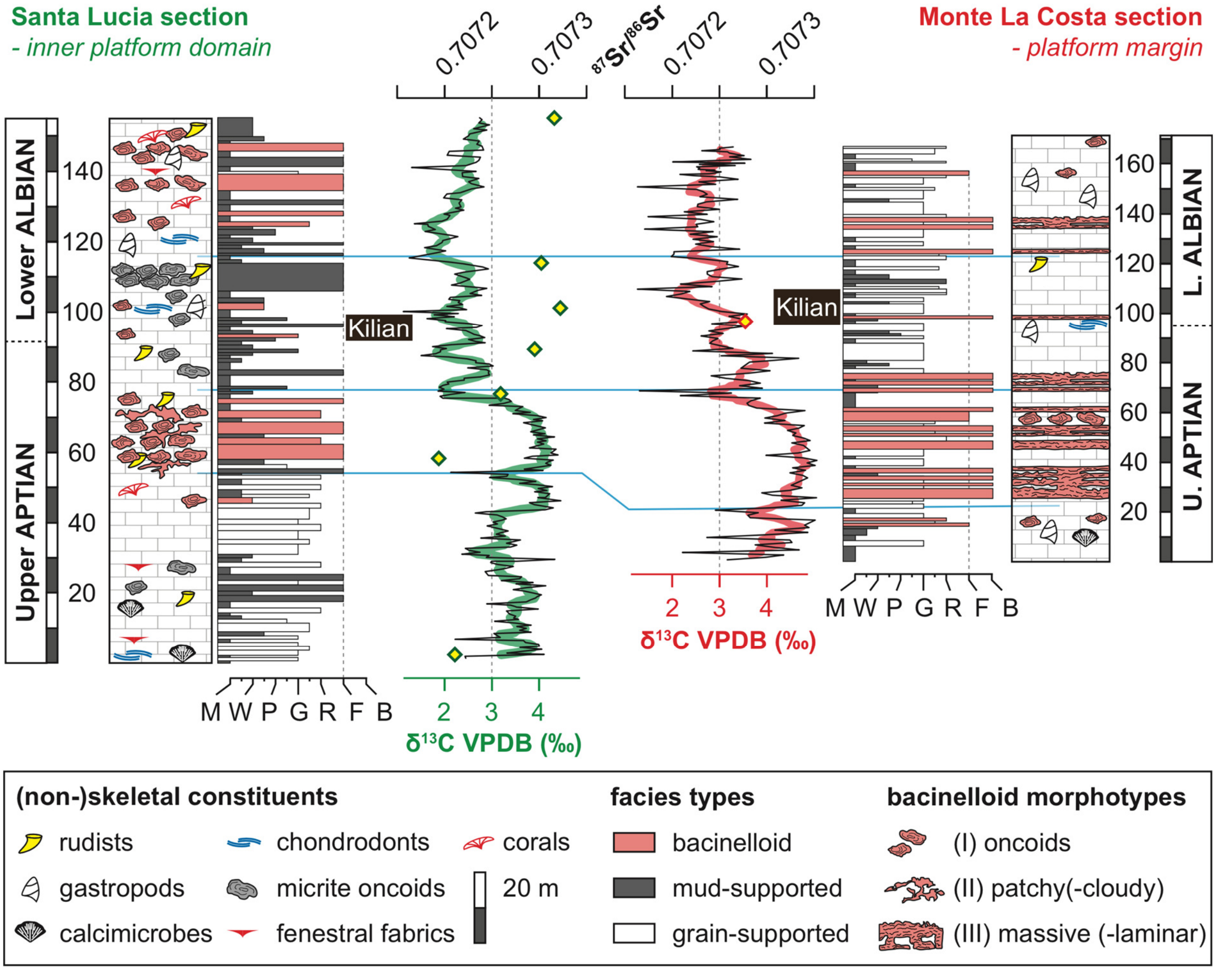

Fig. 4.2: Comparative facies characteristics, lithostratigraphy and chemostratigraphy (C, Sr) of the SL and the MLC sections. Correlation of both sections (blue lines) is based on characteristic carbon isotope trends and inflexion points. Green and red bold lines represent the 5-point moving average curves. Note the coeval appearance of bacinelloid microencrusters during the Upper Aptian at both sites.

Both sections, although ~ 60 km apart, show a remarkably similar stratigraphic $\delta^{13}C$ pattern characterized by a double-peaked positive carbon isotope excursion (CIE) reaching up to 4.5 ‰ (MLC). The CIE is followed by sinusoidal $\delta^{13}C$ variations (amplitude of 1 ‰) that are superimposed on a gradual negative trend (Fig. 4.2). Bivalve shell calcite from selected horizons exhibits $^{87}Sr/^{86}Sr$ ratios ranging between 0.707194 ($\pm 5*10^{-6}$) and 0.707316 ($\pm 5*10^{-6}$) indicative of the latest Aptian-earliest Albian interval (~ 115–111 Myr; McArthur et al., 2001;). The pristine preservation state of considered bivalve shells is proven both by well-defined growth increments composed of fibrous low-Mg calcite as well as elemental characteristics such as high Sr (rudists mean: 1161 ppm; chondrodonts mean: 676 ppm) and low Mn (rudists mean: 4 ppm; chondrodonts mean: 5 ppm) and Fe (rudists mean: 1 ppm; chondrodonts mean: 3 ppm) concentrations (Supplementary Information DR1).

4.5 Discussion

4.5.1 Platform-wide expansion of microbial carbonate production

Considering the chemostratigraphic findings, a pronounced change in facies towards an overwhelming dominance of bacinelloid microencrusters starts in the upper part of the positive CIE at both sites. This facies change marks the onset of rapid alternations between pervasive bacinelloid microencruster growth and typical photozoan carbonate production. At the SL site, the initial onset and major phase of bacinelloid microencruster growth corresponds to a ~ 17 m-thick package essentially composed of morphotypes I and II. The dominance of large bacinelloid oncoids at the SL locality points to low hydrodynamic conditions coupled with reduced sedimentation rates in a lagoonal setting (Védrine et al., 2007). At the MLC site the second peak of the CIE correlates with a ~ 47 m-thick unit composed of massive bacinelloid morphotype III. The dominance of massive crusts at the platform margin provides evidence that bacinelloid microencrusters developed morphological strategies for growth under high-energy conditions. These interpretations are in line with Early Aptian *Lithocodium-Bacinella* microencruster morphotypes identified along the Arabian carbonate platform, where delicate, autochthonous morphotypes characterize calm deeper water environments and more robust or reworked forms are typically found in high-energy settings (Rameil et al., 2010). Following an initial phase of pronounced growth, the over-lying beds are characterized by more intermittent and successively declining bacinelloid occurrence at both study sites.

A platform-wide and synchronous ecosystem shift towards microbial dominance is supported by comparison with existing studies from the ACP. Di Lucia et al. (2012) document a latest Aptian interval rich in *Lithocodium-Bacinella* nodules of subtidal open lagoon facies from the Mt. Tobenna section, located 90 km south of the MLC site (Fig. 4.1 B). In the Sbregavitelli section in the vicinity of MLC (Central ACP), large reworked *Lithocodium-Bacinella* oncoids form part of Upper Aptian channel-fill deposits (Ruberti et al., 2013). In summary, the contemporaneous invasion of bacinelloid microencrusters into lagoonal as well as marginal carbonate platform settings results in a fundamental change in shallow water platform ecology and carbonate production mode and highlights their role as ecological generalists.

4.5.2 Implications for mid-Cretaceous *Lithocodium-Bacinella* mass occurrences

The new geochemical results enable the stratigraphic correlation with a well-dated pelagic reference $\delta^{13}C$ record from the adjacent Umbria Marche Basin in central Italy (Piobbico core: Bottini et al., 2015) and show that the onset of pervasive bacinelloid microencruster growth on the ACP falls within the uppermost portion of a prolonged Late Aptian positive CIE (Fig. 4.3). Strontium isotope ratios indicate that the platform-wide ecosystem turnover slightly postdates the Late Aptian minimum of the global marine $^{87}Sr/^{86}Sr$ composite record (McArthur et al., 2001). Considering the GTS2012 timescale (Ogg and Hinnov, 2012), the $^{87}Sr/^{86}Sr$ minimum can be placed at ~ 115 Myr (*H. jacobi* ammonite zone), stratigraphically positioned between the 113 (Jacob) and Kilian black-shale levels of the OAE1b multi-event.

The initial expansion of bacinelloid-dominated facies occurs during a phase of peculiar climatic conditions referred to as Late Aptian 'cold snap' (Mutterlose et al., 2009; Millán et al., 2014; Bodin et al., 2015; O'Brien et al., 2017). Evidence for global cooling during the Late Aptian is provided by the southward migration of boreal taxa (Mutterlose et al., 2009) and glendonite occurrences in high latitudes (Herrle et al., 2015; Grasby et al., 2017). Open ocean SST estimates based on TEX_{86} data from the eastern North Atlantic (DSDP Site 545) show a distinct drop from ~ 32°C during the early Late Aptian (NC7B) towards ~28°C in the latest Aptian (NC8A) (McAnena et al., 2013), compared to exceptionally warm TEX_{86}–derived SST estimates of ~ 34°C prevailing during the middle Albian (O'Brien et al., 2017). In the Umbria Marche Basin (Piobbico core), the stratigraphic interval between the 113 and Kilian levels is composed of organic-poor, red-colored marlstone indicative of well-oxygenated and probably cool bottom waters (Bottini and Erba, 2018). Chemostratigraphic correlation reveals that the main phase of bacinelloid growth on the ACP took place during the final stage of the Late Aptian SST minimum and the subsequent temperature increase (Fig. 4.3). Individual black shale levels indicative of basinal anoxia and associated with short-lasting hyperthermal conditions (McAnena et al., 2013; Bottini and Erba, 2018) show no clear lithological expression in the shallow water deposits on the ACP. This clearly contrasts with Early Aptian *Lithocodium-Bacinella* episodes related to OAE1a, which were proposed to be associated with shallow water platform hypoxia during a phase of global ocean oxygen deficiency (Hüter et al., 2019).

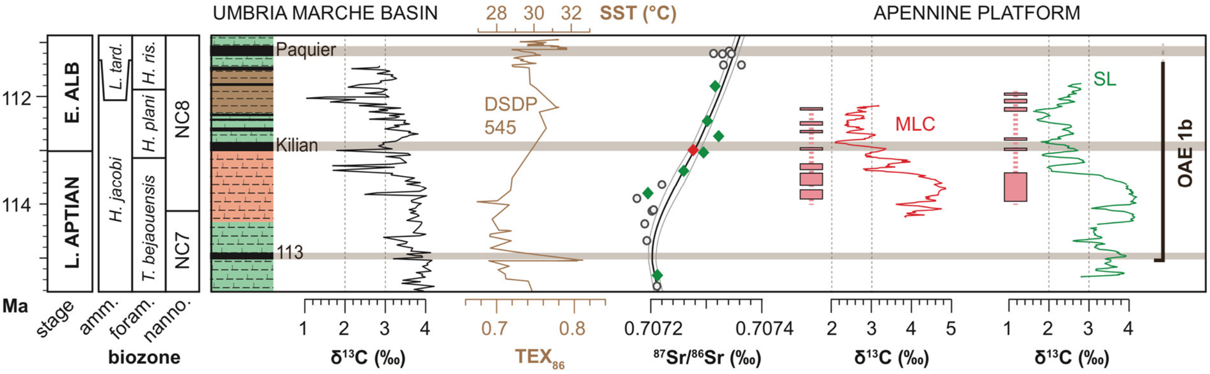

Fig. 4.3: Correlation of the SL and MLC carbon isotope profiles with a well-dated pelagic composite $\delta^{13}C$ record from the adjacent Umbria Marche Basin (Piobicco core: Bottini et al., 2015). Age assignments of the SL and MLC sections are calibrated by means of strontium isotope stratigraphy. Sea surface temperature estimates are based on TEX_{86} data (McAnena et al., 2013). The evolution of global marine $^{87}Sr/^{86}Sr$ values (LOWESS curve) is from McArthur et al. (2001). All data are calibrated to the GTS 2012 timescale (Gradstein et al., 2012). Brown bars represent the stratigraphic positions of pelagic organic-rich levels referred to as 113 (Jacob), Kilian and Paquier episodes (Bottini et al., 2015). Lithostratigraphic log of the Piobbico core after Bottini and Erba (2018) contains black shales (black), marlstones (green), pink to reddish marlstones (red) and brown claystones (brown).

At the MLC site, deposition of the bacinelloid interval postdates an unconformity, which marks a significant Late Aptian hiatus (Graziano and Raspini, 2015). Evidence for widespread platform exposure due to a Late Aptian sea level drop of arguable glacio-eustatic nature comes from Iberia and the Arabian plate, where deep incised valley systems back-filled with locally condensed iron-rich siliciclastics (Greselle and Pittet, 2005; Maurer et al., 2013; Bover-Arnal et al., 2014). According to Maurer et al. (2013), the long-lasting Late Aptian lowstand was followed by a rapid sea level rise in the range of ~ 40 m. On the Arabian plate, this subsequent sea level rise has been placed in the APT6 3rd order sequence which corresponds to the stratigraphic interval located between the 113 (Jacob) and Paquier levels (*H. jacobi* ammonite zone). These observations indicate that the onset of sedimentation at the MLC site may reflect the APT6 sea level rise with the massive bacinelloid deposits representing a transgressive facies.

In summary, pervasive bacinelloid microencruster growth on the ACP occurs during a phase of climatic transition at the end of the Late Aptian cooling. The observed connection with relatively cool conditions and well oxygenated ocean waters clearly contrasts with shallow water *Lithocodium-Bacinella* microbial episodes during OAE1a, generally considered as a phase of outstanding global warmth (Mutterlose et al., 2014; Naafs and Pancost, 2016). Transient episodes of microbial carbonate proliferation should thus not be exclusively considered as indicator of hyperthermal and hypoxic conditions in Earth history.

Acknowledgements

We thank Christiane Wenske (LUH) for laboratory assistance and Fritz-Lukas Stoepke (LUH) for thin section preparation. Financial support from German Research Foundation (DFG) project HU 2258/2-1 (SH) and HE 4467/8-1 (UH) is gratefully acknowledged.

4.6 References

Bodin, S., Meissner, P., Janssen, N. M., Steuber, T., Mutterlose, J., 2015. Large igneous provinces and organic carbon burial: Controls on global temperature and continental weathering during the Early Cretaceous: Global and Planetary Change 133, 238–253.

Bottini, C., Erba, E., 2018. Mid-Cretaceous paleoenvironmental changes in the western Tethys. Climate of the Past 14, 1147-1163.

Bottini, C., Erba, E., Tiraboschi, D., Jenkyns, H.C., Schouten, S., Sinninghe Damsté, J.S., 2015. Climate variability and ocean fertility during the Aptian Stage. Climate of the Past 11, 383-402.

Bover-Arnal, T., Salas, R., Guimerà, J., Moreno-Bedmar, J. A., 2014. Deep incision in an Aptian carbonate succession indicates major sea-level fall in the Cretaceous. Sedimentology 61, 1558-1593.

Di Lucia, M., Trecalli, A., Mutti, M., Parente, M., 2012. Bio-chemostratigraphy of the Barremian-Aptian shallow water carbonates of the southern Apennines (Italy): pinpointing the OAE1a in a Tethyan carbonate platform: Solid Earth 3, 1–28.

Di Stefano, R., Fiorentino, A., Marino, M., Perini, P., 2011. Verso uno schema litostratigrafico dell'Appennino meridionale. Rendiconti online della Società Geologica Italiana 12, 59-61.

Erba, E., Bottini, C., Weissert, H. J., Keller, C.E., 2010. Calcareous nannoplankton response to surface-water acidification around Oceanic Anoxic Event 1a. Science 329, 428-432.

Erba, E., Duncan, R.A., Bottini, C., Tiraboschi, D., Weissert, H., Jenkyns, H.C., Malinverno, A., 2015. Environmental consequences of Ontong Java Plateau and Kerguelen Plateau volcanism. In: Neal, C.R., Sager, W.W, Sano, T., and Erba, E., eds., The Origin, Evolution, and Environmental Impact of Oceanic Large Igneous Provinces: Geological Society of America Special Paper 511, 271–303.

Frijia, G., Parente, M., 2008. Strontium isotope stratigraphy in the upper Cenomanian shallow-water carbonates of the southern Apennines: Short-term perturbations of marine $^{87}Sr/^{86}Sr$ during the oceanic anoxic event 2. Palaeogeography, Palaeoclimatology, Palaeoecology 261, 15-29.

Gradstein, F.M., Ogg, J.G., Schmitz, M.D., Ogg, G., 2012. The Geologic Time Scale 2012. Elsevier, Amsterdam, pp. 1139.

Grasby, S.E., McCune, G.E., Beauchamp, B., Galloway, J.M., 2017. Lower Cretaceous cold snaps led to widespread glendonite occurrences in the Sverdrup Basin, Canadian High Arctic. Bulletin 129, 771-787.

Graziano, R., Raspini, A., 2015. Long-and short-term hydroclimatic variabilities in the Aptian Tethys: Clues from the orbital chronostratigraphy of evaporite-rich beds in the Apennine carbonate platform (Mt. Faito, southern Italy). Palaeogeography, Palaeoclimatology, Palaeoecology 418, 319-343.

Gréselle, B., Pittet, B., 2005. Fringing carbonate platforms at the Arabian Plate margin in northern Oman during the Late Aptian-Middle Albian: Evidence for high-amplitude sea-level changes: Sedimentary Geology 175, 367–390.

Herrle, J.O., Schröder-Adams, C.J., Davis, W., Pugh, A.T., Galloway, J.M., Fath, J., 2015. Mid-Cretaceous High Arctic stratigraphy, climate, and oceanic anoxic events. Geology 43, 403-406.

Huber, B. T., Leckie, R. M., 2011. Planktic foraminiferal species turnover across deep-sea Aptian/Albian boundary sections. The Journal of Foraminiferal Research 41, 53-95.

Huber, B.T., MacLeod, K.G., Gröcke, D.R., Kucera, M., 2011. Paleotemperature and paleosalinity inferences and chemostratigraphy across the Aptian/Albian boundary in the subtropical North Atlantic. Paleoceanography and Paleoclimatology 26, PA4221.

Huck, S., Rameil, N., Korbar, T., Heimhofer, U., Wieczorek, T.D., Immenhauser, A., 2010. Latitudinally different responses of Tethyan shallow-water carbonate systems to the Early Aptian oceanic anoxic event (OAE1a): Sedimentology 57, 1585–1614.

Huck, S., Heimhofer, U., Immenhauser, A., 2012. Early Aptian algal bloom in a neritic proto-North Atlantic setting: Harbinger of global change related to OAE1a?. GSA Bull. 124, 1810–1825.

Hüter, A., Huck, S., Bodin, S., Heimhofer, U., Weyer, S., Jochum, K.P., Immenhauser, A., 2019. Central Tethyan platform-top hypoxia during Oceanic Anoxic Event 1a. Clim. Past Discuss., in review.

Immenhauser, A., Hillgärtner, H., van Bentum, E., 2005. Microbial–foraminiferal episodes in the Early Aptian of the southern Tethyan margin: ecological significance and possible relation to oceanic anoxic event 1a: Sedimentology 52, 77–99.

Jenkyns, H.C., 2010. Geochemistry of oceanic anoxic events: Geochemistry, Geophysics, Geosystems 11, Q03004.

Kershaw, S., Crasquin, S., Li, Y., Collin, P.-Y., Forel, M.-B., Mu, X., Baud, A., Wang, Y., Xie, S., Maurer, F., Guo, L., 2012. Microbialites and global environmental change across the Permian−Triassic boundary: a synthesis: Geobiology 10, 25–47.

Maurer, F., Van Buchem, F.S., Eberli, G.P., Pierson, B.J., Raven, M.J., Larsen, P.H., Vincent, B., 2013. Late Aptian long-lived glacio-eustatic lowstand recorded on the Arabian Plate. Terra Nova 25, 87-94.

McAnena, A., Flögel, S., Hofmann, P., Herrle, J.O., Griesand, A., Pross, J., Talbot., M., Rethemeyer, J., Wallmann, K., Wagner, T., 2013. Atlantic cooling associated with a marine biotic crisis during the mid-Cretaceous period: Nature Geoscience 6, 558–561.

McArthur, J.M., Howarth, R.J., Bailey, T.R., 2001. Strontium isotope stratigraphy: LOWESS version 3: best fit to the marine Sr-isotope curve for 0–509 Ma and accompanying look-up table for deriving numerical age: J. Geol. 109, 155–170.

Millán, M. I., Weissert, H.J., López-Horgue, M.A., 2014. Expression of the Late Aptian cold snaps and the OAE1b in a highly subsiding carbonate platform (Aralar, northern Spain). Palaeogeography, palaeoclimatology, palaeoecology 411, 167-179.

Mutterlose, J., Bornemann, A., Herrle, J. O., 2009. The Aptian-Albian cold snap: Evidence for mid Cretaceous icehouse interludes: Neues Jahrbuch für Geologie und Paläontologie Abhandlungen 232, 217–225.

Mutterlose, J., Bottini, C., Schouten, S., Sinninghe Damsté, J.S., 2014. High sea-surface temperatures during the early Aptian Oceanic Anoxic Event 1a in the Boreal Realm. Geology 42, 439-442.

Naafs, B.D.A., Pancost, R.D., 2016. Sea-surface temperature evolution across Aptian Oceanic Anoxic Event 1a: Geology 44, 959–962.

Neuweiler F., Reitner, J., 1992. Karbonatbänke mit *Lithocodium aggregatum* Elliott/Bacinella irregularis Radoičić. Paläobathymetrie, Paläoökologie und stratigraphisches Äquivalent zu thrombolithischen Mud Mounds, Berliner Geowiss. Abhandlungen 3, 273–293.

O'Brien, C.L., Robinson, S.A., Pancost, R.D., Damsté, J.S.S., Schouten, S., Lunt, D.J., Alsenz, H., Bornemann, A., Bottini, C., Brassell, S.C., Farnsworth, A., Forster, A., Huber, B.T., Inglis, G.N., Jenkyns, H., C., Linnert, C., Littler, K., Markwick, P., McAnena, A., Mutterlose, J., Naafs, B., D., A., Püttmann, W., Sluijs, A., Helmond, N., A., G., M. van, Vellekoop, J., Wagner, T., Wrobel, N., E., 2017. Cretaceous sea-surface temperature evolution: Constraints from TEX_{86} and planktonic foraminiferal oxygen isotopes. Earth-science reviews 172, 224-247.

Pietsch, C., Bottjer, D.J., 2014. The importance of oxygen for the disparate recovery patterns of the benthic macrofauna in the Early Triassic: Earth-Science Reviews 137, 65–84.

Pomar, L., Hallock, P., 2008. Carbonate factories: A conundrum in sedimentary geology: Earth Science Reviews 87, 134–169.

Rameil, N., Immenhauser, A., Warrlich, G., Hillgaertner, H., Droste, H. J., 2010. Morphological patterns of Aptian *Lithocodium–Bacinella* geobodies: relation to environment and scale: Sedimentology 57, 883–911.

Ruberti, D., Bravi, S., Carannante, G., Vigorito, M., Simone, L., 2013. Decline and recovery of the Aptian carbonate factory in the southern Apennine carbonate shelves (southern Italy): climatic/oceanographic vs. local tectonic controls: Cretaceous Research 39, 112–132.

Schlagintweit, F., Bover-Arnal, T., Salas, R., 2010. New insights into *Lithocodium aggregatum* Elliott 1956 and Bacinella irregularis Radoičić 1959 (Late Jurassic–Lower Cretaceous): two ulvophycean green algae (? Order Ulotrichales) with a heteromorphic life cycle (epilithic/euendolithic): Facies 56, 509–547.

Schubert, J.K., Bottjer, D.J., 1992. Early Triassic stromatolites as post-mass extinction disaster forms: Geology 20, 883–886.

Sun, Y., Joachimski, M.M., Wignall, P.B., Yan, C., Chen, Y., Jiang, H., Wang, L, Lai, X., 2012. Lethally hot temperatures during the Early Triassic greenhouse. Science 338, 366-370.

Védrine, S., Strasser, A., Hug, W., 2007. Oncoid growth and distribution controlled by sea-level fluctuations and climate (Late Oxfordian, Swiss Jura Mountains). Facies 53, 535–552.

Waite, L.E., Scott, R.W., Kerans, C., 2007. Middle Albian age of the regional dense marker bed of the Edwards Group, Pawnee Field, south-central Texas: Gulf Coast Association of Geological Societies Transactions 57, 759–774.

Webb, G. E., 1996. Was Phanerozoic reef history controlled by the distribution of non-enzymatically secreted reef carbonates (microbial carbonate and biologically induced cement)?. Sedimentology 43, 947–971.

5. Radiolitid Rudists: An Underestimated Archive for Climate Reconstruction?

K. SCHMITT, U. HEIMHOFER, M. KRUMMACKER, N.J. DE WINTER., S. HUCK

Abstract

Rudist shells are often used for palaeoenvironmental reconstructions in the greenhouse world of the Cretaceous. Radiolitids, a family of rudists, dominated the shallow marine carbonate platforms during the mid-Creatceous. Still, due to their very complex low-Mg calcite outer shell layer, they are often neglected for palaeoenvironmental reconstructions. The aim of this study is to use a combination of high-resolution analytical techniques, such as µXRF and IRMS, in order to make radiolitid shells accessible as an archive for seasonal temperature or salinity changes during the mid-Cretaceous. Four *Eoradiolitites* shells were analysed in detail: two right valves (RV), a left valve (LV) plus its articulated RV and a LV. The results show that the valves of radiolitid rudists are a suitable archive for palaeoenvironmental reconstructions.

5.1 Introduction

The climate of the Cretaceous is famous for its prolonged greenhouse conditions, which were only interrupted by a few short-lived but prominent cooling events (Skelton et al., 2003; Steuber et al., 2005; Bornemann et al., 2008; Mutterlose et al., 2009). Cretaceous palaeoclimate is often reconstructed by $\delta^{18}O$ data derived from belemnites (e.g. Bodin et al., 2015), planktonic foraminifera (e.g. Bottini et al., 2015) and TEX_{86} (e.g. O'Brien et al., 2017). As all of them or their respective organisms are floating or migrating through the water, their isotope record contains temperatures of serval habitat changes (e.g. Eggins et al., 2003). In order to avoid this open marine temperature signal, sessile organisms are favoured for analyses.

In the Cretaceous, sessile rudists bivalves dominated shallow marine, low latitude carbonate platform settings in the Tethyan Ocean and are therefore suitable for paleoenvironmental reconstruction (Ross and Skelton, 1993; Scott et al., 1995; Skelton and Gili, 2012; Steuber and Schlüter, 2012). After their first appearance in the Oxfordian (Late Jurassic) (Skelton, 1978), they evolved to the most important carbonate-producing biota (Steuber and Veizer, 2002) until they went extinct at the Creatceous/Paleogene boundary (Skelton et al., 2003). Although various forms had evolved over time, all species can be assigned to one of three morphotypes (recumbents, clingers or elevators), which were identified in previous taxonomic studies (Schumann and Steuber, 1997; Skelton and Gili, 1991).

However, all species built shells following a similar basic shell design: An outer layer composed of fibrous prismatic low-Mg calcite and (two) inner aragonitic layers (Kennedy and Taylor 1968;

Skelton 1974; Sanders, 1999; Pons and Vicens, 2008). The aragonitic layers are usually replaced by diagenetic low-Mg calcite during fossilization, but the outer low-Mg calcite layer provides material with a high potential to act as an archive for seawater chemistry, as it is resistant to diagenesis (Al-Aasm and Veizer 1986 a, b). For instance, previous studies have shown that the outer low-Mg calcite layer of Cretaceous rudist shells is a precious archive for the strontium isotope composition of ocean waters (Steuber et al., 2005; Frijia and Parente, 2008; Frijia et al., 2015; Huck and Heimhofer, 2015). Additionally, it is suitable as palaeoenvironemntal archive as the secretive processes of the shells were affected by palaeoclimatic (seasonal temperature variations), palaeochemical (salinity changes) and palaeobiological (growth rate and carbonate production) parameters (e.g. Steuber 1996; Regidor-Higuera et al., 2007; de Winter et al., 2017a).

Rudists have proven to be very suitable for climate reconstruction in the Lower Cretaceous (Steuber et al., 2005) but during the mid-Cretaceous the climate record is incomplete as the suitable material is missing. This is partly due to the fact that radiolitids, a family often overlooked as a palaeoclimate archive, became dominant during the middle Aptian (Masse and Gallo Maresca, 1997; Fenerci-Masse et al., 2006; Skelton and Gili, 2012). The taxonomy of the shells of radiolitids was discussed and defined in various previous studies (Pons and Vicens, 2008; Cestari, 1992; Schumann, 1995; Skelton, 1978): In general, the right attached valve (RV) of radiolitids is described as conical to cylindro-conical, while the left free valve (LV) is reduced to a cap-like form with a compact structure (Pons and Vicens, 2008). The most significant feature of radiolitid shells is the special structure in their outer layer of the RV, where compact and non-compact structures are alternating. The non-compact portion is often distinct as honeycomb (Woo et al., 1993; Steuber, 1999), boxwork (Hamama, 2010), cellular (Masse and Maresca, 1997; Masse et al., 2007) or celluloprismatic structure (Pons and Vicens, 2008). It is formed by two kinds of laminae (or plates): the funnel plates and the radial plates (muri or walls). The latter is arranged orthogonal to the funnel plates (Masse et al., 2007; Fig. 5.1) creating an intraskeletal pore space, which was probably originally filled with organic material (Regidor Higuera et al, 2007). This material decomposed after death and was filled post-mortem with diagenetic low-Mg calcite cement (Tibljaš et al., 2004; Mansour, 2004). For a more detailed description of the radiolitid shell structure, please refer to Regidor-Higuera et al. (2007).

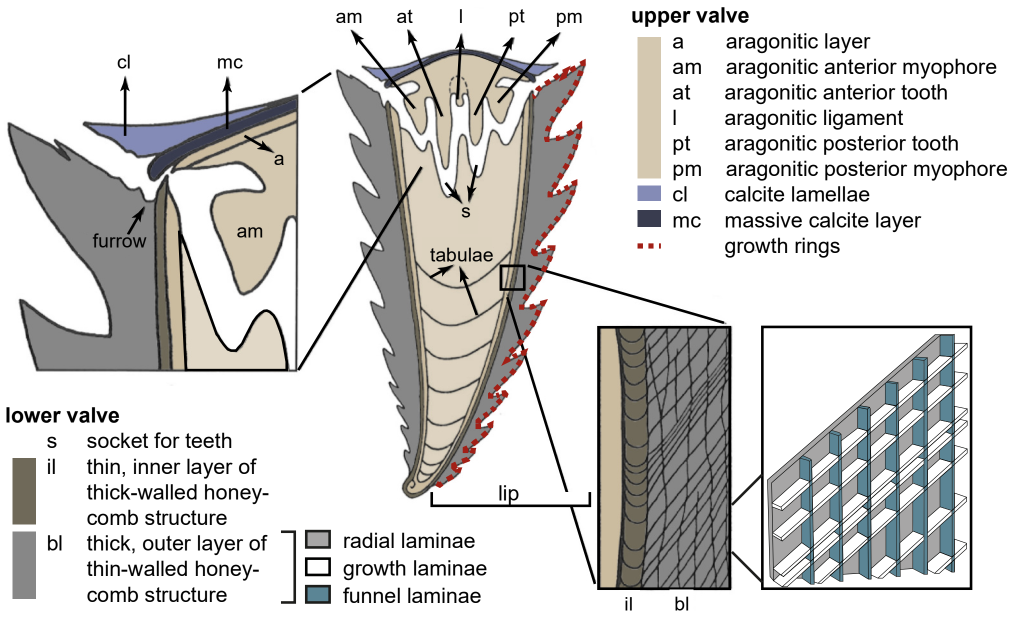
cl
mc
a
am
furrow
am
at
l
pt
pm
s
tabulae
lip
upper valve
a aragonitic layer
am aragonitic anterior myophore
at aragonitic anterior tooth
l aragonitic ligament
pt aragonitic posterior tooth
pm aragonitic posterior myophore
cl calcite lamellae
mc massive calcite layer
growth rings
lower valve
s socket for teeth
il thin, inner layer of thick-walled honeycomb structure
bl thick, outer layer of thin-walled honeycomb structure
radial laminae
growth laminae
funnel laminae
il
bl

Fig. 5.1: Schematic construction of a radiolitid shell showing the cone shaped lower (right) valve with detailed view of the boxwork structure and the cap like upper (left) valve (modified after Sanders, 1999 and Pons and Vicens, 2008).

Only few studies deal with the elemental and isotopic composition of radiolitid shells (Steuber, 1999; Regidor-Higuera et al., 2007; Tibljaš et al., 2004). They suggest that radiolitids are not suitable for palaeoenvironmental reconstructions, as their porous outer shell layer allows fluids to circulate through the pores causing diagenetic alteration. Additionally, sampling for unaltered material is difficult due to the alternation of compact and non-compact parts. The aim of this study is twofold:

(I) Firstly, high-resolution geochemical analyses (isotope ratio mass spectrometry and micro-X-ray fluorescence) and classical sclerochronology (macro and microstructures) are combined to identify diagenetically altered parts.

(II) Secondly, the suitability of radiolitid shells as palaeoenvironmental archive (palaeotemperture, palaeosalinity, living habitat) is tested.

5.2 Material

Radiolitid rudists evolved and spread during the late Aptian-Albian to become the most diverse family among the rudists (Masse et al., 2007; Steuber and Löser, 2000). The outer shell layer of radiolitids contains micro- and megarhythms, which are caused by tidal or biological cycles (Sanders, 1999; Pons and Vicens, 2008). Megarhythms (annual cycles) are defined as major variations in the shells' ornamentation, visible in thin sections due to the change in the microstructure or in variations in the stable oxygen isotope record. Schumann (1995) proposed that a complete annual cycle includes 24-25 growth lamellae. Each growth lamella is designated as a microrhythm that is expressed as a change in colour (light and dark). They can be distinguished by width, stacking and structure. Notably, Regidor-

Higuera et al. (2007) state that the number of lamellae per year can vary between different genera and species, depending on the environment of the shell.

For this study, several radiolitid shells were collected from a shallow marine marginal carbonate platform setting in the central Tethys, today outcropping in the east-west oriented Matese Mountain Massif in southern Italy (Monte La Costa section; Fig. 5.2). Based on an integrated bio- and chemostratigraphic approach, the corresponding stratigraphic interval is dated to an Early Albian age (~ 112 Ma). Collected shells were screened with a magnifying glass to identify specimens that showed best preserved visible growth lamellae and low bioerosion. Finally, four very well preserved *Eoradiolitites* shell fragments (A – D) were selected from a 31 m-thick stratigraphic interval, with shell B and D originating from the same interval (MLC 387 m), followed by fragment A (MLC 401 m) and shell C (MLC 418 m). Fragments A, B and the lower part of fragment C represent different ontogenetic stages of a right valve (RV), while the upper part of fragment C and fragment D represent different portions of a left valve (LV). For further information about the lithostratigraphy and the dating, please refer to Schmitt et al. (in preparation).

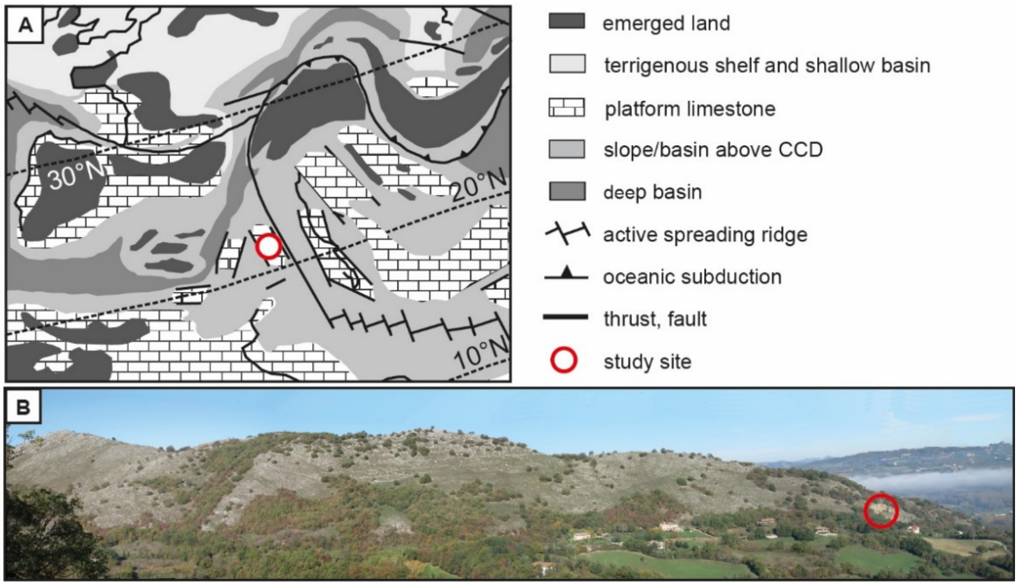

Fig. 5.2: A. Palaeogeographic map of the Upper Cretaceous with the studied area of the Apennine Carbonate Platform in the Tethyan realm. B. Study site in the Matese Mountains, Itlay.

Radial cuts, perpendicular to the growth laminae, of representative shells were used to prepare thin sections and slabs, which allow to identify changes in the microstructure and to assess sclerochronological changes in isotopic and elemental compositions, respectively. The length of RV fragments varies from 27.6 mm (shell B) to 52.5 mm (shell A). The LV (shell D) fragment is 59.5 mm in diameter. Shell C consists of an articulated LV (13 mm) and RV (26.2 mm). The inner aragonitic layer (al), the inner part of the outer layer (il), the outer layer (bl) and borings were identified in all shell parts (Fig. 5.2). Detected mineral fractions are micrite and sparite. The former aragonitic parts are recrystallized and preserved as blocky diagenetic low-Mg calcite and are thus excluded from further analyses.

5.3 Methods

Selected valves were cut along their perpendicular axis, cleaned with distilled water and dried for 24 h at 40 °C. Afterwards, thin sections and polished slabs were prepared (Fig. 5.3).

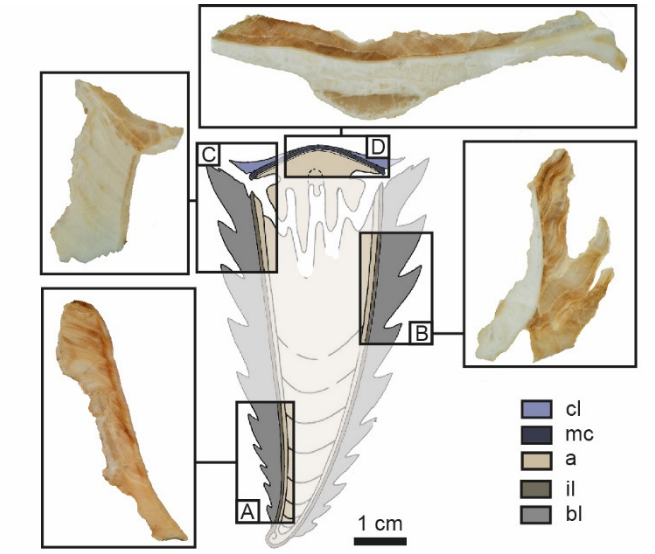

Fig. 5.3: Schematic representation of a radiolitid shell with the selected shells of this study. (A) Right valve; (B) Right valve; (C) Articulated right and left valve; (D) Left valve.

The preservation state of collected shell samples was tested using cathodoluminescence (CL) microscopy. CL was applied to thin sections and slabs using a Reliontron (Relion, U.S.A) cold-cathode luminescence device hosted at the University of Texas at San Antonio (USA). The CL microscope is characterized by an acceleration voltage ranging from 10 to 15 kV and a current intensity ranging from 0.8 to 1.2 mA. The CL chamber was mounted on a Leica DM2700 microscope equipped with 2.5x, 4x, 10x and 20x magnification objectives.

Following petrographic inspections, the elemental composition of shells representing different ontogenetic stages of the animal were measured by means of a Tornado M4 micro X-ray fluorescence (µXRF) scanner (Bruker nano GmbH, Berlin, Germany), hosted at the Analytical, Environmental and Geochemistry research group of the Vrije Universiteit (Brussel). The µXRF scanner is equipped with a Rh source and two X Flash 430 Silicon Drift detectors. First, semi-quantitative µXRF-maps were created in order to assess the distribution of major and trace elements across the surface of shell fragments. Polished shell surfaces were scanned in the µXRF mapping mode using a short acquisition time of 1 ms per pixel. Maps were created by focusing the X-ray beam on a circular spot with a diameter of 25 µm and dragging the beam across the polished surface, collecting µXRF spectra every 50 µm in X and Y direction. This procedure yielded ~ 10^6 µXRF spectra per sample, which allowed semi-quantitative maps of elemental distribution to be created based on differences in the area of peaks in the µXRF spectrum associated with elements (ROI counts; see de Winter and Claeys, 2016). This mapping procedure allowed maps of a range of elements to be created, a selection of which is used in this study (magnesium, manganese, iron and strontium). µXRF mapping together with CL was used to check the preservation of the samples and to guide sampling for further analyses.

Quantitative point-by-point µXRF line scans were performed perpendicular to growth lamellae along the maximum growth axis of each shell fragment with a sampling resolution of 100 µm. Point-by-point line scans allow the X-ray beam to remain on each point for 60 s at maximized energy settings (50 kV, 600 µA, no source filter). This time of analysis represents the ideal compromise between lowering the signal-to-noise ratio (by increasing measurement time) and increasing the spatial sampling resolution (by increasing the amount of measurements). This causes the signal-to-noise ratio of individual spectra to be high enough to allow quantification of individual spectra to produce accurate and reproducible measurements of concentrations of a range of major and trace elements (see discussion in de Winter et al., 2017b). Therefore, XRF spectra in line scans yield quantitative major and trace element profiles, contrary to spectra of pixels in XRF maps, which can only be used to measure relative changes in element abundances. While concentrations of many elements could be quantified in line scans, only concentrations of strontium (Sr), manganese (Mn), magnesium (Mg) and iron (Fe) are used in this study.

For stable isotope analysis, shells were sampled perpendicular to visible growth lamellae on a sub-millimetre scale. The length of shell transects ranges from 27.6 to 59.5 mm. Carbonate powders (~ 150-200 µg) were extracted using a ESI New Wave micromill equipped with a Brassler® USA scriber point carbide drill bit (Ø 0.08 mm). The spacing between the samples was <0.1 mm. A total of 432 samples (A: n=105; B: n=80; C: n=39; D: n=208) were analysed in the stable isotope laboratory of the Institute for Geology, Leibniz University Hannover, Germany using a Thermo Fisher Scientific Gasbench II carbonate device connected to a Thermo Fisher Scientific Delta 5 Advantage isotope ratio mass spectrometer. One hour before the measurements were started, 72°C hot viscous water-free (98 g mol^{-1}) orthophosphoric acid was added to the sample powders, resulting in the release of CO_2. Repeated analyses of certified carbonate standards (NBS 19, IAEA 603, NBS 18 and Carrara Marble) show an external reproducibility of ≤ 0.06 ‰ for $\delta^{13}C$ and 0.08 ‰ for $\delta^{18}O$. Isotope ratios are reported as conventional delta values relative to the Vienna-Pee Dee Formation belemnite (VPDB) international standard, in parts per thousand (‰).

Sea surface temperatures (SST) were calculated using the equation of Anderson and Arthur (1983):

$$T\,[°C] = 16 - 4.14 * (\delta^{18}O_{CaCO_3} - \delta^{18}O_{H_2O(seawater)}) + 0.13 * (\delta^{18}O_{CaCO_3} - \delta^{18}O_{H_2O(seawater)})^2$$

with an estimated $\delta^{18}O_{H_2O(seawater)}$ of -1 ‰ for the Tethys ocean under ice-free conditions in the Barremian to Campanian (Friedrich et al., 2012; Anderson and Arthur, 1983; Shackelton and Kennett, 1975; Steuber, 1996; Steuber and Rauch, 2005).

5.4 Results

5.4.1 Shell micro- and macrostructures (sclerochronology *sensu stricto*)

On a macroscopic scale, all analysed shell fragments exhibit clearly distinguishable growth lamellae as well as colour variations (transparent to dark brown) (Fig. 5.4 to 5.7). An exception is the RV shell fragment C, whose sparite-filled, celluloprismatic structure produces a significantly lighter colour (Fig. 5.6; A). Due to their different shell structure, all shells were assigned to three categories: (I) non-compact (RV: shell A and B), (II) compact (LV: shell D and C) and (III) celluloprismatic (RV: shell C).

In general, whitish to transparent parts of analysed outer shell layers match the areas of the corresponding thin sections where growth lamellae are non-compact, which is expressed in shell A and B as blurry, incomplete, sinuous and/or not distinguished appearance (dashed lines in Fig. 5.4 to 5.7). In the non-compact parts, the width of the alternating dark and light growth lamellae is highly variable (their stacking is uneven). Darker coloured shell parts correspond to the areas of the shell with a compact fibrous microstructure. Here, cyclic alternations of distinct light and dark, densely packed growth lamellae with an even stacking, are visible (solid lines in Fig. 5.4 to 5.7). The RV of shell C shows the classical celluloprismatic structure described in Pons and Vicens (2008). All shell fragments contain borings and/or cracks that interrupt or destroy the growth lamellae.

The flame-like shaped growth rings (concentric rugae), i.e. arranged lamellae sets, are visible on a macroscopic scale (Fig. 5.2; Fig. 5.5 F). On a microscopic scale, they can be seen due to changes in the inclination of the growth lamellae (Fig. 5.4 G). A detailed analysis of thin sections revealed that a downwards concentric fold is visible in all RVs, surrounding the recrystallized inner part of the outer layer (il; see Fig. 5.4 F; 5.5 E; 5.6 E).

In total, shell fragment A comprises 144 growth lamellae. Only the outermost margin of the lip is formed by a compact fibrous microstructure (Fig. 5.4 G). Most parts of the shell are characterized by non-compact growth lamellae (Fig. 5.4 E).

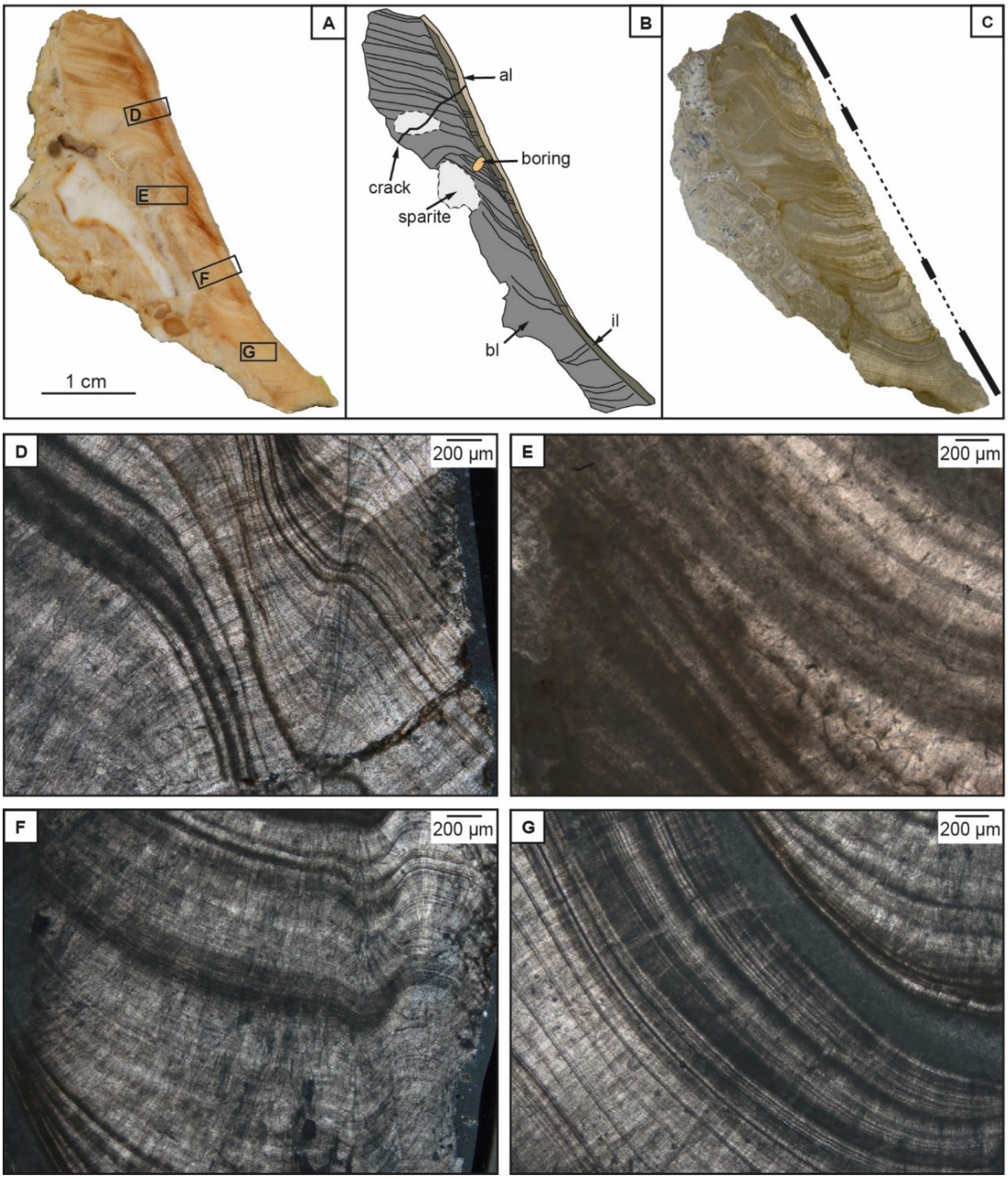

Fig. 5.4: Shell A: (A) Image of the slab with areas shown in detailed photomicrographs marked as black boxes. (B)Schematic sketch of the most important features of the shell. (C) Thin section (ppl) with non-compact (dashed line) and compact parts (solid line). (D) Steeply inclined growth lamellae. (E) Non-compact growth lamellae. (F) Detailed view (plane-polarized light) showing the transition from il (concentric fold) to bl (outer boxwork layer,). (G) The thickness and expression of single growth lamellae is highly variable.

Shell fragment B contains 54 growth lamellae characterized by variable development and stacking pattern (Fig. 5.5 G). The shell exhibits compact structured parts with very prominent, steeply inclined growth lamellae (Fig. 5.5 E) alternating with non-compact parts, containing a non-distinguishable structure. The outer part of the flame-like shape of the growth rings is often surrounded by a micritic seam. One prominent micrite filled boring trace occurs in the ontogenetically oldest part of the shell (Fig. 5.5 D).

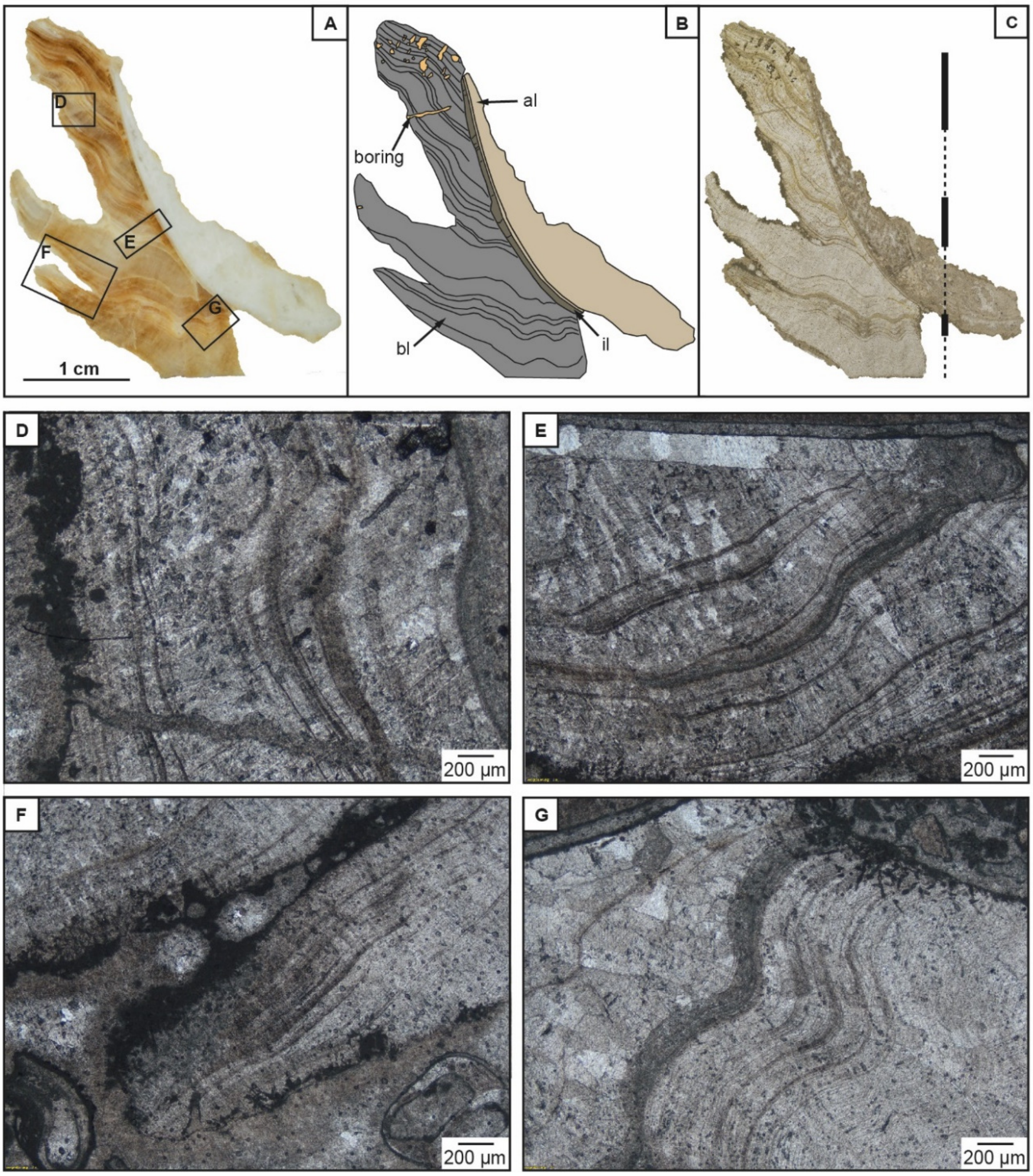

Fig. 5.5: Shell B: (A) Image of the slab with areas shown in detailed photomicrographs marked as black boxes. (B) Schematic sketch and the most important features of the shell. (C) Thin section (ppl) with non-compact (dashed line) and compact parts (solid line). (D) Boring filled with micritic calcite. (E) Steeply inclined growth lamellae. (F) Flame-like shape of growth rings on a macroscopic scale. (G) Variation of expression and the stacking of the growth lamellae.

Shell C comprises 130 growth lamellae (LV: n=22; RV: n=108). The right valve shows a predominant regular alternation of growth lamellae and voids, creating a roughly regular radial pattern, which is classified as 'compact with radial elongated voids', following Pons and Vicens (2008) (Fig. 5.6 G). All cells are filled with blocky calcite. The bl disintegrates at the outer margin of the lip into single cells. At the transition from the LV to the RV the radial furrow is preserved (Fig. 5.6 F). The LV features a small protrusion composed of the massive calcite layer (mc) and the former aragonitic layer (al), which matches the il and the calcite lamellae (cl) of the RV. Compact lamellae of the left valve are parallel near the il but incline softly towards the margin (Fig. 5.6 E).

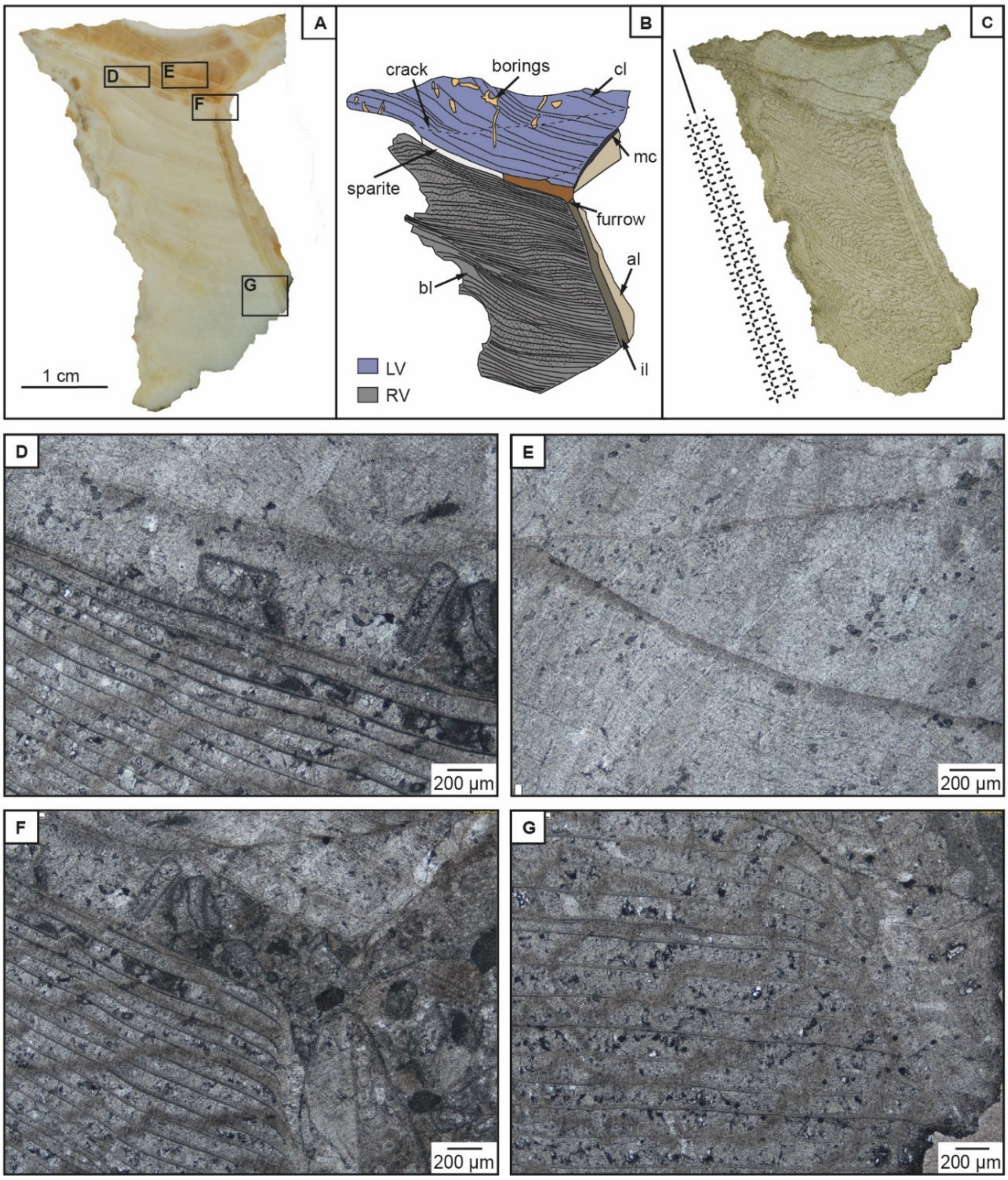

Fig. 5.6: Shell C: (A) Image of the slab with areas shown in detailed photomicrographs marked as black boxes. (B) Schematic sketch and the most important features of the shell. (C) Thin section (ppl) with celluloprismatic structured (cross-hatched double line) and compact parts (solid line). (D) transition of LV(compact) and RV (celluloprismatic structure). (E) compact

structure of the LV. (F) Transition from the RV to the LV with furrow. (G) Detailed view of the celluloprismatic structure of the bl.

In total, 238 equally distributed growth lamellae were counted in shell D (Fig 5.7 G). Occasionally, particularly pronounced growth lamellae appear (Fig. 5.7 H), which differ from the others due to their very dark colour and higher diameter. Most parts of the shell show a fibrous prismatic structure. Special features of the shell represent borings that are refilled with fine grained micritic calcite (Fig. 5.7 E). At some parts the shell margin is micritized.

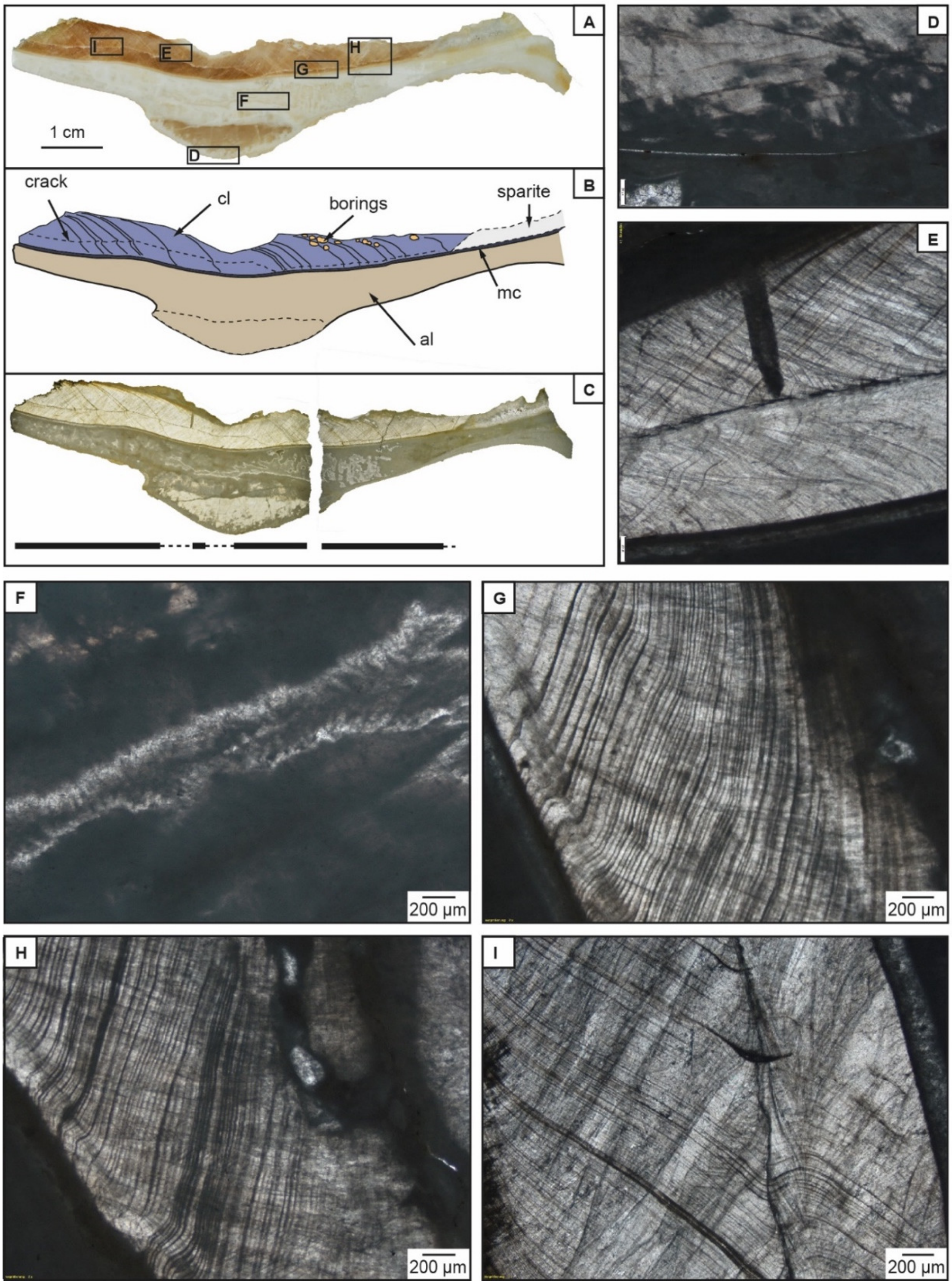

Fig. 5.7: Shell D: (A) Image of the slab with areas shown in detailed photomicrographs marked as black boxes. (B) Schematic

sketch and the most important features of the shell. (C) Thin section (plane-polarized light) with blurry (dashed line) and compact parts (solid line). (D) Lowermost part of the ligament. (E) Boring. (F) Middle part of the ligament. (G) Continuous stacking. (H) Particularly pronounced growth lamellae. (I) Changed inclination of the growth lamellae caused by a crack.

All sclerochronological and sclerochemical results are summarized in Tab. 5.1.

Tab. 5.1: Identified $\delta^{18}O$ cycles, number of growth lamellae per cycle, distance describes the measured length of the cycles, calculated growth per year (mm) and mean growth lamellae diameter per cycle. Measured maximum and minimum values of $\delta^{13}C$ and $\delta^{18}O$ values and their calculated median. T(°C) was calculated for all $\delta^{18}O$ values.

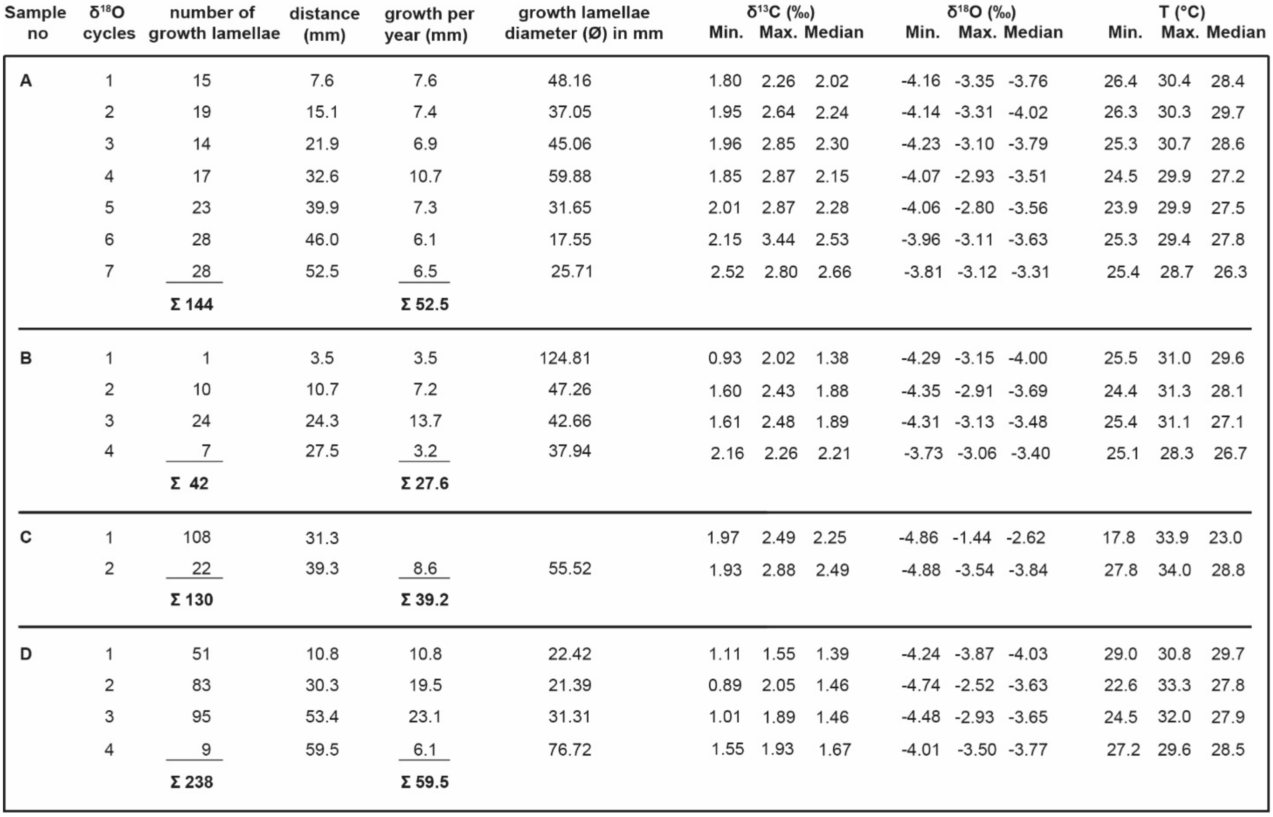

Sample no	$\delta^{18}O$ cycles	number of growth lamellae	distance (mm)	growth per year (mm)	growth lamellae diameter (Ø) in mm	$\delta^{13}C$ (‰) Min.	Max.	Median	$\delta^{18}O$ (‰) Min.	Max.	Median	T (°C) Min.	Max.	Median
A	1	15	7.6	7.6	48.16	1.80	2.26	2.02	-4.16	-3.35	-3.76	26.4	30.4	28.4
	2	19	15.1	7.4	37.05	1.95	2.64	2.24	-4.14	-3.31	-4.02	26.3	30.3	29.7
	3	14	21.9	6.9	45.06	1.96	2.85	2.30	-4.23	-3.10	-3.79	25.3	30.7	28.6
	4	17	32.6	10.7	59.88	1.85	2.87	2.15	-4.07	-2.93	-3.51	24.5	29.9	27.2
	5	23	39.9	7.3	31.65	2.01	2.87	2.28	-4.06	-2.80	-3.56	23.9	29.9	27.5
	6	28	46.0	6.1	17.55	2.15	3.44	2.53	-3.96	-3.11	-3.63	25.3	29.4	27.8
	7	28	52.5	6.5	25.71	2.52	2.80	2.66	-3.81	-3.12	-3.31	25.4	28.7	26.3
		Σ 144		**Σ 52.5**										
B	1	1	3.5	3.5	124.81	0.93	2.02	1.38	-4.29	-3.15	-4.00	25.5	31.0	29.6
	2	10	10.7	7.2	47.26	1.60	2.43	1.88	-4.35	-2.91	-3.69	24.4	31.3	28.1
	3	24	24.3	13.7	42.66	1.61	2.48	1.89	-4.31	-3.13	-3.48	25.4	31.1	27.1
	4	7	27.5	3.2	37.94	2.16	2.26	2.21	-3.73	-3.06	-3.40	25.1	28.3	26.7
		Σ 42		**Σ 27.6**										
C	1	108	31.3			1.97	2.49	2.25	-4.86	-1.44	-2.62	17.8	33.9	23.0
	2	22	39.3	8.6	55.52	1.93	2.88	2.49	-4.88	-3.54	-3.84	27.8	34.0	28.8
		Σ 130		**Σ 39.2**										
D	1	51	10.8	10.8	22.42	1.11	1.55	1.39	-4.24	-3.87	-4.03	29.0	30.8	29.7
	2	83	30.3	19.5	21.39	0.89	2.05	1.46	-4.74	-2.52	-3.63	22.6	33.3	27.8
	3	95	53.4	23.1	31.31	1.01	1.89	1.46	-4.48	-2.93	-3.65	24.5	32.0	27.9
	4	9	59.5	6.1	76.72	1.55	1.93	1.67	-4.01	-3.50	-3.77	27.2	29.6	28.5
		Σ 238		**Σ 59.5**										

5.4.2 Elemental and isotope compositions

CL was applied to compact, non-compact and celluloprismatic shell structures (Fig. 5.8 A – F). Compact shell portions show a dim, orange luminescence between single growth lamellae. Growth lamellae themselves are non-luminescent. Within single cells of non-compact structures (celluloprismatic), dark brown to light orange CL colours provide evidence for various cement generations (Fig. 5.8 E and F). µXRF element mapping provides valuable information with respect to the preservation state of considered shells. Inclusions with higher concentrations of Fe and Mn indicate recrystallized or bioeroded parts (borings) of the shells. The light blue to green coloured parts of the shells are associated with higher Sr concentrations than the surrounding matrix (Fig. 5.8 G – J).

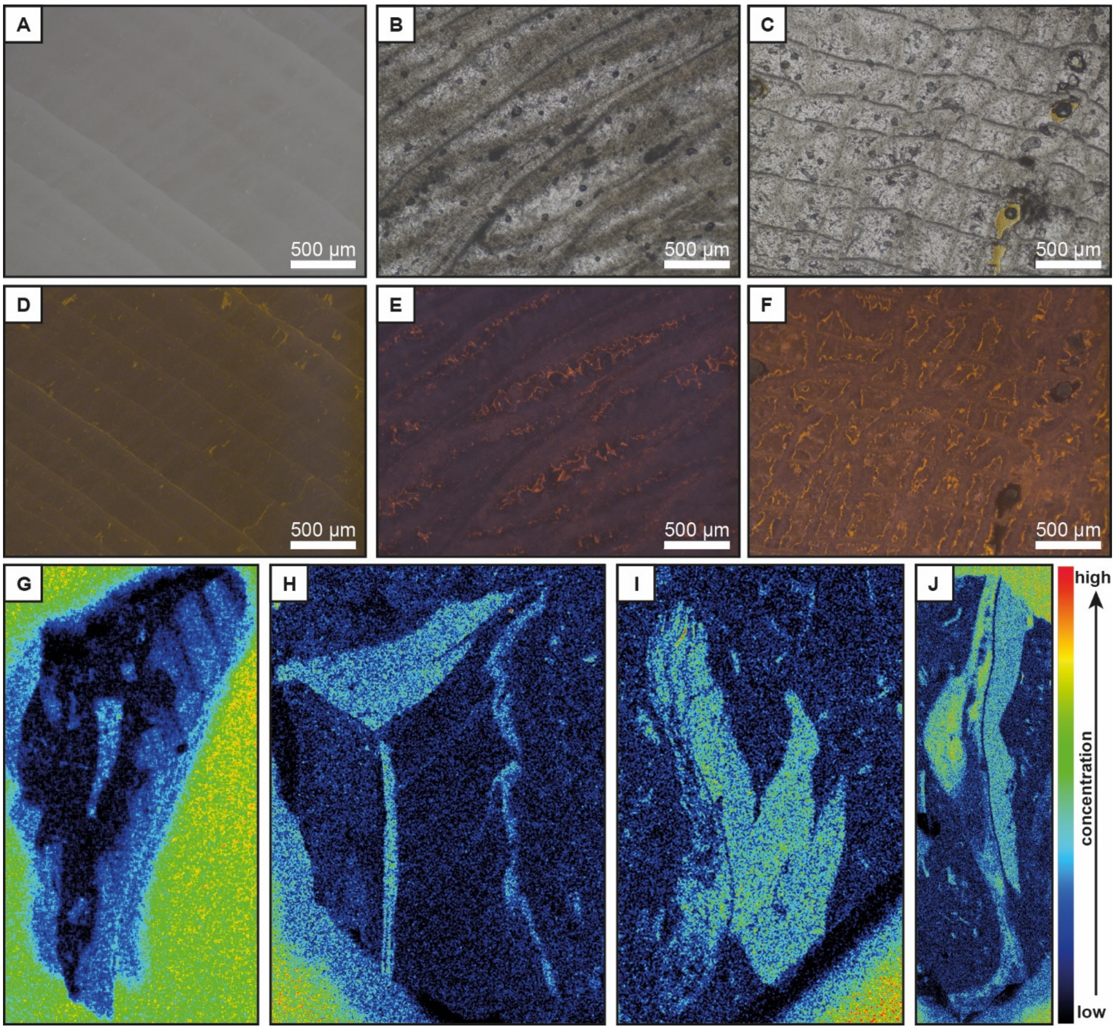

Fig. 5.8: (A) Slab of a compact shell part. (B) and (C) Thin sections of non-compact parts under ppl. (D) and (E) Compact parts are quenching CL (caused by Fe^{2+}), while fine fractures and the non-compact parts are enriched in Mn^{2+}, which enhances CL. (G) to (J) strontium variations in the µXRF maps. Especially in shells B (H), C (I) and D (J) the variability in Sr between shell structures is clearly visible. At shell C (H) and D (J) the cap (LV) is displayed. In the scans of A (G) and B (H), on the other hand, single micro and macro structures cannot be distinguished.

Due to the high-resolution and the extensive dataset on a µm scale of the µXRF line scans, the data were filtered to eliminate analytical outliers. Their occurrence was linked to irregularities, such as boreholes or cracks in the shell. In addition, thresholds were defined following Steuber (1999) and cross-plots were used to delimit clustering data points from outliers (Fig. 5.9). All Sr values below 900 µg/g and above 1500 µg/g, all Mn values > 200 µg/g and all Fe values > 300 µg/g were excluded from further analysis. Finally, 10pt-averages were calculated. Raw data and selected values are summerized in Tab. 5.2.

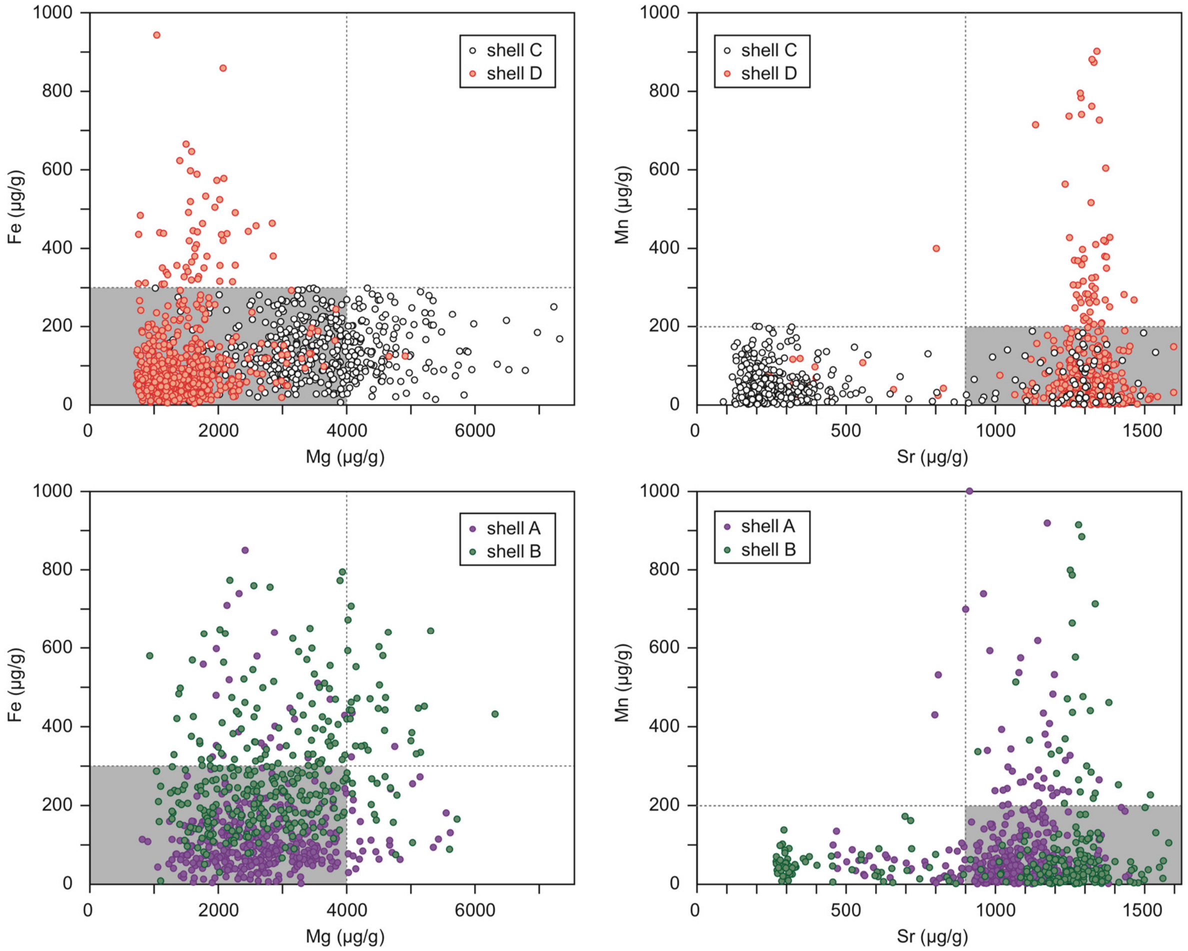

Fig. 5.9: Fe vs Mg and Mn vs. Sr of the here analysed shells. Due to their clustering thresholds were assumed: Sr 900-1500 µg/g, Fe: < 300 µg/g, Mn < 200 µg/g for further analysis. For Mg, no threshold was applied as the data points scatter widely.

Tab. 5.2: Elemental compositions (µg/g) of selected low-Mg carbonate rudist shells of the Monte La Costa section before (a) and after (b) the thresholds were applied. Data provided in (b) are the basis for further analysis.

	Sample no	Sr (ug/g)			Fe (ug/g)			Mn (ug/g)			Mg (ug/g)		
		Min.	Max.	Mean	Min.	Max.	Mean	Min.	Max.	Mean	Min.	Max.	Mean
a	A	456	1448	1058	2	848	130	0	531	81	826	5628	2697
	B	266	1582	1085	8	1307	288	0	914	89	942	6327	2907
	C	88	1537	462	6	299	145	0	200	52	976	8501	3674
	D	241	1902	1283	1	942	126	0	1329	101	737	4921	1548
b	A	933	1350	1102	37	191	92	0	156	48	1669	4923	2587
	B	924	1435	1239	132	267	199	0	111	45	1004	3520	2260
	C	161	1425	487	75	247	145	0	110	47	1661	4835	3018
	D	1118	1495	1313	25	274	92	0	186	49	1074	2300	1459

Oxygen isotope values of shell A (Fig. 5.10) vary between -2.8 ‰ and -4.23 ‰ (mean: -3.66 ‰; s.d.: 0.33 ‰), whereas carbon isotope values range from 1.80 ‰ to 3.44 ‰ (mean: 2.32 ‰; s.d.: 0.31 ‰). In total, five $\delta^{18}O$ cycles with amplitudes of < 1 ‰ were identified, showing either a periodic triangular or a saw tooth shape (Fig. 5.10). Most $\delta^{13}C$ values oscillate around a value of 1.20 ‰. Superimposed rapid changes in $\delta^{13}C$ towards more positive values weakly correlate with corresponding positive shifts in $\delta^{18}O$ (Fig.5.6: 1.8-3.8 cm: $r^2=0.2$). µXRF line scanning provides evidence for periodic changes in Mg concentrations (period: 0.3-0.6 cm), ranging from 1669 to 3500 µg/g. An exception from this pattern is a prominent positive spike reaching Mg concentrations of 4923 µg/g (Fig. 5: 2.1 cm). Sr concentrations fluctuate between 933 µg/g and 1102 µg/g. Significantly higher amounts of Sr (< 1350 µg/g) are recorded in the lower third of the shell (Fig. 5.10: 1.3 to 1.8 cm). Fe concentrations are highly variable (37 µg/g to 191 µg/g), with values oscillating around a mean value of about 92 µg/g. Mn concentrations range from 0 µg/g to 156 µg/g, exhibiting a superimposed cyclic pattern with higher frequency in the upper part of the shell (Fig.5.6: 3-4.2 cm).

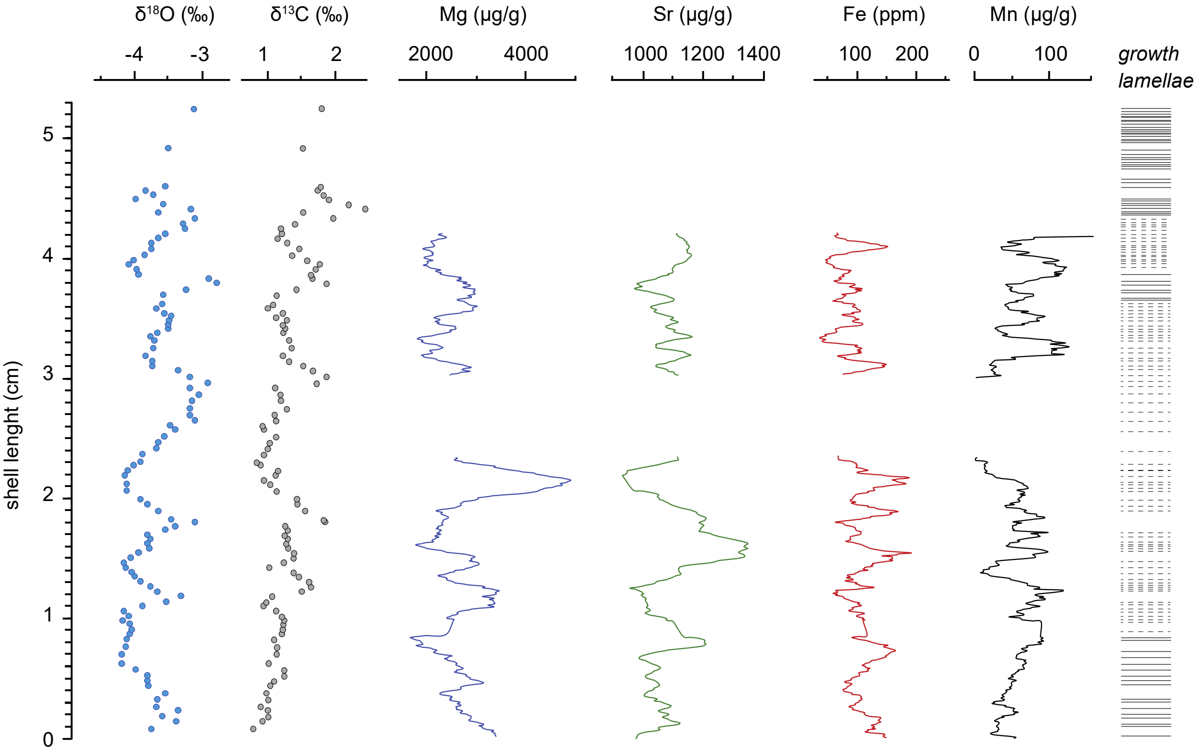

Fig. 5.10: Oxygen and carbon isotopic composition with Sr, Fe, Mn and Mg variations plotted against the identified and counted growth lamellae of shell A. Dashed lines show the non-compact shell structure parts, solid lines show compact parts.

Oxygen isotope values of shell B (Fig. 5.11) vary between -2.91 ‰ and -4.35 ‰ (mean: -3.59 ‰; s.d.: 0.36 ‰), whereas carbon isotope values range from 0.93 ‰ to 2.48 ‰ (mean: 1.82 ‰; s.d.: 0.30 ‰). Identified $\delta^{18}O$ cycles (n=2) exhibit a triangular to sinusoidal shape with a mean amplitude of 1.3 ‰ and a wavelength of 0.7 cm and 1.4 cm, respectively (Fig. 5.11). Gradually decreasing values characterizing the second cycle are likely explained by a slightly oblique cut through growth lamellae. Carbon isotopes lack a similar cyclic pattern and fluctuate around a background value of about 1.6 ‰. In the lower part of the shell (Fig.5.11: 0.3-1.2 cm), however, rapid negative and positive shifts in $\delta^{13}C$ correlate well with corresponding shifts in $\delta^{18}O$ ($r^2=0.4$). Mg concentrations are characterized by periodic fluctuations (wavelength: 0.2-0.5 cm; amplitude: 1000 µg/g to 2000 µg/g) that are superimposed on a cyclic sinusoidal pattern with a range from 1004 to 3520 µg/g. Sr concentrations range from 924 µg/g to 1435 µg/g (median: 1239 µg/g) and provide evidence for a cyclic pattern. Fe concentrations exhibit a short term cyclicity (132 µg/g to 267 µg/g), with values oscillating around a median value of 199 µg/g. Mn concentrations show a cyclicity (5 µg/g to 111 µg/g), with values oscillating around 45 µg/g.

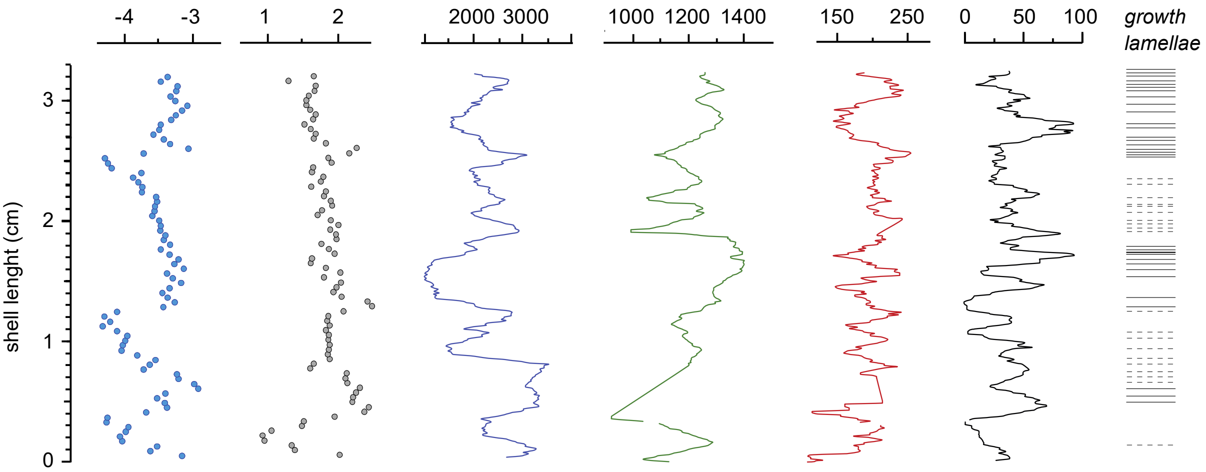

Fig. 5.11: Oxygen and carbon isotopic composition with Sr, Fe, Mn and Mg variations plotted against the identified and counted growth lamellae of shell B. Dashed lines show the non-compact shell structure parts, solid lines show compact parts.

Oxygen isotope values of shell C (Fig. 5.12) vary between -1.44 ‰ and -4.88 ‰ (mean: -3.51 ‰; s.d.: 0.81 ‰), whereas carbon isotope values range from 1.93 ‰ to 2.88 ‰ (mean: 2.41 ‰; s.d.: 0.23 ‰). In total, the values derived from the RV are highly variable, while the values of the LV show one broadly symmetrical sinusoidal $\delta^{18}O$ cycle with an amplitude of <1.3 ‰ (Fig. 5.12). The $\delta^{13}C$ values of the RV oscillate within a range between 1.9 to 2.4 ‰. A pattern is not notable. The $\delta^{13}C$ values of the LV oscillate within a range between 2.2 to 2.7 ‰. µXRF line scanning of the RV shows a highly variable record with oscillations of ~ 500 µg/g, while the LV provides evidence for periodic changes in Mg concentrations (wavelength: 0.2-0.4 cm), the latter ranging from 1661 to 4588 µg/g. The Sr concentrations of the RV fluctuate between 161 µg/g and 264 µg/g. The LV contains significantly higher amounts of Sr (range: 919-1428 µg/g) with cyclic oscillations (0.4 cm wavelength) (Fig. 5.12). Fe concentrations provide evidence for a small scale cyclicity (75 µg/g to 247 µg/g), with values oscillating around a mean value of about 145 µg/g. Significant differences between the valves cannot be observed. Mn concentrations range from 0 µg/g to 110 µg/g, exhibiting a superimposed cyclic pattern with wavelengths oscillating around 0.3 cm (Fig.5.12).

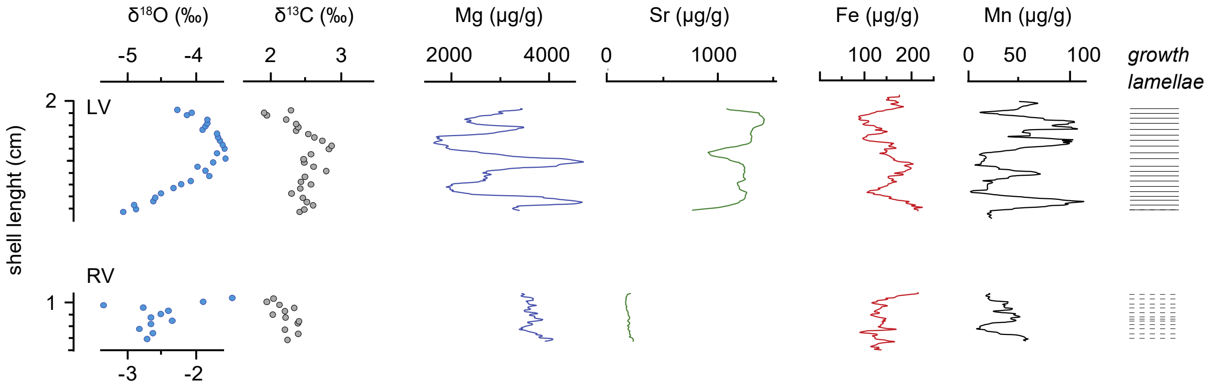

Fig. 5.12: Oxygen and carbon isotopic composition with Sr, Fe, Mn and Mg variations plotted against the identified and counted growth lamellae of shell C. Dashed lines show the non-compact shell structure parts, solid lines show compact parts.

Oxygen isotope values of shell D (Fig. 5.13) vary between -2.52 ‰ and -4.74 ‰ (mean: -3.74 ‰; s.d.: 0.47 ‰). Carbon isotope values range from 0.89 ‰ to 2.05 ‰ (mean: 1.48 ‰; s.d.: 0.20 ‰). In total, two prominent δ^{18}O cycles with amplitudes of <1.7 ‰ were identified, showing a broadly symmetrical sinusoidal pattern (Fig. 5.13). Most δ^{13}C values oscillate around 1.5 ‰. Superimposed rapid changes in δ^{13}C towards more positive values correlate strongly with corresponding positive shifts in δ^{18}O (Fig.5.9: 1.1-1.4 cm: R^2=0. 6 and 2.8-3.1 cm: R^2=0.8). Mg concentrations are highly variable (1074 to 2300 µg/g). Sr concentrations are positively correlated with δ^{18}O values, expressed by two symmetrical sinusoidal cycles. Concentrations range from 1118 µg/g to 1495 µg/g. Fe concentrations show small scale cyclic changes, with values varying from around 25 µg/g to 274 µg/g (mean: 92 µg/g). Mn concentrations show a highly fluctuating record with a range from 0 µg/g to 186 µg/g.

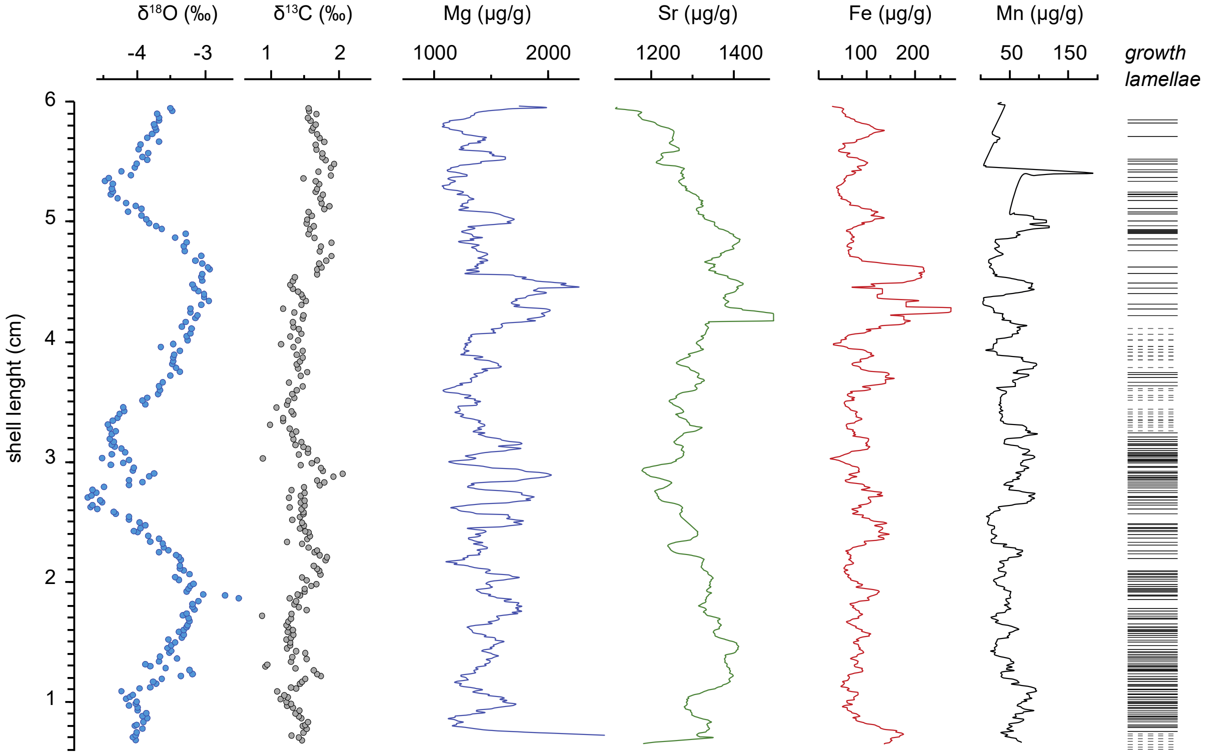

Fig. 5.13: Oxygen and carbon isotopic composition with Sr, Fe, Mn and Mg variations plotted against the identified and counted

growth lamellae of shell D. Dashed lines show the non-compact shell structure parts, solid lines show compact parts.

5.5 Discussion

5.5.1 Preservation state

To analyse the preservation state of the shells, the elemental and isotopic datasets were studied individually for diagenetic alteration. In elemental data, diagenesis is characterised by an increase in Mn and Fe concentrations and a decrease in the Mg and Sr concentrations (Steuber, 1999). Additionally, the correlation factor (R^2) of isotopic values was calculated to indicate diagenetic alteration (Steuber, 1999).

5.5.1.1 Elemental dataset

A cross-plot of Sr and Mg concentrations reveals that the majority of data points from shell A and D as well as samples extracted from the LV of shell C and B cluster around or close to the regression line of recent biotic calcite (blue ellipse, Fig. 5.14). Similar results were previously obtained from well-preserved *Gorjanovicia* cf. *costata* (Steuber, 1999) and *Praeradiolites ciryi* shells (Regidor-Higuera et al., 2007). As expected, the celluloprismatic RV of shell C provides Sr and Mg concentrations that plot along the abiotic calcite line (grey ellipse, Fig. 5.14). Comparable diagenetic values were reported by Tibljas et al. (2004) for various radiolitid shells. Fe and Mn concentrations are within the range of those described in Steuber (1999) and Regidor-Higuera et al. (2007). Compared to the Mn concentrations of Tibljaš et al. (2004), the measured values are significantly higher.

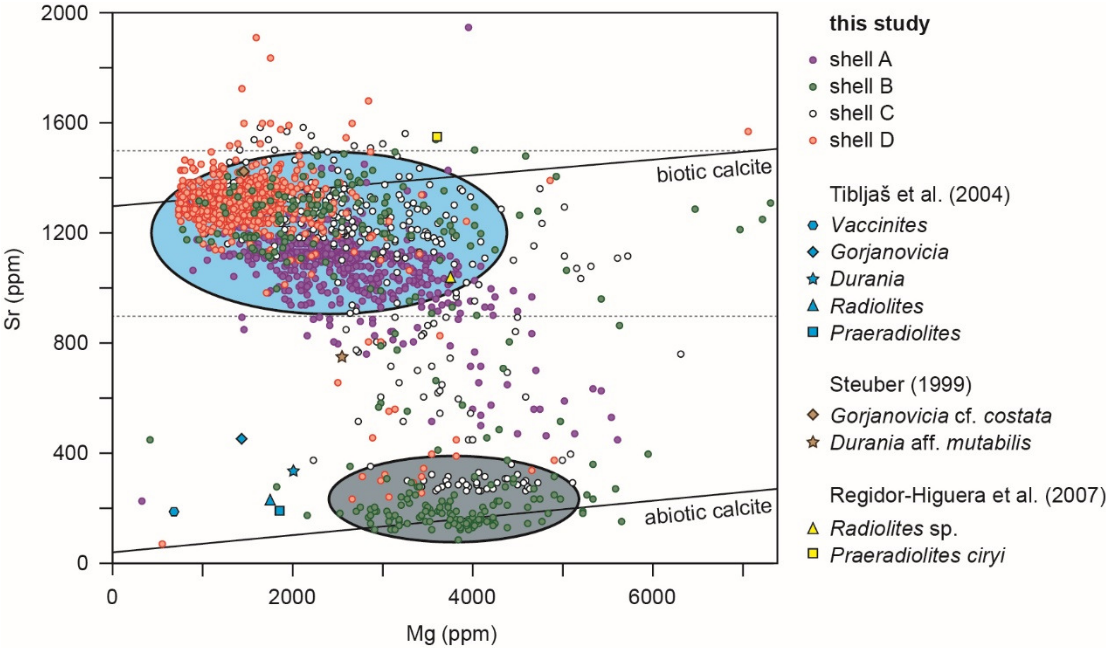

Fig. 5.14: Mg and Sr compositions of rudist shell A (purple), B (green), C (white) and D (red) compared with mean compositions of recent biotic (upper solid line) and abiotic (lower solid line) marine calcite (Carpenter and Lohmann 1992;

Steuber 1999). Dashed lines show Sr thresholds after Steuber (1999). Also shown: radiolitids from Croatia (Tibljaš et al., 2004), Greece, United Arab Emirates (Steuber, 1999) and Spain (Regidor-Higuera et al., 2007).

The variable microstructure characterizing the outer low-Mg calcite shell layer of radiolitid rudists is expected to cause locally different elemental concentrations. The shells with a non-compact structure (Fig. F. 5.10 and Fig. 5.11) show a negative covariation between Sr and Mg. Both elements are linked to variations in metabolic activity (Rosenberg and Hughes, 1991, Klein et al., 1996) and kinetic fractionation (Carpenter and Lohmann, 1992). For this reason, it seems plausible to assume that these variations were caused by the aforementioned and not by diagenetic alteration. The compact structure of shells D (Fig. 5.13) shows a covariance of the Sr concentrations with $\delta^{18}O$. To explain this covariance is beyond the scope of this work. The celluloprismatic structure of the RV of shell C is considered to provide diagenetically altered results, which can be detected in low Mg and Sr but high Mn and Fe concentrations (Al-Aasm and Veizer, 1986; Steuber, 1999; Tibljaš et al., 2004). It is assumed that this is caused by the filling of the former hollow cells with secondary cement (Regidor-Higuera et al., 2007). However, diagenetic alteration can only be partially confirmed using this elemental dataset. On the one hand, very low Sr concentrations (< 200 µg/g) attest to diagenetic alteration, but on the other hand, the highest measured Mg values of this complete study (3500-4000 µg/g) are not easily explained by diagenesis as diagenetic altered calcite should contain less Mg (Al-Aasm and Veizer, 1986; Steuber, 1999; Tibljaš et al., 2004). Additionally, the Fe and Mn concentrations are in the range of the other here analysed shells (Fig. 5.12).

5.5.1.2 Isotopic dataset

The variation in the $\delta^{18}O$ pattern seems to be related to microstructural changes in the shell: Non-compact parts, described in shell A (Fig. 5.10) and B (Fig. 5.11), RVs, generate sharp shifts to positive values in the $\delta^{18}O$ records. These sharp shifts might be the result of growth cessations caused by e.g. periods of reproduction, competition for space or critical water temperatures or salinities exceeding ecological tolerance levels (Steuber, 1996; Regidor-Higuera et al., 2007). However, the non-compact shell structure, found in shell A and B, does not automatically indicate diagenetic altered values, as no/low correlations and similar range of the $\delta^{18}O$ values demonstrate unambiguously. A compact structure provides oxygen isotope values within an almost stable/constant range with a gradually, smooth sine function pattern, as visible in the shell D (Fig. 5.13) and C (Fig. 5.12), both LVs. This pattern of the LVs, indicates the record of seasonal changes, without any significant growth cessations. The celluloprismatic structure of the RV of shell C contains a highly variable $\delta^{18}O$ pattern, lacking a cyclic variation. Seasonality cylces are not identifiable due to the celluloprismatic structure filled with sparite.

Although individual sclerochronological patterns are variable, all shells provide an almost identical range of $\delta^{18}O$ values (Tab. 5.1: median range -3.31 ‰ to -4.03 ‰). Observed cyclic variations of $\delta^{18}O$ and $\delta^{13}C$ in shell A contain a covariance, which is slightly out of phase. This is not necessarily a sign for diagenetic alteration, especially as the applied cross-plots show no (A, D), very low (B) and low correlations (C) (Fig. 5.15). These $\delta^{13}C$ variations are supposedly due to recorded seasonal variations in marine productivity and its effect on marine dissolved bicarbonate (Arthur et al., 1983; Steuber, 1996).

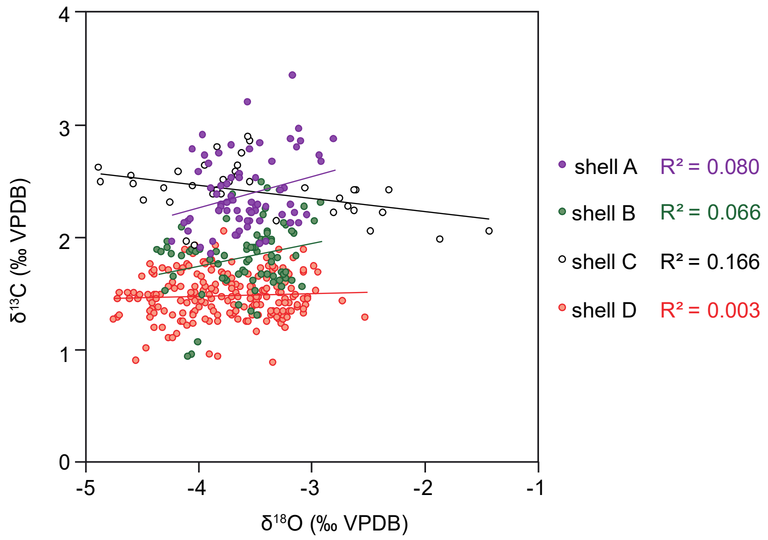

Fig. 5.15: Cross-plot of $\delta^{18}O$ and $\delta^{13}C$ of the studied shells and their correlation factor (R^2).

5.5.2 Growth variations

Annual cycles can be determined through growth rings on a macroscopic scale (shell B), through a change in shell structure on a microscopic scale (shell A) or through variations in the isotopic pattern (shell D). The relatively fragile, flame-like structure of the growth rings is often absent due to the reworking of shell fragments in high-energy marginal settings. The microscopic attempt to identify annual growth cycles is difficult due to the lack of structural changes in the growth lamellae. Therefore, isotopic values, to be more precise the values between two $\delta^{18}O$ minima, are used to identify the annual growth. In shell A, five isotopic cycles with 14 to 28 growth lamellae per year were found and a growth rate of 6.1 to 10.7 mm/a was calculated. Shell B contains 2 complete isotopic cycles with a lower quantity of growth lamellae per year (10 to 24) but an increased growth rate (7.2 to 13.7 mm/a). The annual growth rate of shell C, depicted by $\delta^{18}O$ in the LV, is 8.6 mm/a and represented by 22 growth lamellae. Oxygen isotope cycles (n=2) and corresponding growth lamellae (83 and 95) identified in shell D provide evidence for a much larger annual growth rate, the latter ranging between 19.5 and 23.1 mm/a. The number of growth lamellae per year of shell A (14-28) and B (10 and 24) is comparable to the dataset of Regidor-Higuera et al. (2007), who counted 16 to 22 growth lamellae per year for a *Radiolites* sp. and 11 to 27 growth lamellae per year for a *P. ciryi*. The longitudinal growth rate varies between 3-4 mm/a (Steuber, 1996) and 3.5-15 mm/a (Regidor-Higuera et al., 2007), which is within the range of shell A and B (6.1 to 13.7 mm/a). Shell D, in contrast, differs significantly with a growth rate of up to

26.4 mm/a, which is caused by the dominance of radial growth over the vertical one (Fig. 5.16). The slower growth rates in the RVs are caused by the vertical growth, which is favoured before the radial (Fig. 5.16) in order to adapt to an unstable environment in a high-energy setting (Steuber, 1996; Pons and Vicens, 2008).

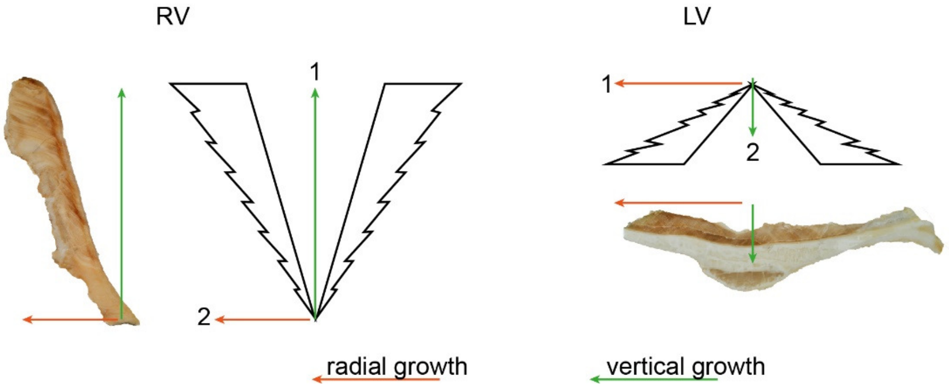

Fig. 5.16: Schematic radial (red) and vertical growth (green) of radiolitids (modified after Pons and Vicens, 2008). In the RV vertical (1) dominates radial (2) growth, while in the LV the radial (1) dominates the vertical (2) growth.

5.5.3 Palaeoenvironmental implications

In order to reconstruct the prevailing environmental conditions of the shells' living habitat, both petrographic and chemical results were combined. First, the distribution of growth lamellae was used to reconstruct the living position of the shells with regard to the overall marine habitat. In general, growth lamellae are divided into growth lines (dark) and growth increments (light). During emersion phases (low tides), when the shell is closed and the pH value decreases, dark lamellae are produced. During an immersion (high tides), the shell opens and the pH value of the extrapallial fluid increases to values similar to the surrounding water (~ 7.8) and light lamellae are produced (Regidor-Higuera et al., 2007). The durations of the immersion or the emersion phases are responsible for the width of the single lamellae. As the alternation of growth lamellae is often regular, a continuous immersion is assumed with recurring emersion phases in the intertidal domain. An intertidal habitat of rudist shells analysed in this study is in line with the high-energy setting (well-sorted and rounded shell debris) prevailing at the margin of the MLC section. Assuming an intertidal habitat, variations in salinity affect shell isotope records less than a restricted habitat would do. A minor influence of salinity changes on MLC shells was confirmed by the limited variability in $\delta^{13}C$ values (amplitude: 1-1.5 ‰), which indicates a maximum change of 2-3 p.s.u. in the surrounding water (Steuber et al., 2005). Furthermore, water temperature variations of the shells' surrounding water were calculated using cyclic variations in the $\delta^{18}O$ record (Steuber, 1999). For shell A, B and D similar ranges of seasonal temperature changes were calculated with a T_{max} range between 28.66 °C and 33.92 °C and a T_{min} range between 22.5 °C and 28.95 °C (Fig. 5.17; Tab. 5.2). Steuber et al. (2005) state that mean temperatures, derived from skeletal carbonates, are not higher than 32°C and that most of the values oscillate in a 20 to 25 °C range for the early Cretaceous. Especially at the Aptian-Albian transition (106 to 111 Myr), the calculated temperatures from shells found in Spain range between 24 and 25°C. The calculated mean values (~ 28°C) of the here analysed shells are slightly higher but the uncertainty about the $\delta^{18}O$ value of the ancient sea due to latitudinal difference and salinity content might cause this deviation (Steuber et al., 2005).

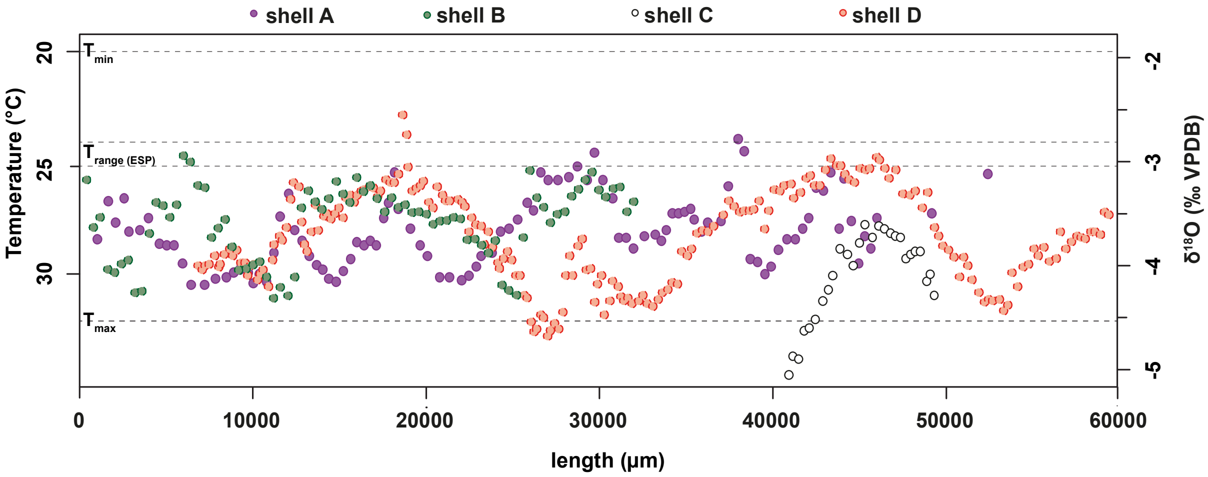

Fig. 5.17: The $\delta^{18}O$ values and correlated temperature of the surrounding water of shells A (purple), B (green), LV of C (white), D (red) are plotted against the length (µm). T_{min} and T_{max} values from Steuber et al. (2005) are shown as dashed lines. $T_{range\ (ESP)}$ depict the values derived from the successions of Spain (Aptian-Albian transition).

5.6 Conclusions

In this study, a first approach was made to combine sclerochronological and chemical results to determine if radiolitids are a valuable archive for palaeoenvironmental reconstruction. In previous studies, radiolitids were rarely used for climate reconstruction due to their porous outer shell structure, as the embedded diagenetic calcite filling the pores might compromise data collection. The following conclusions were formulated based on the data collected within the scope of this study:

(I) Neither the isotopic nor the elemental datasets indicate a diagenetic alteration of shell A, B, the LV of C and D. Only the RV of shell C, which contains a cement-filled celluloprismatic structure, shows highly variable isotopic and elemental datasets and is therefore classified as diagenetically altered.

(II) The highly compact LV of shell C and D records a gradually, smooth sine function as $\delta^{18}O$ pattern and is therefore a promising archive for palaeotemperature reconstruction.

(III) The RV of shell A and B, which contains an alternation of compact and non-compact parts, shows often sharply accented shifts to positive values in the $\delta^{18}O$ record. Nevertheless, cyclic variations are visible. The temperatures derived from the RVs are within range of temperatures derived from the LVs and are in turn comparable to the temperatures calculated by Steuber et al. (2005). Therefore, the here analysed radiolitid shells are suitable for palaeoenvironemantal reconstructions.

(IV) Due to regular alternation of the growth lamellae, the intertidal is assumed as former living habitat of the shells. Additionally, large fluctuations in salinity of the surrounding water were excluded due to small oscillations in the $\delta^{13}C$ values.

Summing up, the sampling of radiolitid shells shows that it is possible to use them as a palaeoenvironmental archive. Especially the LV is suitable for the resonctruction of palaeotemperatures. The RV can be used as an archive too with the requirement that the celluloprismatic structure is not pronounced. This implies that shells having a structure similar to the RV of C are not suitable material. However, if the shells show a structure like shells A and B, i.e. a variation of compact and non-compact parts, they may be a suitable archive. Before they can be used as such, the common methods need to be applied to exclude diagenetic alteration (cross-plot of isotopic values and elementel data). Celluloprismatic structures as shown in the RV of shell C cannot be used as palaeotemperature archives, but they provide important information about the living habitat of animals.

5.7 References

Al-Aasm, I.S., Veizer, J., 1986a. Diagenetic stabilization of aragonite and low-Mg calcite; I, Trace elements in rudists. Journal of Sedimentary Research 56, 138-152.

Al-Aasm, I.S., Veizer, J., 1986b. Diagenetic stabilization of aragonite and low-Mg calcite; II, Stable isotopes in rudists. Journal of Sedimentary Research 56, 763-770.

Anderson, T.F., Arthur, M.A., 1983. Stable isotopes of oxygen and carbon and their application to sedimentologic and paleoenvironmental problems. Unknown Journal.

Arthur, M.A., Williams, D.F., Jones, D.S., 1983. Seasonal temperature-salinity changes and thermocline development in the mid-Atlantic Bight as recorded by the isotopic composition of bivalves. Geology 11, 655–659.

Bodin, S., Meissner, P., Janssen, N.M., Steuber, T., Mutterlose, J., 2015. Large igneous provinces and organic carbon burial: Controls on global temperature and continental weathering during the Early Cretaceous. Global and Planetary Change 133, 238-253.

Bornemann, A., Norris, R.D., Friedrich, O., Beckmann, B., Schouten, S., Sinninghe Damsté, J.S., Vogel, J., Hofmann, P., Wagner, T., 2008. Isotopic evidence for glaciation during the Cretaceous supergreenhouse. Science 319, 189-192.

Bottini, C., Erba, E., Tiraboschi, D., Jenkyns, H.C., Schouten, S., Sinninghe Damsté, J.S., 2015. Climate variability and ocean fertility during the Aptian Stage. Climate of the Past 11, 383-402.

Carpenter, S.J., Lohmann, K.C., 1992. Sr/Mg ratios of modern marine calcite: Empirical indicators of ocean chemistry and precipitation rate. Geochimica et Cosmochimica Acta 56, 1837-1849.

Cestari, R., 1992. Biometrical analysis on Gorjanovicias and on other radiolitids (Radiolitidae, Hippuritoida). Geologica Romana 28, 1-25.

de Winter, N.J., Claeys, P., 2016. Micro X-ray fluorescence (µXRF) line scanning on Cretaceous rudist bivalves: A new method for reproducible trace element profiles in bivalve calcite. Sedimentology 64, 231-251.

de Winter, N.J., Goderis, S., Dehairs, F., Jagt, J.W.M., Fraaije, R.H.B., Van Malderen, S.J.M., Vanhaecke, F., Claeys, P., 2017a. Tropical seasonality in the late Campanian (late Cretaceous): Comparison between multiproxy records from three bivalve taxa from Oman. Palaeogeography, Palaeoclimatology, Palaeoecology 485, 740-760.

de Winter, N.J., Sinnesael, M., Makarona, C., Vansteenberge, S., Claeys, P., 2017b. Trace element analyses of carbonates using portable and micro-X-ray fluorescence: performance and optimization of measurement parameters and strategies. Journal of Analytical Atomic Spectrometry 32, 1211–1223.

Eggins, S., De Deckker, P., Marshall, J., 2003. Mg/Ca variation in planktonic foraminifera tests: implications for reconstructing palaeo-seawater temperature and habitat migration. Earth and Planetary Science Letters 212, 291-306.

Fenerci-Masse, M., Masse, J. P., Arias, C., Vilas, L., 2006. Archaeoradiolites, a new genus from the Upper Aptian of the Mediterranean region and the origin of the rudist family Radiolitidae. Palaeontology 49, 769-794.

Friedrich, O., Norris, R.D., Erbacher, J., 2012. Evolution of middle to Late Cretaceous oceans - a 55 my record of Earth's temperature and carbon cycle. Geology 40, 107-110.

Frijia, G., Parente, M., 2008. Strontium isotope stratigraphy in the upper Cenomanian shallow-water carbonates of the southern Apennines: Short-term perturbations of marine $^{87}Sr/^{86}Sr$ during the oceanic anoxic event 2. Palaeogeography, Palaeoclimatology, Palaeoecology 261, 15–29.

Frijia, G., Parente, M., Di Lucia, M., Mutti M., 2015. Carbon and strontium isotope stratigraphy of the Upper Cretaceous (Cenomanian-Campanian) shallow-water carbonates of southern Italy: Chronostratigraphic calibration of larger foraminifera biostratigraphy. Cretaceous Research 53, 110–139.

Hamama, H., 2010. Morphology and wall structure of some Turonian rudists (bivalvia, Hippuritoida) of Gabal Yelleg, northern Sinai, Egypt. Journal of American Science 6.

Huck S., Heimhofer, U., 2015. Improving shallow-water carbonate chemostratigraphy by means of rudist bivalve sclerochemistry. Geochemistry, Geophysics, Geosystems 16, 3111–3128.

Kennedy, W.J., Taylor, J.D., 1968. Aragonite in rudists. Proc. Geol. Soc. London 1645, 325-331.

Klein, R.T., Lohmann, K.C., Thayer, C.W., 1996. Sr/Ca and $^{13}C/^{12}C$ ratios in skeletal calcite of Mytilus trossulus: Covariation with metabolic rate, salinity, and carbon isotopic composition of seawater. Geochimica et Cosmochimica Acta 60, 4207-4221.

Mansour, A. S. M., 2004. Diagenesis of Upper Cretaceous rudist bivalves, Abu Roash area, Egypt: a petrographic study. Geologia Croatica 57, 55-66.

Masse, J. P., Fenerci-Masse, M., Vilas, L., Arias, C., 2007. Late Aptian-Albian primitive Radiolitidae (bivalves, hippuritoidea) from Spain and SW France. Cretaceous Research 28, 697-718.

Masse, J. P., Maresca, M. G., 1997. Late Aptian Radiolitidae (rudist bivalves) from the Mediterranean and Southwest Asiatic regions: taxonomic, biostratigraphic and palaeobiogeographic aspects. Palaeogeography, Palaeoclimatology, Palaeoecology 128, 101-110.

Mutterlose, J., Bornemann, A., Herrle, J., 2009. The Aptian–Albian cold snap: Evidence for. Neues Jahrbuch für Geologie und Paläontologie-Abhandlungen 252, 217-225.

O'Brien, C.L., Robinson, S.A., Pancost, R.D., Damsté, J.S.S., Schouten, S., Lunt, D.J., Alsenz, H., Bornemann, A., Bottini, C., Brassell, S.C., Farnsworth, A., Forster, A., Huber, B.T., Inglis, G.N., Jenkyns, H., C., Linnert, C., Littler, K., Markwick, P., McAnena, A., Mutterlose, J., Naafs, B., D., A., Püttmann, W., Sluijs, A., Helmond, N., A., G., M. van, Vellekoop, J., Wagner, T., Wrobel, N., E., 2017. Cretaceous sea-surface temperature evolution: Constraints from TEX86 and planktonic foraminiferal oxygen isotopes. Earth-science reviews 172, 224-247.

Pons, J.M., Vicens, E., 2008. The structure of the outer shell layer in radiolitid rudists, a morphoconstructional approach. Lethaia 41, 219-234.

Regidor-Higuera, I., García-Garmilla, F., Skelton, P.W., 2007. Sclerochronology and diagenesis of Late Cretaceous radiolitids (Bivalvia, Hippuritoidea), Spain. Cretaceous Rudists and Carbonate Platforms: Environmental Feedback, SEPM Special Publication 87, 115-140.

Rosenberg, G.D., Hughes, W.W., 1991, A metabolic model for the determination of shell composition in the bivalve mollusc, Mytilus edulis. Lethaia 24, 83–96.

Ross, D. J., Skelton, P.W., 1993. Rudist formations of the Cretaceous: a palaeoecological, sedimentological and stratigraphical review. Sedimentology review 1, 73-91.

Sanders, D., 1999. Shell disintegration and taphonomic loss in rudist biostromes. Lethaia 32, 101-112.

Schmitt, K., Heimhofer., Frijia, G., Di Lucia, M., Huck, S., 2019. Deciphering the fragmentary nature of Cretaceous shallow water limestone archives: A case study from the subtropical Apennine carbonate platform. Manuscript in preparation.

Schumann, D., 1995. Upper cretaceous rudist and stromatoporid associations of Central Oman (Arabian Peninsula). Facies 32, 189-202.

Schumann, D., Steuber, T., 1997. Rudisten. Erfolgreiche Siedler und Riffbauer der Kreidezeit. Städte unter Wasser-2 Milliarden Jahre.-Kleine Senckenberg-Reihe 24, 117-122.

Scott, R.W., 1995. Global environmental controls on Cretaceous reefal ecosystems. Palaeogeography, Palaeoclimatology, Palaeoecology 119, 187-199.

Shackleton, N. J., Kennett, J. P., 1975, Paleotemperature history of the Cenozoic and the initiation of Antarctic glaciation: Oxygen and carbon isotope analyses in DSDP sites 277, 279, and 281, in Initial reports of the Deep Sea Drilling Project, Volume 29: Washington, D. C., U.S. Government Printing Office, 743–755.

Skelton, P.W., 1974. Aragonitic shell structures in the rudist Biradiolites, and some palaeobiological inferences. Géologie méditerranéenne 1, 63-74.

Skelton, P.W., 1978. The evolution of functional design in rudists (Hippuritacea) and its taxonomic implications. Phil. Trans. R. Soc. Lond. B 284, 305-318.

Skelton, P.W., 2003. Changing Climate and biota in the marine record. In: Skelton, P.W. (Ed.), The Cretaceous World. Cambridge University Press, Cambridge, 163-184.

Skelton, P.W., Gili, E., 1991. Palaeoecological classification of rudist morphotypes. In First International Conference on Rudists, Proccedings, Serbian Geological Society, Belgrade, 71-86.

Skelton, P.W., Gili, E., 2012. Rudists and carbonate platforms in the Aptian: a case study on biotic interactions with ocean chemistry and climate. Sedimentology 59, 81-117.

Steuber, T., 1996. Stable isotope sclerochronology of rudist bivalves: growth rates and Late Cretaceous seasonality. Geology 24, 315-318.

Steuber, T., Löser, H., 2000. Species richness and abundance patterns of Tethyan Cretaceous rudist bivalves (Mollusca: Hippuritacea) in the central-eastern Mediterranean and Middle East, analysed from a palaeontological database. Palaeogeography, Palaeoclimatology, Palaeoecology 162, 75-104.

Steuber, T., Rauch, M., 2005. Evolution of the Mg/Ca ratio of Cretaceous seawater: implications from the composition of biological low-Mg calcite. Marine Geology 217, 199-213.

Steuber, T., Rauch, M., Masse, J.P., Graaf, J., Malkoč, M., 2005. Low-latitude seasonality of Cretaceous temperatures in warm and cold episodes. Nature 437, 1341.

Steuber, T., Schlüter, M., 2012. Strontium-isotope stratigraphy of Upper Cretaceous rudist bivalves: biozones, evolutionary patterns and sea-level change calibrated to numerical ages. Earth-Science Reviews, 114(1-2), 42-60.

Steuber, T., Veizer, J., 2002. Phanerozoic record of plate tectonic control of seawater chemistry and carbonate sedimentation. Geology 30, 1123-1126.

Steuber. T., 1999. Isotopic and chemical intra-shell variations in low-Mg calcite of rudist bivalves (Mollusca-Hippuritacea): disequilibrium fractionations and late Cretaceous seasonality. Int Journ Earth Sciences 88, 551–570.

Tibljaš, D., Moro, A., Ostrež, Ž., 2004. Mineral and chemical composition of rudist valves from Upper Cretaceous limestones of Southern Istria, Croatia. Geologia Croatica 57, 73-79.

Woo, K. S., Anderson, T. F., Sandberg, P.A., 1993. Diagenesis of skeletal and nonskeletal components of mid-Cretaceous limestones. Journal of Sedimentary Research 63, 18-32.

6. Summary and Outlook

The main point of this thesis is the reconstruction of major environmental events during the mid-Cretaceous on the Apennine Carbonate Platform (ACP). Three main questions were postulated, as seen in 1.5. The following chapter gives a brief summary of this thesis, firstly stating the posed questions followed by the acquired insights.

(1) **To what extant can a continuous sedimentation of the Apennine Carbonate Platform be confirmed?**

Two sections, the open lagoon Santa Lucia (SL) and the platform marginal Monte La Costa (MLC), located on the Apennine Carbonate Platform, were analysed. Using integrated bio- and chemostratigraphy a precise chronostratigraphic framework was established. During this process, the fragmentary record of the Apennine Carbonate Platform became apparent: The Santa Lucia succession, ranging from Barremian to Cenomanian, reveals that about 61% of the time (~ 20.7 Myr) is lost in three major hiatal surfaces including intervals of the Early Aptian (~ 3.2 Myr), Late Aptian (~ 3.3 Myr) and Middle Albian to uppermost Middle Cenomanian (~ 14.2 Myr). The Late Aptian hiatus is also found in the less expanded Monte La Costa section, dated to Aptian-Albian. The related exposure surfaces were determined and documented, so that their chemical features (e.g. C-anomalies), their field expression (e.g. bauxite, breccia, and soil formation) and the time loss can be compared with each other.

(2) **When was the onset of the microbial bloom in each analysed section and what environmental conditions can be reconstructed for this period?**

Using the established chronostratigraphic framework, a platform-wide, synchronous onset of pervasive bacinelloid microencrusters in both the inner (Santa Lucia) and marginal (Monte La Costa) carbonate platform domain is dated to the period between the Jacob and Kilian black-shale levels of the Late Aptian OAE1b multi-event. With its initial phase during the late stage of the so-called Late Aptian ‘cold snap’, the detected period of bacinelliod growth gives an insight towards the prevailing environmental parameters during this time: leading from cold temperatures to an increase in temperature and a paralleled significant rise of the sea level.

(3) **To what extent are radiolitids a viable basis for environmental reconstruction, especially temperature, salinity and habitat?**

Radiolitids, the main carbonate producers of the Apennine Carbonate Platform, are often neglected as a palaeoenvironmental archive. Although they contain an outer shell layer composed of low-Mg calcite, its porous structure poses a challenge for palaeoenvironmental studies. High-resolution sampling, using a combination of elemental and isotopic data as well as sclerochronological descriptions, shows that the right valve (RV) and the left valve (LV) differ greatly with regard to their usability as archives. The highly compact left valve recorded a gradually, smooth sine function as $\delta^{18}O$ pattern and is therefore an excellent archive for palaeotemperature reconstructions. The regular alternation of the growth lamellae of the right valve is an indicator for the intertidal as former living habitat.

By raising three key questions and gathering conclusive insights, this thesis contributes to the unravelling of shallow marine carbonate platforms. With the newly established framework previous biostratigraphically defined sections of the Apennine Carbonate Platform can now be integrated in the generated framework, allowing their more accurate chronostratigraphic dating.

But still, further research opportunities can be proposed for (I) the environmental conditions causing a microbial bloom and (II) the combination of elemental and isotopic data sampling.

(I) As described in various other studies, several *Lithocodium-Bacinella* occurances were reported from other sections of the Apennine Carbonate Platform. Before the driving factors of microbial episodes can be deciphered, it is necessary to evaluate the temporal and spatial distribution of microencrusters. By using the newly established framework, a precise dating is made possible, allowing the integration of previously recorded data and achieving a higher degree of temporal accuracy. Since previous studies often show only a vague description of the microencrusters, the comparability of different sections is low. To solve this problem, the morphotypical classification of Rameil et al. (2010) is suggested, to systematically document occurring microencrusters for each section.

(II) By combining high-resolution sampling of elemental with isotopic data, a promising methodology for palaeoenvironmental reconstruction is created. The first results of the applied isotopic measurements show encouraging results, yielding reliable cyclic patterns of $\delta^{18}O$. Furthermore, using the elemental dataset, diagentically altered shell material can be quickly detected. For future research, it is important to precisely define and document transects before measurements, to make sure that the obatined datasets can be linked and mapped to the shell. Additionally, µXRF measurements can be supported with ICP-OES data, to maintain reliable results.

7. Author contributions

Katharina E. Schmitt carried out logging and sampling during field campaigns. She executed all laboratory work (thin-section preparation, sample preparation for IRMS and ICP- OES measurements). She interpreted the analyzed data, wrote all the text including the manuscript chapters 3-5 and prepared all figures and tables.

Stefan Huck conceived and designed the project with input from Ulrich Heimhofer. Stefan Huck coordinated the project and organized external funding. He assisted during field work and with data interpretation and reviewed and improved text and figures of the manuscript chapters 3-5.

Ulrich Heimhofer assisted with data interpretation. Furthermore, he reviewed and improved of the manuscript chapters 3-5.

Gianluca Frijia and Matteo DiLucia established the biostratigraphy used in this thesis.

Malte Krummacker assisted with Micromill-based shell sampling (chapter 5).

Niels de Winter performed µXRF measurement and assisted with data interpretation (chapter 5).

8. Appendices

CARBONATE BULK, SANTA LUCIA SECTION

Sample (no.)	Height [m]	$\delta^{13}C$ [VPDB]	$\delta^{13}C$ [VPDB] s.d.	$\delta^{18}O$ [VPDB]	$\delta^{18}O$ [VPDB] s.d.
SL 00	**0**	2.10	0.04	-1.91	0.05
SL 0.5	**0.5**	1.85	0.04	-1.87	0.06
SL 1	**1**	1.95	0.03	-2.19	0.07
SL 1.5	**1.5**	1.95	0.04	-2.38	0.04
SL 2	**2**	2.04	0.04	-2.03	0.04
SL 2.5	**2.5**	1.70	0.03	-2.53	0.06
SL 3	**3**	1.84	0.03	-2.41	0.09
SL 3.5 c	**3.5**	1.95	0.03	-2.40	0.05
SL 4.5	**4.5**	1.99	0.03	-1.64	0.03
SL 5	**5**	1.71	0.04	-0.90	0.05
SL 5.5	**5.5**	1.04	0.04	-1.52	0.05
SL 6	**6**	1.79	0.04	-1.37	0.08
SL 6.5	**6.5**	1.34	0.04	-1.85	0.04
SL 7	**7**	1.57	0.03	-2.47	0.05
SL 7.5	**7.5**	1.40	0.05	-2.35	0.04
SL 8	**8**	1.83	0.02	-1.59	0.04
SL 8.5	**8.5**	1.98	0.04	-2.09	0.03
SL 9	**9**	1.65	0.02	-2.10	0.06
SL 9.5	**9.5**	1.95	0.04	-1.98	0.05
SL 10	**10**	1.91	0.03	-2.41	0.04
SL 10.5	**10.5**	1.98	0.03	-2.80	0.08
SL 11	**11**	2.05	0.02	-1.95	0.04
SL 11.5	**11.5**	1.60	0.04	-1.70	0.06
SL 12	**12**	1.91	0.03	-2.07	0.06
SL 12.5	**12.5**	1.16	0.04	-2.02	0.04
SL 13	**13**	1.06	0.03	-3.32	0.05
SL 13.5	**13.5**	1.48	0.11	-2.78	0.09
SL 14	**14**	1.90	0.03	-2.50	0.06
SL 14.5	**14.5**	1.44	0.04	-2.52	0.05
SL 15	**15**	1.67	0.02	-2.88	0.07
SL 15.5	**15.5**	2.11	0.03	-1.47	0.05
SL 16	**16**	2.13	0.04	-1.39	0.07
SL 16.5	**16.5**	1.87	0.03	-1.83	0.03
SL 17	**17**	1.19	0.02	-2.22	0.02
SL 17.5	**17.5**	1.92	0.04	-2.26	0.05
SL 18	**18**	1.80	0.03	-2.42	0.07
SL 18.5	**18.5**	1.90	0.04	-1.81	0.07
SL 19	**19**	1.15	0.03	-1.56	0.06
SL 19.5	**19.5**	1.56	0.03	-1.67	0.05
SL 20	**20**	2.20	0.03	-1.19	0.04
SL 20.5	**20.5**	2.22	0.03	-1.53	0.06
SL-21.0	**21.0**	1,86	0,03	-1,47	0,03
SL 21.5	**21.5**	1,59	0,07	-3,04	0,07
SL 22	**22.0**	1,79	0,02	-2,00	0,06
SL-22.5	**22.5**	1,76	0,03	-1,87	0,05
SL 23	**23**	1.70	0.06	-2.32	0.05
SL 23.5	**23.5**	1.73	0.05	-2.28	0.08
SL 24	**24**	1.42	0.03	-2.10	0.06
SL 24.5	**24.5**	1.57	0.04	-2.92	0.06
SL 25	**25**	1.80	0.06	-2.16	0.06
SL 25.5	**25.5**	2.02	0.10	-1.84	0.07
SL 26	**26**	1.98	0.07	-2.28	0.06
SL 27	**27**	2.05	0.04	-1.97	0.04
SL 27.5	**27.5**	1.00	0.04	-2.74	0.06
SL 28	**28**	2.13	0.05	-1.69	0.05
SL 28.5	**28.5**	2.25	0.06	-1.61	0.06
SL 29	**29**	2.08	0.06	-1.84	0.09
SL 29.5	**29.5**	2.11	0.02	-1.99	0.04
SL 30	**30**	1.82	0.02	-2.97	0.05
SL 30.5	**30.5**	2.26	0.04	-1.92	0.04
SL 31	**31**	2.01	0.03	-2.43	0.06
SL 31.5	**31.5**	1.98	0.02	-2.15	0.05
SL 32	**32**	1.85	0.03	-2.20	0.05
SL 32.5	**32.5**	2.09	0.04	-2.00	0.05
SL33	**33**	0.75	0.10	-2.42	0.09
SL 33.5	**33.5**	2.35	0.05	-1.74	0.06
SL 34	**34**	2.32	0.04	-1.69	0.04
SL 34.5	**34.5**	2.31	0.05	-1.83	0.07
SL 35.5	**35.5**	2.02	0.06	-2.02	0.05
SL 36	**36**	1.83	0.03	-1.88	0.04
SL 36.5	**36.5**	1.73	0.04	-1.72	0.07
SL 37	**37**	1.72	0.03	-2.58	0.04
SL 37.5	**37.5**	1.72	0.03	-1.97	0.07
SL 38	**38**	1.97	0.05	-1.82	0.06
SL 38.5	**38.5**	1.63	0.04	-2.30	0.05
SL 39	**39**	1.58	0.07	-1.87	0.06
SL 39.5	**39.5**	1.64	0.04	-2.03	0.07
SL 40	**40**	1.74	0.04	-1.63	0.06
SL 40.5	**40.5**	1.53	0.02	-1.80	0.05
SL 41	**41**	1.55	0.08	-2.09	0.07
SL 41.5	**41.5**	1.60	0.02	-1.98	0.07
SL 42	**42**	1.78	0.06	-1.72	0.06
SL 42.5	**42.5**	1.64	0.04	-1.69	0.06
SL 43	**43**	2.00	0.03	-1.48	0.04
SL 43.5	**43.5**	1.94	0.02	-1.96	0.04
SL 44	**44**	1.83	0.05	-1.45	0.06

Sample (no.)	**Height** [m]	$\delta^{13}C$ [VPDB]	$\delta^{13}C$ [VPDB] s.d.	$\delta^{18}O$ [VPDB]	$\delta^{18}O$ [VPDB] s.d.
SL 44.5	**44.5**	1.46	0.08	-1.72	0.07
SL 45	**45**	1.71	0.03	-1.87	0.04
SL 45.5	**45.5**	1.64	0.07	-2.06	0.09
SL 46	**46**	1.31	0.07	-1.68	0.08
SL 46.5	**46.5**	0.72	0.06	-2.37	0.04
SL 47	**47**	1.50	0.04	-1.65	0.07
SL 47.5	**47.5**	1.77	0.02	-2.85	0.07
SL 48	**48**	1.61	0.04	-2.88	0.09
SL 48.5	**48.5**	1.46	0.03	-1.97	0.06
SL 49	**49**	1.63	0.05	-2.31	0.08
SL 49.5	**49.5**	1.29	0.05	-2.11	0.05
SL 50	**50**	2.07	0.05	-2.20	0.07
SL 50.5	**50.5**	1.84	0.04	-2.30	0.08
SL 51	**51**	2.13	0.05	-2.03	0.04
SL 51.5	**51.5**	2.11	0.04	-1.90	0.04
SL 52	**52**	1.59	0.06	-1.65	0.07
SL 52.5	**52.5**	2.01	0.05	-2.74	0.05
SL 53	**53**	1.97	0.03	-2.68	0.04
SL 53.5	**53.5**	2.20	0.05	-2.21	0.08
SL 54	**54**	2.16	0.05	-2.15	0.05
SL 54.5	**54.5**	2.16	0.03	-2.24	0.05
SL 55	**55**	2.18	0.04	-2.17	0.06
SL 55.5	**55.5**	1.82	0.04	-2.72	0.03
SL 56	**56**	1.92	0.04	-2.00	0.07
SL 56.5	**56.5**	2.32	0.05	-1.88	0.05
SL 57	**57**	2.02	0.03	-2.08	0.05
SL 57.5	**57.5**	2.29	0.04	-1.66	0.06
SL 58	**58**	1.68	0.03	-1.99	0.04
SL 58.5	**58.5**	1.72	0.03	-2.10	0.03
SL 59	**59**	1.84	0.05	-1.89	0.06
SL 59.5	**59.5**	2.36	0.03	-1.58	0.05
SL 60	**60**	2.23	0.02	-1.59	0.04
SL 60.5	**60.5**	2.21	0.04	-1.60	0.05
SL 61	**61**	0.41	0.05	-2.27	0.06
SL 61.5	**61.5**	1.55	0.02	-1.53	0.02
SL 62	**62**	2.34	0.04	-0.82	0.05
SL 62.5	**62.5**	2.47	0.04	-1.90	0.05
SL 63	**63**	2.45	0.04	-1.68	0.07
SL 63.5	**63.5**	2.75	0.04	-1.27	0.06
SL 64	**64**	2.37	0.05	-1.95	0.06
SL 64.5	**64.5**	2.63	0.05	-1.16	0.03
SL 65	**65**	2.76	0.03	-1.42	0.06
SL 65.5	**65.5**	2.60	0.04	-1.97	0.06
SL 66.5	**66.5**	2.62	0.04	-1.75	0.06
SL 67	**67**	2.82	0.07	-1.63	0.06
SL 67.5-1	**67.5**	2.67	0.04	-1.92	0.06
SL 67.5-2	**67.5**	2.61	0.05	-1.53	0.08
SL 68	**68**	2.82	0.04	-1.49	0.04
SL68.5	**68.5**	2.51	0.04	-1.65	0.05
SL 69	**69**	2.84	0.05	-1.43	0.04
SL 69	**69**	2.18	0.05	-2.89	0.05
SL 69.5	**69.5**	2.50	0.05	-1.30	0.07
SL 70	**70**	2.66	0.05	-1.59	0.05
SL 70.5	**70.5**	2.41	0.04	-1.55	0.05
SL 71	**71**	2.50	0.03	-2.14	0.04
SL 71.5	**71.5**	1.97	0.03	-2.61	0.04
SL 72	**72**	2.32	0.03	-1.72	0.05
SL 72.5	**72.5**	1.81	0.03	-0.93	0.04
SL 73	**73**	2.94	0.02	-1.38	0.04
SL 73.5	**73.5**	2.47	0.03	-1.82	0.04
SL 74	**74**	2.36	0.05	-1.31	0.06
SL74.5	**74.5**	2.37	0.03	-1.69	0.07
SL 75	**75**	2.54	0.04	-1.93	0.05
SL75.5	**75.5**	2.52	0.04	-2.11	0.03
SL76	**76**	2.13	0.03	-2.73	0.04
SL 76.5	**76.5**	2.62	0.06	-1.73	0.06
SL 77	**77**	2.68	0.02	-1.73	0.04
SL 77.5	**77.5**	2.77	0.03	-1.85	0.05
SL 78	**78**	2.40	0.03	-2.18	0.07
SL 78.5	**78.5**	2.82	0.04	-1.73	0.08
SL 79	**79**	3.02	0.06	-1.50	0.07
SL 79.5	**79.5**	2.69	0.03	-2.39	0.04
SL 80	**80**	2.75	0.06	-1.70	0.04
SL 80.5	**80.5**	2.51	0.03	-2.55	0.06
SL 81-1	**81**	2.57	0.03	-2.03	0.04
SL 81-2	**81**	1.80	0.05	-2.27	0.03
SL 82	**82**	2.59	0.04	-2.13	0.05
SL 82.5	**82.5**	2.12	0.04	-1.57	0.07
SL 83	**83**	2.59	0.02	-1.34	0.05
SL 83.5	**83.5**	2.09	0.02	-2.04	0.03
SL 84	**84**	2.19	0.03	-2.18	0.06
SL 84.5	**84.5**	2.30	0.05	-1.73	0.06
SL 85	**85**	2.29	0.01	-1.87	0.05
SL 85.5	**85.5**	2.30	0.03	-2.87	0.07
SL 85.5	**85.5**	1.85	0.06	-2.69	0.05
SL 86	**86**	2.43	0.03	-2.24	0.03
SL 86.5	**86.5**	2.48	0.06	-2.32	0.05
SL 87	**87**	2.05	0.03	-2.25	0.03
SL 87.5	**87.5**	2.33	0.03	-2.14	0.06
SL 88	**88**	2.30	0.02	-2.14	0.03
SL 88.5	**88.5**	1.96	0.04	-1.79	0.05
SL 89	**89**	2.21	0.03	-1.55	0.04
SL 89.5	**89.5**	2.04	0.02	-1.62	0.05
SL 90-1	**90**	2.00	0.03	-1.83	0.06

Sample (no.)	**Height [m]**	**δ^{13}C [VPDB]**	**δ^{13}C [VPDB] s.d.**	**δ^{18}O [VPDB]**	**δ^{18}O [VPDB] s.d.**
SL 90-2	**90**	2.13	0.04	-2.14	0.05
SL 90.5	**90.5**	2.49	0.04	-1.42	0.04
SL 91	**91**	2.17	0.03	-1.64	0.04
SL 91.5	**91.5**	2.65	0.09	-1.93	0.10
SL 92	**92**	2.49	0.05	-2.02	0.07
SL 92.5	**92.5**	2.01	0.02	-2.23	0.06
SL 93	**93**	2.31	0.04	-2.16	0.05
SL 93.5	**93.5**	-1.03	0.04	-3.15	0.06
SL 94	**94**	-2.59	0.04	-3.54	0.05
SL 94.5-1	**94.5**	1.13	0.05	-1.43	0.07
SL 94.5-2	**94.5**	-0.88	0.04	-1.76	0.05
SL 95	**95**	2.21	0.05	-1.92	0.06
SL 95.5	**95.5**	2.14	0.06	-1.95	0.06
SL 96	**96**	2.18	0.02	-1.83	0.06
SL 96.5	**96.5**	1.77	0.04	-2.10	0.08
SL 97	**97**	1.63	0.07	-0.97	0.06
SL 97.5	**97.5**	2.01	0.04	-2.05	0.02
SL 98	**98**	2.52	0.03	-1.34	0.05
SL 98.5	**98.5**	2.08	0.06	-1.91	0.03
SL 99	**99**	1.85	0.03	-2.49	0.09
SL 99.5	**99.5**	1.88	0.02	-2.18	0.05
SL100	**100**	1.97	0.05	-1.53	0.06
SL 100.5	**100.5**	1.41	0.04	-2.27	0.06
SL 101	**101**	1.63	0.03	-2.04	0.05
SL 101.5	**101.5**	-0.12	0.05	-2.55	0.05
SL 102	**102**	1.74	0.04	-1.77	0.04
SL 102.5	**102.5**	1.76	0.03	-2.46	0.04
SL 103	**103**	2.04	0.05	-1.81	0.09
SL 103.5	**103.5**	2.10	0.06	-1.82	0.04
SL 104	**104**	2.03	0.06	-1.81	0.05
SL 104.5	**104.5**	2.30	0.06	-2.16	0.06
SL 105	**105**	2.16	0.05	-1.69	0.04
SL 105.5	**105.5**	1.82	0.05	-2.63	0.04
SL 106	**106**	1.24	0.03	-2.18	0.03
SL 106.5	**106.5**	1.85	0.03	-1.19	0.07
SL 108	**108**	-11.21	0.04	-5.19	0.04
SL 109	**109**	1.74	0.06	-2.30	0.06
SL 109.5	**109.5**	1.70	0.04	-3.25	0.04
SL 110.5	**110.5**	0.54	0.05	-3.50	0.05
SL 111	**111**	1.79	0.03	-2.94	0.06
SL 111.5	**111.5**	1.91	0.05	-2.66	0.08
SL 112	**112**	1.18	0.04	-3.37	0.05
SL 112.5	**112.5**	1.57	0.03	-2.40	0.06
SL113	**113**	1.41	0.02	-2.55	0.06
SL 113.5	**113.5**	1.37	0.05	-2.73	0.06
SL 114	**114**	1.74	0.04	-1.98	0.04
SL 114.5	**114.5**	1.25	0.04	-1.50	0.04
SL 115	**115**	1.71	0.04	-2.25	0.06
SL 115.5	**115.5**	1.57	0.04	-2.80	0.05
SL 116	**116**	2.00	0.06	-2.41	0.05
SL 116.5	**116.5**	1.02	0.04	-2.52	0.05
SL 117	**117**	1.66	0.03	-2.08	0.06
SL 117.5	**117.5**	-1.07	0.05	-3.20	0.04
SL 118	**118**	-1.47	0.05	-3.82	0.04
SL 118.5	**118.5**	-1.58	0.04	-3.80	0.04
SL 119	**119**	1.27	0.02	-2.36	0.05
SL 119.5	**119.5**	2.03	0.04	-1.59	0.05
SL 120	**120**	2.11	0.05	-2.09	0.05
SL 120.5	**120.5**	2.04	0.05	-2.40	0.05
SL 121	**121**	1.82	0.04	-2.57	0.04
SL 121.5	**121.5**	2.03	0.03	-3.02	0.04
SL 122	**122**	2.11	0.04	-2.65	0.06
SL 122.5	**122.5**	2.18	0.02	-2.18	0.06
SL 123	**123**	2.22	0.05	-2.61	0.06
SL 124	**124**	2.53	0.02	-2.30	0.06
SL 124.5	**124.5**	2.52	0.04	-2.03	0.04
SL 125	**125**	2.46	0.06	-2.41	0.06
SL 125.5	**125.5**	2.84	0.03	-1.85	0.06
SL 126	**126**	2.58	0.03	-2.16	0.07
SL 126.5	**126.5**	2.84	0.04	-1.75	0.06
SL 127	**127**	2.52	0.04	-1.63	0.02
SL 127.5	**127.5**	2.11	0.05	-2.51	0.05
SL 128	**128**	2.45	0.04	-2.16	0.05
SL 128.5	**128.5**	2.45	0.04	-1.45	0.07
SL 129	**129**	2.30	0.03	-1.93	0.05
SL 129.5	**129.5**	2.19	0.06	-1.34	0.07
SL 130	**130**	2.37	0.04	-1.42	0.06
SL 130.5	**130.5**	2.45	0.04	-1.19	0.04
SL 131	**131**	2.68	0.03	-2.22	0.07
SL 131.5	**131.5**	2.68	0.06	-2.28	0.06
SL 132.5	**132.5**	2.05	0.02	-2.35	0.03
SL 132.5	**132.5**	2.23	0.06	-2.64	0.04
SL 133	**133**	2.70	0.04	-1.66	0.05
SL 133.5	**133.5**	2.31	0.02	-1.10	0.03
SL 134	**134**	2.52	0.04	-1.83	0.08
SL 135	**135**	2.63	0.02	-2.47	0.04
SL 135.5	**135.5**	2.40	0.04	-2.16	0.04
SL 136	**136**	1.39	0.03	-3.12	0.03
SL 136.5-1	**136.5**	2.22	0.05	-3.07	0.03
SL 136.5-2	**136.5**	1.74	0.03	-2.91	0.03
SL 137	**137**	1.82	0.03	-1.66	0.04
SL 137.5	**137.5**	2.42	0.05	-1.08	0.06
SL 138	**138**	2.48	0.04	-1.64	0.03
SL 138.5	**138.5**	2.51	0.04	-2.37	0.04

Sample (no.)	Height [m]	$\delta^{13}C$ [VPDB]	$\delta^{13}C$ [VPDB] s.d.	$\delta^{18}O$ [VPDB]	$\delta^{18}O$ [VPDB] s.d.
SL 139	**139**	2.84	0.05	-1.98	0.06
SL 139.5	**139.5**	2.68	0.03	-2.18	0.05
SL 140	**140**	2.68	0.04	-2.24	0.07
SL 140.5	**140.5**	2.86	0.06	-2.02	0.05
SL 141	**141**	2.30	0.03	-0.99	0.05
SL 141.5	**141.5**	2.19	0.05	-2.61	0.03
SL 142.5	**142.5**	1.67	0.04	-3.58	0.02
SL 143	**143**	2.37	0.04	-1.36	0.06
SL 143.5	**143.5**	2.25	0.04	-1.64	0.05
SL 144	**144**	1.88	0.04	-2.02	0.03
SL 144.5	**144.5**	1.78	0.05	-1.98	0.05
SL 145	**145**	1.75	0.04	-2.03	0.05
SL 145.5-1	**145.5**	2.20	0.03	-1.69	0.05
SL 145.5-2	**145.5**	2.22	0.04	-1.24	0.06
SL 146	**146**	1.64	0.04	-2.41	0.06
SL 146.5	**146.5**	1.83	0.06	-2.10	0.06
SL 147.5	**147.5**	1.72	0.03	-1.60	0.07
SL 147.5	**147.5**	1.39	0.02	-2.69	0.03
SL 148	**148**	2.67	0.05	-1.32	0.09
SL 148.5	**148.5**	2.35	0.04	-1.88	0.03
SL 149	**149**	1.98	0.07	-1.85	0.06
SL 149.5	**149.5**	2.04	0.04	-1.97	0.06
SL 150	**150**	2.04	0.05	-2.18	0.04
SL 150.5	**150.5**	2.44	0.03	-1.88	0.07
SL 151	**151**	2.37	0.09	-2.27	0.09
SL 151.5	**151.5**	1.97	0.04	-2.95	0.04
SL 152	**152**	2.43	0.03	-2.06	0.05
SL 152.5	**152.5**	2.39	0.03	-2.58	0.06
SL 153	**153**	2.61	0.03	-2.02	0.04
SL 153.5	**153.5**	2.21	0.03	-1.46	0.07
SL 154	**154**	2.36	0.08	-2.16	0.09
SL 154.5	**154.5**	2.48	0.03	-2.18	0.06
SL 155	**155**	1.69	0.04	-2.92	0.07
SL 155.5	**155.5**	2.08	0.03	-2.16	0.06
SL 156	**156**	1.53	0.02	-1.99	0.04
SL 156.5	**156.5**	2.57	0.03	-2.11	0.04
SL 157	**157**	2.90	0.05	-1.20	0.06
SL 157.5	**157.5**	2.19	0.03	-2.47	0.03
SL 158	**158**	0.71	0.02	-3.63	0.07
SL 158.5	**158.5**	1.16	0.03	-1.91	0.05
SL 159	**159**	1.81	0.04	-2.27	0.04
SL 159.5	**159.5**	-0.20	0.04	-3.12	0.06
SL 160	**160**	1.60	0.03	-2.28	0.07
SL 160.5	**160.5**	2.47	0.03	-2.12	0.07
SL 161	**161**	2.45	0.04	-1.63	0.06
SL 161.5	**161.5**	2.57	0.03	-2.00	0.07
SL 162	**162**	3.16	0.03	-1.28	0.02
SL 162.5	**162.5**	2.95	0.05	-1.53	0.06
SL 163	**163**	3.01	0.03	-1.27	0.04
SL 163.5	**163.5**	3.19	0.04	-1.68	0.04
SL 164	**164**	2.84	0.03	-1.55	0.06
SL 164.5	**164.5**	2.59	0.05	-1.06	0.07
SL 165	**165**	2.66	0.03	-1.68	0.05
SL 165.5	**165.5**	2.55	0.10	-1.98	0.09
SL 166	**166**	2.12	0.03	-2.03	0.05
SL 166	**166**	2.15	0.02	-2.31	0.04
SL 167	**167**	1.80	0.09	-2.21	0.08
SL 167.5	**167.5**	2.09	0.05	-2.06	0.04
SL 168	**168**	2.10	0.04	-2.36	0.04
SL 168.5-1	**168.5**	2.01	0.03	-2.05	0.05
SL 168.5-2	**168.5**	2.28	0.03	-2.27	0.05
SL 169	**169**	2.23	0.06	-2.35	0.06
SL 170	**170**	2.47	0.03	-2.48	0.03
SL 170.5	**170.5**	2.40	0.03	-2.15	0.05
SL 171	**171**	2.36	0.04	-1.54	0.06
SL 171.5	**171.5**	2.52	0.02	-1.71	0.05
SL 172	**172**	2.15	0.02	-2.34	0.09
SL 172.5	**172.5**	1.23	0.03	-2.56	0.04
SL 173	**173**	1.28	0.04	-2.70	0.06
SL 173.5	**173.5**	1.85	0.09	-1.77	0.08
SL 174	**174**	2.04	0.05	-2.32	0.05
SL 174.5	**174.5**	2.32	0.03	0.21	0.04
SL 175	**175**	1.66	0.02	-2.31	0.06
SL 175.5	**175.5**	2.46	0.03	-2.21	0.04
SL 176	**176**	1.52	0.04	-2.53	0.05
SL 176.5	**176.5**	2.30	0.03	-2.12	0.03
SL 177	**177**	2.12	0.04	-2.16	0.03
SL 177.5	**177.5**	2.24	0.04	-2.48	0.05
SL 178	**178**	1.19	0.02	-2.47	0.04
SL 178.5	**178.5**	1.18	0.04	-1.71	0.05
SL 179	**179**	1.42	0.02	-2.41	0.07
SL 179.5	**179.5**	2.32	0.04	-2.23	0.05
SL 180	**180**	1.91	0.02	-2.27	0.05
SL 180.5	**180.5**	2.17	0.03	-2.81	0.08
SL 181	**181**	2.80	0.03	-1.93	0.06
SL 181.5	**181.5**	2.50	0.06	-1.15	0.03
SL 182	**182**	2.50	0.03	-1.46	0.04
SL 182.5	**182.5**	3.01	0.05	-1.55	0.06
SL 183-2	**183**	2.09	0.04	-1.75	0.05
SL 183	**183**	2.52	0.05	-1.90	0.04
SL 183.5	**183.5**	2.12	0.04	-1.96	0.05
SL 184	**184**	2.69	0.02	-1.21	0.07
SL 184.5	**184.5**	2.61	0.03	-1.26	0.04
SL 185	**185**	2.48	0.03	-2.06	0.04

Sample (no.)	Height [m]	δ^{13}C [VPDB]	δ^{13}C [VPDB] s.d.	δ^{18}O [VPDB]	δ^{18}O [VPDB] s.d.
SL 185.5	**185.5**	2.69	0.03	-2.37	0.04
SL 186	**186**	3.06	0.03	-1.80	0.05
SL 186.5	**186.5**	3.14	0.03	-2.01	0.07
SL 187	**187**	2.85	0.04	-2.08	0.03
SL 187.5	**187.5**	1.82	0.02	-2.34	0.07
SL 188	**188**	3.12	0.04	-1.83	0.05
SL 188.5	**188.5**	3.09	0.05	-2.23	0.04
SL 189	**189**	3.14	0.04	-1.38	0.02
SL 189.5	**189.5**	3.59	0.04	-2.01	0.04
SL 190	**190**	3.14	0.03	-2.20	0.04
SL 190.5	**190.5**	3.11	0.04	-2.09	0.03
SL 191	**191**	2.73	0.02	-2.44	0.05
SL 192-1	**192**	3.27	0.02	-1.64	0.06
SL 192-2	**192**	2.99	0.04	-1.65	0.05
SL 193	**193**	2.97	0.04	-1.83	0.04
SL 195.5	**193.5**	3.04	0.04	-1.98	0.05
SL 194	**194**	2.57	0.04	-2.75	0.04
SL 195	**195**	3.30	0.05	-2.14	0.04
SL 196	**196**	3.09	0.05	-1.83	0.05
SL 196.5	**196.5**	2.67	0.04	-1.04	0.07
SL 197	**197**	2.37	0.06	-1.93	0.10
SL 198.5	**198.5**	2.44	0.04	-1.59	0.07
SL 199	**199**	2.40	0.02	-2.50	0.05
SL 199.5	**199.5**	2.85	0.03	-1.73	0.04
SL200a	**200**	3.00	0.05	-2.56	0.07
SL 201	**201**	2.46	0.03	-2.36	0.05
SL 201.5	**201.5**	2.30	0.03	-1.41	0.07
SL 202	**202**	2.55	0.03	-1.67	0.08
SL 203	**203**	2.70	0.04	-1.78	0.05
SL 204	**204**	2.47	0.03	-1.37	0.04
SL 205.5	**205.5**	2.67	0.05	-1.53	0.04
SL 206.5	**206.5**	2.15	0.03	-1.76	0.07
SL 207	**207**	2.49	0.04	-1.31	0.04
SL 207.5	**207.5**	2.69	0.06	-1.53	0.06
SL 208	**208**	2.20	0.02	-1.51	0.04
SL 208.5	**208.5**	2.10	0.05	-1.32	0.08
SL 209	**209**	2.44	0.07	-1.55	0.06
SL 209.5	**209.5**	2.39	0.04	-1.48	0.05
SL 210	**210**	2.43	0.02	-2.09	0.05
SL 210.5	**210.5**	1.86	0.02	-1.82	0.05
SL 211	**211**	2.42	0.05	-1.95	0.04
SL 211.5	**211.5**	2.48	0.06	-1.16	0.07
SL 212	**212**	2.31	0.03	-1.69	0.04
SL 213	**213**	2.59	0.03	-1.94	0.05
SL 214	**214**	2.32	0.03	-1.82	0.05
SL 215.5	**215.5**	2.42	0.05	-2.04	0.04
SL 216	**216**	2.31	0.03	-1.49	0.05
SL 216.5	**216.5**	2.28	0.05	-1.72	0.05
SL 217	**217**	2.36	0.03	-1.89	0.05
SL 217.5	**217.5**	2.27	0.02	-1.73	0.03
SL 218	**218**	2.29	0.03	-1.77	0.05
SL 218.5	**218.5**	2.39	0.04	-2.03	0.04
SL 219	**219**	2.26	0.02	-1.12	0.05
SL 219.5	**219.5**	2.23	0.03	-2.23	0.05
SL 220	**220**	2.43	0.04	-1.68	0.06
SL 220	**220**	2.07	0.03	-1.61	0.05
SL 220.5	**220.5**	2.28	0.05	-2.21	0.04
SL 221	**221**	2.16	0.05	-1.70	0.04
SL 221.5	**221.5**	2.26	0.03	-2.25	0.04
SL 222.5	**222.5**	1.93	0.05	-2.13	0.04
SL 223	**223**	1.89	0.04	-2.05	0.06
SL 223.5	**223.5**	2.42	0.04	-1.92	0.04
SL 224	**224**	2.60	0.04	-1.58	0.04
SL 224.5	**224.5**	2.31	0.03	-1.75	0.07
SL 225	**225**	2.03	0.04	-2.77	0.06
SL 225.5	**225.5**	3.35	0.05	-1.38	0.04
SL 226	**226**	3.28	0.02	-1.81	0.05
SL 226.5	**226.5**	3.30	0.06	-1.57	0.06
SL 227	**227**	3.48	0.05	-1.11	0.06
SL 227.5	**227.5**	3.35	0.03	-1.44	0.08
SL 228	**228**	3.41	0.04	-1.29	0.03
SL 229	**229**	3.11	0.05	-1.61	0.08
SL 229.5	**229.5**	2.72	0.02	-1.11	0.06
SL 230	**230**	2.81	0.04	-1.64	0.06
SL 231	**231**	2.70	0.02	-1.43	0.06
SL 232	**232**	2.67	0.07	-1.31	0.06
SL 232.5	**232.5**	2.81	0.05	-1.15	0.05
SL 233	**233**	3.03	0.03	-1.40	0.05
SL 236-1	**236**	0.48	0.04	-2.20	0.03
SL 236-2	**236**	2.12	0.06	-1.75	0.08
SL 237	**237**	3.19	0.04	-1.43	0.05
SL 237.5	**237.5**	3.20	0.02	-1.26	0.05
SL 238	**238**	3.38	0.03	-1.33	0.07
SL 238.5	**238.5**	3.06	0.03	-1.17	0.05
SL 239	**239**	2.73	0.06	-1.29	0.06
SL 240	**240**	2.94	0.03	-1.91	0.04
SL 240.5	**240.5**	2.38	0.04	-2.93	0.07
SL 241	**241**	2.57	0.03	-2.40	0.05
SL 241.5	**241.5**	2.80	0.02	-1.68	0.04
SL 242	**242**	2.71	0.04	-2.25	0.05
SL 242.5	**242.5**	2.85	0.04	-1.58	0.05
SL 243	**243**	2.87	0.03	-1.93	0.04
SL 243.5	**243.5**	1.90	0.05	-1.10	0.07
SL 244	**244**	2.81	0.05	-1.56	0.06

Sample (no.)	Height [m]	$\delta^{13}C$ [VPDB]	$\delta^{13}C$ [VPDB] s.d.	$\delta^{18}O$ [VPDB]	$\delta^{18}O$ [VPDB] s.d.
SL 244.5	**244.5**	2.80	0.03	-1.48	0.03
SL 245	**245**	2.79	0.03	-1.58	0.07
SL 245.5	**245.5**	2.68	0.03	-1.53	0.06
SL 246	**246**	2.08	0.04	-1.40	0.04
SL 246.5	**246.5**	1.47	0.03	-1.60	0.05
SL 247	**247**	1.60	0.05	-1.74	0.05
SL 247.5	**247.5**	2.92	0.03	-1.25	0.06
SL 248	**248**	2.09	0.02	-1.52	0.06
SL 248.5	**248.5**	1.96	0.03	-1.72	0.06
SL 249	**249**	3.63	0.04	-1.35	0.06
SL 249.5	**249.5**	3.43	0.02	-1.46	0.04
SL 250	**250**	3.40	0.04	-1.13	0.05
SL 250.5	**250.5**	3.21	0.04	-1.10	0.05
SL 251	**251**	3.38	0.02	-1.41	0.04
SL 251.5	**251.5**	3.16	0.04	-1.53	0.04
SL 252	**252**	3.28	0.02	-1.95	0.07
SL 252.5	**252.5**	2.12	0.04	-1.55	0.04
SL 253	**253**	1.85	0.02	-1.26	0.07
SL 253.5	**253.5**	1.86	0.02	-1.73	0.03
SL 254	**254**	1.17	0.03	-1.08	0.06
SL 254.5	**254.5**	1.50	0.10	-1.36	0.07
SL 255	**255**	1.67	0.03	-1.26	0.04
SL 255.5	**255.5**	1.80	0.03	-1.33	0.06
SL 256	**256**	1.39	0.03	-1.31	0.04
SL 256.5	**256.5**	1.54	0.02	-0.65	0.03
SL 257	**257**	2.38	0.03	-1.35	0.04
SL 257.5	**257.5**	1.98	0.04	-0.97	0.05
SL 258	**258**	2.55	0.05	-1.64	0.04
SL 258.5	**258.5**	2.06	0.05	-1.27	0.03
SL 259.5	**259.5**	2.52	0.01	-1.02	0.05
SL 260.5	**260.5**	2.07	0.03	-1.33	0.04
SL 262	**262**	1.70	0.08	-1.37	0.04
SL 262.1	**262.1**	1.40	0.12	-1.25	0.05
SL 262.2	**262.2**	1.44	0.04	-1.05	0.07
SL 262.3	**262.3**	0.78	0.07	-1.01	0.07
SL 262.4	**262.4**	0.83	0.08	-1.09	0.09
SL 262.5	**262.5**	0.48	0.10	-1.83	0.06
SL 262.6	**262.6**	-0.21	0.04	-1.98	0.03
SL 262.7	**262.7**	0.78	0.03	-0.98	0.06
SL 262.8	**262.8**	0.54	0.09	-1.04	0.06
SL 262.9	**262.9**	0.79	0.07	-1.03	0.03
SL 263	**263**	0.70	0.03	-1.13	0.09
SL 263.1	**263.1**	-1.29	0.05	-1.80	0.05
SL 263.2	**263.2**	1.10	0.04	-0.76	0.04
SL 263.3	**263.3**	1.19	0.04	-1.21	0.06
SL 263.4	**263.4**	1.38	0.07	-1.00	0.06
SL 263.5	**263.5**	1.18	0.05	-0.89	0.04
SL 263.6	**263.6**	1.32	0.08	-1.27	0.02
SL 263.7	**263.7**	1.53	0.07	-0.84	0.05
SL 263.8	**263.8**	1.58	0.05	-0.89	0.05
SL 263.9	**263.9**	1.70	0.04	-0.72	0.06
SL 264	**264**	1.37	0.02	-0.59	0.05
SL 264	**264**	1.78	0.02	-1.12	0.06
SL 264.1	**264.1**	1.80	0.05	-1.10	0.07
SL 264.2	**264.2**	2.01	0.07	-0.82	0.07
SL 264.3	**264.3**	2.06	0.03	-1.18	0.03
SL 264.4	**264.4**	2.42	0.04	-0.75	0.07
SL 264.5	**264.5**	1.69	0.04	-1.39	0.08
SL 265	**265**	0.08	0.02	-1.51	0.09
SL 265.5	**265.5**	3.41	0.03	-1.12	0.05
SL 266	**266**	1.71	0.05	-0.93	0.06
SL 266.5	**266.5**	2.45	0.05	-1.16	0.07
SL 267	**267**	2.43	0.06	-1.12	0.04
SL 267.5	**267.5**	4.11	0.03	-1.11	0.03
SL 268	**268**	3.32	0.05	-1.82	0.06
SL 268.5	**268.5**	3.68	0.03	-1.87	0.07
SL 269	**269**	4.06	0.04	-1.56	0.05
SL 269.5	**269.5**	3.60	0.03	-1.31	0.07
SL 270	**270**	4.00	0.05	-1.10	0.06
SL 270.5	**270.5**	3.99	0.06	-1.15	0.08
SL 271	**271**	3.72	0.03	-1.33	0.07
SL 271.5	**271.5**	3.67	0.05	-1.51	0.06
SL 272	**272**	2.22	0.03	-2.14	0.06
SL 272.5	**272.5**	3.18	0.05	-1.79	0.04
SL 273.5	**273.5**	3.04	0.03	-1.39	0.04
SL 274	**274**	3.83	0.06	-1.44	0.08
SL 274.5	**274.5**	3.59	0.05	-0.79	0.05
SL 275	**275**	3.73	0.03	-1.42	0.03
SL 275.5	**275.5**	3.53	0.03	-1.39	0.06
SL 276	**276**	3.84	0.04	-1.16	0.06
SL 276.5	**276.5**	3.52	0.04	-0.78	0.05
SL 277	**277**	3.06	0.03	-1.21	0.04
SL 277.5	**277.5**	3.56	0.03	-1.24	0.06
SL 278	**278**	3.47	0.03	-1.19	0.06
SL 278.5	**278.5**	3.50	0.05	-1.18	0.10
SL 279	**279**	3.38	0.03	-1.21	0.07
SL 280	**280**	3.31	0.06	-1.40	0.05
SL 280.5	**280.5**	3.98	0.03	-1.09	0.05
SL 281	**281**	3.52	0.04	-1.34	0.10
SL 281.2	**281.2**	3.49	0.03	-1.21	0.09
SL 281.5	**281.5**	3.39	0.03	-1.03	0.05
SL 282	**282**	2.89	0.06	-4.88	0.12
SL 282.5	**282.5**	3.73	0.03	-1.41	0.08
SL 283	**283**	3.81	0.04	-1.40	0.06

Sample (no.)	Height [m]	δ^{13}C [VPDB]	δ^{13}C [VPDB] s.d.	δ^{18}O [VPDB]	δ^{18}O [VPDB] s.d.
SL 283.5	**283.5**	3.92	0.02	-1.16	0.03
SL 284	**284**	3.96	0.03	-1.46	0.07
SL 284.5	**284.5**	4.05	0.03	-1.61	0.05
SL 285	**285**	3.87	0.03	-1.36	0.06
SL 285.5	**285.5**	3.67	0.02	-1.45	0.04
SL 286	**286**	3.46	0.03	-1.55	0.06
SL 286.5	**286.5**	3.72	0.05	-1.35	0.05
SL 287	**287**	4.14	0.02	-1.40	0.04
SL 287.5	**287.5**	3.51	0.03	-1.31	0.07
SL 288	**288**	3.87	0.04	-1.51	0.05
SL 288.5	**288.5**	3.20	0.06	-1.53	0.05
SL 289	**289**	3.59	0.03	-1.38	0.06
SL 289.5	**289.5**	3.63	0.03	-1.41	0.08
SL 290	**290**	2.93	0.04	-2.17	0.08
SL 291	**291**	2.86	0.02	-1.87	0.07
SL 291.5	**291.5**	3.15	0.04	-2.02	0.06
SL 292	**292**	3.29	0.03	-1.98	0.07
SL 292.5	**292.5**	3.45	0.03	-1.91	0.03
SL 293	**293**	3.13	0.04	-1.43	0.05
SL 293.5	**293.5**	2.98	0.03	-1.92	0.09
SL 294	**294**	2.99	0.04	-3.00	0.06
SL 294	**294**	3.53	0.04	-2.19	0.03
SL 294.5	**294.5**	4.34	0.03	-1.81	0.05
SL 295	**295**	2.88	0.02	-1.44	0.06
SL 295.5	**295.5**	2.94	0.05	-1.59	0.05
SL 296	**296**	2.36	0.03	-1.40	0.05
SL 296.5	**296.5**	2.75	0.03	-1.73	0.07
SL 297	**297**	2.52	0.04	-1.60	0.05
SL 297.5	**297.5**	2.44	0.04	-2.10	0.03
SL 298	**298**	3.40	0.02	-1.16	0.06
SL 298.5	**298.5**	3.53	0.02	-1.49	0.05
SL 299	**299**	3.31	0.06	-0.94	0.06
SL 300	**300**	3.61	0.03	-1.34	0.03
SL 300.5	**300.5**	2.76	0.05	-1.62	0.04
SL 301	**301**	3.29	0.03	-1.33	0.04
SL 301.5	**301.5**	3.09	0.02	-1.57	0.04
SL 302	**302**	3.18	0.05	-1.88	0.03
SL 302.5	**302.5**	3.34	0.05	-1.82	0.03
SL 304	**304**	2.90	0.04	-1.65	0.06
SL 304.5	**304.5**	3.12	0.03	-1.51	0.04
SL 305	**305**	3.03	0.04	-1.30	0.06
SL 305.5	**305.5**	3.22	0.04	-1.63	0.05
SL 306	**306**	3.30	0.05	-1.56	0.03
SL 306.5	**306.5**	3.23	0.05	-1.79	0.05
SL 307	**307**	3.11	0.03	-2.26	0.02
SL307.5	**307.5**	2.65	0.04	-1.84	0.03
SL 308	**308**	2.89	0.03	-2.36	0.05
SL 308.5	**308.5**	4.12	0.03	-1.31	0.07
SL 309	**309**	4.30	0.03	-1.44	0.05
SL 309.5	**309.5**	4.07	0.03	-1.51	0.06
SL 310	**310**	3.90	0.04	-1.73	0.08
SL310.5	**310.5**	3.80	0.05	-1.93	0.06
SL 311	**311**	4.46	0.04	-1.72	0.06
SL 312	**312**	3.97	0.02	-1.90	0.08
SL 312	**312**	4.14	0.03	-2.24	0.05
SL 313	**313**	4.22	0.04	-1.90	0.06
SL 313.5	**313.5**	3.91	0.03	-1.62	0.07
SL 314	**314**	4.17	0.04	-1.63	0.06
SL 314.5	**314.5**	3.98	0.07	-1.79	0.05
SL 315	**315**	4.29	0.03	-2.30	0.02
SL 315.5	**315.5**	3.93	0.03	-1.46	0.07
SL 316	**316**	3.59	0.04	-1.88	0.04
SL 316.5	**316.5**	3.93	0.02	-1.65	0.06
SL 317	**317**	3.57	0.04	-1.78	0.05
SL 317.5	**317.5**	2.95	0.05	-1.96	0.07
SL 318	**318**	3.32	0.03	-1.67	0.04
SL 318.5	**318.5**	3.34	0.06	-1.88	0.05
SL 319	**319**	2.13	0.03	-2.54	0.04
SL 319.5	**319.5**	4.09	0.02	-1.89	0.07
SL 320a	**320**	3.69	0.06	-1.47	0.04
SL 320.5	**320.5**	3.96	0.03	-1.57	0.03
SL 321	**321**	4.26	0.03	-1.34	0.05
SL 321.5	**321.5**	4.14	0.03	-1.58	0.06
SL 322a	**322**	4.19	0.09	-1.77	0.15
SL 322.5	**322.5**	4.30	0.04	-1.68	0.03
SL 323a	**323**	3.69	0.03	-1.40	0.03
SL 323.5	**323.5**	3.86	0.03	-1.94	0.06
SL 324	**324**	4.40	0.02	-1.44	0.06
SL 324.5	**324.5**	4.25	0.05	-1.91	0.07
SL 325.5	**325.5**	4.36	0.02	-1.48	0.04
SL 326	**326**	3.80	0.03	-1.29	0.06
SL 327	**327**	4.10	0.02	-1.43	0.05
SL 327.5	**327.5**	3.97	0.03	-1.97	0.04
SL 328	**328**	4.15	0.04	-1.71	0.06
SL 328.5	**328.5**	3.97	0.05	-1.63	0.05
SL 329	**329**	4.33	0.04	-1.82	0.08
SL 329.5	**329.5**	3.88	0.03	-2.14	0.02
SL 330	**330**	4.12	0.04	-1.65	0.03
SL 330.5	**330.5**	3.82	0.02	-2.16	0.05
SL 331.5	**331.5**	4.13	0.03	-1.66	0.04
SL 333	**333**	3.67	0.03	-1.25	0.05
SL 333.5	**333.5**	4.08	0.06	-1.58	0.06
SL 334	**334**	3.88	0.02	-1.94	0.05
SL 334.5	**334.5**	4.15	0.03	-1.85	0.05

Sample (no.)	Height [m]	$\delta^{13}C$ [VPDB]	$\delta^{13}C$ [VPDB] s.d.	$\delta^{18}O$ [VPDB]	$\delta^{18}O$ [VPDB] s.d.
SL 335a	**335**	3.96	0.04	-2.19	0.06
SL 335.5a	**335.5**	3.45	0.05	-1.78	0.07
SL 336	**336**	3.82	0.04	-1.59	0.04
SL 336.5	**336.5**	3.49	0.04	-1.33	0.06
SL 337	**337**	3.57	0.04	-1.92	0.06
SL 337.5	**337.5**	3.66	0.02	-1.57	0.06
SL 338a	**338**	2.94	0.04	-1.79	0.06
SL 338.5a	**338.5**	3.25	0.05	-1.69	0.05
SL 339	**339**	3.41	0.05	-1.81	0.05
SL 339.5	**339.5**	3.36	0.05	-1.41	0.07
SL 340	**340**	3.27	0.06	-1.34	0.07
SL2-0	**340**	1.96	0.03	-1.88	0.05
SL2-0.5	**340.5**	1.91	0.03	-1.48	0.06
SL2-1	**341**	2.14	0.05	-1.40	0.07
SL2-1.5	**341.5**	2.43	0.05	-1.70	0.04
SL2-2	**342**	1.86	0.04	-1.48	0.04
SL2-2.5	**342.5**	1.98	0.04	-1.22	0.04
SL2-3	**343**	1.88	0.05	-1.44	0.05
SL2-3.5	**343.5**	1.97	0.04	-1.16	0.08
SL2-4	**344**	2.09	0.03	-1.46	0.06
SL2-4.5	**344.5**	2.05	0.03	-0.91	0.04
SL2-5a	**345**	2.41	0.03	-1.06	0.05
SL2-5.5	**345.5**	2.42	0.04	-1.11	0.07
SL2-6	**346**	2.76	0.02	-1.11	0.04
SL2-6.5	**346.5**	2.95	0.04	-1.02	0.04
SL2-7	**347**	2.92	0.05	-1.36	0.06
SL2-7.5	**347.5**	2.94	0.03	-1.21	0.03
SL2-8	**348**	2.90	0.04	-1.10	0.06
SL2-8.5	**348.5**	2.49	0.04	-1.40	0.06
SL2-9	**349**	3.02	0.04	-1.43	0.03
SL2-9.5	**349.5**	2.94	0.04	-1.46	0.07
SL2-10a	**350**	2.66	0.03	-0.99	0.04
SL2-10.5	**350.5**	2.67	0.03	-1.47	0.07
SL2-11	**351**	2.48	0.04	-1.60	0.08
SL2-11.5	**351.5**	2.08	0.05	-1.09	0.07
SL2-12	**352**	1.50	0.04	-1.03	0.05
SL2-12.5	**352.5**	1.81	0.05	-1.18	0.07
SL2-13	**353**	1.91	0.04	-1.06	0.06
SL2-13.5	**353.5**	1.91	0.04	-1.18	0.07
SL2-14	**354**	2.03	0.06	-1.43	0.09
SL2-14.5	**354.5**	1.74	0.07	-1.06	0.07
SL2-15	**355**	2.14	0.02	-0.69	0.03
SL2-15.5	**355.5**	2.86	0.03	-1.34	0.05
SL2-16a	**356**	2.65	0.03	-1.43	0.08
SL2-16.5	**356.5**	2.51	0.05	-1.25	0.05
SL2-17	**357**	2.85	0.04	-1.15	0.04
SL2-17.5	**357.5**	2.74	0.05	-1.48	0.08
SL2-18	**358**	2.62	0.03	-1.28	0.03
SL2-18.5	**358.5**	2.54	0.06	-1.30	0.07
SL2-19	**359**	2.44	0.04	-1.18	0.06
SL2-19.5	**359.5**	2.04	0.03	-1.46	0.05
SL2-20	**360**	2.67	0.05	-1.28	0.04
SL2-20.5	**360.5**	2.79	0.04	-1.34	0.06
SL2-21	**361**	2.54	0.04	-1.57	0.05
SL2-21.5	**361.5**	2.01	0.03	-1.24	0.09
SL2-22	**362**	2.02	0.04	-1.09	0.06
SL2-22.5	**362.5**	1.63	0.03	-1.85	0.03
SL2-23	**363**	2.21	0.03	-1.60	0.04
SL2-23.5	**363.5**	1.78	0.04	-1.28	0.04
SL2-24	**364**	2.29	0.05	-1.25	0.04
SL2-24.5	**364.5**	1.12	0.05	-1.94	0.06
SL2-25	**365**	2.46	0.04	-1.43	0.07
SL2-25.5	**365.5**	2.32	0.04	-1.17	0.04
SL2-26	**366**	2.04	0.03	-1.52	0.04
SL2-26.5	**366.5**	2.38	0.03	-1.15	0.06
SL2-27	**367**	2.29	0.05	-1.65	0.05
SL2-27.5	**367.5**	2.32	0.03	-1.19	0.06
SL2-28a	**368**	2.08	0.03	-1.40	0.06
SL2-28.5	**368.5**	2.12	0.02	-1.67	0.04
SL2-29	**369**	2.79	0.03	-1.15	0.06
SL2-29.5	**369.5**	2.54	0.03	-1.08	0.04
SL2-30.5	**370.5**	2.71	0.03	-1.77	0.06
SL2-31	**371**	2.89	0.04	-1.51	0.08
SL2-32	**372**	2.14	0.04	-1.26	0.05
SL2-32.5	**372.5**	2.32	0.06	-1.51	0.03
SL2-33.5	**373.5**	2.53	0.07	-2.14	0.08
SL2-34	**374**	2.47	0.03	-1.86	0.05
SL2-35	**375**	2.21	0.04	-1.49	0.06
SL2-35.5	**375.5**	2.41	0.04	-1.74	0.04
SL2-36.5	**376.5**	2.92	0.07	-2.38	0.06
SL2-37	**377**	2.81	0.03	-1.49	0.07
SL2-38	**378**	2.40	0.04	-1.41	0.07
SL2-38.5	**378.5**	2.06	0.04	-1.90	0.08
SL2-39.5	**379.5**	1.25	0.02	-1.32	0.05
SL2-41	**381**	1.83	0.04	-1.27	0.08
SL2-41.5	**381.5**	2.02	0.05	-1.38	0.05
SL2-42.5	**382.5**	1.57	0.05	-1.52	0.03
SL2-43	**383**	1.82	0.03	-1.39	0.06
SL2-44	**384**	1.94	0.02	-1.42	0.06
SL2-44.5	**384.5**	1.96	0.04	-1.37	0.06
SL2-45.5	**385.5**	2.28	0.05	-1.73	0.05
SL2-46	**386**	2.14	0.02	-1.30	0.05
SL2-47	**387**	1.58	0.03	-1.17	0.05
SL2-47.5	**387.5**	1.80	0.06	-1.16	0.06

Sample (no.)	Height [m]	$\delta^{13}C$ [VPDB]	$\delta^{13}C$ [VPDB] s.d.	$\delta^{18}O$ [VPDB]	$\delta^{18}O$ [VPDB] s.d.
SL2-48.5	**388.5**	1.65	0.03	-1.16	0.08
SL2-49	**389**	1.64	0.03	-1.51	0.04
SL2-49.2	**389.2**	1.35	0.06	-1.31	0.07
SL2-50	**390**	1.95	0.06	-1.36	0.07
SL2-50.5	**390.5**	2.05	0.05	-1.36	0.06
SL2-51.5	**391.5**	2.11	0.06	-1.24	0.08
SL2-52	**392**	1.99	0.05	-1.61	0.04
SL2-53	**393**	2.40	0.04	-1.40	0.06
SL2-53.5	**393.5**	2.23	0.05	-2.06	0.04
SL2-54	**394**	2.34	0.06	-1.57	0.05
SL2-55	**395**	2.31	0.04	-1.81	0.03
SL2-56	**396**	2.36	0.05	-1.60	0.08
SL2-56.5	**396.5**	1.98	0.03	-1.54	0.04
SL2-57.5	**397.5**	2.04	0.04	-1.63	0.06
SL2-58	**398**	2.33	0.06	-1.45	0.09
SL2-59	**399**	2.57	0.04	-1.48	0.08
SL2-59.5	**399.5**	2.83	0.03	-1.45	0.04
SL2-60.5	**400.5**	2.57	0.07	-1.69	0.10
SL2-61	**401**	2.50	0.04	-1.86	0.06
SL2-62	**402**	2.73	0.07	-1.81	0.07
SL2-62.5	**402.5**	2.38	0.06	-1.66	0.06
SL2-63.5	**403.5**	2.37	0.03	-1.21	0.08
SL2-64	**404**	2.66	0.03	-1.44	0.05
SL2-65	**405**	1.30	0.05	-1.63	0.04
SL2-65.5	**405.5**	2.45	0.04	-1.39	0.07
SL2-66.5	**406.5**	2.67	0.02	-1.62	0.04
SL2-67	**407**	2.73	0.05	-1.65	0.06
SL2-68	**408**	2.76	0.04	-1.61	0.06
SL2-68.5	**408.5**	2.05	0.03	-1.24	0.06
SL2-69.5	**409.5**	2.10	0.04	-1.69	0.05
SL2-70	**410**	2.83	0.03	-1.75	0.06
SL2-71	**411**	2.79	0.03	-1.72	0.07
SL2-71.5	**411.5**	2.68	0.04	-1.71	0.04
SL2-72.5	**412.5**	2.73	0.03	-1.51	0.07
SL2-73	**413**	2.40	0.05	-1.70	0.06
SL2-74	**414**	2.51	0.04	-1.88	0.07
SL2-74.5	**414.5**	2.54	0.03	-1.80	0.05
SL2-75.5	**415.5**	2.90	0.02	-1.10	0.03
SL2-76	**416**	2.61	0.03	-1.67	0.05
SL2-77	**417**	2.95	0.03	-1.54	0.05
SL2-77.5	**417.5**	2.72	0.06	-1.70	0.05
SL2-78.5	**418.5**	2.79	0.04	-1.66	0.05
SL2-79	**419**	2.74	0.06	-1.77	0.06
SL2-80	**420**	2.73	0.03	-2.07	0.08
SL2-80.5	**420.5**	2.60	0.06	-1.98	0.07
SL2-81.5	**421.5**	2.54	0.03	-1.67	0.04
SL2-82	**422**	2.30	0.03	-2.16	0.04
SL2-83	**423**	2.23	0.04	-1.82	0.03
SL2-83.5	**423.5**	2.92	0.03	-1.50	0.06
SL2-84.5	**424.5**	2.86	0.03	-1.67	0.05
SL2-85	**425**	2.55	0.04	-1.90	0.05
SL2-86	**426**	2.94	0.04	-1.44	0.07
SL2-86.5	**426.5**	2.77	0.06	-1.66	0.06
SL2-87.5	**427.5**	2.27	0.05	-1.61	0.07
SL2-88	**428**	2.23	0.06	-1.56	0.08
SL2-89	**429**	2.72	0.04	-1.79	0.06
SL2-89.5	**429.5**	2.66	0.03	-2.12	0.03
SL2-90.5	**430.5**	2.59	0.03	-2.12	0.07
SL2-91	**431**	2.65	0.03	-1.99	0.05
SL2-92	**432**	2.50	0.04	-2.27	0.07
SL2-92.5	**432.5**	2.70	0.07	-2.02	0.06
SL2-93.5	**433.5**	2.22	0.07	-2.63	0.08
SL2-94	**434**	3.07	0.03	-1.61	0.04
SL2-95	**435**	3.02	0.05	-1.83	0.05
SL2-95.5	**435.5**	2.98	0.03	-1.99	0.05
SL2-96.5	**436.5**	2.43	0.04	-2.11	0.04
SL2-97	**437**	2.71	0.03	-2.08	0.06
SL2-98	**438**	2.40	0.05	-2.00	0.06
SL2-98.5	**438.5**	2.63	0.06	-1.86	0.05
SL2-99.5	**439.5**	2.32	0.04	-1.93	0.06
SL2-100	**440**	2.06	0.03	-2.14	0.04
SL2-101	**441**	2.10	0.02	-2.15	0.05
SL2-101.5	**441.5**	2.72	0.03	-1.79	0.06
SL2-102.5	**442.5**	2.84	0.02	-1.91	0.04
SL2-103	**443**	2.38	0.04	-1.87	0.05
SL2-103.5	**443.5**	1.51	0.02	-1.36	0.06
SL2-104	**444**	2.81	0.04	-2.00	0.04
SL2-105.5	**445.5**	2.91	0.03	-1.88	0.06
SL2-106	**446**	2.70	0.07	-1.87	0.10
SL2-107	**447**	2.40	0.05	-1.91	0.07
SL2-107.5	**447.5**	2.03	0.06	-2.34	0.11
SL2-108.5	**448.5**	2.25	0.06	-1.98	0.17
SL2-110.5	**450.5**	2.88	0.07	-2.13	0.12
SL2-111.5	**451.5**	2.45	0.06	-2.16	0.07
SL2-113	**453**	1.81	0.08	-0.44	0.11
SL2-113.5	**453.5**	2.56	0.08	-2.24	0.06
SL2-114.5	**454.5**	2.37	0.07	-2.14	0.09
SL2-115	**455**	2.87	0.05	-2.12	0.08
SL2-116	**456**	2.67	0.03	-1.65	0.08
SL2-116.5	**456.5**	2.36	0.04	-1.68	0.06
SL2-117.5	**457.5**	0.53	0.04	-2.12	0.04
SL2-118	**458**	2.71	0.04	-1.68	0.04
SL2-119	**459**	1.86	0.07	-0.81	0.08
SL2-119.5	**459.5**	1.84	0.06	-1.77	0.04

Sample (no.)	Height [m]	$\delta^{13}C$ [VPDB]	$\delta^{13}C$ [VPDB] s.d.	$\delta^{18}O$ [VPDB]	$\delta^{18}O$ [VPDB] s.d.
SL2-120.5	**460.5**	1.98	0.04	-2.11	0.04
SL2-121	**461**	1.99	0.04	-1.85	0.05
SL2-122	**462**	2.18	0.07	-1.65	0.08
SL2-122.5	**462.5**	2.15	0.05	-1.86	0.06
SL2-124	**464**	1.41	0.04	-1.61	0.06
SL2-125	**465**	2.22	0.03	-1.90	0.05
SL2-127	**467**	2.39	0.09	-1.77	0.08
SL2-128.5	**468.5**	1.96	0.09	-1.29	0.13
SL2-129.5	**469.5**	1.67	0.05	-2.12	0.08
SL2-130	**470**	1.68	0.06	-1.96	0.06
SL2-131	**471**	1.42	0.04	-1.86	0.04
SL2-131.5	**471.5**	1.60	0.03	-2.18	0.08
SL2-132.5	**472.5**	1.58	0.05	-2.15	0.08
SL2-133	**473**	2.04	0.05	-2.01	0.09
SL2-134	**474**	1.60	0.05	-2.11	0.09
SL2-134.5	**474.5**	2.02	0.02	-1.65	0.07
SL2-135.5	**475.5**	2.30	0.03	-1.68	0.06
SL2-136	**476**	1.97	0.07	-1.82	0.08
SL2-137	**477**	2.38	0.04	-1.71	0.05
SL2-137.5	**477.5**	1.91	0.04	-1.78	0.06
SL2-138.5	**478.5**	2.31	0.04	-1.85	0.04
SL2-139	**479**	2.10	0.06	-1.92	0.08
SL2-140	**480**	2.12	0.05	-1.89	0.07
SL2-140.5	**480.5**	2.15	0.02	-1.91	0.03
SL2-141.5	**481.5**	1.45	0.05	-2.01	0.04
SL2-142	**482**	1.34	0.03	-2.33	0.05
SL2-143	**483**	2.07	0.03	-1.51	0.06
SL2-143.5	**483.5**	1.83	0.03	-2.27	0.05
SL2-144.5	**484.5**	2.14	0.02	-2.20	0.06
SL2-145	**485**	1.79	0.04	-2.11	0.04
SL2-146	**486**	2.10	0.03	-1.84	0.05
SL2-146.5	**486.5**	1.17	0.03	-2.12	0.02
SL2-147.5	**487.5**	1.37	0.04	-2.32	0.06
SL2-148	**488**	0.81	0.03	-2.12	0.05
SL2-149	**489**	0.92	0.03	-2.12	0.07
SL2-149.5	**489.5**	0.47	0.05	-2.27	0.09
SL2-152	**492**	1.27	0.04	-2.06	0.05
SL2-154	**494**	1.14	0.04	-2.46	0.06
SL2-156	**496**	1.94	0.06	-1.60	0.04
SL2-158	**498**	1.82	0.04	-1.99	0.06
SL2-159	**499**	0.29	0.03	-2.34	0.07
SL2-160	**500**	2.14	0.05	-1.98	0.05
SL2-162	**502**	0.52	0.04	-1.86	0.06
SL2-163	**503**	0.03	0.04	-2.13	0.05
SL2-164	**504**	0.02	0.04	-2.20	0.04
SL2-165	**505**	1.20	0.07	-2.48	0.07
SL2-166	**506**	-0.17	0.03	-2.20	0.03
SL2.2-1	**507**	0.19	0.04	-2.38	0.04
SL2.2-2	**508**	-0.92	0.06	-2.41	0.04
SL2.2-3	**509**	-3.63	0.04	-4.52	0.04
SL2.2-4	**510**	0.20	0.03	-2.22	0.07
SL2.2-5	**511**	-0.86	0.04	-2.44	0.05
SL2.2-6	**512**	0.85	0.06	-2.20	0.04
SL2.2-7	**513**	0.04	0.05	-1.88	0.06
SL2.2-8	**514**	0.37	0.06	-2.33	0.04
SL2.2-9	**515**	-1.71	0.03	-3.17	0.05
SL2.2-10	**516**	-1.61	0.02	-2.95	0.07
SL2.2-11	**517**	-2.20	0.06	-3.10	0.03
SL2.2-12	**518**	1.21	0.06	-1.42	0.06
SL2.2-13	**519**	0.64	0.04	-2.21	0.07
SL2.2-14	**520**	1.47	0.09	-1.80	0.02
SL2.2-15	**521**	0.90	0.06	-1.83	0.04
SL2.2-16	**522**	1.64	0.04	-2.14	0.04
SL2.2-17	**523**	1.50	0.05	-2.07	0.05
SL2.2-18	**524**	1.14	0.11	-2.11	0.07
SL2.2-19	**525**	0.51	0.03	-2.60	0.05
SL2.2-20	**526**	1.69	0.06	-2.19	0.07
SL2.2-21	**527**	-1.10	0.05	-3.40	0.04
SL2.2-22	**528**	1.10	0.06	-2.52	0.03
SL2.2-23	**529**	1.45	0.03	-2.68	0.05
SL2.2-24	**530**	0.91	0.05	-2.35	0.04
SL2.2-25	**531**	1.12	0.05	-2.00	0.04
SL2.2-26	**532**	-0.47	0.04	-1.59	0.07
SL2.2-27	**533**	1.14	0.09	-2.02	0.05
SL2.2-28	**534**	0.07	0.06	-2.96	0.05
SL2.2-29	**535**	-0.06	0.07	-2.82	0.06
SL2.2-30	**536**	1.06	0.05	-2.67	0.04
SL2.2-31	**537**	1.58	0.04	-2.10	0.05
SL2.2-32	**538**	1.37	0.08	-1.93	0.05
SL2.2-33	**539**	1.88	0.03	-1.99	0.06
SL2.2-34	**540**	1.82	0.03	-2.24	0.05
SL2.2-35	**541**	1.54	0.06	-2.87	0.04
SL2.2-36	**542**	0.15	0.06	-2.80	0.04
SL2.2-37	**543**	-2.16	0.06	-3.30	0.03
SL2.2-38	**544**	0.23	0.05	-2.24	0.02
SL2.2-39	**545**	1.00	0.04	-1.77	0.03
SL2.2-40	**546**	1.23	0.04	-1.46	0.07
SL2.2-41	**547**	0.71	0.04	-2.64	0.03
SL2.2-42	**548**	0.21	0.06	-3.30	0.06
SL2.2-43	**549**	0.88	0.05	-3.12	0.06
SL2.2-44	**550**	1.25	0.05	-2.68	0.03
SL2.2-45	**551**	1.11	0.04	-2.71	0.05
SL2.2-46	**552**	1.84	0.04	-2.13	0.04
SL2.2-47	**553**	1.75	0.04	-1.65	0.04

Sample (no.)	Height [m]	$\delta^{13}C$ [VPDB]	$\delta^{13}C$ [VPDB] s.d.	$\delta^{18}O$ [VPDB]	$\delta^{18}O$ [VPDB] s.d.
SL2.2-48	**554**	1.55	0.08	-0.96	0.05
SL2.2-49	**555**	-0.54	0.05	-2.52	0.04
SL2.2-71	**578**	-1.13	0.02	-3.46	0.07
SL2.2-72	**579**	-0.24	0.05	-2.99	0.04
SL2.2-73	**580**	0.93	0.02	-2.93	0.07
SL2.2-74	**581**	0.08	0.06	-3.11	0.02
SL2.2-75	**582**	-2.14	0.06	-2.05	0.04
SL2.2-76	**583**	0.14	0.03	-3.15	0.06
SL2.2-77	**584**	0.23	0.04	-2.73	0.05
SL2.2-78	**585**	-2.97	0.06	-3.66	0.05
SL2.2-79	**586**	-1.40	0.07	-3.20	0.02

Sample (no.)	Height [m]	$\delta^{13}C$ [VPDB]	$\delta^{13}C$ [VPDB] s.d.	$\delta^{18}O$ [VPDB]	$\delta^{18}O$ [VPDB] s.d.
SL2.2-80	**587**	-2.88	0.04	-4.04	0.03
SL2.2-81	**588**	1.12	0.05	-2.42	0.07
SL2.2-82	**589**	1.69	0.07	-1.79	0.03
SL2.2-83	**590**	1.35	0.04	-2.60	0.06
SL2.2-84	**591**	0.57	0.03	-2.20	0.06
SL2.2-85	**592**	2.06	0.08	-1.89	0.05
SL2.2-86	**593**	0.82	0.07	-2.23	0.04
SL2.2-87	**594**	0.90	0.04	-2.74	0.06
SL2.2-88	**595**	2.16	0.03	-2.57	0.07
SL2.2-89	**596**	2.25	0.05	-2.06	0.04
SL2.2-90	**597**	1.98	0.05	-2.37	0.04

CARBON AND OXYGEN ISOTOPES OF LOW-MG-CALCITE SHELLS, SANTA LUCIA SECTION

Sample (no.)	Height [m]	$\delta^{13}C$ [VPDB]	$\delta^{18}O$ [VPDB]
SL 28.4 R	**28.4**	3.66	-3.46
SL 69 R	**69**	2.18	-2.89
SL 92 R	**92**	1.84	-2.11
SL 251.5 R	**251.5**	2.51	-2.52
SL 267.5 Chon	**267.5**	5.03	-0.98
SL 271 R	**271**	5.11	-0.31
SL 280 Chon	**280**	3.88	-1.62
SL 323 R	**323**	3.22	-3.09
SL2 49 R	**389**	2.14	-1.63

Sample (no.)	Height [m]	$\delta^{13}C$ [VPDB]	$\delta^{18}O$ [VPDB]
SL2 79 R	**419**	1.66	-3.58
SL2 93.5-1 R	**433.5**	2.60	-2.27
SL2 93.5-2 R	**433.5**	2.88	-2.18
SL2 93.5-3 R	**433.5**	2.95	-1.97
SL2 96.5 R	**436.5**	2.45	-3.27
SL2 97 R	**437**	2.01	-3.35
SL2 103.3 Chon	**443.3**	3.70	-1.70
SL2 103.5 R	**443.5**	3.29	-3.25
SL2 140 R	**480**	0.83	-2.82

R	unclassified rudist shell
Chon	chondrodont shell

C-AND O-ISOTOPES OF LOW-MG-CALCITE SHELLS AND BULK CARBONATE, SANTA LUCIA SECTION

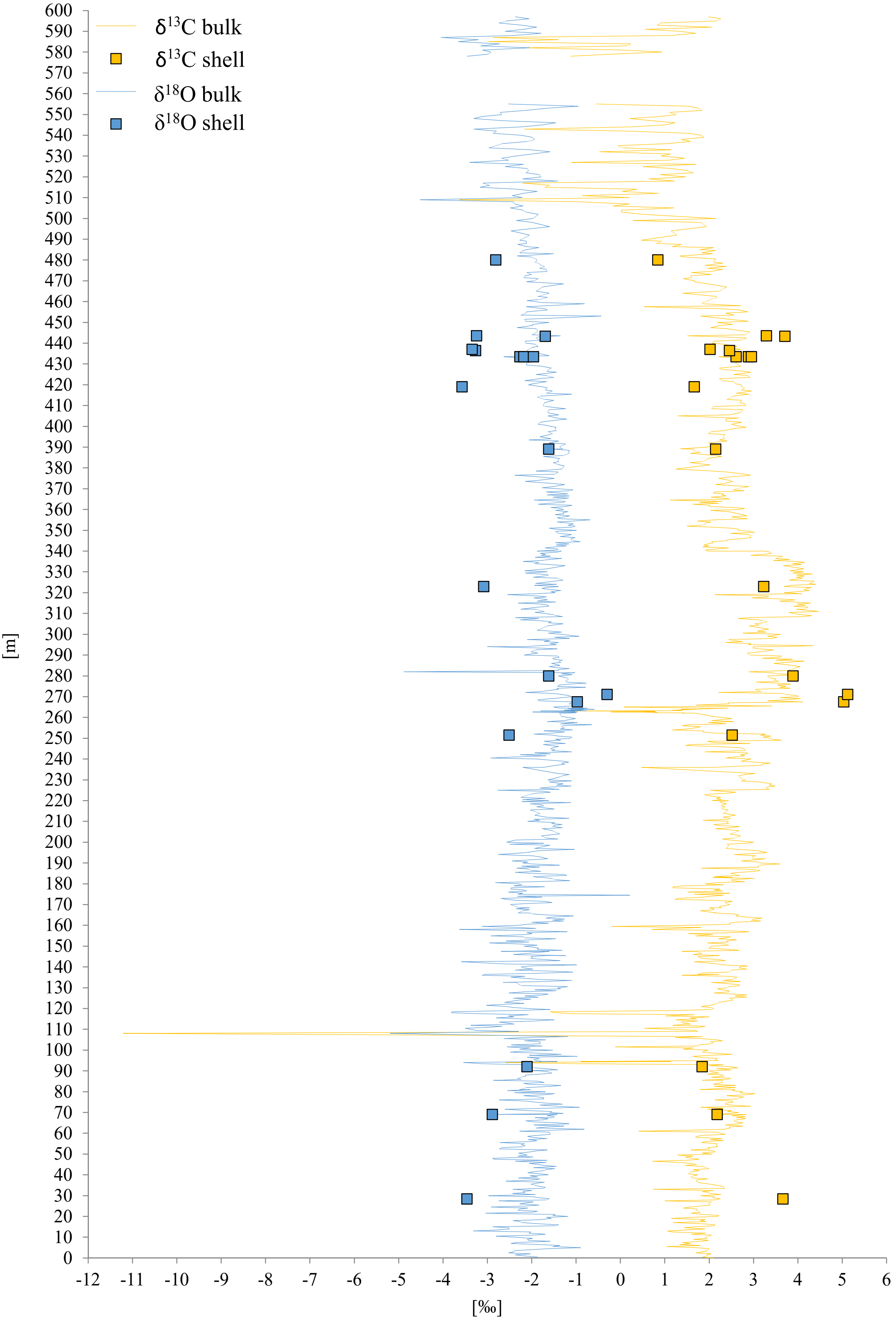

TRACE ELEMENT RESULTS OF RUDIST AND CEMENTS, SANTA LUCIA SECTION

Sample (no.)	Lab #	Height [m]	Ca [ppm]	Mg [ppm]	Sr [ppm]	Fe [ppm]	Mn [ppm]	Ba [ppm]
SL 1.5 Cem	ICP-40	**1.5**	388700	3273	100	70	6.6	0.4
SL 28.4 B	SR 1	**28.4**	406350	2080	923	12	0.7	0.5
SL 39 Cem	ICP-41	**39**	396390	2831	111	53	9.0	0.1
SL 46.5 Cem	ICP-42	**46.5**	389180	3458	134	269	13.0	1.7
SL 69	SR 47	**69**	392670	3575	929	6	2.1	0.4
SL 92 B	SR 2	**92**	409250	2164	1095	15	3.1	1.7
SL 99 Cem	ICP-43	**99**	398020	2286	88	33	9.7	-0.2
SL103.3 Chon	SR 49	**103.3**	394130	3244	492	46	2.8	2.3
SL 126 Cem	ICP-44	**126**	395560	3299	108	78	14.0	0.3
SL 153 Cem	ICP-45	**153**	397310	3485	120	69	5.1	0.4
SL 159 Cem	ICP-46	**159**	395230	3632	149	28	17.2	0.3
SL 178.5 Cem	ICP-47	**178.5**	397370	2558	226	19	14.3	0.3
SL 189 Cem	ICP-48	**189**	401360	2992	93	65	47.1	0.8
SL 214 Cem	ICP-49	**214**	403370	2165	91	11	8.7	-0.3
SL 242.5 R	C 1	**242.5**	396900	1343	1038.0	3.9	1.3	0.3
SL 251.5 B	SR 3	**251.5**	407700	1324	867	5	1.8	0.1
SL 267.5 B	SR 4	**267.5**	406880	2915	679	7	1.3	0.9
SL 271 B	SR 5	**271**	405170	2928	559	5	1.9	0.6
SL280 Chon	SR 48	**280**	395760	2908	435	44	3.0	0.8
SL 297.5 Cem	ICP-50	**297.5**	386240	3501	298	666	6.6	6.6
SL 323 B	SR 6	**323**	406500	836	1072	3	0.5	0.1
SL 324 Cem	ICP-51	**324**	394850	3345	147	29	2.6	1.1
SL2 1.2 R	C 3	**341.2**	397070	1296	1149.0	2.8	1.4	0.4
SL2 13.8 R	C 4	**353.8**	398310	2024	994.3	10.0	1.9	0.6
SL2 25.5 Chon	C 5	**365.5**	396160	2723	768.9	5.2	2.2	1.0
SL2 38.2 R	C 6	**378.5**	398690	1333	1048	1.8	0.1	0.2
SL2 49	SR 14	**389**	404220	2978	276	38	5.0	0.7
SL2 79a	SR 15	**419**	406460	2377	1610	4	0.4	0.9
SL2 93.51-1	SR 7	**433.5**	405470	2607	498	6	1.3	1.5
SL2 93.5a-2	SR 8	**433.5**	405550	3243	590	9	1.4	2.2
SL2 93.5a-3	SR 9	**433.5**	404430	2959	484	5	1.4	1.8
SL2 96.5	SR 10	**436.5**	401610	3189	1093	4	1.0	0.6
SL2 97	SR 11	**437**	404540	1644	1326	4	0.3	0.4
SL2 103.5	SR 12	**443.5**	400960	2482	1173	3	3.1	0.5
SL2 140	SR 13	**480**	403410	3876	610	11	1.4	3.2
SL 517 R (bx)	C 8	**517**	397340	2076	1309	7.3	1.0	1.4

R	unclassified rudist shell
Chon	chondrodont shell
Cem	cement
B	unclassified Bivalve

STRONTIUM ISOTOPE VALUES, SANTA LUCIA SECTION

Sample (no.)	**Lab #**	**Height [m]**	**^{87}Sr/^{86}Sr measured**	**± 2 σ mean**	**^{87}Sr/^{86}Sr** sample corrected to difference: NBS 987 value McArthur and NBS 987 measured with sample	**^{87}Sr/^{86}Sr** sample corrected to difference: USGS EN-1 value McArthur and USGS EN-1 measured with sample	**^{87}Sr/^{86}Sr** sample corrected to difference: NBS 987 value McArthur and NBS 987 Bochum mean value	**^{87}Sr/^{86}Sr** sample corrected to difference: USGS EN-1 value McArthur and USGS EN-1 Bochum mean value
SL 28.4 B	SR-1	**28.4**	0.707179	0.000007	0.707192	0.707210	0.707185	0.707194
SL 69	SR-47	**69**	0.707460	0.000005	0.707472	0.707484	0.707466	0.707475
SL 92 B	SR-2	**92**	0.707467	0.000005	0.707480	0.707498	0.707473	0.707482
SL 242.5 R	C1	**242.5**	0.707322	0.000005	0.707326	0.707337	0.707328	0.707338
SL 251.5 B	SR-3	**251.5**	0.707278	0.000005	0.707291	0.707309	0.707284	0.707293
SL 267.5 B	SR-4	**267**	0.707196	0.000005	0.707209	0.707227	0.707202	0.707211
SL 323 B	SR-6	**323**	0.707179	0.000006	0.707192	0.707210	0.707185	0.707194
SL2 1.2 R	C3	**341.2**	0.707243	0.000005	0.707247	0.707258	0.707249	0.707259
SL2 13.8 R	C4	**353.8**	0.707279	0.000004	0.707283	0.707294	0.707285	0.707295
SL2 25.5 Chon	C5	**365.5**	0.707306	0.000005	0.707310	0.707321	0.707312	0.707322
SL2 38.2 R	C6	**378.5**	0.707286	0.000004	0.707290	0.707301	0.707292	0.707302
SL2-79	SR-15	**419**	0.707310	0.000005	0.707325	0.707350	0.707316	0.707325
SL2-93.5	SR-8	**433.5**	0.707375	0.000005	0.707388	0.707406	0.707381	0.707390
SL2-96.5	SR-10	**436.5**	0.707372	0.000005	0.707387	0.707412	0.707378	0.707387
SL2-97	SR-11	**437**	0.707331	0.000005	0.707346	0.707371	0.707337	0.707346
SL2-103.5a	SR-12	**443.5**	0.707441	0.000006	0.707456	0.707481	0.707447	0.707456
SL 517 R (bx)	C8	**517**	0.707382	0.000005	0.707386	0.707397	0.707388	0.707398

Standards	**Value McArthur**	**Mean Value Bochum**	**± 2 σ standard error**	**± 2 σ standard deviation**	**number of repetitions [n]**
NIST NBS 987	0.710247	0.710241	0.000001	0.000031	458
USGS EN-1	0.709175	0.709159	0.000002	0.000032	392

R	unclassified rudist shell
Chon	chondrodont shell
B	unclassified Bivalve

CARBONATE BULK, MONTE LA COSTA SECTION

Sample (no.)	Height [m]	$\delta^{13}C$ [VPDB]	$\delta^{13}C$ [VPDB] s.d.	$\delta^{18}O$ [VPDB]	$\delta^{18}O$ [VPDB] s.d.
A 1	**1**	2.41	0.07	-2.76	0.02
A 2	**2**	2.24	0.10	-3.10	0.04
A 3	**3**	2.86	0.07	-3.08	0.04
A 4	**4**	3.31	0.09	-2.42	0.03
A 5	**5**	2.95	0.08	-2.09	0.04
A 6	**6**	3.15	0.09	-2.42	0.06
A 7	**7**	3.24	0.12	-2.14	0.05
A 8	**8**	2.37	0.07	-2.60	0.04
A 9	**9**	2.51	0.07	-3.18	0.05
A 10	**10**	2.28	0.08	-2.53	0.03
A 11	**11**	2.82	0.06	-2.74	0.04
A 12	**12**	2.66	0.05	-0.93	0.04
A 13	**13**	2.73	0.05	-2.42	0.04
A 14	**14**	2.55	0.03	-1.59	0.03
A 16	**16**	1.98	0.03	-4.27	0.07
A 17	**17**	2.33	0.11	-2.92	0.04
A 18	**18**	1.90	0.06	-2.63	0.05
A 19	**19**	2.49	0.11	-2.47	0.04
A 20	**20**	1.85	0.10	-4.08	0.05
A 21	**21**	-0.54	0.04	-6.20	0.07
A 22	**22**	2.23	0.06	-3.66	0.04
A 23	**23**	2.40	0.05	-1.65	0.05
A 24	**24**	2.33	0.05	-3.19	0.04
A 25	**25**	2.23	0.12	-3.54	0.05
A 26	**26**	1.53	0.05	-3.39	0.05
A 27	**27**	1.76	0.06	-3.40	0.06
A 28	**28**	1.63	0.05	-3.93	0.08
A 29	**29**	1.35	0.03	-4.66	0.07
A 30	**30**	1.22	0.09	-3.90	0.08
A 31	**31**	2.58	0.03	-0.92	0.04
A 32	**32**	3.29	0.06	-2.85	0.07
A 33	**33**	2.83	0.10	-4.58	0.07
A 34	**34**	2.21	0.08	-2.18	0.05
A 35	**35**	4.81	0.05	-3.15	0.04
A 36	**36**	4.18	0.10	-2.35	0.04
A 37	**37**	4.36	0.04	-1.60	0.08
A 38	**38**	2.19	0.03	-2.18	0.06
A 39	**39**	2.39	0.12	-4.25	0.05
A 40	**40**	2.02	0.13	-0.67	0.07
A 41	**41**	4.50	0.03	-1.55	0.05
A 42	**42**	2.04	0.03	-0.60	0.04
A 43	**43**	3.61	0.09	-2.57	0.05
A 44	**44**	4.24	0.07	-1.83	0.04
A 45	**45**	4.59	0.07	-2.22	0.04
A 46	**46**	4.14	0.04	-2.81	0.06
A 47	**47**	4.64	0.07	-2.35	0.04
A 49	**49**	3.91	0.08	-2.82	0.06
A 50	**50**	4.61	0.05	-2.87	0.03
A 51	**51**	3.07	0.08	-0.90	0.03
A 52	**53**	3.30	0.11	-3.57	0.05
A 53	**52**	2.24	0.03	-1.22	0.05
A 54	**54**	3.16	0.10	-0.77	0.08
A 55	**55**	3.98	0.06	-2.45	0.07
A 56	**56**	4.35	0.07	-2.10	0.03
A 57	**57**	2.22	0.03	-0.10	0.06
A 58	**58**	4.68	0.09	-2.26	0.04
A 59	**59**	4.16	0.03	-2.86	0.05
A 60	**60**	3.75	0.10	-2.59	0.05
A 61	**61**	4.53	0.07	-2.10	0.04
A 62	**62**	4.48	0.09	-2.24	0.05
A 63	**63**	2.73	0.07	-2.80	0.06
A 64	**64**	3.93	0.04	-2.37	0.04
A 65	**65**	4.86	0.06	-2.23	0.06
A 66	**66**	4.17	0.05	-2.53	0.05
A 67	**67**	4.89	0.11	-1.59	0.05
A 69	**69**	4.79	0.05	-1.88	0.04
A 70	**70**	5.02	0.12	-1.90	0.05
A 71	**71**	3.65	0.04	-0.45	0.06
A 72	**72**	3.60	0.07	-3.07	0.03
A 73	**73**	3.82	0.09	-0.09	0.05
A 74	**74**	2.91	0.04	-1.15	0.07
A 75	**75**	4.13	0.11	-2.53	0.06
A 76	**76**	4.74	0.05	-2.15	0.04
A 77	**77**	4.80	0.04	-2.05	0.05
A 78	**78**	4.30	0.06	-3.31	0.03
A 79	**79**	5.05	0.08	-1.86	0.03
A 80	**80**	4.11	0.07	-2.75	0.05
A 81	**81**	3.89	0.02	-4.17	0.07
A 82	**82**	4.49	0.08	-3.23	0.05
A 83	**83**	4.74	0.09	-3.78	0.03
A 86	**86**	4.51	0.07	-3.21	0.05
A 87	**87**	4.86	0.04	-2.19	0.06
A 88	**88**	4.76	0.08	-2.11	0.04
A 89	**89**	4.49	0.07	-3.01	0.07
A 90	**90**	4.81	0.04	-2.12	0.06
A 91	**91**	4.54	0.06	-3.45	0.06
A 92	**92**	5.02	0.04	-2.65	0.06
A 93	**93**	4.85	0.04	-2.88	0.05
A 94	**94**	5.06	0.11	-1.93	0.05
A 95	**95**	4.77	0.06	-2.51	0.05

Sample (no.)	Height [m]	$\delta^{13}C$ [VPDB]	$\delta^{13}C$ [VPDB] s.d.	$\delta^{18}O$ [VPDB]	$\delta^{18}O$ [VPDB] s.d.
A 96	**96**	3.98	0.10	-2.12	0.04
A 97	**97**	4.66	0.06	-2.21	0.04
A 99	**99**	4.91	0.11	-3.38	0.06
A 100	**100**	4.77	0.07	-2.63	0.05
A 101	**101**	4.53	0.07	-2.48	0.05
A 102	**102**	4.91	0.02	-2.33	0.07
A 103	**103**	4.77	0.06	-2.28	0.07
A 104	**104**	4.54	0.07	-2.31	0.05
A 105	**105**	4.61	0.07	-2.46	0.04
A 106	**106**	4.44	0.03	-2.44	0.04
A 107	**107**	4.68	0.10	-1.98	0.04
A 108	**108**	4.79	0.04	-1.55	0.06
A 109	**109**	3.95	0.08	-2.42	0.04
A 110	**110**	4.38	0.06	-2.68	0.08
A 112	**112**	4.22	0.05	-2.59	0.05
A 113	**113**	4.39	0.05	-2.69	0.06
A 114	**114**	4.80	0.06	-1.93	0.06
A 115	**115**	3.78	0.06	-1.93	0.05
A 116	**116**	3.62	0.07	-1.76	0.03
A 117	**117**	3.58	0.09	-1.63	0.03
A 118	**118**	3.67	0.04	-1.60	0.04
A 119	**119**	3.86	0.07	-1.51	0.03
A 120	**120**	2.17	0.08	-2.86	0.07
A 121	**121**	3.25	0.03	-1.25	0.05
A 122	**122**	1.31	0.03	-2.08	0.07
A 123	**123**	3.90	0.02	-2.23	0.09
A 124	**124**	3.42	0.03	-0.15	0.07
A 125	**125**	3.86	0.09	-2.34	0.05
A 126	**126**	3.62	0.05	-2.96	0.04
A 127	**127**	3.13	0.07	-2.68	0.03
A 128	**128**	2.82	0.11	-2.54	0.04
A 129	**129**	3.60	0.09	-2.51	0.03
A 130	**130**	4.06	0.09	-2.60	0.05
A 132.5	**132.5**	3.45	0.04	-2.91	0.06
A 133	**133**	3.63	0.07	-2.56	0.04
A 134	**134**	4.02	0.08	-2.27	0.07
A 135	**135**	4.67	0.04	-2.11	0.04
A 136	**136**	3.03	0.04	-1.42	0.05
A 137	**137**	4.12	0.03	-2.42	0.05
A 138	**138**	2.43	0.06	-3.74	0.05
A 139	**139**	3.28	0.04	-1.75	0.06
A 140	**140**	3.03	0.03	-1.63	0.06
A 141	**141**	2.79	0.04	-0.73	0.04
A 142	**142**	2.85	0.02	-1.79	0.06
A 143	**143**	2.97	0.03	-1.38	0.05
A 144	**144**	2.61	0.04	-1.64	0.06
A 145	**145**	3.07	0.06	-1.51	0.03
A 147	**147**	2.77	0.07	-1.99	0.04
A 148	**148**	3.53	0.07	-3.49	0.05
A 149	**149**	2.84	0.04	-1.17	0.06
A 150	**150**	3.55	0.04	-2.10	0.08
A 151	**151**	3.45	0.03	-2.22	0.04
A 152	**152**	3.20	0.07	-2.42	0.05
A 153	**153**	3.59	0.05	-2.24	0.03
A 154	**154**	3.04	0.02	-2.10	0.07
A 155	**155**	2.77	0.04	-3.33	0.02
A 156	**156**	2.67	0.04	-2.35	0.06
A 157	**157**	2.59	0.07	-2.92	0.04
A 159	**159**	2.79	0.06	-2.20	0.02
A 160	**160**	1.88	0.08	-2.73	0.08
A 161	**161**	2.19	0.02	-2.76	0.06
A 162	**162**	2.37	0.09	-2.31	0.08
A 163	**163**	1.27	0.06	-2.73	0.05
A 164	**164**	2.84	0.02	-1.85	0.07
A 165	**165**	2.17	0.03	-0.83	0.05
A 166	**166**	2.90	0.04	-1.93	0.07
A 167	**167**	3.47	0.06	-3.08	0.03
A 168	**168**	2.84	0.05	-2.07	0.04
A 169	**169**	2.74	0.08	-2.96	0.05
A 170	**170**	2.74	0.05	-2.42	0.03
A 171	**171**	3.03	0.07	-2.22	0.05
A 172	**172**	3.40	0.03	-2.38	0.06
A 173	**173**	3.15	0.10	-1.88	0.08
A 174	**174**	3.17	0.03	-2.24	0.09
A 175	**175**	2.69	0.02	-2.67	0.07
A 176	**176**	1.98	0.07	-2.43	0.03
A 177	**177**	2.04	0.05	-2.65	0.06
A 178	**178**	2.04	0.05	-2.65	0.06
A 179	**179**	3.42	0.05	-2.34	0.09
A 180	**180**	2.83	0.03	-3.31	0.08
A 181	**181**	2.49	0.05	-2.37	0.06
A 182	**182**	2.87	0.03	-1.70	0.05
A 183	**183**	2.44	0.04	-2.42	0.02
A 184	**184**	2.95	0.06	-0.76	0.04
A 185	**185**	2.38	0.09	-2.87	0.06
A 186	**186**	2.86	0.04	-1.97	0.03
A 187	**187**	1.42	0.05	-0.06	0.04
A 188	**188**	2.54	0.04	-6.56	0.19
A 189	**189**	2.50	0.05	-1.88	0.04
A 190	**190**	2.88	0.04	-2.00	0.04
A 191	**191**	2.58	0.07	-2.52	0.07
A 192	**192**	1.49	0.05	0.09	0.05

Sample (no.)	Height [m]	$\delta^{13}C$ [VPDB]	$\delta^{13}C$ [VPDB] s.d.	$\delta^{18}O$ [VPDB]	$\delta^{18}O$ [VPDB] s.d.
A 193	**193**	2.74	0.08	-2.58	0.05
A 194	**194**	2.26	0.03	-2.79	0.05
A 195	**195**	3.00	0.05	-2.56	0.05
A 196	**196**	2.53	0.07	-2.10	0.07
A 197	**197**	2.54	0.07	-1.79	0.04
A 198	**198**	2.72	0.09	-2.55	0.04
A 199	**199**	3.38	0.02	-2.02	0.06
A 200	**200**	2.58	0.12	-1.90	0.05
A 201	**201**	2.74	0.12	-3.05	0.05
A 202	**202**	2.66	0.03	-3.26	0.06
A 203	**203**	2.52	0.06	-2.44	0.06
A 204	**204**	1.27	0.08	-2.73	0.06
A 205	**205**	2.92	0.04	-1.17	0.08
A 206	**206**	0.04	-2.42	0.05	0.07
SA 0	**208**	3.39	0.03	-1.80	0.05
SA 0.5	**208,5**	3.01	0.05	-2.55	0.03
SA 1	**209**	2.46	0.03	-2.21	0.07
SA 1.2	**209,2**	2.16	0.08	-2.40	0.08
SA 1.5	**209,5**	2.78	0.03	-1.86	0.08
SA 2	**210**	2.90	0.08	-1.74	0.10
SA 2.5	**210,5**	3.03	0.04	-2.13	0.05
SA 2.7	**210,7**	2.72	0.05	-1.42	0.07
SA 3	**211**	2.90	0.02	-2.29	0.08
SA 3.5	**211.5**	2.55	0.04	-2.90	0.06
SA 4	**212**	2.58	0.10	-2.12	0.07
SA 4.5	**212.5**	2.51	0.05	-2.06	0.07
SA 5	**213**	3.33	0.04	-2.10	0.05
SA 5.5	**213.5**	2.57	0.03	-2.88	0.05
SA 6	**214**	3.54	0.03	-2.80	0.05
SA 7	**215**	2.01	0.03	-2.19	0.07
SA 8	**216**	3.66	0.03	-2.03	0.04
SA 8.5	**216.5**	3.21	0.04	-2.06	0.03
SA 9	**217**	3.52	0.04	-1.71	0.05
SA 9.5	**217.5**	3.35	0.06	-1.72	0.05
SA 10	**218**	3.21	0.02	-2.65	0.09
SA 10.5	**218.5**	3.17	0.06	-3.02	0.05
SA 11	**219**	2.63	0.04	-2.39	0.05
SA 11.5	**219.5**	3.01	0.05	-3.03	0.06
SA 13.5	**221.5**	3.06	0.07	-3.14	0.04
SA 14	**222**	3.00	0.06	-2.27	0.05
SA 16	**224**	3.14	0.06	-3.18	0.05
SA 16.5	**224.5**	3.45	0.07	-2.55	0.09
SA 17	**225**	2.91	0.03	-1.84	0.06
SA 17.5	**225.5**	3.69	0.06	-2.19	0.05
SA 18	**226**	2.94	0.03	-2.37	0.06
SA 18.5	**226.5**	3.13	0.04	-2.69	0.07
SA 19	**227**	2.81	0.04	-2.91	0.06
SA 20.5	**228.5**	2.77	0.05	-2.32	0.06
SA 21	**229**	2.63	0.04	-2.25	0.04
SA 22	**230**	3.04	0.05	-0.71	0.06
SA 22.5	**230.5**	2.82	0.06	-2.41	0.05
SA 23	**231**	2.81	0.06	-0.36	0.08
SA 23.5	**231.5**	2.89	0.06	-2.21	0.08
SA 24	232	2.54	0.05	-2.56	0.09
SA 24.5	**232.5**	3.19	0.04	-2.28	0.06
SA 25	**233**	2.34	0.07	-3.13	0.06
SA 25.5	**233.5**	3.32	0.04	-2.33	0.07
SA 26	**234**	3.10	0.05	-2.34	0.05
SA 26.5	**234.5**	1.97	0.05	-2.46	0.05
SA 28	**236**	2.61	0.06	-2.16	0.08
SA 29	**237**	2.31	0.03	-3.27	0.05
SA 29.5	**237.5**	2.52	0.07	-2.44	0.09
SA 30	**238**	2.59	0.09	-3.69	0.09
SA 30.5	**238.5**	3.07	0.09	-2.28	0.15
SA 31	**239**	2.13	0.06	-2.93	0.10
SA 32.5	**240.5**	3.20	0.07	-2.15	0.05
SA 33	**241**	2.92	0.07	-2.78	0.10
SA 33.5	**241.5**	3.31	0.08	-2.49	0.07
SA 34.5	**242.5**	2.91	0.10	-3.66	0.07
SA 35	**243**	2.78	0.07	-2.65	0.06
SA 36	**244**	2.97	0.10	-2.81	0.06
SA 36.5	**244.5**	2.94	0.06	-2.28	0.05
SA 37	**245**	2.96	0.08	-3.97	0.08
SA 38	**246**	3.29	0.05	-2.65	0.14
SA 38.5	**246.5**	3.28	0.07	-3.58	0.10
SA 39	**247**	3.10	0.03	-2.37	0.05
SA 40	**248**	3.26	0.05	-1.75	0.07
SA 40.5	**248.5**	3.07	0.05	-2.49	0.06
SA 41.5	**249.5**	3.15	0.04	-2.69	0.12
SA 42	**250**	3.07	0.04	-2.40	0.08
SA 42.5	**250.5**	3.33	0.04	-1.73	0.07
SA 43	**251**	3.53	0.04	-2.61	0.07
SA 44	**252**	2.74	0.05	-2.21	0.05
SA 46	**254**	3.06	0.04	-2.03	0.10
SA 46.5	**254.5**	2.68	0.04	-2.16	0.07
SA 47.5	**255.5**	3.08	0.05	-2.23	0.09
SA 48.3	**256.3**	3.06	0.06	-2.49	0.07
SA 49.5	**257.5**	2.99	0.05	-2.06	0.06
SA 50	**258**	3.00	0.05	-2.49	0.05
SA 50.5	**258.5**	2.62	0.04	-2.93	0.03
SA 51	**259**	2.51	0.05	-2.32	0.06
SA 51.5	**259.5**	3.03	0.03	-1.95	0.08

Sample (no.)	Height [m]	$\delta^{13}C$ [VPDB]	$\delta^{13}C$ [VPDB] s.d.	$\delta^{18}O$ [VPDB]	$\delta^{18}O$ [VPDB] s.d.
SA 52	**260**	2.97	0.06	-2.38	0.06
SA 52.5	**260.5**	3.05	0.05	-1.79	0.09
SA 54.5	**262.5**	2.51	0.05	-1.98	0.05
SA 53.5	**261.5**	2.85	0.07	-2.62	0.04
SA 54	**262**	2.42	0.05	-3.15	0.06
SA 55	**263**	2.38	0.09	-2.16	0.07
SA 55.5	**263.5**	2.91	0.04	-2.23	0.03
SA 56	**264**	2.52	0.03	-2.40	0.03
SA 56.5	**264.5**	2.66	0.05	-2.43	0.08
SA 57	**265**	2.56	0.04	-2.62	0.06
SA 57.5	**265.5**	1.50	0.05	-2.43	0.06
SA 58	**266**	2.61	0.05	-2.19	0.04
SA 58.5	**266.5**	2.05	0.04	-1.95	0.04
SA 59	**267**	3.11	0.03	-2.17	0.07
SA 59.5	**267.5**	2.71	0.04	-2.27	0.05
SA 60	**268**	2.56	0.06	-2.22	0.09
SA 60.5	**268.5**	2.48	0.03	-3.21	0.06
SA 61	**269**	3.24	0.04	-2.58	0.06
SA 61.5	**269.5**	2.71	0.05	-2.92	0.05
SA 62	**270**	2.78	0.05	-2.01	0.04
SA 63	**271**	3.34	0.02	-2.74	0.08
SA 63.5	**271.5**	3.41	0.09	-2.12	0.09
SA 64	**272**	3.02	0.03	-3.12	0.07
SA 64.5	**272.5**	2.90	0.03	-2.30	0.07
SA 65	**273**	2.78	0.02	-2.41	0.04
SA 66	**274**	2.89	0.05	-2.67	0.06
SA 66.5	**274.5**	2.49	0.12	-1.92	0.13
SA 67	**275**	2.47	0.12	-2.04	0.13
SA 67.5	**275.5**	2.93	0.09	-2.16	0.09
SA 68	**276**	2.73	0.21	-2.02	0.19
SA 69	**277**	2.74	0.09	-2.06	0.18
SA 70	**278**	2.57	0.08	-2.60	0.13
SA 70.5	**278.5**	3.06	0.05	-1.29	0.11
SA 71	**279**	2.59	0.04	-3.04	0.07
SA 71.5	**279.5**	2.78	0.07	-2.16	0.13
SA 72	**280**	3.29	0.07	-1.83	0.12
SA 72.5	**280.5**	2.76	0.05	-3.02	0.08
SA 73	**281**	2.72	0.04	-2.84	0.08
SA 73.5	**281.5**	3.14	0.06	-2.43	0.12
SA 74	**282**	3.07	0.07	-2.45	0.08
SA 74.5	**282.5**	3.03	0.10	-2.04	0.13
SA 75	**283**	3.23	0.06	-1.98	0.14
SA 75.5	**257.5**	2.67	0.06	-1.92	0.11
SA 76	**284**	2.88	0.05	-2.27	0.08
SA 76.5	**284.5**	2.61	0.05	-2.41	0.06
SA 77	**285**	2.22	0.05	-2.31	0.12
SA 77.5	**285.5**	2.45	0.06	-2.61	0.11
SA 78	**286**	2.38	0.08	-2.35	0.14
SA 78.5	**286.5**	2.39	0.07	-2.28	0.10
SA 79	**287**	2.38	0.06	-2.55	0.15
SA 79.5	**287.5**	2.71	0.09	-2.15	0.15
SA 80	**288**	3.27	0.08	-2.47	0.18
SA 80.5	**288.5**	2.72	0.08	-2.59	0.17
SA 81	**289**	2.93	0.08	-2.59	0.07
SA 81.5	**289.5**	2.82	0.07	-2.72	0.14
SA 82	**290**	2.77	0.10	-2.27	0.12
SA 83	**291**	2.40	0.07	-2.49	0.08
SA 85	**293**	2.55	0.07	-2.64	0.14
SA 85.5	**293.5**	2.73	0.05	-1.87	0.08
SA 86	**294**	3.49	0.06	-1.81	0.14
SA 86.3	**294.3**	3.03	0.10	-2.83	0.18
SA 86.5	**294.5**	2.44	0.06	-2.71	0.05
SA 87	**295**	3.00	0.05	-2.16	0.11
SA 87.5	**295.5**	3.14	0.07	-2.71	0.15
SA 88	**296**	2.82	0.05	-2.85	0.14
SA 88.5	**296.5**	2.86	0.03	-3.02	0.10
SA 89.5	**297.5**	2.94	0.08	-3.50	0.16
SA 90	**298**	2.50	0.06	-3.16	0.13
SA 90.5	**298.5**	2.32	0.07	-2.93	0.14
SA 91	**299**	2.39	0.10	-3.57	0.11
SA 91.3	**299.3**	2.21	0.07	-3.33	0.19
SA 91.5	**299.5**	2.47	0.14	-1.83	0.22
SA 92.3	**300.3**	2.63	0.08	-3.44	0.20
SA 92.5	**300.5**	2.35	0.12	-2.89	0.23
SA 93	**301**	2.13	0.15	-3.22	0.18
SA 93.5	**301.5**	2.12	0.09	-3.17	0.15
SA 94	**302**	2.47	0.10	-2.28	0.18
SA 94.5	**302.5**	2.24	0.13	-2.67	0.33
SA 95	**303**	2.17	0.12	-2.80	0.15
SA 95.5	**303.5**	2.63	0.06	-3.55	0.15
SA 96.5	**304.5**	2.49	0.08	-2.94	0.15
SA 98	**306**	2.59	0.12	-3.63	0.19
SA 99	**307.0**	3.78	0.07	-2.74	0.16
SA 100	**308.0**	2.85	0.08	-3.37	0.16
SA 101	**309.0**	2.81	0.13	-4.19	0.20
SA 101.5	**309.5**	3.01	0.06	-3.21	0.09
SA 102.5	**310.5**	3.68	0.02	-3.20	0.05
SA 103.5	**311.5**	2.73	0.02	-2.99	0.06
SA 104	**312.0**	2.19	0.03	-2.71	0.05
SA 104.5	**312.5**	2.09	0.02	-3.04	0.07
SA 105.5	**313.5**	3.13	0.04	-2.69	0.03
SA 106	**314.0**	-0.69	0.03	-4.94	0.09

Sample (no.)	Height [m]	$\delta^{13}C$ [VPDB]	$\delta^{13}C$ [VPDB] s.d.	$\delta^{18}O$ [VPDB]	$\delta^{18}O$ [VPDB] s.d.
SA 106.5	**314.5**	3.02	0.05	-2.49	0.03
SA 107	**315.0**	3.08	0.04	-3.03	0.04
SA 109	**317.0**	2.23	0.05	-2.47	0.04
SA 109.5	**317.5**	2.65	0.03	-2.01	0.04
SA 110	**318.0**	2.68	0.06	-2.20	0.05
SA 110.5	**318.5**	2.74	0.04	-3.13	0.06
SA 112.5	**320.5**	2.95	0.03	-2.32	0.05
SA 113	**321.0**	2.47	0.04	-2.44	0.03
SA 113.5	**321.5**	2.37	0.03	-2.94	0.03
SA 114	**322.0**	2.29	0.03	-2.71	0.04
SA 114.5	**322.5**	2.69	0.04	-2.78	0.06
SA 115	**323.0**	2.82	0.03	-2.62	0.07
SA 115.5	**323.5**	2.59	0.04	-2.62	0.05
SA 116	**324.0**	2.31	0.01	-2.47	0.05
SA 116.5	**324.5**	2.85	0.03	-2.85	0.04
SA 116.7	**324.7**	2.83	0.02	-2.83	0.04
SA 117	**325.0**	1.86	0.04	-3.64	0.03
SA 117.5	**325.5**	2.75	0.02	-3.36	0.06
SA 118	**326.0**	2.46	0.04	-2.51	0.03
SA 118.5	**326.5**	2.71	0.03	-2.92	0.03
SA 119	**327.0**	2.90	0.04	-3.09	0.04
SA 119.5	**327.5**	2.63	0.06	-2.17	0.10
SA 120	**328.0**	3.19	0.02	-2.62	0.05
SA 121	**329.0**	2.78	0.03	-2.35	0.04
SA 121.5	**329.5**	2.56	0.03	-2.45	0.04
SA 122.5	**330.5**	2.71	0.04	-2.65	0.05
SA 123	**331.0**	2.61	0.07	-2.44	0.04
SA 123.5	**331.5**	2.49	0.04	-2.20	0.01
SA 124	**332.0**	2.46	0.03	-2.63	0.06
SA 125	**333.0**	2.47	0.04	-2.41	0.05
SA 125.5	**333.5**	3.31	0.04	-2.78	0.04
SA 126	**334.0**	2.88	0.05	-2.37	0.04
SA 127	**335.0**	2.51	0.04	-2.58	0.04
SA 127.5	**335.5**	2.75	0.04	-3.10	0.03
SA 128	**336.0**	2.45	0.04	-3.06	0.04
SA 128.5	**336.5**	2.93	0.05	-2.09	0.06
SA 129	**337.0**	2.04	0.04	-3.72	0.04
SA 129.5	**337.5**	2.17	0.07	-2.38	0.06
SA 130.5	**338.5**	1.51	0.04	-2.76	0.05
SA 131	**339.0**	2.80	0.04	-2.68	0.05
SA 131.5	**339.5**	3.13	0.03	-2.59	0.03
SA 132	**340.0**	2.94	0.03	-2.34	0.04
SA 132.5	**340.5**	3.19	0.02	-2.44	0.05
SA 133	**341.0**	2.71	0.03	-2.62	0.04
SA 133.5	**341.5**	2.60	0.06	-2.69	0.04
SA 134	**342.0**	2.50	0.06	-2.59	0.08
SA 134.5	**342.5**	1.70	0.05	-2.73	0.04
SA 135	**343.0**	2.72	0.03	-3.19	0.04
SA 135.5	**343.5**	2.18	0.04	-2.80	0.05
SA 136	**344**	1.56	0.03	-2.75	0.05
SA 136.5	**344.5**	3.01	0.06	-2.39	0.06
SA 138	**346**	2.42	0.12	-2.73	0.13
SA 138.5	**346.5**	2.59	0.03	-2.89	0.06
SA 139	**347**	3.06	0.02	-2.90	0.04
SA 139.5	**347.5**	2.74	0.04	-3.02	0.06
SA 140	**348**	2.69	0.07	-3.16	0.04
SA 140.5	**348.5**	2.69	0.03	-2.78	0.05
SA 141	**349**	2.82	0.04	-2.41	0.04
SA 141.5	**349.5**	2.84	0.05	-2.38	0.03
SA 142	**350**	2.74	0.04	-2.44	0.05
MLC 0	**351**	2.82	0.04	-2.71	0.07
MLC 0.5	**351.5**	2.93	0.04	-2.97	0.07
MLC 1	**352**	3.07	0.05	-1.87	0.06
MLC 1.5	**352.5**	3.57	0.04	-1.84	0.08
MLC 2	**353**	3.43	0.08	-1.88	0.05
MLC 2.5	**353.5**	3.29	0.05	-2.49	0.06
MLC 3	**354**	3.04	0.05	-1.77	0.07
MLC 3.5	**354.5**	3.05	0.12	-2.11	0.09
MLC 4	**355**	3.04	0.04	-2.44	0.06
MLC 4.5	**355.5**	3.37	0.05	-1.84	0.06
MLC 5	**356**	3.13	0.05	-2.54	0.06
MLC 5.5	**356.5**	2.95	0.06	-2.15	0.07
MLC 6	**357**	2.67	0.04	-2.81	0.02
MLC 6.5	**357.5**	3.04	0.05	-2.14	0.06
MLC 7	**358**	3.16	0.07	-2.31	0.06
MLC 7.5	**358.5**	2.93	0.03	-2.45	0.04
MLC 8	**359**	2.84	0.03	-1.00	0.03
MLC 8.5	**359.5**	2.49	0.06	-1.75	0.04
MLC 9	**360**	3.02	0.08	-2.48	0.06
MLC 9.5	**360.5**	3.60	0.05	-2.03	0.06
MLC 10	**361**	3.61	0.03	-2.20	0.07
MLC 10.5	**361.5**	3.15	0.14	-2.45	0.09
MLC 11	**362**	3.20	0.02	-2.01	0.06
MLC 11.5	**362.5**	3.12	0.11	-2.02	0.07
MLC 12	**363**	3.11	0.05	-2.75	0.03
MLC 12.5	**363.5**	2.98	0.03	-2.55	0.05
MLC 13	**364**	2.88	0.03	-3.09	0.08
MLC 13.5	**364.5**	2.94	0.03	-4.32	0.09
MLC 14.5	**365.5**	3.41	0.04	-2.53	0.07
MLC 15	**366**	3.49	0.03	-2.25	0.07
MLC 15.5	**366.5**	2.54	0.04	-2.74	0.05
MLC 16	**367**	2.85	0.03	-3.88	0.04

Sample (no.)	**Height [m]**	**$\delta^{13}C$ [VPDB]**	**$\delta^{13}C$ [VPDB] s.d.**	**$\delta^{18}O$ [VPDB]**	**$\delta^{18}O$ [VPDB] s.d.**
MLC 16.5	**367.5**	3.20	0.06	-2.06	0.03
MLC 17	**368**	3.31	0.05	-1.73	0.05
MLC 17.5	**368.5**	3.20	0.03	-2.28	0.07
MLC 18	**369**	3.52	0.04	-2.50	0.05
MLC 18.5	**369.5**	3.16	0.03	-2.79	0.08
MLC 19	**370**	3.03	0.05	-2.86	0.06
MLC 19.5	**370.5**	3.42	0.05	-1.70	0.07
MLC 20	**371**	3.34	0.04	-1.69	0.10
MLC 20	**371**	2.54	0.08	-3.08	0.04
MLC 20.1	**371.1**	2.76	0.09	-2.25	0.05
MLC 20.2	**371.2**	2.88	0.04	-1.76	0.06
MLC 20.3	**371.3**	2.64	0.03	-2.09	0.08
MLC 20.4	**371.4**	2.45	0.06	-3.00	0.08
MLC 20.5	**371.5**	3.13	0.02	-2.06	0.09
MLC 20.6	**371.6**	2.41	0.08	-2.32	0.03
MLC 20.7	**371.7**	3.10	0.04	-2.17	0.08
MLC 20.8	**371.8**	0.47	0.02	-1.54	0.10
MLC 20.99	**371.99**	3.03	0.07	-2.31	0.04
MLC 21-1	**372**	1.18	0.08	0.02	0.04
MLC 21-2	**372**	3.15	0.05	-2.39	0.07
MLC 21.01	**3721**	3.01	0.05	-1.91	0.05
MLC 21.2	**372.2**	3.01	0.05	-2.03	0.03
MLC 21.3	**372.3**	3.13	0.03	-2.07	0.08
MLC 21.4	**372.4**	2.80	0.08	-2.51	0.05
MLC 21.5	**372.5**	2.63	0.03	-2.96	0.09
MLC 21.6	**372.6**	3.43	0.05	-1.83	0.04
MLC 21.7	**372.7**	3.26	0.03	-2.64	0.05
MLC 21.8	**372.8**	2.24	0.02	-1.94	0.10
MLC 21.9	**372.9**	3.18	0.02	-2.01	0.05
MLC 22	**373.0**	3.23	0.04	-1.65	0.07
MLC 22	**373.0**	3.25	0.05	-2.39	0.04
MLC 22.5	**373.5**	3.25	0.07	-1.62	0.04
MLC 23	**374.0**	2.96	0.02	-2.43	0.06
MLC 23.5	**374.5**	3.03	0.02	-2.82	0.07
MLC 24	**375.0**	2.66	0.04	-2.59	0.03
MLC 24.5	**375.5**	2.93	0.03	-2.44	0.06
MLC 25	**376.0**	2.86	0.02	-2.43	0.03
MLC 25.5	**376.5**	3.35	0.03	-1.70	0.06
MLC 26	**377.0**	3.17	0.03	-2.27	0.07
MLC 26.5	**377.5**	3.18	0.03	-2.34	0.06
MLC 27	**378.0**	2.91	0.03	-2.55	0.09
MLC 27.5	**378.5**	2.50	0.04	-1.76	0.06
MLC 28	**379.0**	2.80	0.03	-4.09	0.07
MLC 28.5	**379.5**	2.86	0.03	-3.49	0.04
MLC 29	**380.0**	2.75	0.03	-2.55	0.07
MLC 29.5	**380.5**	3.41	0.03	-2.28	0.04
MLC 30	**381.0**	3.54	0.02	-2.51	0.07
MLC 30.5	**381.5**	2.68	0.03	-2.70	0.05
MLC 31	**382.0**	2.84	0.04	-2.26	0.07
MLC 31.5	**382.5**	2.91	0.04	-2.73	0.05
MLC 32	**383.0**	3.27	0.02	-2.63	0.06
MLC 32.5	**383.5**	2.73	0.02	-2.23	0.08
MLC 33	**384.0**	2.91	0.03	-2.14	0.06
MLC 33.5	**384.5**	2.79	0.05	-2.30	0.05
MLC 34	**385.0**	2.64	0.01	-2.66	0.07
MLC 34.5	**385.5**	2.73	0.03	-3.34	0.05
MLC 35	**386.0**	1.51	0.03	-2.71	0.04
MLC 35.5	**386.5**	1.67	0.06	-2.20	0.06
MLC 36	**387.0**	2.21	0.03	-3.12	0.06
MLC 37	**388.0**	2.70	0.03	-2.31	0.07
MLC 37.5	**388.5**	1.24	0.05	-1.64	0.06
MLC 38.5	**389.5**	1.73	0.10	-1.75	0.08
MLC 39	**390.0**	2.86	0.09	-2.21	0.09
MLC 39.5	**390.5**	2.49	0.07	-2.16	0.09
MLC 39.6	**390.6**	3.94	0.05	-2.36	0.06
MLC 40	**391.0**	2.25	0.03	-1.88	0.06
MLC 41	**392.0**	2.57	0.06	-2.15	0.06
MLC 41.5	**392.5**	2.78	0.05	-2.13	0.08
MLC 42	**393.0**	2.99	0.06	-1.85	0.05
MLC 42.5	**393.5**	1.32	0.05	-2.05	0.05
MLC 42.5	**393.5**	1.26	0.05	-2.95	0.07
MLC 43	**394.0**	1.74	0.06	-3.29	0.08
MLC 44	**395.0**	2.38	0.05	-2.82	0.05
MLC 44	**395.0**	0.34	0.04	-3.77	0.10
MLC 44.5	**395.5**	2.80	0.05	-2.75	0.05
MLC 45.3	**396.3**	3.05	0.04	-1.80	0.06
MLC 45.5	**396.3**	1.80	0.04	-3.14	0.04
MLC 46	**396.6**	2.39	0.05	-3.02	0.06
MLC 46-2	**397.0**	0.82	0.04	-2.93	0.07
MLC 47	**397.0**	2.33	0.02	-3.44	0.05
MLC 47.5	**398.5**	1.22	0.04	-3.03	0.06
MLC 48	**399.0**	1.14	0.05	-2.71	0.06
MLC 48.5	**399.5**	0.99	0.03	-2.81	0.05
MLC 49.5	**400.5**	1.40	0.03	-2.97	0.04
MLC 50	**401.0**	2.13	0.05	-3.06	0.03
MLC 50.5	**401.5**	1.79	0.03	-2.02	0.05
MLC 51	**402.0**	2.34	0.05	-2.64	0.05
MLC 51.5	**402.5**	2.65	0.04	-2.21	0.06
MLC 52	**403.0**	2.96	0.08	-3.00	0.07
MLC 52.5	**403.5**	2.61	0.06	-2.53	0.06
MLC 53	**404.0**	1.78	0.05	-2.15	0.04
MLC 53.5	**404.5**	1.25	0.06	-1.66	0.04

Sample (no.)	Height [m]	$\delta^{13}C$ [VPDB]	$\delta^{13}C$ [VPDB] s.d.	$\delta^{18}O$ [VPDB]	$\delta^{18}O$ [VPDB] s.d.
MLC 54	**405.0**	1.57	0.09	-1.54	0.12
MLC 54.5	**405.5**	1.84	0.05	-1.42	0.05
MLC 55	**406.0**	2.38	0.03	-1.61	0.05
MLC 55.5	**406.5**	2.67	0.05	-1.41	0.07
MLC 57	**408**	1.37	0.05	-1.91	0.05
MLC 57.5	**408.5**	1.86	0.03	-1.80	0.04
MLC 58.5	**409.5**	1.62	0.06	-1.61	0.08
MLC 59.5	**410.5**	2.28	0.03	-3.33	0.08
MLC 60	**411**	2.25	0.03	-3.45	0.05
MLC 60.5	**411.5**	2.78	0.05	-2.93	0.06
MLC 61	**412**	2.92	0.04	-2.49	0.05
MLC 61.5	**412.5**	2.88	0.04	-2.61	0.05
MLC 62	**413**	2.51	0.04	-2.29	0.04
MLC 62.5	**413.5**	2.62	0.04	-2.47	0.05
MLC 63.5	**414.5**	2.88	0.03	-2.50	0.04
MLC 65	**416**	2.49	0.03	-2.10	0.04
MLC 66	**417**	2.31	0.04	-1.87	0.05
MLC 67	**418**	-0.01	0.03	-3.43	0.07
MLC 67.5	**418.5**	2.03	0.02	-3.29	0.05
MLC 68	**419**	2.09	0.04	-4.39	0.07
MLC 68.5	**419.5**	0.64	0.02	-3.76	0.07
MLC 69.5	**420.5**	1.83	0.04	-3.42	0.06
MLC 70	**421**	2.66	0.04	-2.87	0.05
MLC 70.5	**421.5**	2.50	0.02	-3.66	0.05
MLC 70.7	**421.7**	-0.05	0.03	-4.27	0.06
MLC 71	**422**	0.84	0.05	-4.38	0.06
MLC 71.5	**422.5**	2.17	0.02	-3.53	0.06
MLC 72	**423**	-0.92	0.02	-3.26	0.06
MLC 72.5	**423.5**	1.36	0.03	-3.72	0.07
MLC 73.1	**424.1**	1.42	0.03	-3.75	0.06
MLC 73.5	**424.5**	0.79	0.07	-4.00	0.11
MLC 74	**425**	0.92	0.13	-2.83	0.14
MLC 74.5	**425.5**	1.45	0.08	-4.12	0.08
MLC 75	**426**	1.12	0.02	-4.37	0.04
MLC 75.5	**426.5**	-0.05	0.03	-4.10	0.06
MLC 76	**427**	0.02	0.02	-3.67	0.08
MLC 76.5	**427.5**	0.57	0.04	-4.38	0.03
MLC 77	**428**	2.01	0.03	-3.32	0.05
MLC 77.5	**428.5**	-1.51	0.04	-3.93	0.04
MLC 78	**429**	1.47	0.05	-3.23	0.06
MLC 78.5	**429.5**	0.05	0.09	-3.78	0.10
MLC 79	**430**	0.07	0.07	-3.96	0.06
MLC 79.5	**430.5**	-1.55	0.06	-4.83	0.09
MLC 81	**432**	0.49	0.03	-3.70	0.04
MLC 81.5	**432.5**	0.77	0.03	-3.65	0.05
MLC 81.7	**432.7**	0.66	0.03	-3.83	0.06
MLC 82.5	**433.5**	1.98	0.03	-2.42	0.05
MLC 83	**434**	-0.42	0.03	-4.01	0.05
MLC 83.5	**434.5**	2.64	0.05	-2.42	0.08
MLC 84	**435**	-0.03	0.04	-4.23	0.04
MLC 84.5	**435.5**	1.71	0.06	-3.31	0.06
MLC 85	**436**	-0.24	0.04	-4.03	0.05
MLC 85.5	**436.5**	-0.04	0.03	-4.01	0.04
MLC 86	**437.0**	0.15	0.02	-4.57	0.08
MLC 86.5	**437.5**	0.68	0.03	-4.10	0.04
MLC 87	**438.0**	1.45	0.04	-3.83	0.08
MLC 87.5	**438.5**	2.14	0.07	-3.45	0.07
MLC 88	**439.0**	1.38	0.04	-4.35	0.04
MLC 89	**440.0**	-0.10	0.06	-4.09	0.05
MLC 89.5	**440.5**	0.93	0.04	-4.42	0.04
MLC 90	**441.0**	1.43	0.04	-3.58	0.06
MLC 90.5	**441.5**	1.35	0.05	-4.26	0.06
MLC 91	**442.0**	1.51	0.05	-4.22	0.05
MLC 91.5	**442.5**	2.31	0.04	-4.11	0.06
MLC 92	**443.0**	1.78	0.05	-4.45	0.06
MLC 92.5	**443.5**	1.57	0.07	-4.53	0.08
MLC 93	**444.0**	2.38	0.06	-4.07	0.05
MLC 93.5	**444.5**	2.19	0.04	-3.89	0.07
MLC 94	**445.0**	2.09	0.05	-3.48	0.04
MLC 94.5	**445.5**	2.38	0.04	-3.43	0.04
MLC 95	**446.0**	2.92	0.04	-3.99	0.08
B -0.6	**446.4**	2.09	0.05	-4.58	0.06
B 0.5	**447.5**	0.89	0.06	-4.69	0.05
B 1.3	**448.3**	2.21	0.07	-3.97	0.04
B 1.5	**448.5**	1.95	0.04	-4.70	0.07
B 2	**449.0**	2.88	0.04	-3.24	0.07
B 2.5	**449.5**	2.48	0.04	-3.46	0.14
B 3	**450.0**	2.35	0.10	-4.55	0.06
B 3.5	**450.5**	2.65	0.08	-3.73	0.03
B 4	**451.0**	2.09	0.06	-4.30	0.05
B 5	**452.0**	2.53	0.06	-3.44	0.04
B 6	**453.0**	2.21	0.09	-4.23	0.05
B 7	**454.0**	1.28	0.03	-4.48	0.09
B 8	**455.0**	1.96	0.04	-3.70	0.03
B 9	**456.0**	2.03	0.05	-7.98	0.42
B 10	**457.0**	2.52	0.02	-4.00	0.08
B 11	**458.0**	1.92	0.08	-3.68	0.05
B 12	**459.0**	2.76	0.04	-3.01	0.08
B 13	**460.0**	1.50	0.06	-4.48	0.07
B 14	**461.0**	1.62	0.03	-3.86	0.08
B 15	**462.0**	1.58	0.03	-4.80	0.09
B 16	**463.0**	0.99	0.08	-4.67	0.05

Sample (no.)	**Height** [m]	**$\delta^{13}C$** [VPDB]	**$\delta^{13}C$** [VPDB] s.d.	**$\delta^{18}O$** [VPDB]	**$\delta^{18}O$** [VPDB] s.d.
B 16.5	**463.5**	2.70	0.08	-2.59	0.06
B 16.7	**463.7**	1.24	0.08	-1.36	0.05
B 17	**464.0**	-1.10	0.03	-1.22	0.08
B 17.5	**464.5**	1.48	0.07	-0.83	0.10
B 17.8	**464.8**	2.29	0.11	-1.96	0.07
B 18	**465.0**	4.84	0.10	-2.91	0.05

Sample (no.)	**Height** [m]	**$\delta^{13}C$** [VPDB]	**$\delta^{13}C$** [VPDB] s.d.	**$\delta^{18}O$** [VPDB]	**$\delta^{18}O$** [VPDB] s.d.
B 18.8	**465.8**	1.39	0.05	0.10	0.07
B 19	**466.0**	3.00	0.06	-0.49	0.04
B 20	**467.0**	2.58	0.10	-2.63	0.04
B 21	**468.0**	2.08	0.03	-3.75	0.06
B 22	**469.0**	2.51	0.04	-3.86	0.05

CARBON AND OXYGEN ISOTOPES OF LOW-MG-CALCITE SHELLS, MONTE LA COSTA SECTION

Sample (no.)	**Height** [m]	**δ^{13}C** [VPDB]	**δ^{18}O** [VPDB]
SA 2-1 R	**209**	2.60	-2.88
SA 2-2 R	**209**	1.65	-4.65
SA 2.7 R	**210**	4.01	-3.59
SA 3.5-1 R	**210.5**	2.58	-2.12
SA 3.5-2 R	**211**	4.30	-3.33
SA 3.7 R	**210.7**	2.74	-3.40
SA 3.7-1 R	**210.7**	2.84	-2.61
SA 3.7-2 R	**210.7**	2.17	-7.26
SA 3.7-3 R	**210.7**	1.65	-3.54
SA 3.7-4 R	**210.7**	1.99	-4.11
SA 4.5 R	**211.5**	3.33	-2.10
SA 5 R	**212**	2.57	-2.88
SA 5.5 R	**213**	3.48	-2.40
SA 11.5 R	**218.5**	3.00	-3.10
SA 16 S	**223**	2.73	-2.75
SA 17 S	**224**	2.91	-3.04
SA 17-1 B	**224**	2.47	-3.38
SA 17-2 B	**224**	2.92	-3.04
SA 19	**226**	2.77	-2.32
SA 22-1 R	**229**	3.29	-3.30
SA 22-2 R	**229**	2.56	-3.67
SA 22.5 S	**229.5**	2.66	-3.18
SA 23 B	**230**	2.89	-2.21
SA 23 S	**230**	3.32	-3.17
SA 23 B	**230**	3.10	-3.79
SA 23.5 R	**230.5**	2.98	-3.09
SA 28 B	**235**	2.31	-3.27
SA 30.5B	**237.5**	2.13	-2.93
SA 30.5 S	**237.5**	1.82	-3.49
SA 30.5-1 B	**237.5**	3.06	-4.03
SA 30.5-2 B	**237.5**	2.63	-3.96
SA 35 B	**242**	2.97	-2.81
SA 36 B	**243**	2.94	-2.28
SA 36 S	**243**	2.76	-3.61
SA 36.5	**243.5**	2.96	-3.97
SA 37 B	**244**	3.29	-2.65
SA37 R	**244**	2.24	-4.31
SA 38 B	**245**	3.28	-3.58
SA 38 R	**245**	2.86	-4.34
SA 38.5 R	**245.5**	3.10	-2.37
SA 38.5 Chon	**245.5**	5.40	-3.04
SA 38.5 R	**245.5**	3.07	-4.02
SA 39 R	**246**	3.26	-1.75
SA 40 B	**247**	3.07	-2.49
SA 40.5 B	**247.5**	3.15	-2.69
SA 40.5 R	**248**	2.72	-3.19
SA 41.5 R	**248.5**	3.07	-2.40
SA 42.5 R	**250**	2.73	-4.17
SA 43 S	**250**	3.26	-2.24
SA 44 S	**251**	3.02	-2.14
SA 44-1 R	**251**	2.38	-4.35
SA 44-1 R	**251**	2.41	-3.92
SA 45 S	**252**	2.43	-3.67
SA 45-1 B	**252**	2.66	-3.93
SA 45-2 B	**252**	1.82	-3.13
SA 45-3 B	**252**	1.87	-3.21
SA 45-4 Chon	**252**	2.86	-3.59
SA 45-5 B	**252**	3.52	-3.12
SA 45-6 B	**252**	2.70	-3.13
SA 45-7 Chon	**252**	2.54	-4.14
SA 47.5 Chon	**255**	3.98	-3.91
SA 48 S	**255**	3.33	-3.84
SA 48-1 Chon	**255**	2.87	-4.92
SA 48B2 chon	**255**	3.67	-3.27
SA 48.3 B	**255.3**	2.99	-2.06
SA 50 Chon	**257**	3.31	-2.67
SA 50 R	**257**	1.46	-4.23
SA 50.5 R	**258**	1.51	-4.29
SA 53.5 R	**261**	3.68	-2.22
SA 55 B	**262**	2.91	-2.23
SA 55 Chon	**262**	3.47	-2.24
SA 55.5 B	**262.5**	2.52	-2.40
SA 56 S	**263**	1.65	-3.75
SA 56.5 S	**263.5**	2.56	-2.62
SA 56.5 R	**264**	1.63	-4.02
SA 58.5-1 R	**266**	2.80	-3.04
SA 58.5-2 R	**266**	2.51	-3.87
SA 60 B	**267**	2.48	-3.21
SA 60.5 R	**268**	2.88	-3.55
SA 63 S	**270**	2.86	-4.35
SA 63 B	**270**	3.18	-4.34
SA 67.5 B	**274.5**	2.73	-2.02
SA 67.5 S	**274.5**	1.88	-3.89
SA 70.5 S	**277.5**	2.59	-3.04
SA 71.5 S	**278.5**	2.23	-3.72
SA 71.5-1 R_{req}	**278.5**	2.92	-3.26
SA 71.5-2 B	**278.5**	2.25	-2.84
SA 72 B	**279**	2.76	-3.02
SA 72 S	**279**	2.69	-3.08
SA 72-1 B	**279**	2.45	-2.97

Sample (no.)	Height [m]	$\delta^{13}C$ [VPDB]	$\delta^{18}O$ [VPDB]
SA 72-2 B	**279**	2.27	-3.83
SA 72-3 B	**279**	2.73	-3.66
SA 72.5 R	**280**	2.09	-3.95
SA 78.5 R	**286**	2.50	-3.12
SA 79.5 R	**287**	1.91	-3.85
SA 80 R	**287**	2.18	-4.15
SA 82.5 S	**289.5**	2.26	-3.59
SA 82.5-1 B	**289.5**	2.27	-3.04
SA 82.5-2 B	**289.5**	2.95	-3.42
SA 82.5-3 B	**289.5**	2.08	-4.48
SA 82.5-4 B	**289.5**	2.05	-3.67
SA 82.5-5 R_{req} recry.	**289.5**	2.64	-3.13
SA 82.5-6 R_{req}	**289.5**	2.19	-3.48
SA 83.5 R	**291**	2.57	-3.10
SA 86 B	**293**	3.03	-2.83
SA 86 R	**293**	3.11	-2.71
SA 86.3 B	**293.3**	2.44	-2.71
SA 86.5 R	**294**	3.30	-3.49
SA 87 S	**294**	2.93	-3.94
SA 87-1 B	**294**	2.23	-3.75
SA 87-2 B	**294**	2.14	-4.44
SA 87-3 Chon	**294**	2.29	-4.17
SA 87.5 S	**294.5**	2.82	-2.85
SA 87.5 R	**295**	2.34	-4.19
SA 89 R	**296**	2.15	-2.99
SA 90 R	**297**	2.30	-3.37
SA 96 S	**303**	3.21	-2.74
SA 96-1 Chon	**303**	3.46	-3.13
SA 96-2 R_{req}?	**303**	3.02	-3.57
SA 96.5 R	**304**	2.85	-2.62
SA 98.5 S	**305.5**	1.85	-3.88
SA 98.5-1 R_{req}	**305.5**	1.98	-3.73
SA 98.5-2 R_{req}	**305.5**	1.61	-3.66
SA 100.5 R	**308**	1.63	-4.50
SA 101.5 S	**308.5**	2.24	-3.99
SA 101.5-1 B	**308.5**	1.75	-4.28
SA 101.5-2 B	**308.5**	2.42	-3.39
SA 101.5-3 B	**308.5**	1.32	-4.49
SA 101.5-4 B	**308.5**	2.15	-3.77
SA 102.5 S	**309.5**	2.73	-2.99
SA 102.5 Chon	**310**	4.31	-2.00
SA 105 R	**312**	1.15	-3.87
SA 105.5 B	**312.5**	-0.69	-4.94
SA 106 R	**313**	3.33	-4.33
SA 107 R	**314**	2.23	-2.47
SA 107 R	**314**	2.54	-3.89
SA 108.5 S	**315.5**	1.85	-3.79
SA 108.5 B	**315.5**	2.15	-3.92
SA 110 R	**317**	2.22	-3.13
SA 110.5 S	**317.5**	0.84	-4.61
SA 110.5 B	**317.5**	0.93	-3.94
SA 111 R	**318**	2.62	-3.54
SA 113.5 S	**320.5**	2.29	-2.71
SA 115 S	**322**	2.96	-3.73
SA 115 B	**322**	1.32	-3.97
SA 115.5 S	**322.5**	2.31	-2.47
SA 115.5 R	**323**	1.54	-4.15
SA 118 Chon	**325**	2.98	-3.64
SA 118 R	**325**	2.09	-4.36
SA 118.5 S	**325.5**	2.90	-3.09
SA 119.5 R	**327**	2.57	-4.73
SA 120 S	**327**	2.78	-2.35
SA 120 S	**327**	3.05	-3.64
SA 120-1 B	**327**	2.86	-3.54
SA 120-2 B	**327**	2.65	-3.61
SA 120-3 Chon	**327**	2.87	-4.37
SA 121.5 S	**328.5**	1.63	-4.15
SA 121.5 B recry	**328.5**	1.58	-3.80
SA 122 Chon	**329**	3.19	-2.22
SA 124 R	**331**	2.28	-3.27
SA 124.5 R	**332**	1.52	-3.70
SA 128.5 R	**336**	2.46	-3.07
SA 129.5 S	**336.5**	1.96	-2.69
SA 129.5 B recry	**336.5**	1.61	-3.36
SA 134.5 S	**341.5**	2.72	-3.19
SA 136 S	**343**	1.44	-4.13
SA 136 B	**343**	1.46	-4.57
SA 136.5 B	**343.5**	2.85	-3.18
SA 136.5 R	**344**	1.87	-3.01
SA 137 R	**344**	2.42	-2.73
SA 137 S	**344**	4.29	-2.63
SA 137 Chon	**344**	3.23	-1.43
SA 138 R	**345**	2.93	-4.01
SA 140.5 R	**348**	1.82	-3.82
SA 142 S	**349**	2.08	-3.26
SA 142 B	**349**	1.51	-3.88
MLC 2 B	**352**	2.69	-3.99
MLC 3 R	**353**	1.97	-3.45
MLC 3.5 Chon	**353.5**	4.02	-1.09
MLC 4.5-1 S	**354.5**	1.40	-4.24
MLC 4.5-2 R_{req}	**354.5**	1.15	-2.99
MLC 6.5 S	**356.5**	3.16	-2.31
MLC 7.5 S	**357.5**	2.84	-1.00
MLC 9-1 S	**359**	3.60	-2.03

Sample (no.)	Height [m]	δ^{13}C [VPDB]	δ^{18}O [VPDB]
MLC 9-2 S	**359**	3.23	-2.57
MLC 9-1 B	**359**	3.11	-3.08
MLC 9-2 B	**359**	2.31	-2.95
MLC 9-3 B	**359**	3.17	-3.68
MLC 9-4 Chon?	**359**	2.92	-1.34
MLC 9.5 R	**359.5**	3.61	-2.20
MLC 10 R	**360**	2.50	-3.71
MLC 12 S	**362**	2.33	-3.32
MLC 12 B	**362**	2.42	-2.25
MLC 12.5 S	**362.5**	2.88	-3.09
MLC 13 S	**363**	2.94	-4.32
MLC 13.5 R	**364**	3.18	-3.28
MLC 14.5 S	**364.5**	3.49	-2.25
MLC 14.5 R	**365**	2.66	-3.21
MLC 15.5 S	**365.5**	2.85	-3.88
MLC 15.5 R	**366**	2.66	-3.88
MLC 17-1 S	**367**	2.67	-2.77
MLC 17-2 R$_{req}$	**367**	2.48	-3.20
MLC 19 R	**369**	2.69	-4.37
MLC 21 R	**371**	1.55	-4.57
MLC 23 R	**373**	2.68	-4.43
MLC 25 S	**375**	2.76	-3.15
MLC 25.5-1 S	**37.,5**	1,65	-3,17
MLC 25.5-2 B	**375.5**	2.36	-3.76
MLC 25.5-3 B	**375.5**	1.57	-3.29
MLC 26 S	**376**	2.17	-4.71
MLC 26-1 B	**376**	2.38	-4.39
MLC 26-2 B	**376**	1.97	-4.79
MLC 28.5 R	**379**	1.25	-4.85
MLC 29 S	**379**	3.41	-2.28
MLC 31.5 S	**381.5**	3.27	-2.63
MLC 32 R	**382**	1.79	-4.57
MLC 33 S	**383**	1.40	-4.16
MLC 33-1 B	**383**	2.04	-3.49
MLC 33-2 B	**383**	2.30	-3.32
MLC 33.5 R	**384**	1.80	-4.00
MLC 35 S	**385**	3.78	-1.37
MLC 35.5 S	**385.5**	2.21	-3.12
MLC 35.5 R	**386**	1.86	-3.87
MLC 38 R	**388**	1.90	-4.58
MLC 38.5 R	**389**	2.04	-4.62
MLC 39 -1 B	**389**	2.49	-2.16
MLC 39-2 R	**389**	2.59	-4.32
MLC 40 R	**390**	2.46	-4.60
MLC 41.5 R	**392**	2.14	-3.87
MLC 42 R	**392**	1.36	-4.95
MLC 44 R	**394**	1.35	-4.76

Sample (no.)	Height [m]	δ^{13}C [VPDB]	δ^{18}O [VPDB]
MLC 45 R	**395**	1.32	-4.64
MLC 45.3 S	**395.3**	2.26	-4.09
MLC 45.3-1 B	**395.3**	1.96	-3.28
MLC 45.3-2 B	**395.3**	2.45	-3.69
MLC 46 R	**396**	1.96	-3.74
MLC 48 R	**398**	1.88	-3.78
MLC 49 S	**399**	1.26	-4.39
MLC 49-1 B	**399**	1.75	-3.34
MLC 49-2 B	**399**	1.82	-3.18
MLC 50.5 B	**400.5**	1.65	-3.46
MLC 51 B	**401**	3.39	-2.72
MLC 58.5 S	**408.5**	2.28	-3.33
MLC 58.5 R	**409**	2.06	-3.71
MLC 59.5 S	**409.5**	2.25	-3.45
MLC 60 R	**410**	2.88	-4.43
MLC 60.5 R	**411**	2.57	-5.14
MLC 62 S	**412**	1.61	-4.50
MLC 62-1 B	**412**	1.47	-3.88
MLC 62-2 B	**412**	2.51	-2.12
MLC 62.5 R	**413**	3.18	-3.29
MLC 63.5 R	**414**	2.39	-4.51
MLC 67 S	**417**	2.69	-3.83
MLC 67 B	**417**	2.45	-4.22
MLC 68 S	**418**	0.64	-3.76
MLC 68-2 R	**418**	1.47	-3.98
MLC 68-1 R	**418**	3.06	-4.07
MLC 68.5 S	**418.5**	1.83	-3.42
MLC 69.5 S	**419.5**	2.66	-2.87
MLC S 70 S	**420**	2.19	-4.30
MLC 71 S	**421**	2.17	-3.53
MLC S 72.5	**422.5**	1.21	-3.80
MLC 73.1 R	**423**	0.98	-4.61
MLC 73.5 S	**423.5**	0.92	-2.83
MLC 73.5 S	**423.5**	2.93	-4.69
MLC 73.5-1 S	**423.5**	2.65	-4.57
MLC 73.5-2 B	**423.5**	1.33	-4.43
MLC 74.5 R	**425**	2.76	-5.15
MLC 81.5 S	**431.5**	0.66	-3.83
MLC 81.7 S	**431.7**	1.80	-2.82
MLC 81.7 B	**431.7**	2.02	-5.00
MLC 82.5 S	**432.5**	-0.42	-4.01
MLC 84 R	**434**	1.95	-5.09
MLC 89 R	**439**	3.62	-4.75
MLC 91 S	**441**	2.31	-4.11
MLC 94.5 R	**445**	2.48	-4.19
MLC 95 S	**446**	1.65	-5.17

R	unclassified rudist shell	Chon	chondrodont shell
B	unclassified Bivalve	S	undefined shell
R_{req}	requinid rudist		

C-AND O-ISOTOPES OF LOW-MG-CALCITE SHELLS AND BULK CARBONATE, MONTE LA COSTA SECTION

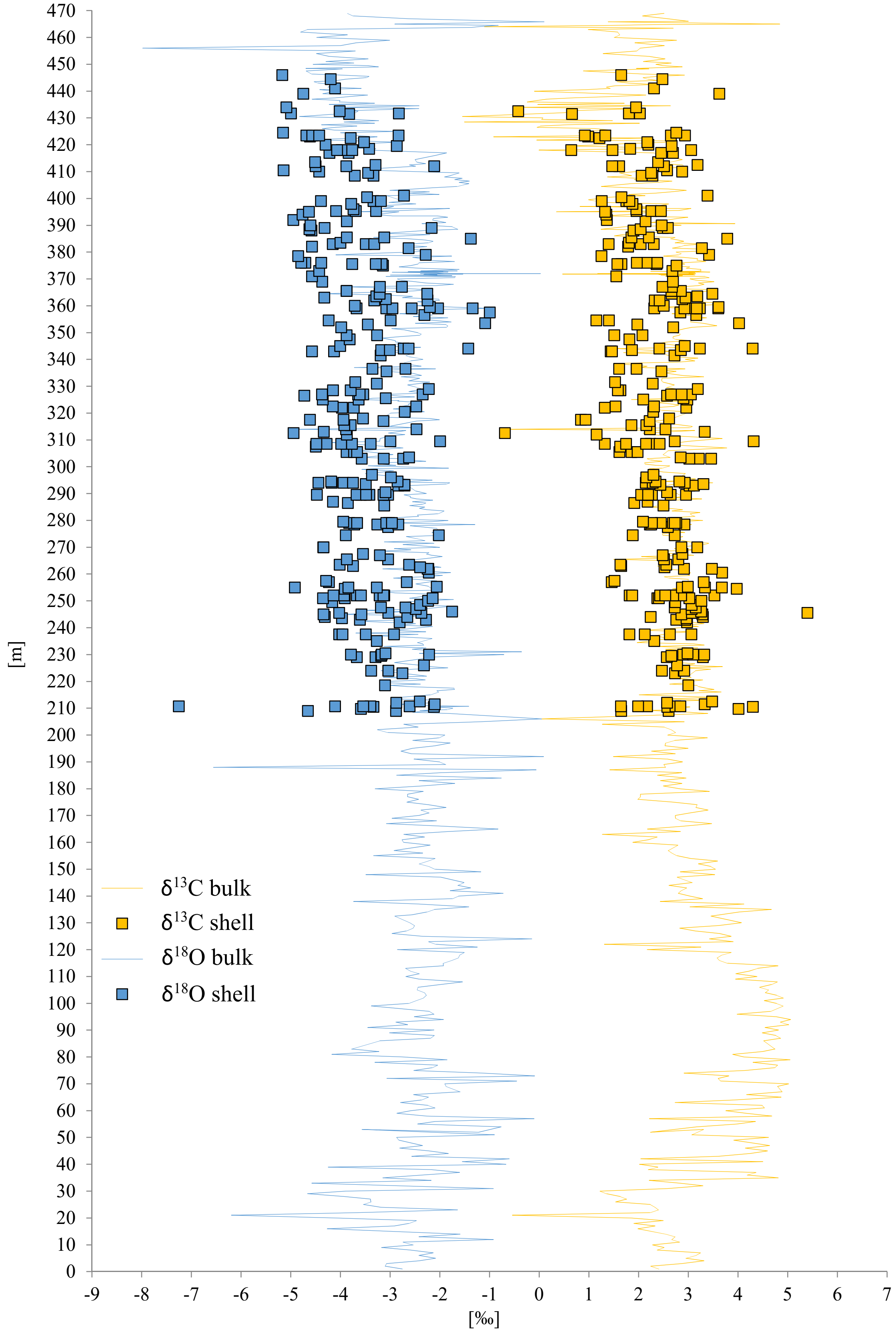

SCLEROCHRONOLOGICAL DATASET OF RUDISTS, MONTE LA COSTA SECTION

Sample (no.)	**Height** [m]	**$\delta^{13}C$** [VPDB]	**$\delta^{13}C$** [VPDB] s.d.	**$\delta^{18}O$** [VPDB]	**$\delta^{18}O$** [VPDB] s.d.
MLC 50-1	**401**	2.14	0.21	-3.93	0.09
MLC 50-2		1.87	0.12	-4.09	0.06
MLC 50-3		2.24	0.09	-3.97	0.05
MLC 50-4		2.03	0.16	-4.20	0.08
MLC 50-5		1.94	0.23	-4.59	0.13
MLC 50-6		2.14	0.12	-4.31	0.06
MLC 50-7		1.98	0.11	-4.25	0.13
MLC 50-8		2.26	0.08	-4.11	0.05
MLC 50-9		2.06	0.08	-4.08	0.10
MLC 50-10		2.51	0.12	-4.09	0.17
MLC 50-11		2.32	0.02	-3.39	0.06
MLC 50-12		2.67	0.04	-3.29	0.06
MLC 50-13		2.43	0.04	-3.84	0.04
MLC 50-14		2.33	0.08	-3.86	0.03
MLC 50-15		2.48	0.03	-3.24	0.06
MLC 50-16		2.68	0.03	-3.47	0.04
MLC 50-17		2.36	0.04	-3.93	0.03
MLC 50-18		2.07	0.04	-4.07	0.04
MLC 50-19		2.13	0.07	-4.04	0.03
MLC 50-20		1.97	0.06	-3.89	0.04
MLC 50-21		2.01	0.04	-3.70	0.04
MLC 50-22		2.03	0.03	-3.34	0.06
MLC 50-23		2.17	0.04	-3.22	0.04
MLC 50-24		2.13	0.04	-3.26	0.03
MLC 50-25		2.31	0.06	-3.17	0.03
MLC 50-26		2.68	0.07	-3.17	0.02
MLC 50-27		2.48	0.03	-3.63	0.03
MLC 50-28		2.36	0.08	-3.73	0.05
MLC 50-29		2.44	0.09	-3.73	0.04
MLC 50-30		2.50	0.07	-3.59	0.03
MLC 50-31		2.24	0.10	-3.55	0.06
MLC 50-32		2.01	0.07	-3.66	0.07
MLC 50-33		2.09	0.07	-3.57	0.04
MLC 50-34		2.14	0.07	-3.56	0.06
MLC 50-35		2.43	0.05	-3.24	0.03
MLC 50-36		2.87	0.08	-2.80	0.06
MLC 50-37		2.66	0.04	-2.91	0.05
MLC 50-38		2.65	0.07	-3.91	0.06
MLC 50-39		2.72	0.10	-3.94	0.03
MLC 50-40		2.77	0.09	-4.06	0.07
MLC 50-41		2.58	0.06	-3.99	0.06
MLC 50-42		2.37	0.03	-3.83	0.06
MLC 50-43		2.47	0.05	-3.74	0.04
MLC 50-44		2.30	0.03	-3.73	0.03
MLC 50-45		2.15	0.07	-3.64	0.05

Sample **(no.)**	**Height** **[m]**	**$\delta^{13}C$** **[VPDB]**	**$\delta^{13}C$** **[VPDB]** **s.d.**	**$\delta^{18}O$** **[VPDB]**	**$\delta^{18}O$** **[VPDB]** **s.d.**
MLC 50-46	**401**	2.22	0.06	-3.53	0.05
MLC 50-47		2.20	0.06	-3.25	0.05
MLC 50-48		2.41	0.05	-3.27	0.04
MLC 50-49		2.97	0.10	-3.11	0.04
MLC 50-50		2.53	0.08	-3.63	0.05
MLC 50-51		3.44	0.07	-3.16	0.05
MLC 50-52		3.19	0.06	-3.56	0.06
MLC 50-53		2.91	0.04	-3.96	0.04
MLC 50-54		2.83	0.09	-3.71	0.07
MLC 50-55		2.75	0.04	-3.81	0.05
MLC 50-56		2.79	0.07	-3.54	0.04
MLC 50-57		2.52	0.07	-3.49	0.06
MLC 50-58		2.80	0.04	-3.12	0.08

Sample **(no.)**	**Height** **[m]**	**$\delta^{13}C$** **[VPDB]**	**$\delta^{13}C$** **[VPDB]** **s.d.**	**$\delta^{18}O$** **[VPDB]**	**$\delta^{18}O$** **[VPDB]** **s.d.**
MLC 67-1	**418**	2.15	0.09	-3.32	0.03
MLC 67-2		1.97	0.06	-1.86	0.06
MLC 67-3		2.06	0.06	-1.44	0.05
MLC 67-4		2.43	0.06	-3.06	0.03
MLC 67-5		2.49	0.10	-4.86	0.06
MLC 67-6		2.62	0.05	-4.88	0.03
MLC 67-7		2.53	0.08	-4.59	0.05
MLC 67-8		2.48	0.09	-4.57	0.05
MLC 67-9		2.31	0.07	-4.49	0.03
MLC 67-10		2.44	0.02	-4.30	0.06
MLC 67-11		2.59	0.05	-4.18	0.04
MLC 67-12		2.45	0.03	-4.05	0.04
MLC 67-13		2.51	0.04	-3.78	0.06
MLC 67-14		2.80	0.05	-3.84	0.06
MLC 67-15		2.63	0.03	-3.94	0.07
MLC 67-16		2.49	0.05	-3.72	0.04
MLC 67-17		2.49	0.06	-3.54	0.04
MLC 67-18		2.59	0.03	-3.67	0.02
MLC 67-19		2.84	0.08	-3.55	0.04
MLC 67-20		2.88	0.10	-3.57	0.04
MLC 67-21		2.75	0.02	-3.61	0.05
MLC 67-22		2.63	0.08	-3.64	0.02
MLC 67-23		2.55	0.02	-3.66	0.08
MLC 67-24		2.38	0.03	-3.87	0.06
MLC 67-25		2.41	0.05	-3.83	0.02
MLC 67-26		2.38	0.07	-3.80	0.04
MLC 67-27		2.24	0.06	-3.81	0.05
MLC 67-28		1.96	0.02	-4.10	0.04
MLC 67-29		1.93	0.02	-4.03	0.05
MLC 67-30		2.30	0.02	-4.25	0.10

Sample **(no.)**	**Height** **[m]**	**$\delta^{13}C$** **[VPDB]**	**$\delta^{13}C$** **[VPDB]** **s.d.**	**$\delta^{18}O$** **[VPDB]**	**$\delta^{18}O$** **[VPDB]** **s.d.**
MLC 36 B-1	**387**	2.02	0.03	-3.15	0.03
MLC 36 B-2		1.38	0.13	-3.63	0.05
MLC 36 B-3		1.33	0.03	-3.53	0.06
MLC 36 B-4		0.95	0.04	-4.05	0.03
MLC 36 B-5		0.93	0.06	-4.09	0.02
MLC 36 B-6		1.06	0.03	-4.00	0.04
MLC 36 B-7		1.48	0.03	-3.96	0.02
MLC 36 B-8		1.51	0.05	-4.29	0.02
MLC 36 B-9		1.95	0.05	-4.27	0.01
MLC 36 B-10		2.37	0.04	-3.69	0.05
MLC 36 B-11		2.43	0.10	-3.38	0.05
MLC 36 B-12		2.20	0.07	-3.41	0.03
MLC 36 B-13		2.21	0.03	-3.53	0.05
MLC 36 B-14		2.25	0.06	-3.40	0.03
MLC 36 B-15		2.30	0.09	-2.91	0.04
MLC 36 B-16		2.12	0.05	-2.97	0.04
MLC 36 B-17		2.10	0.06	-3.21	0.06
MLC 36 B-18		2.11	0.08	-3.23	0.06
MLC 36 B-19		1.60	0.04	-3.73	0.05
MLC 36 B-20		1.65	0.02	-3.64	0.06
MLC 36 B-21		1.88	0.03	-3.55	0.03
MLC 36 B-22		1.85	0.03	-3.83	0.03
MLC 36 B-23		1.87	0.06	-4.06	0.03
MLC 36 B-24		1.88	0.06	-4.04	0.03
MLC 36 B-25		1.86	0.04	-4.00	0.03
MLC 36 B-26		1.87	0.04	-3.97	0.04
MLC 36 B-27		1.82	0.11	-4.13	0.08
MLC 36 B-28		1.87	0.11	-4.35	0.04
MLC 36 B-29		1.84	0.06	-4.23	0.06
MLC 36 B-30		1.86	0.08	-4.32	0.05
MLC 36 B-31		2.07	0.11	-4.13	0.06
MLC 36 B-32		2.48	0.10	-3.44	0.04
MLC 36 B-33		2.41	0.07	-3.26	0.06
MLC 36 B-34		2.05	0.07	-3.37	0.06
MLC 36 B-35		1.93	0.06	-3.45	0.05
MLC 36 B-36		1.98	0.11	-3.35	0.08
MLC 36 B-37		2.04	0.09	-3.17	0.04
MLC 36 B-38		1.80	0.06	-3.29	0.09
MLC 36 B-39		2.03	0.09	-3.38	0.06
MLC 36 B-40		1.82	0.07	-3.13	0.04
MLC 36 B-41		1.61	0.07	-3.27	0.04
MLC 36 B-42		1.62	0.03	-3.21	0.05
MLC 36 B-43		1.95	0.03	-3.34	0.05
MLC 36 B-44		1.86	0.05	-3.47	0.05
MLC 36 B-45		1.76	0.05	-3.34	0.04

Sample (no.)	Height [m]	$\delta^{13}C$ [VPDB]	$\delta^{13}C$ [VPDB] s.d.	$\delta^{18}O$ [VPDB]	$\delta^{18}O$ [VPDB] s.d.
MLC 36 B-46	**387**	1.97	0.06	-3.43	0.02
MLC 36 B-47		1.96	0.04	-3.40	0.03
MLC 36 B-48		1.89	0.06	-3.48	0.03
MLC 36 B-49		2.00	0.06	-3.48	0.04
MLC 36 B-50		1.89	0.05	-3.50	0.04
MLC 36 B-51		1.70	0.04	-3.60	0.02
MLC 36 B-52		1.77	0.05	-3.57	0.05
MLC 36 B-53		1.91	0.12	-3.56	0.09
MLC 36 B-54		1.89	0.06	-3.53	0.03
MLC 36 B-55		1.79	0.09	-3.54	0.08
MLC 36 B-56		1.82	0.09	-3.76	0.04
MLC 36 B-57		1.62	0.08	-3.75	0.07
MLC 36 B-58		1.75	0.09	-3.81	0.07
MLC 36 B-59		1.79	0.07	-3.89	0.07
MLC 36 B-60		1.63	0.09	-3.77	0.06
MLC 36 B-61		1.64	0.09	-4.21	0.04
MLC 36 B-62		1.90	0.06	-4.27	0.05
MLC 36 B-63		1.86	0.06	-4.31	0.03
MLC 36 B-64		2.16	0.08	-3.73	0.04
MLC 36 B-65		2.26	0.05	-3.06	0.05
MLC 36 B-66		1.83	0.06	-3.33	0.05
MLC 36 B-67		1.65	0.09	-3.43	0.04
MLC 36 B-68		1.68	0.06	-3.59	0.04
MLC 36 B-69		1.60	0.07	-3.50	0.03
MLC 36 B-70		1.52	0.07	-3.48	0.04
MLC 36 B-71		1.65	0.11	-3.32	0.04
MLC 36 B-72		1.68	0.07	-3.25	0.04
MLC 36 B-73		1.59	0.07	-3.16	0.04
MLC 36 B-74		1.54	0.07	-3.08	0.06
MLC 36 B-75		1.55	0.10	-3.26	0.04
MLC 36 B-76		1.58	0.07	-3.33	0.07
MLC 36 B-77		1.66	0.04	-3.24	0.04
MLC 36 B-78		1.68	0.09	-3.22	0.06
MLC 36 B-79		1.29	0.06	-3.48	0.07
MLC 36 B-80		1.65	0.09	-3.37	0.02

Sample (no.)	Height [m]	$\delta^{13}C$ [VPDB]	$\delta^{13}C$ [VPDB] s.d.	$\delta^{18}O$ [VPDB]	$\delta^{18}O$ [VPDB] s.d.
MLC 36 C-1	**387**	1.46	0.09	-4.03	0.05
MLC 36 C-2		1.42	0.08	-4.08	0.04
MLC 36 C-3		1.32	0.10	-4.04	0.07
MLC 36 C-4		1.49	0.12	-4.01	0.05
MLC 36 C-5		1.53	0.08	-3.94	0.05
MLC 36 C-6		1.47	0.07	-4.04	0.05
MLC 36 C-7		1.51	0.09	-4.01	0.05

Sample **(no.)**	**Height** **[m]**	**$\delta^{13}C$** **[VPDB]**	**$\delta^{13}C$** **[VPDB]** **s.d.**	**$\delta^{18}O$** **[VPDB]**	**$\delta^{18}O$** **[VPDB]** **s.d.**
MLC 36 C-8	**387**	1.55	0.08	-3.92	0.04
MLC 36 C-9		1.45	0.10	-3.87	0.05
MLC 36 C-10		1.42	0.08	-3.92	0.05
MLC 36 C-11		1.37	0.10	-3.87	0.06
MLC 36 C-12		1.43	0.09	-4.00	0.05
MLC 36 C-13		1.33	0.11	-4.00	0.11
MLC 36 C-14		1.25	0.11	-4.13	0.05
MLC 36 C-15		1.30	0.08	-4.03	0.04
MLC 36 C-16		1.23	0.09	-4.02	0.07
MLC 36 C-17		1.15	0.06	-4.18	0.05
MLC 36 C-18		1.26	0.11	-4.11	0.12
MLC 36 C-19		1.21	0.12	-4.08	0.05
MLC 36 C-20		1.11	0.13	-4.24	0.05
MLC 36 C-21		1.38	0.06	-3.97	0.05
MLC 36 C-22		1.30	0.08	-3.81	0.02
MLC 36 C-23		1.44	0.10	-3.73	0.02
MLC 36 C-24		1.46	0.07	-3.77	0.07
MLC 36 C-25		1.51	0.11	-3.65	0.04
MLC 36 C-26		1.74	0.11	-3.36	0.08
MLC 36 C-27		1.68	0.05	-3.20	0.03
MLC 36 C-28		1.63	0.12	-3.24	0.05
MLC 36 C-29		1.37	0.08	-3.58	0.04
MLC 36 C-30		0.94	0.05	-3.82	0.05
MLC 36 C-31		0.96	0.08	-3.89	0.06
MLC 36 C-32		1.30	0.07	-3.69	0.03
MLC 36 C-33		1.53	0.03	-3.41	0.04
MLC 36 C-34		1.32	0.02	-3.68	0.05
MLC 36 C-35		1.51	0.04	-3.53	0.04
MLC 36 C-36		1.38	0.07	-3.51	0.05
MLC 36 C-37		1.25	0.08	-3.56	0.04
MLC 36 C-38		1.30	0.10	-3.50	0.06
MLC 36 C-39		1.30	0.07	-3.45	0.05
MLC 36 C-40		1.24	0.05	-3.54	0.08
MLC 36 C-41		1.30	0.04	-3.35	0.07
MLC 36 C-42		1.34	0.12	-3.33	0.05
MLC 36 C-43		1.26	0.17	-3.39	0.08
MLC 36 C-44		1.33	0.10	-3.32	0.07
MLC 36 C-45		1.27	0.15	-3.27	0.06
MLC 36 C-46		1.24	0.08	-3.26	0.07
MLC 36 C-47		1.26	0.01	-3.23	0.06
MLC 36 C-48		1.31	0.07	-3.24	0.03
MLC 36 C-49		0.89	0.04	-3.33	0.04
MLC 36 C-50		1.32	0.09	-3.27	0.06
MLC 36 C-51		1.53	0.12	-3.16	0.04
MLC 36 C-52		1.42	0.08	-3.19	0.06
MLC 36 C-53		1.35	0.05	-3.19	0.05
MLC 36 C-54		1.38	0.07	-3.11	0.04

Sample **(no.)**	**Height** **[m]**	**$\delta^{13}C$** **[VPDB]**	**$\delta^{13}C$** **[VPDB]** **s.d.**	**$\delta^{18}O$** **[VPDB]**	**$\delta^{18}O$** **[VPDB]** **s.d.**
MLC 36 C-55	**387**	1.28	0.05	-2.52	0.03
MLC 36 C-56		1.44	0.08	-2.71	0.04
MLC 36 C-57		1.40	0.07	-3.03	0.06
MLC 36 C-58		1.50	0.13	-3.27	0.03
MLC 36 C-59		1.50	0.08	-3.26	0.04
MLC 36 C-60		1.60	0.05	-3.22	0.04
MLC 36 C-61		1.68	0.07	-3.18	0.07
MLC 36 C-62		1.53	0.04	-3.39	0.04
MLC 36 C-63		1.46	0.06	-3.46	0.06
MLC 36 C-64		1.73	0.04	-3.23	0.03
MLC 36 C-65		1.71	0.06	-3.32	0.03
MLC 36 C-66		1.68	0.04	-3.37	0.01
MLC 36 C-67		1.64	0.06	-3.38	0.05
MLC 36 C-69		1.81	0.07	-3.37	0.08
MLC 36 C-70		1.82	0.08	-3.39	0.03
MLC 36 C-71		1.72	0.07	-3.43	0.04
MLC 36 C-72		1.64	0.05	-3.69	0.03
MLC 36 C-73		1.68	0.11	-3.55	0.05
MLC 36 C-74		1.56	0.09	-3.61	0.03
MLC 36 C-75		1.46	0.04	-3.63	0.04
MLC 36 C-76		1.25	0.05	-3.82	0.04
MLC 36 C-77		1.54	0.04	-3.69	0.03
MLC 36 C-78		1.58	0.09	-3.84	0.03
MLC 36 C-79		1.56	0.06	-4.00	0.05
MLC 36 C-80		1.51	0.08	-4.05	0.02
MLC 36 C-81		1.43	0.04	-3.97	0.05
MLC 36 C-82		1.49	0.11	-3.89	0.06
MLC 36 C-83		1.47	0.07	-3.97	0.03
MLC 36 C-84		1.32	0.09	-4.12	0.03
MLC 36 C-85		1.44	0.09	-4.14	0.05
MLC 36 C-86		1.48	0.09	-4.32	0.06
MLC 36 C-87		1.49	0.03	-4.36	0.06
MLC 36 C-88		1.45	0.14	-4.59	0.06
MLC 36 C-89		1.29	0.08	-4.69	0.06
MLC 36 C-90		1.51	0.09	-4.67	0.03
MLC 36 C-91		1.45	0.04	-4.52	0.02
MLC 36 C-92		1.50	0.06	-4.55	0.05
MLC 36 C-93		1.28	0.03	-4.74	0.05
MLC 36 C-94		1.45	0.05	-4.69	0.02
MLC 36 C-95		1.50	0.05	-4.61	0.04
MLC 36 C-96		1.31	0.08	-4.67	0.06
MLC 36 C-97		1.50	0.06	-4.50	0.04
MLC 36 C-98		1.72	0.05	-4.12	0.04
MLC 36 C-99		1.79	0.09	-3.93	0.06
MLC 36 C-100		1.68	0.08	-4.13	0.03
MLC 36 C-101		1.92	0.04	-3.83	0.05
MLC 36 C-102		2.05	0.05	-3.76	0.04

Sample **(no.)**	**Height** **[m]**	**$\delta^{13}C$** **[VPDB]**	**$\delta^{13}C$** **[VPDB]** **s.d.**	**$\delta^{18}O$** **[VPDB]**	**$\delta^{18}O$** **[VPDB]** **s.d.**
MLC 36 C-103	**387**	1.77	0.06	-4.08	0.04
MLC 36 C-104		1.74	0.08	-4.06	0.04
MLC 36 C-105		1.45	0.11	-4.40	0.05
MLC 36 C-106		1.61	0.10	-4.21	0.04
MLC 36 C-107		1.68	0.16	-4.13	0.07
MLC 36 C-108		0.89	0.04	-4.53	0.08
MLC 36 C-109		1.42	0.05	-4.39	0.04
MLC 36 C-110		1.55	0.10	-4.19	0.04
MLC 36 C-111		1.55	0.05	-4.25	0.04
MLC 36 C-112		1.49	0.08	-4.34	0.04
MLC 36 C-113		1.37	0.08	-4.39	0.02
MLC 36 C-114		1.46	0.06	-4.36	0.04
MLC 36 C-115		1.35	0.06	-4.41	0.04
MLC 36 C-116		1.32	0.06	-4.38	0.04
MLC 36 C-117		1.38	0.09	-4.33	0.04
MLC 36 C-118		1.28	0.08	-4.41	0.03
MLC 36 C-119		1.01	0.10	-4.44	0.05
MLC 36 C-120		1.19	0.07	-4.37	0.02
MLC 36 C-121		1.19	0.08	-4.29	0.05
MLC 36 C-122		1.34	0.10	-4.27	0.04
MLC 36 C-123		1.31	0.11	-4.20	0.06
MLC 36 C-124		1.10	0.09	-4.21	0.04
MLC 36 C-125		1.25	0.07	-3.89	0.04
MLC 36 C-126		1.26	0.08	-3.93	0.06
MLC 36 C-127		1.35	0.09	-3.85	0.09
MLC 36 C-128		1.32	0.10	-3.70	0.04
MLC 36 C-129		1.39	0.07	-3.68	0.06
MLC 36 C-130		1.48	0.09	-3.68	0.06
MLC 36 C-131		1.28	0.05	-3.64	0.06
MLC 36 C-133		1.45	0.08	-3.53	0.04
MLC 36 C-134		1.54	0.10	-3.38	0.05
MLC 36 C-135		1.40	0.10	-3.43	0.06
MLC 36 C-136		1.39	0.05	-3.49	0.03
MLC 36 C-137		1.44	0.05	-3.47	0.05
MLC 36 C-138		1.48	0.07	-3.47	0.04
MLC 36 C-139		1.39	0.08	-3.47	0.04
MLC 36 C-140		1.47	0.07	-3.38	0.05
MLC 36 C-141		1.34	0.07	-3.66	0.05
MLC 36 C-142		1.17	0.06	-3.47	0.05
MLC 36 C-143		1.41	0.03	-3.27	0.06
MLC 36 C-144		1.29	0.08	-3.28	0.05
MLC 36 C-145		1.46	0.08	-3.22	0.04
MLC 36 C-146		1.41	0.05	-3.21	0.02
MLC 36 C-147		1.35	0.06	-3.34	0.04
MLC 36 C-148		1.34	0.10	-3.29	0.06
MLC 36 C-149		1.47	0.05	-3.15	0.05
MLC 36 C-150		1.48	0.07	-3.13	0.04

Sample **(no.)**	**Height** **[m]**	**$\delta^{13}C$** **[VPDB]**	**$\delta^{13}C$** **[VPDB]** **s.d.**	**$\delta^{18}O$** **[VPDB]**	**$\delta^{18}O$** **[VPDB]** **s.d.**
MLC 36 C-151	**387**	1.35	0.09	-3.23	0.04
MLC 36 C-152		1.19	0.04	-3.22	0.05
MLC 36 C-152		1.45	0.06	-3.06	0.04
MLC 36 C-153		1.52	0.09	-2.95	0.06
MLC 36 C-154		1.47	0.06	-3.02	0.07
MLC 36 C-155		1.45	0.10	-3.02	0.04
MLC 36 C-156		1.40	0.07	-3.11	0.04
MLC 36 C-157		1.33	0.05	-3.16	0.04
MLC 36 C-158		1.29	0.08	-3.20	0.04
MLC 36 C-159		1.33	0.06	-3.06	0.07
MLC 36 C-160		1.36	0.09	-3.06	0.04
MLC 36 C-161		1.46	0.09	-4.03	0.05
MLC 36 C-162		1.68	0.11	-3.06	0.03
MLC 36 C-163		1.68	0.06	-2.93	0.04
MLC 36 C-164		1.75	0.04	-2.97	0.09
MLC 36 C-165		1.71	0.06	-3.06	0.03
MLC 36 C-166		1.81	0.08	-3.15	0.05
MLC 36 C-167		1.89	0.09	-3.06	0.05
MLC 36 C-168		1.72	0.04	-3.31	0.06
MLC 36 C-169		1.74	0.03	-3.32	0.06
MLC 36 C-170		1.89	0.09	-3.27	0.07
MLC 36 C-171		1.64	0.08	-3.45	0.08
MLC 36 C-172		1.56	0.05	-3.30	0.02
MLC 36 C-173		1.58	0.03	-3.65	0.06
MLC 36 C-174		1.63	0.07	-3.73	0.03
MLC 36 C-175		1.53	0.11	-3.83	0.08
MLC 36 C-176		1.54	0.05	-3.88	0.03
MLC 36 C-177		1.60	0.06	-3.94	0.02
MLC 36 C-178		1.56	0.02	-4.14	0.06
MLC 36 C-179		1.78	0.08	-3.94	0.03
MLC 36 C-180		1.86	0.07	-4.03	0.05
MLC 36 C-181		1.75	0.11	-4.18	0.05
MLC 36 C-182		1.73	0.05	-4.30	0.04
MLC 36 C-183		1.76	0.08	-4.40	0.04
MLC 36 C-184		1.66	0.07	-4.37	0.06
MLC 36 C-185		1.68	0.08	-4.39	0.05
MLC 36 C-186		1.71	0.06	-4.37	0.03
MLC 36 C-187		1.66	0.05	-4.48	0.05
MLC 36 C-188		1.49	0.05	-4.42	0.08
MLC 36 C-189		1.88	0.18	-4.11	0.10
MLC 36 C-190		1.70	0.11	-4.25	0.03
MLC 36 C-191		1.88	0.12	-4.04	0.07
MLC 36 C-192		1.93	0.15	-4.01	0.06
MLC 36 C-193		1.80	0.11	-3.86	0.05
MLC 36 C-194		1.76	0.12	-3.93	0.05
MLC 36 C-195		1.76	0.09	-3.85	0.05
MLC 36 C-196		1.67	0.10	-3.99	0.03

Sample **(no.)**	**Height** **[m]**	**$\delta^{13}C$** **[VPDB]**	**$\delta^{13}C$** **[VPDB]** **s.d.**	**$\delta^{18}O$** **[VPDB]**	**$\delta^{18}O$** **[VPDB]** **s.d.**
MLC 36 C-197	**387**	1.66	0.08	-3.96	0.05
MLC 36 C-198		1.78	0.07	-3.69	0.02
MLC 36 C-199		1.72	0.18	-3.86	0.08
MLC 36 C-200		1.69	0.13	-3.78	0.04
MLC 36 C-201		1.60	0.09	-3.74	0.07
MLC 36 C-202		1.63	0.09	-3.75	0.10
MLC 36 C-203		1.66	0.13	-3.77	0.08
MLC 36 C-204		1.58	0.12	-3.70	0.05
MLC 36 C-205		1.55	0.15	-3.68	0.06
MLC 36 C-206		1.68	0.19	-3.72	0.10
MLC 36 C-207		1.57	0.11	-3.50	0.03
MLC 36 C-208		1.56	0.14	-3.52	0.08

TRACE ELEMENT RESULTS OF RUDIST AND CEMENTS. MONTE LA COSTA SECTION

Sample	Lab #	Height	Ca	Mg	Sr	Fe	Mn	Ba
(no.)		[m]	[ppm]	[ppm]	[ppm]	[ppm]	[ppm]	[ppm]
A 15 Chon	A 2	**15**	394550	3062	583	2	1	1
A 49 Chon	A 3	**49**	392130	3391	589	9	8	8
A 131 Chon	A 7	**131**	396070	2876	431	2	4	4
A 149 Chon	A 9	**149**	395590	3477	594	2	4	4
SA 3.7 B	SR 16	**211.7**	395950	2677	373	13	5.8	5.8
SA 3.7-1 Cem	ICP-24	**211.7**	392800	1363	210	119	29.1	29.1
SA 17 B	SR 17	**225**	397420	1735	1095	7	0.7	0.7
SA 17 Cem	ICP-25	**225**	393460	1157	147	209	97.3	97.3
SA 43 B	SR 18	**251**	393520	3560	206	328	10.4	10.4
SA 43 Cem	ICP-26	**251**	395470	1807	108	8	61.1	61.1
SA 45-2 B	SR 19	**253**	396130	1076	1279	11	5.0	5.0
SA 45-6 B	SR 20	**253**	397560	2882	269	38	29.5	29.5
SA 45-7 B	SR 21	**253**	396370	2129	413	16	55.5	55.5
SA 45-1 Cem	ICP-27	**253**	393570	1490	194	125	38.9	38.9
SA 71.5-2 B	SR 22	**279.5**	395600	2101	917	38	8.8	8.8
SA 82.5-2 B	SR 23	**290.5**	397360	3077	845	19	6.7	6.7
SA 82.5-3 B	SR 24	**290.5**	401230	1786	1102	8	1.6	1.6
SA 82.5-5 B	SR 25	**290.5**	403320	574	1121	7	1.4	1.4
SA 82.5-6 B	SR 26	**290.5**	399580	2418	1504	9	3.3	3.3
SA 82.5 Cem	ICP-28	**290.5**	392650	1816	227	108	24.6	24.6
SA 96-1 B	SR 27	**304**	401590	2694	626	7	12.1	12.1
SA 120-2 B	SR 28	**328**	400920	2403	1149	14	4.3	4.3
SA 120-3 B	SR 29	**328**	402630	2567	434	20	18.5	18.5
SA 120 Cem	ICP-29	**328**	392270	1913	328	77	20.1	20.1
SA 137-1 B	SR 30	**345**	398970	3032	918	20	3.0	3.0
SA 137 Cem	ICP-30	**345**	386280	2813	153	84	54.5	54.5
MLC 3.5 B	SR 31	**354.5**	395920	3698	1180	5	1.3	1.3
MLC 9-1 B	SR 32	**360**	401250	2910	767	14	4.7	4.7
MLC 12 B	SR 33	**363**	400230	2751	419	26	29.1	29.1
MLC 12 Cem	ICP-31	**363**	390860	1180	170	125	63.0	63.0
MLC 17-1 Cem	ICP-32	**368**	390860	2531	188	28	9.5	9.5
MLC 17-2 Cem	ICP-33	**368**	393620	1773	299	44	36.1	36.1
MLC 25.5-1 B	SR 34	**376.5**	398620	2590	1130	90	2.4	2.4
MLC 25.5 Cem	ICP-34	**376.5**	396030	2466	120	35	75.2	75.2
MLC 26-1 B	SR 35	**377**	402070	2011	1182	9	2.0	2.0
MLC 35 B	SR 36	**386**	396640	3493	868	31	3.0	3.0
MLC 45.3 B	SR 37	**394.3**	402840	1662	1062	13	2.2	2.2
MLC 45.3 Cem	ICP-35	**394.3**	394350	4669	1127	6	0.8	0.8
MLC 49-2 B	SR 38	**400**	402840	947	1231	7	1.3	1.3
MLC 49-1 Cem	ICP-36	**400**	396390	2424	186	25	8.1	8.1
MLC 49-2 Cem	ICP-37	**400**	397000	1849	283	124	18.5	18.5
MLC 51 B	SR 39	**402**	402700	2149	1192	16	2.1	2.1
MLC 51 Cem	ICP-38	**402**	395780	2180	116	12	495.0	495.0
MLC 62-1 B	SR 40	**413**	400040	1668	1212	9	0.9	0.9
MLC 72.5 Cem	ICP-39	**423.5**	398170	1231	273	92	58.5	58.5
MLC 73.5-1 B	SR 41	**424.5**	401650	1649	1225	15	2.1	2.1

Sample **(no.)**	**Lab #**	**Height** **[m]**	**Ca** **[ppm]**	**Mg** **[ppm]**	**Sr** **[ppm]**	**Fe** **[ppm]**	**Mn** **[ppm]**	**Ba** **[ppm]**
MLC 81.7-1 B	SR 42	**432.7**	404040	2311	202	51	36.2	36.2
MLC 81.7-2 B	SR 43	**432.7**	392830	2248	1248	18	6.3	6.3
B 1.3 Chon	B 1	**446.3**	396040	2748	656	2	4	4

Chon	chondrodont shell
Cem	cement
B	unclassified bivalve

STRONTIUM ISOTOPE VALUES, MONTE LA COSTA SECTION

Sample (no.)	**Lab #**	**Height [m]**	**$^{87}Sr/^{86}Sr$ measured**	**± 2 σ mean**	**$^{87}Sr/^{86}Sr$** sample corrected to difference: NBS 987 value McArthur and NBS 987 measured with sample	**$^{87}Sr/^{86}Sr$** sample corrected to difference: USGS EN-1 value McArthur and USGS EN-1 measured with sample	**$^{87}Sr/^{86}Sr$** sample corrected to difference: NBS 987 value McArthur and NBS 987 Bochum mean value	**$^{87}Sr/^{86}Sr$** sample corrected to difference: USGS EN-1 value McArthur and USGS EN-1 Bochum mean value
A 15 Chon	A2	**15**	0.707418	0.000005	0.707422	0.707433	0.707424	0.707434
A 49 Chon	A3	**49**	0.707230	0.000004	0.707234	0.707245	0.707236	0.707246
A 149 Chon	A9	**149**	0.707261	0.000005	0.707265	0.707276	0.707267	0.707277
SA 17-1 B	SR-17	**225**	0.707258	0.000007	0.707273	0.707298	0.707264	0.707273
SA 45-2 B	SR-19	**253**	0.707301	0.000005	0.707316	0.707341	0.707307	0.707316
SA 71.5-2 B	SR-22	**279,5**	0.707314	0.000005	0.707329	0.707354	0.707320	0.707329
SA 82.5-3 B	SR-24	**290,5**	0.707331	0.000005	0.707346	0.707371	0.707337	0.707346
SA 82.5-6 B	SR-26	**290,5**	0.707391	0.000005	0.707406	0.707431	0.707397	0.707406
SA 96-1 B	SR-27	**304**	0.707442	0.000005	0.707457	0.707482	0.707448	0.707457
SA 120-2 B	SR-28	**328**	0.707332	0.000004	0.707347	0.707372	0.707338	0.707347
SA 137-1 B	SR-30	**345**	0.707378	0.000005	0.707393	0.707405	0.707384	0.707393
MLC 3.5 B	SR-31	**354,5**	0.707355	0.000006	0.707370	0.707382	0.707361	0.707370
MLC 25.5-1 B	SR-34	**376,5**	0.707342	0.000005	0.707357	0.707369	0.707348	0.707357
MLC 26-1 B	SR-35	**377**	0.707350	0.000006	0.707365	0.707377	0.707356	0.707365
MLC 35 B	SR-36	**386**	0.707385	0.000005	0.707397	0.707409	0.707391	0.707400
MLC 45.3 B	SR-37	**394,3**	0.707389	0.000005	0.707404	0.707416	0.707395	0.707404
MLC 49-2 B	SR-38	**400**	0.707360	0.000005	0.707375	0.707387	0.707366	0.707375
MLC 51 B	SR-39	**402**	0.707362	0.000005	0.707374	0.707386	0.707368	0.707377
MLC 62-1 B	SR-40	**413**	0.707405	0.000005	0.707420	0.707432	0.707411	0.707420
MLC 73.5-1 B	SR-41	**424,5**	0.707352	0.000005	0.707367	0.707379	0.707358	0.707367
MLC 81.7-2 B	SR-43	**432,7**	0.707354	0.000005	0.707369	0.707381	0.707360	0.707369
B 1.3 Chon	B1	**446,3**	0.707398	0.000005	0.707402	0.707413	0.707404	0.707414

Standards	**Value McArthur**	**Mean Value Bochum**	**± 2 σ standard error**	**± 2 σ standard deviation**	**number of repetitions [n]**
NIST NBS 987	0.710247	0.710241	0.000001	0.000031	458
USGS EN-1	0.709175	0.709159	0.000002	0.000032	392

Chon	chondrodont shell
B	unclassified bivalve

µXRF MAPPING OF ALL SHELL FRAGMENTS

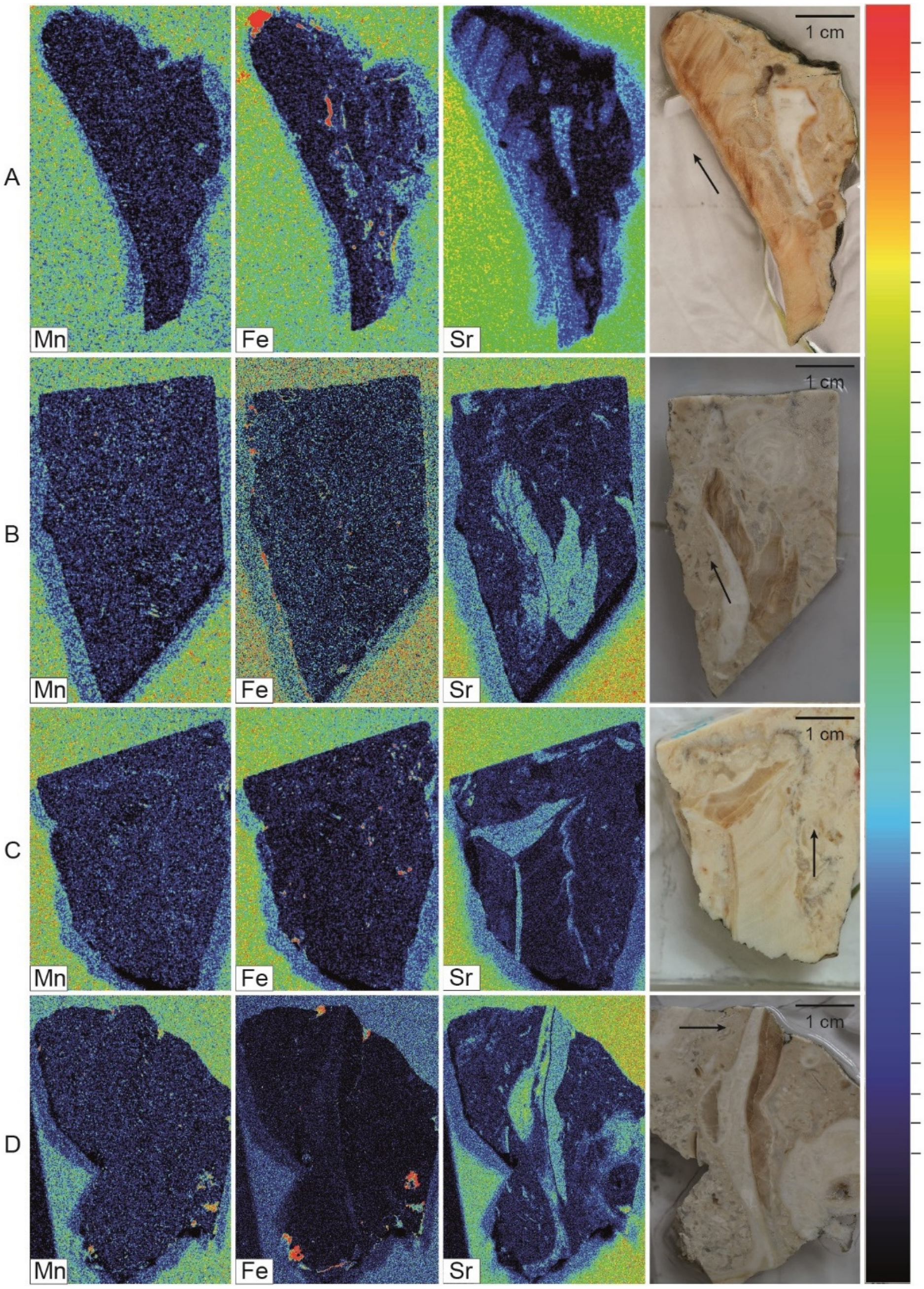

A
B
C
D
Mn
Fe
Sr
1 cm
97
95
93
90
88
85
83
81
78
76
74
71
69
67
64
62
60
57
55
53
50
48
45
43
41
38
36
34
31
29
27
24
22
20
17
15
13
10

Overview of the element concentration of Mn, Fe, Mg and Sr using µXRF mapping as well as an original photograph of the shell. No structures are visible in the scans for manganese, iron and magnesium. In shell D, the outlines of the last two elements can be detected. Strontium is the only element that is clearly visible in all four shells. Especially in the shells B, C and D the structures are clearly visible. At C and D, the cap is clearly displayed. In the scans of A and B, on the other hand, single micro and macro structures cannot be distinguished. For A and C no Mg scans are available. Arrow indicates growth direction of the shell.

µXRF Line Scan Raw Data of Shell Fragment A

distance [µm]	Mg [ug/g]	Sr [ug/g]	Mn [ug/g]	Fe [ug/g]
80	2979	955	37	195
160	3849	944	91	131
240	3204	989	152	37
320	3395	1009	111	131
400	3736	985	47	287
480	3107	980	11	155
560	3627	986	14	53
640	2771	988	9	99
720	3604	963	11	145
800	3104	839		255
880	4096	714	35	434
960	2825	764	57	371
1040	3753	949	13	130
1120	3263	1003	9	64
1200	2937	1021	21	91
1280	3410	1034	29	86
1360				
1440				
1520				
1600				
1680				
1760				
1840				
1920				
2000				
2080				
2160	2267	1269	26	159
2240				
2320				
2400				
2480	2713	932	42	73
2560	2452	936	57	131
2640	2862	978	72	74
2720				
2800	2330	1162	107	143
2880	2402	1162	92	93
2960	2926	1141	5	101
3040	2080	1110	69	73
3120	2134	1078	2	61
3200	2680	1039		54
3280	2693	1081		95
3360	2637	1067	55	56
3440	3496	1078	1	71
3520	2699	1027	15	100
3600	2762	883	21	218
3680	2915	826	18	139
3760	2177	831	21	118
3840	1480	851	29	149
3920	1452	898	62	73
4000	2530	948	105	100
4080	2414	1066	65	68
4160				
4240	2148	1001	33	76
4320	1974	956	42	54
4400	1918	962	2	76
4480	2829	997	7	79
4560	3365	1020	47	147
4640	3424	1044	45	60
4720	3166	1057	37	57
4800	2589	1051	70	63
4880	2678	1075	91	90
4960	2301	1143	127	121
5040	3535	1105	25	83
5120	3227	1085	8	90
5200	3556	1033	71	92
5280	3735	1012	8	101
5360	3130	975	4	96
5440	2712	1008	43	49
5520	2949	1016	52	22
5600	1867	1002	53	115
5680	1914	992	119	128
5760	2751	988	54	83
5840	1765	993	55	158
5920	3169	1035		115
6000	3363	1054		181
6080				
6160				
6240	2185	1081	30	82
6320				
6400				
6480				
6560				
6640				
6720	1351	1043	56	76
6800	2552	1023	53	119
6880	3271	999	64	119
6960	3155	959	54	127
7040				
7120				
7200	2088	1004	35	124
7280				
7360	2314	895	95	212

distance [µm]	Mg [ug/g]	Sr [ug/g]	Mn [ug/g]	Fe [ug/g]
7440				
7520	2352	1009	47	185
7600	2256	1035	57	125
7680	912	1067	61	108
7760				
7840				
7920				
8000				
8080				
8160	1909	1194	74	176
8240	1898	1236	35	131
8320	1292	1277	30	113
8400				
8480				
8560				
8640				
8720				
8800				
8880				
8960				
9040				
9120				
9200				
9280				
9360				
9440				
9520				
9600				
9680				
9760	1918	1160	155	4
9840	3658	1099	189	83
9920	1971	1035	59	79
10000	2709	1119	48	128
10080	2629	1150	171	116
10160	1511	1196	46	55
10240	2676	1161	28	68
10320	3402	1127	59	52
10400	2608	1095	81	228
10480	2697	1031	68	295
10560				
10640	2112	989	21	37
10720	2110	1016	55	38
10800	1875	1048	42	101
10880	3493	1068	27	58
10960	2901	1013	19	55
11040	2483	988	144	66
11120	3122	962	140	142
11200	3201	1025	60	419
11280	2957	1011	26	165
11360				
11440	3780	1052	46	58
11520	2987	1039	84	88
11600	4210	1000	89	64
11680				
11760				
11840	2185	1025	130	149
11920	3757	1021	392	39
12000	3441	935	61	106
12080	2838	1029	16	136
12160	2938	992	54	74
12240				
12320	2953	1040	243	12
12400	4042	1024	200	29
12480	3132	1042	297	25
12560	2913	961	738	
12640	4518	914	1009	
12720	3351	809	531	70
12800	4085	662	61	323
12880	3233	797	429	49
12960				
13040				
13120	2408	982	592	
13200	2180	974	339	518
13280	2421	868		207
13360				
13440	2238	887	104	118
13520	1921	1050	86	65
13600	2340	990	31	20
13680	2434	1055	27	67
13760	2871	1115	62	52
13840	3232	1115		67
13920	1068	1099	11	44
14000	2153	1104	12	199
14080	2291	1127	0	79
14160	1925	1140		108
14240	2342	1193	10	152
14320	1999	1152	6	70
14400	3344	1138		63
14480	2958	1135		146
14560	3118	1093		84
14640	3830	1070		107
14720	3229	1092	29	81
14800				
14880	2521	1085		117
14960	3228	1133	33	102
15040	2613	1167	17	578

distance **[µm]**	**Mg** **[ug/g]**	**Sr** **[ug/g]**	**Mn** **[ug/g]**	**Fe** **[ug/g]**
15120	2850	1210	12	280
15200	2781	1274	46	49
15280				
15360				
15440				
15520				
15600				
15680				
15760				
15840				
15920	2442	1435	185	99
16000	1921	1355	124	323
16080				
16160	1678	1267	34	223
16240	826	1311	35	113
16320	1898	1347	85	291
16400				
16480	1657	1354	41	47
16560	1513	1371	9	74
16640	2168	1355	5	79
16720	2826	1379	2	82
16800	1733	1354	41	65
16880	1543	1368	66	78
16960	3278	1348	264	67
17040	2479	1317		143
17120	2624	1282	33	55
17200	1620	1245	183	159
17280	1865	1193	154	94
17360	2230	1197	12	80
17440	1669	1190	66	65
17520	2828	1198	531	80
17600	1982	1193	482	352
17680	2196	1206	232	132
17760	2362	1246	50	157
17840	2398	1249		96
17920	3063	1235	20	143
18000	2652	1094	188	63
18080	2046	1063	1	98
18160	1423	1219	16	63
18240	1535	1225	23	73
18320	2106	1193	224	62
18400	2710	1235	314	55
18480	2612	1227	240	30
18560	2690	1251	327	37
18640	2122	1224	80	131
18720	2448	1161	434	
18800	3292	1177	354	18
18880	2655	1178	131	168
18960	2177	1174	45	240
19040	2068	1245	234	229
19120	1899	1249	63	136
19200	2187	1200	141	183
19280	2203	1157	244	53
19360	2122	1133	28	258
19440	2091	1172		137
19520	2084	1158		158
19600	2676	1150	12	122
19680	1970	1133	43	172
19760	2799	1081	122	81
19840	3841	1094	260	46
19920	3853	1082	25	116
20000	2850	1079	41	93
20080	2585	1075	19	54
20160	2805	1035		67
20240	2065	1040	16	71
20320	2034	1088	136	67
20400	2488	1105	2	104
20480	2977	1085	258	201
20560	3846	1051	105	81
20640	3752	1024	129	68
20720	4263	968	33	84
20800	3851	888	39	129
20880	4682	833	47	99
20960	4036	768	47	77
21040	4718	702	54	80
21120	5365	638	67	94
21200	4224	578	71	159
21280	4007	563	60	231
21360	4101	543	61	187
21440	4115	502	57	214
21520	4514	471	74	64
21600	4842	468	134	63
21680				
21760	5155	471	40	272
21840	5563	533	34	181
21920	4697	560	25	242
22000	5041	592	42	254
22080	5444	632	74	114
22160	4392	648	16	111
22240				
22320	3982	719	39	428
22400	3412	860	16	320
22480	3798	940	1	192
22560	3558	934	12	65
22640	4155	931	8	39
22720	4217	928		109

distance [µm]	Mg [ug/g]	Sr [ug/g]	Mn [ug/g]	Fe [ug/g]
22800	3529	976	8	71
22880	4682	969	2	111
22960	3014	958	11	98
23040	3446	957	30	179
23120	2979	955	35	194
23200	2617	1124		61
23280	2223	1130		72
23360	2658	1113	0	79
23440				
23520	2310	1122		57
23600	2352	1126	3	83
23680	2093	1111		78
23760	2546	1111		63
23840	2855	1115		73
23920	2067	1125		52
24000	2738	1113		65
24080				
24160	1981	1116		65
24240	1956	1113		80
24320	2231	1120		72
24400	2174	1114		66
24480	2147	1129		64
24560	1911	1122		60
24640	2756	1114		71
24720	1531	1125		66
24800	3169	1123		86
24880	2020	1123		72
24960				
25040	2425	1121	0	76
25120	2332	1127		71
25200	2418	1120		64
25280				
25360	2498	1112		71
25440	2822	1124		70
25520	2921	1121		72
25600	2378	1123		61
25680	1956	1128		68
25760				
25840	2724	1119		62
25920	2104	1114		42
26000	1928	1120		71
26080	2243	1120		71
26160	2228	1118		78
26240	2032	1114		70
26320				
26400	1683	1121		76
26480	2152	1125		73
26560	2459	1116		66
26640	2370	1126		84
26720	2679	1122		81
26800	2189	1127		88
26880	2503	1113		63
26960	2578	1135		73
27040	2543	1130		58
27120	2389	1116		78
27200	2216	1118		64
27280	2529	1125		68
27360	1301	1125		66
27440				
27520	2549	1128		68
27600				
27680				
27760	2649	1126		83
27840	2258	1117		60
27920	1349	1121		63
28000	2220	1117		75
28080	2806	1120		70
28160	2151	1115	2	62
28240	1758	1109		63
28320	2711	1112		64
28400	2577	1121		61
28480	2243	1124		72
28560	2842	1118		68
28640				
28720	2070	1123		82
28800	2340	1121		77
28880	2181	1105		82
28960	2237	1107		86
29040	2507	1122		68
29120	2103	1120		74
29200	2516	1120		74
29280	1901	1128	2	77
29360	2623	1121		72
29440	2695	1119		70
29520	2554	1126		63
29600	1953	1124		71
29680	1948	1119	0	60
29760	2469	1120		71
29840	2352	1114		75
29920	2030	1129		70
30000	1728	1124	6	62
30080	2505	1124		64
30160	3109	1120		64
30240	2404	1122		78
30320	2157	1124		66
30400	2598	1119	2	62

distance [µm]	Mg [ug/g]	Sr [ug/g]	Mn [ug/g]	Fe [ug/g]
30480	1954	1122		82
30560				
30640	2261	1121		61
30720	2077	1128	2	65
30800	2037	1132		60
30880	3207	1104		69
30960	2767	1080	49	139
31040	2156	1130	84	45
31120	2712	1007	5	113
31200				
31280	3126	813	15	446
31360	3982	955	12	243
31440	2329	1092	14	386
31520	1776	1076	6	558
31600	2677	1038	24	358
31680	3483	1015	28	154
31760	2647	1006	66	95
31840	1953	1085	38	106
31920	1598	1159	0	98
32000	1364	1217		77
32080	2560	1183		143
32160	2315	1147	206	13
32240	2382	1167	381	
32320	1623	1163	269	5
32400	1433	1161	165	21
32480	1590	1155	21	97
32560	1957	1124	1	58
32640	2491	1131	168	57
32720	1527	1158	177	274
32800	2889	1037	172	196
32880	2513	801	3	204
32960	2461	804		91
33040	1972	988		61
33120	2208	1013	106	38
33200	3631	920	157	61
33280	2001	937	99	44
33360	1957	1085	149	16
33440	1470	1131	82	16
33520	1949	1145	289	
33600	1078	1143	618	
33680	947	1174	918	
33760	1743	1181	407	
33840	1847	1165	55	52
33920	2317	1150	56	68
34000	1810	1168		72
34080	2793	1193	52	6
34160	2361	1211	26	28
34240	2655	1151	23	54

distance [µm]	Mg [ug/g]	Sr [ug/g]	Mn [ug/g]	Fe [ug/g]
34320	3451	1020		57
34400	2797	1044	7	29
34480	2152	942	84	121
34560	2167	1004	20	139
34640	2728	1101	0	101
34720	2272	1166		39
34800	1959	1186	243	57
34880	2959	1022	1244	
34960	3041	1057	286	
35040	2147	1164	33	708
35120	2709	1153	48	217
35200	1598	1132	87	160
35280	1314	1118	182	40
35360	1508	1100		108
35440	2495	1097		44
35520	1896	1040	5	70
35600	2954	1032	151	64
35680	2341	1112	65	120
35760	2373	1099		44
35840	2269	1085	574	
35920	2710	1043	203	39
36000	3512	1014	61	92
36080				
36160				
36240				
36320				
36400	4112	1076	80	72
36480	3246	1082	4	45
36560	2313	1002	8	76
36640	2181	1007	34	45
36720	2633	1068	48	27
36800	3481	1121	25	47
36880				
36960				
37040	2739	1161	189	28
37120	3037	1140	250	
37200	2412	1142	105	17
37280	2768	1119	59	122
37360	2970	1086	88	347
37440				
37520	3869	911	39	55
37600	2809	986	89	52
37680	2668	1001	91	60
37760				
37840	3018	970	13	233
37920	2431	884	9	848
38000	2895	888	40	400
38080	2797	954	25	76

distance [µm]	Mg [ug/g]	Sr [ug/g]	Mn [ug/g]	Fe [ug/g]
38160	2527	965	71	47
38240	3195	1038	57	190
38320	1597	1052	343	36
38400	3303	1026	238	2
38480	4244	901	698	
38560	2902	873	84	89
38640	2099	942	30	86
38720	2131	1053	179	19
38800	3279	1079	35	51
38880	1638	1135	54	16
38960	1805	1117		161
39040	3493	1102	125	81
39120	2712	1079	536	149
39200	2085	1133	102	326
39280	1724	1129	199	51
39360	2695	1099	189	45
39440	1839	1062	28	110
39520	1557	1086		147
39600	2435	1085		58
39680	2415	1086	45	38
39760	1240	1115	124	52
39840	2912	1117	272	7
39920	2508	1107	136	13
40000	1584	1119		81
40080				
40160	1471	1172	131	26
40240	1779	1168	169	13
40320	2604	1208	34	57
40400	1736	1175	11	107
40480	2563	1160	66	80
40560	2159	1122	173	36
40640	2522	1127	165	24
40720	2114	1170	55	57
40800	1618	1148		54
40880	1292	1158	9	62
40960	2189	1172	9	122
41040	2503	1177	8	99
41120	2141	1130	20	203
41200	2336	1100	132	738
41280	2023	1172	80	186
41360	2116	1162	14	254
41440	1980	1096	14	598
41520	1688	1180	32	140
41600				
41680	2171	1165		110
41760	2918	1140	0	85
41840	2633	1167	156	9
41920	2412	1113		69
42000	1875	1112		75
42080	2298	1125		63
42160	1718	1116		64
42240	2033	1112		55
42320	3034	1106		68
42400	2055	1116		76
42480	2759	1108		65
42560	2659	1107		72
42640	2538	1111		70
42720	1916	1118		71
42800	1752	1117		55
42880				
42960	2369	1118		65
43040	2938	1104		78
43120	2672	1107		74
43200	1885	1118		61
43280	1983	1114		72
43360	2104	1128		86
43440	2245	1126		70
43520	2695	1116		80
43600	2812	1114		75
43680	2127	1116		72
43760				
43840	1706	1124		57
43920	2583	1108		75
44000	2140	1116		82
44080	2109	1113		82
44160	1983	1124		73
44240	2544	1117		71
44320	2599	1118		65
44400	2856	1123		71
44480	2185	1119		71
44560	2269	1120		63
44640	3599	1108		74
44720	1784	1128		68
44800				
44880				
44960	1899	1113	3	79
45040	1859	1117		80
45120	2490	1121		68
45200	2176	1115		58
45280	2154	1119		72
45360	2501	1116		72
45440	1773	1119		56
45520	2888	1117		70
45600	2012	1113		63
45680	2866	1114		58
45760	2092	1116		66

distance [µm]	Mg [ug/g]	Sr [ug/g]	Mn [ug/g]	Fe [ug/g]
45840	2665	1106		62
45920	2464	1117		67
46000	1616	1112		70
46080	3105	1113		71
46160	2154	1120		74
46240	2762	1120		68
46320	2381	1104		60
46400	2543	1125		64
46480	1686	1112		78
46560				
46640	2500	1105		62
46720	2670	1119		68
46800	2241	1122		79
46880	2484	1109		65
46960				
47040	2372	1126		68
47120				
47200	2055	1126		74
47280	2195	1118		76
47360	2112	1111		61
47440	2297	1115		60
47520	2697	1116		60
47600	2675	1124		65
47680	1759	1131		67
47760	1515	1114		54
47840	1611	1121		71
47920	1811	1106		52
48000	2029	1115		63
48080	2719	1121		73
48160	2072	1124		58
48240				
48320	2550	1120		81
48400	2213	1116		57
48480	2537	1116		75
48560	1616	1112		67
48640	2168	1118		64
48720	1724	1119		55
48800	2378	1126		61
48880	2633	1116		65
48960	1987	1123		88
49040	2938	1110		71
49120	1802	1100		56
49200	3149	1109		62
49280	1976	1113		73
49360	2605	1112		78
49440				
49520	2618	1109		67
49600	2744	1121	0	69
49680	2572	1125		82
49760	1888	1110		69
49840				
49920	1793	1124		68
50000	2220	1115		64
50080	2760	1125		79
50160	2711	1112		78
50240	2222	1125		59
50320	2177	1123		70
50400				
50480	2065	1127		54
50560				
50640	2818	1115		66
50720	2123	1110		64
50800				
50880				
50960	1917	1113		66
51040	2664	1104		89
51120	2068	1109		64
51200	1603	1112		68
51280				
51360	2642	1113		65
51440	2439	1120		67
51520	2572	1113		81
51600	2779	1124		58
51680	2663	1110		85
51760	1804	1119	0	71
51840	2250	1115		66
51920	2246	1114		70
52000	2104	1116		62
52080	2508	1111		73
52160	2609	1116		76
52240				
52320	1787	1134		74
52400	2853	1117		75
52480				

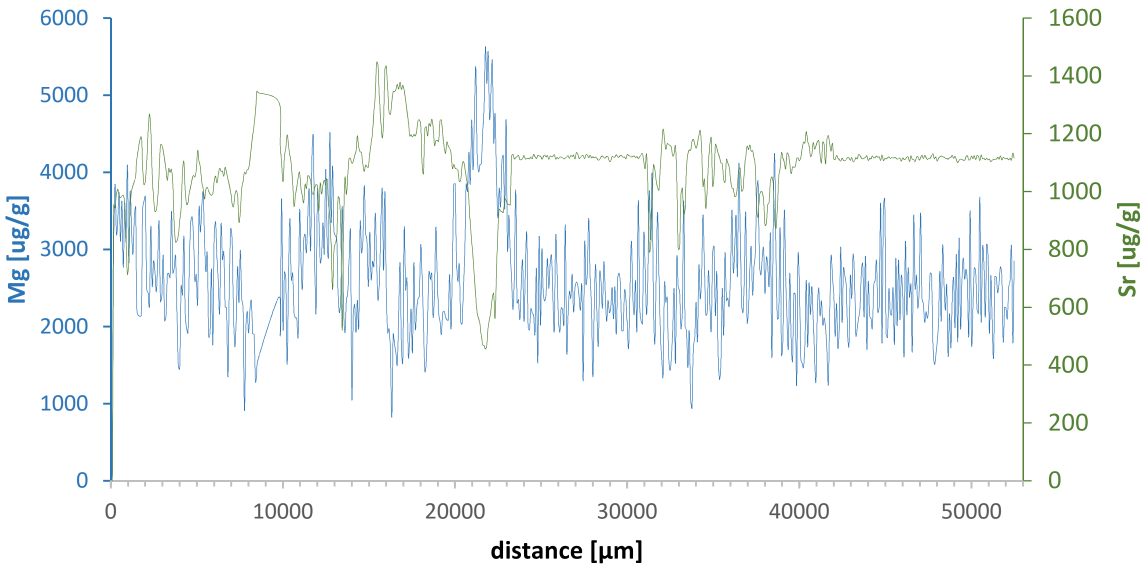

Plotted raw data of Mg and Sr of shell A.

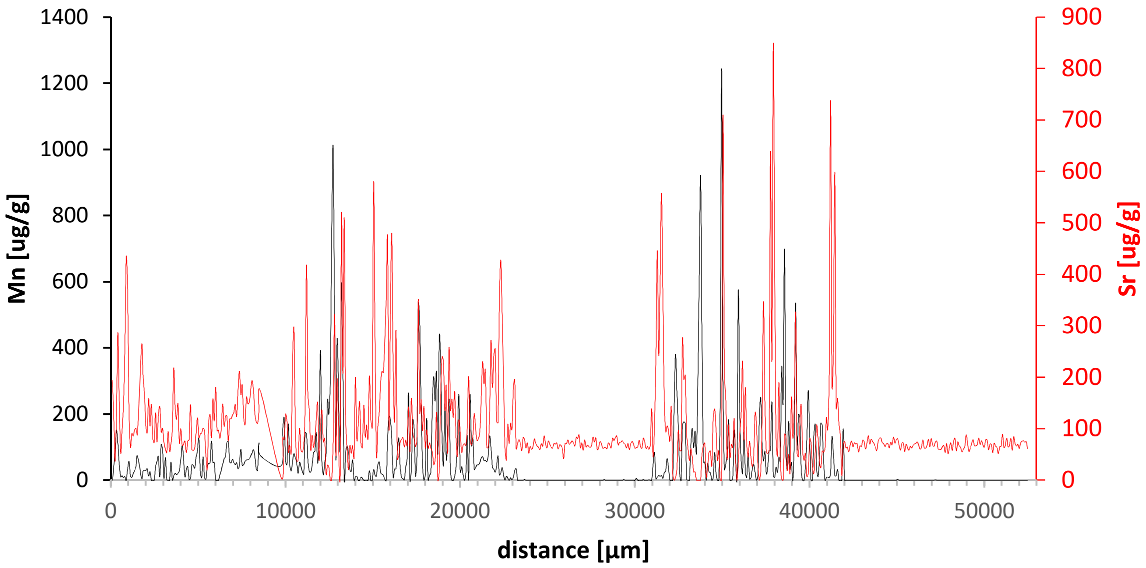

Plotted raw data of Mn and Fe of shell A.

µXRF LINE SCAN RAW DATA OF SHELL FRAGMENT B

distance [µm]	Mg [ug/g]	Sr [ug/g]	Mn [ug/g]	Fe [ug/g]
80	1049	1200		286
160	2581	1194	5	129
240	2029	1279	264	30
320	1760	1318	128	117
400	2457	1337	11	126
480	2741	771		328
560	3249	1229	64	269
640	2236	1490	25	177
720	3627	1231	205	159
800	4102	1167	32	256
880	3507	1183	52	298
960	2955	1205	6	396
1040	2761	1165		342
1120	5733	1115	8	165
1200	3880	1357		405
1280	3311	1401	57	236
1360	2623	1414	5	248
1440	3034	1371	28	180
1520	2265	1348		316
1600	2591	1374		312
1680	2582	1356	2	287
1760	2371	1315		394
1840	3286	1302	177	225
1920	4794	1235	8	226
2000	2847	1208	65	297
2080	3337	1185	67	180
2160	2986	1106	39	187
2240	2329	1211		432
2320	2107	1281	85	270
2400	2275	1286	75	218
2480	1786	1250	9	82
2560	3113	1216	14	189
2640	2285	1237	27	121
2720	2227	1318	440	135
2800	3214	1324	65	181
2880	5029	1293	5	384
2960	2013	1325	20	347
3040	2038	1299	41	646
3120	2280	1350	34	219
3200	1528	1337	38	96
3280	1933	1341	6	109
3360	2182	1331	55	246
3440	1976	1321	284	202
3520	2710	1291	114	164
3600	1795	1289	884	50
3680	2640	1269	576	105
3760	2300	1335	712	185
3840	2523	1426		176
3920	2219	1344	131	111
4000	1692	1286	85	92
4080	1329	1296	57	238
4160	2313	1274	128	244
4240	1945	1241	470	156
4320	2507	1259	435	80
4400	1882	1292	30	318
4480	3519	1285	234	120
4560	3063	1271	59	167
4640	3591	1131	45	225
4720	1862	1270	145	183
4800	3495	1206	281	143
4880	3070	1195	118	137
4960	3044	1261		234
5040	2894	1279	29	221
5120	1872	1234	369	121
5200	2119	1183	3	636
5280	2910	1107	16	272
5360	3040	1238	37	267
5440	3958	1019	28	261
5520	3256	1108	4	386
5600	2073	1185	24	410
5680	3946	1017	24	174
5760	3632	618	30	424
5840	2997	610	90	243
5920	3244	520	37	289
6000	3473	605	31	458
6080	4612	607	19	272
6160	6327	765	0	431
6240	5227	1036	6	451
6320	2472	1152	5	241
6400	2474	1208	87	78
6480	1455	1177	24	240
6560	1815	1150	24	229
6640	2615	1187	2	446
6720	2575	1194	12	361
6800	3649	1178	42	132
6880	2640	1215	61	205
6960	2462	1237		277
7040	2850	1183	0	267
7120	3817	1181	66	192
7200	1861	1232	47	144
7280	2251	1214	339	111
7360	2684	1238	21	254

distance [µm]	**Mg** [ug/g]	**Sr** [ug/g]	**Mn** [ug/g]	**Fe** [ug/g]
7440	1690	1250	13	246
7520	2410	1286		228
7600	3807	1297		116
7680	2823	1296	9	225
7760	2706	1222	59	174
7840	3804	1252	36	215
7920	2765	1280	2	298
8000	2365	1186	9	170
8080	2481	1158	74	156
8160	2612	1142	38	132
8240	2671	942	336	317
8320	3554	716	161	183
8400	3722	894		292
8480	3487	1275	39	330
8560	2724	917	62	183
8640	3026	800	76	236
8720	3462	838	18	176
8800	3098	719	90	221
8880	3405	704	35	330
8960	2712	780	42	153
9040	3142	893	24	280
9120	3835	965	20	469
9200	4487	845	8	256
9280	3104	1254	34	151
9360	2657	1350	20	167
9440	2924	1323	33	153
9520	2152	1253	32	143
9600	1305	1306	300	181
9680	2562	1310	71	254
9760	2247	1266	1	275
9840	2551	1101	124	544
9920	3345	1187	330	213
10000	2095	1233	7	563
10080	3521	1196	56	277
10160	3683	1157		236
10240	2912	1193		234
10320	3755	747	13	555
10400	3186	656	4	255
10480	3172	947		327
10560	3441	825		226
10640	3641	550	62	392
10720	3767	1024	98	374
10800	4396	698	172	202
10880	3865	597	21	244
10960	3668	653	39	209
11040	4013	450	71	419
11120	2876	357	65	514
11200	4603	304	64	390
11280	3283	305	47	477
11360	2775	1315	116	141
11440	1924	1334	231	263
11520	1623	1357	25	425
11600	1397	1392		207
11680	2551	1339	15	235
11760	3205	1407		155
11840	2871	1506		261
11920	1808	1499	11	175
12000	2223	1550	43	473
12080	3006	1520	226	67
12160	3901	1350	115	137
12240	3392	1284	176	570
12320	3173	1479	3	623
12400	1734	1535		248
12480	2128	1582		104
12560	1642	1581	105	141
12640	1593	1538	131	375
12720	2261	1502	194	104
12800	1810	1413	252	260
12880	1485	1277	53	251
12960	1290	1373	10	165
13040	1320	1453	57	328
13120	1746	1465	39	316
13200	2034	1464	3	294
13280	1418	1501		497
13360	1726	1427		357
13440	1540	1397		132
13520	1788	1379	16	635
13600	1293	1389		298
13680	1991	1326	27	242
13760	1112	1347	60	248
13840	1079	1341		209
13920	1365	1383		420
14000	1761	1368	42	301
14080	1933	1328	218	127
14160	1115	1294	476	8
14240	1534	1305	110	205
14320	2192	1329	94	772
14400	1499	1319	56	290
14480	942	1297	19	579
14560	2501	1326	12	150
14640	1826	1270	106	75
14720	1720	1252	798	363
14800		1279	914	152
14880	1785	1268	16	187
14960	1379	1312	33	235
15040	1885	1294	24	300

distance [µm]	Mg [ug/g]	Sr [ug/g]	Mn [ug/g]	Fe [ug/g]
15120	2373	1286		176
15200	1739	1308		237
15280	1092	1343		158
15360	2059	1317		332
15440	1269	1334		231
15520	2444	1316		121
15600	1438	1333		202
15680	1728	1375		193
15760	2425	1329		460
15840	5325	1076		643
15920	4524	897		505
16000	3166	1059		260
16080	3580	1180	7	193
16160	1395	1273	18	482
16240	2198	1283		293
16320	2230	1297		296
16400	3723	1266		360
16480	5619	1106	27	89
16560	4019	1083	73	282
16640	3168	1108	87	121
16720	5165	1069	513	334
16800	4475	1098	108	162
16880	3144	1170	44	143
16960	1839	1116	17	167
17040	1292	1159		185
17120	1577	1191		145
17200	3332	1211	15	131
17280	2167	1195	0	192
17360	2456	1209		224
17440	3463	1189	2	365
17520	3396	1210		213
17600	1975	1211		265
17680	2860	1214	3	191
17760	2324	1262	9	290
17840	5041	1115	366	105
17920	3071	1023		351
18000	3009	1132	2	278
18080	1928	1213	127	195
18160	1608	1258	663	568
18240	2618	1258	786	205
18320	1838	1275	19	153
18400	1412	1241	87	152
18480	1854	1299	73	159
18560	1848	1300	64	127
18640	1924	1249		179
18720	2586	1204	7	360
18800	1887	1234	12	125
18880	2556	1197	91	161
18960	2570	1237		424
19040	2341	1197		138
19120	2484	1207		289
19200	1049	1200		286
19280		!		
19360		!		
19440		!		
19520	5013	376	70	363
19600	3982	551	75	327
19680	3973	455	46	183
19760	5097	402	48	330
19840	4443	364	57	177
19920	4082	331	43	461
20000	4032	313	33	671
20080	4505	328	42	445
20160	3570	329	50	311
20240	4157	319	41	551
20320	4288	299	54	352
20400	4068	291	41	419
20480	4102	266	57	230
20560	4172	273	41	472
20640	4610	266	52	442
20720	3978	285	38	1307
20800	3439	284	8	649
20880	4019	455	5	266
20960	3810	1085	17	250
21040	3510	868	2	533
21120	3753	319	25	351
21200	4376	312	25	470
21280	3471	303	14	599
21360	3908	306	9	771
21440	3727	308	30	413
21520	4403	309	90	267
21600	4050	298	53	442
21680	5132	295	86	447
21760	4241	275	56	350
21840	4081	268	35	706
21920	3942	287	102	316
22000	3946	270	27	793
22080	3742	288	20	496
22160	4739	295	79	157
22240	3666	282	35	509
22320	3614	266	70	309
22400	4619	280	61	473
22480	3627	274	41	315
22560	4659	278	98	639
22640	3867	292	137	169
22720	4516	293	44	602

distance [µm]	**Mg** [ug/g]	**Sr** [ug/g]	**Mn** [ug/g]	**Fe** [ug/g]
22800	4575	298	41	580
22880		!		
22960	2239	381		382
23040	2738	520		181
23120	3645	626	7	251
23200	2943	803		306
23280	2662	912		218
23360	2609	852		236
23440	3586	869		499
23520	2514	1023		276
23600	3055	1155		93
23680	2295	1180	3	438
23760	3520	1188		395
23840	3597	1170		306
23920	3145	1171		212
24000	2565	1201	62	758
24080	2681	1195		192
24160	2569	1219	4	193
24240	2460	1262	23	345
24320	2820	1198	34	755
24400	3307	1271	3	157
24480	2569	1271		203

distance [µm]	**Mg** [ug/g]	**Sr** [ug/g]	**Mn** [ug/g]	**Fe** [ug/g]
24560	2890	1331		255
24640	3995	1333	5	269
24720	2478	1352		120
24800	3193	1336	11	89
24880	4344	1285	75	340
24960	4775	1358	6	75
25040	4694	1156	9	245
25120	3335	1180	28	429
25200	4150	1105	32	350
25280	4030	951	37	592
25360	4086	1013	56	441
25440	3413	1128	50	301
25520	1708	1456	35	139
25600	3534	1376	41	228
25680	3834	980		358
25760	3171	1124		436
25840	3321	1239	31	282
25920	2223	1380	460	296
26000	1488	1452	7	111
26080	2466	1464		238
26160	3430	1429		276
26240	2704	1512	36	498

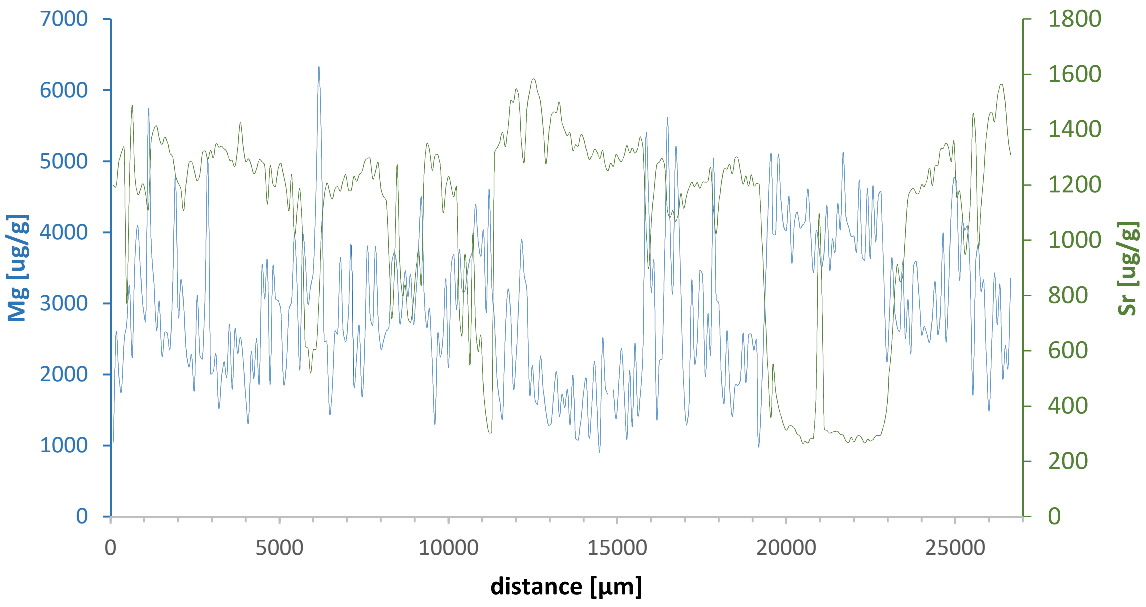

Plotted raw data of Mg and Sr of shell B.

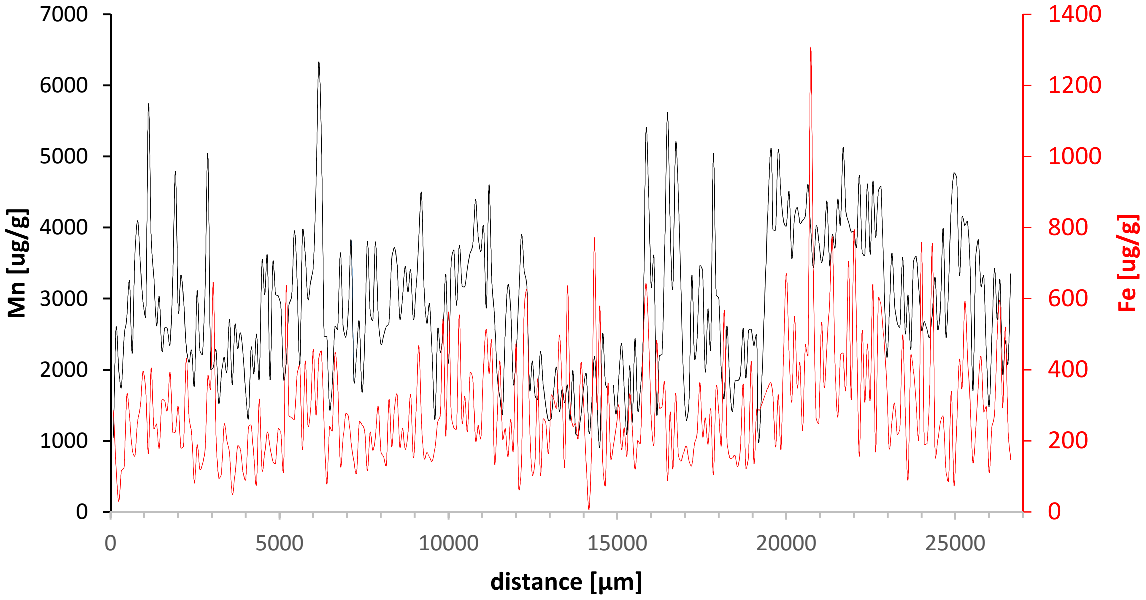

Plotted raw data of Mn and Fe of shell B.

µXRF Line Scan Raw Data of Shell Fragment C

distance [µm]	Mg [ug/g]	Sr [ug/g]	Mn [ug/g]	Fe [ug/g]
70	3491	198	7	209
140	3026	184	9	138
210	3224	189	43	46
280	2628	226	274	20
350	2998	198	353	69
420	4062	197	200	65
490	3534	203	53	137
560	3494	211	82	117
630	3526	201	18	245
700	5329	256	8	234
770	5844	146	355	25
840	4218	135	158	140
910	2663	237	10	61
980	3252	239	22	93
1050	3793	183	78	107
1120	3609	216	94	57
1190	2929	362	46	123
1260	3876	253	15	579
1330	3473	259	53	77
1400	2971	359	50	134
1470	3946	200	32	27
1540	3518	213	29	64
1610	3899	307	46	111
1680	4227	205	26	69
1750	3629	233	37	87
1820	6361	226	60	104
1890	4607	209	199	199
1960	3471	179	281	363
2030	4021	203	64	29
2100	3199	248	89	40
2170	4405	267	42	22
2240	4064	224	30	84
2310	5296	186	23	279
2380	4031	168	22	93
2450	3210	335	29	93
2520	4108	244	63	202
2590	3675	357	46	226
2660	4080	454	20	109
2730	5522	515	26	90
2800	3672	220	66	159
2870	3417	204	62	88
2940	2954	175	122	49
3010	4738	362	13	168
3080	4086	183	29	113
3150	3793	194	24	64
3220	3867	266	43	197
3290	2877	286	45	204
3360	2751	273	49	121
3430	3507	251	189	187
3500	4549	173	75	61
3570	4436	179	77	100
3640	3877	356	42	193
3710	4475	209	32	77
3780	2797	174	57	173
3850	3556	230	42	177
3920	4519	369	13	202
3990	3019	210	19	62
4060	3121	162	8	137
4130	3746	225	15	1803
4200	4147	364	10	130
4270	3872	333	28	145
4340	4160	188	64	54
4410	3964	180	131	80
4480	2853	154	18	388
4550	4092	248	27	135
4620	4144	360	58	164
4690	3131	172	32	186
4760	2907	167	15	172
4830	4545	390	53	78
4900	3788	199	66	223
4970	4340	119	71	138
5040	4580	356	22	72
5110	3635	302	13	113
5180	3627	184	43	225
5250	3470	180	97	355
5320	3829	199	61	317
5390	4760	378	43	262
5460	4645	285	24	467
5530	2907	263	49	91
5600	4225	336	70	94
5670	3642	204	89	226
5740	4511	143	52	497
5810	2988	154	19	78
5880	3068	236		96
5950	3917	404	21	86
6020	3233	225	67	160
6090	2821	159	113	89
6160	3489	160	219	119
6230	2673	172	2	107
6300	2140	220	14	242
6370	4071	329	64	67
6440	6543	312	70	90

distance [µm]	Mg [ug/g]	Sr [ug/g]	Mn [ug/g]	Fe [ug/g]
6510	3447	156	34	484
6580	4573	180	30	117
6650	3953	285	47	344
6720	5776	304	0	137
6790	5375	314	9	85
6860	5249	533	29	212
6930	3956	170	32	56
7000	3684	175	9	170
7070	3231	209	39	54
7140	4401	407	132	102
7210	5327	451	76	323
7280	4204	185	46	270
7350	3068	229	10	63
7420	5335	332	171	203
7490	5398	606	573	14
7560	3776	312	187	176
7630	3086	369	32	185
7700	5008	353	32	127
7770	4670	229	20	102
7840	2948	227	2	92
7910	3857	233	50	329
7980	2898	353	78	135
8050	2610	446	39	117
8120	5492	379	9	186
8190	3873	345	30	151
8260	5259	451	7	23
8330	4597	225	94	111
8400	3570	221	399	
8470	3912	250	40	108
8540	3685	440	35	353
8610	7523	647	28	334
8680	4297	242	45	91
8750	4207	223		258
8820	5163	337	147	289
8890	4597	350	50	584
8960	4525	256		830
9030	4139	284	35	125
9100	4192	330	47	140
9170	3636	212	57	123
9240	4993	237	23	177
9310	4582	233	70	186
9380	4043	204	105	123
9450	3762	135		79
9520	4497	175	46	279
9590	3122	263	39	193
9660	3538	257	88	157
9730	3748	231	43	221
9800	4044	261	69	400
9870	4696	260	66	278
9940	4046	271	206	102
10010	3320	345	54	4895
10080	4538	277	61	2381
10150	4245	297	22	591
10220	4570	271	14	223
10290	4410	199	43	283
10360	3350	177	100	215
10430	2685	272	46	521
10500	3542	314	21	152
10570	2976	288	79	487
10640	3076	218	16	265
10710	3387	289	18	588
10780	3532	290	35	683
10850	3516	202	99	123
10920	3320	238	59	294
10990	3301	271	41	342
11060	3191	332	55	506
11130	3930	293	119	212
11200	3776	217	284	90
11270	3063	242	161	185
11340	3460	338	34	150
11410	4932	352	50	126
11480	5202	297	257	304
11550	3736	318	198	177
11620	4239	349	21	213
11690	3996	236	5	164
11760	2987	195	6	153
11830	3096	201	29	469
11900	2985	279	81	466
11970				
12040	3247	462	48	184
12110	6030	528	14	607
12180	4410	450	147	136
12250	2780	489	32	155
12320	4010	413	28	347
12390	3852	392	48	403
12460	4149	361	38	762
12530	3944	369	32	1148
12600	2647	349	38	142
12670	4426	301	45	40
12740	4560	233	35	427
12810	3846	251	56	232
12880	4219	257	28	161
12950	5995	304	35	206
13020	3948	207	161	365
13090	3939	256	37	221
13160	3726	241	182	52

distance [µm]	**Mg** [ug/g]	**Sr** [ug/g]	**Mn** [ug/g]	**Fe** [ug/g]
13230	3729	227	195	34
13300	3756	226	38	368
13370	3356	246	28	450
13440	4412	172	397	620
13510	3465	189	44	104
13580	3700	204	6	351
13650	3549	227	16	679
13720	3275	250	62	356
13790	3288	190	127	180
13860	3164	184	11	128
13930	3256	233	35	294
14000	2903	232	3	117
14070	3992	252	30	136
14140	4790	296	10	197
14210	4557	229	8	668
14280	3377	211	11	535
14350	5752	233	98	101
14420	3322	350	36	107
14490	3861	456	320	124
14560	4637	219	89	333
14630	3532	262	133	485
14700	3737	240	31	247
14770	3530	270	145	69
14840	3936	253	372	257
14910	4657	243	45	449
14980	3539	208	25	272
15050	3201	159	4	187
15120	3282	183	44	128
15190	3298	177		95
15260	3153	254	5	114
15330	3116	166	116	89
15400	3677	200	6	255
15470	3741	168	29	510
15540	4154	208	128	87
15610	4089	209	53	201
15680	2436	191	64	312
15750	4000	193	120	577
15820	2830	209	69	174
15890	3016	207	44	267
15960	3234	243	73	156
16030	3635	237	35	259
16100	5346	318	4	539
16170	4689	237	12	304
16240	4144	167	21	81
16310	3323	300	23	259
16380	3006	241	29	244
16450	3237	248	26	205
16520	3909	228	67	174
16590	5662	279	114	231
16660	5249	226	148	166
16730	3917	402	108	176
16800	2792	308	71	332
16870	3555	268	32	403
16940	4772	279	6	219
17010	4036	392	9	780
17080	4070	230	6	510
17150	3411	321	67	225
17220	4101	366	24	315
17290	4621	564		907
17360	4986	509		664
17430	4333	498	67	299
17500	3750	507	47	430
17570	3249	268		106
17640	3190	248	2	78
17710	3169	354	32	70
17780	3221	268	7	176
17850	3104	213		79
17920	4889	349	6	212
17990	3224	200	11	483
18060	4105	158		159
18130	3857	152		197
18200	4100	194	48	171
18270	4140	209	6	60
18340	3844	188	383	29
18410	4556	305	164	111
18480	4774	276	234	129
18550	4620	198	111	135
18620	3918	229	213	6
18690	3812	308	154	30
18760	4322	336	8	108
18830	4457	155	6	245
18900	3230	146		153
18970	3335	166	37	143
19040	4057	218	41	312
19110	3807	174		66
19180	3720	216	57	169
19250	3292	235	346	
19320	5707	229	2	74
19390	5880	171	18	137
19460	3028	198	73	50
19530	3527	185	501	121
19600	3538	198	503	28
19670	2536	181	260	265
19740	3710	242	132	195
19810	3368	253	113	61
19880	4556	291	27	94

distance [µm]	Mg [ug/g]	Sr [ug/g]	Mn [ug/g]	Fe [ug/g]
19950	6799	385	2	88
20020	3992	225	29	161
20090	3373	196	5	389
20160	3008	194		173
20230	4066	219	9	454
20300	4470	437	10	175
20370	4779	253	9	146
20440	4153	146	8	320
20510	3463	125	12	680
20580	2949	177	148	233
20650	2621	257	205	522
20720	3247	219	412	541
20790	5374	434	87	359
20860	5071	207	135	63
20930	4314	201	24	211
21000	3058	250	32	78
21070	3919	167	38	40
21140	2999	172	60	114
21210	2504	320	70	255
21280	3537	681	72	207
21350	4560	251	72	60
21420	2815	129		61
21490	4136	161	24	252
21560	3015	186	286	76
21630	4472	291	232	77
21700	4519	453	44	153
21770	5906	369	7	135
21840	3289	242	13	272
21910	3354	227	41	187
21980	3246	277	66	279
22050	4111	239	83	181
22120	5031	368	39	249
22190	4504	172	63	268
22260	3911	195	141	191
22330	3425	159	78	103
22400	3431	205	35	297
22470	3505	180	59	542
22540	3191	290	24	219
22610	3373	175	40	87
22680	4179	160	49	109
22750	3845	162	15	219
22820	3098	127	143	28
22890	3882	131	7	103
22960	4219	290	36	247
23030	5965	404	40	90
23100	4789	155	115	97
23170	3870	135	128	99
23240	3739	216	496	85
23310	3338	298	40	136
23380	3101	173	17	567
23450	2949	197	393	
23520	4929	317	71	135
23590				
23660	3557	131	164	470
23730	3188	156	71	265
23800	3074	158	122	395
23870	3500	214	100	394
23940	3634	192	22	170
24010	4236	218	52	167
24080	4035	317	130	201
24150				
24220	3374	251	30	160
24290	4690	239	21	61
24360	3204	168	6	259
24430	4618	152	24	231
24500	3659	191	28	795
24570	2711	191	27	490
24640	3996	168	27	500
24710	4392	218	14	322
24780	4477	301		163
24850	5232	191		236
24920	4238	168	82	132
24990	3498	158	203	298
25060	4856	190	131	60
25130	3056	197	144	81
25200	3304	222	33	126
25270	4235	169	36	170
25340	4283	231	41	530
25410	3751	207	35	621
25480	5610	274	46	343
25550	5675	154	91	459
25620	3960	166	42	87
25690	3223	217	27	26
25760	4775	239	371	21
25830	3547	202	105	294
25900	3805	253	97	26
25970	4689	275	25	130
26040	5362	365	2	267
26110	5295	251	242	108
26180	4632	213	25	146
26250	3669	232	69	29
26320	4382	282		104
26390	4138	209		160
26460	3762	230		77
26530	3644	210	21	160
26600	1832	282	21	448

distance [µm]	Mg [ug/g]	Sr [ug/g]	Mn [ug/g]	Fe [ug/g]
26670	3292	241	0	2566
26740	2928	191	13	123
26810	3523	209	41	325
26880	4391	376	54	129
26950	5363	242	32	203
27020	4013	172	13	64
27090	3565	184	32	466
27160	3775	190	24	264
27230	4255	149	75	216
27300	3222	247	153	65
27370	4481	316	53	83
27440				
27510	4016	136	97	74
27580	3965	128	18	351
27650	4177	159	18	308
27720	3059	313	101	167
27790	3673	186	6	148
27860	4246	146	8	690
27930	3547	156	10	429
28000	3190	145	1	518
28070	3404	286	17	330
28140	3081	177	7	157
28210	3769	154	11	207
28280	3292	151	4	397
28350	3435	175		60
28420	2857	172		77
28490	3788	180	22	323
28560	3421	281	42	173
28630	4921	250	10	749
28700	3978	157	7	149
28770	4075	150	22	162
28840	3942	146	48	426
28910	2884	149	49	318
28980	2878	203	49	253
29050	3319	258	129	109
29120	5248	185	82	94
29190	4111	177	32	88
29260	4058	154	2	44
29330	2180	183	6	102
29400	4306	228	21	85
29470	4115	163	92	78
29540	3856	142	11	201
29610	2933	131	14	257
29680	3145	130	30	144
29750	4391	132	66	135
29820	2758	208	17	604
29890	3152	183	2	767
29960	3817	151	208	129
30030	4158	191	112	83
30100	3449	182	82	115
30170	4082	166	27	102
30240	3745	145	19	183
30310	4045	139	0	368
30380	3862	88	15	139
30450	3943	149	38	73
30520	2883	178	44	100
30590	2542	186	60	217
30660	2932	208	8	306
30730	3770	166		213
30800	3889	164	3	211
30870	4987	242	13	82
30940	4013	185	18	269
31010	3840	194	5	217
31080	3491	198	7	209
31150	2648	356	26	281
31220	2995	586		269
31290	3167	774	48	581
31360	2986	991	95	212
31430	2388	1092		338
31500	2934	1125		141
31570	4097	1198	130	399
31640	4042	1227	122	311
31710	3479	1298	48	152
31780	4032	1292	187	161
31850	4531	1261	133	268
31920	2385	1291	84	351
31990	6504	1284	148	215
32060	8501	1283	91	480
32130	7245	1252	62	251
32200	3644	1241	93	88
32270	3308	1188	107	55
32340	2796	1225	17	112
32410	2323	1263		83
32480	1612	1299		190
32550	2573	1322		141
32620	2130	1319		128
32690	2388	1297	2	72
32760	2900	1319		66
32830	1773	1106		137
32900	1824	1001		82
32970	2465	1041	4	125
33040	2104	1105		88
33110	1383	1193		275
33180	1254	1268	30	158
33250	1849	1261	140	151
33320	1864	1239	11	235

distance [µm]	Mg [ug/g]	Sr [ug/g]	Mn [ug/g]	Fe [ug/g]
33390	2171	1274		171
33460	2418	1285		152
33530	1994	1285		87
33600	2564	1239		148
33670	2365	1279		147
33740	2247	1268	9	168
33810	2989	1258	27	180
33880	3703	1206	22	344
33950	3998	1151	18	181
34020	2494	1196	51	507
34090	2988	1238	134	302
34160	1641	1301	211	403
34230	3079	1279	107	1119
34300	2273	1300		150
34370	2025	1316	19	281
34440	2213	1298	229	146
34510	3049	1273	174	56
34580	3787	1206	82	249
34650	2788	1209		263
34720	3009	1198	1	343
34790	3329	1192		220
34860	3027	1194		239
34930	3764	1223		222
35000	4750	1281		179
35070	3835	1191	4	103
35140	5063	1067		205
35210	6987	1211	12	184
35280	5642	863	16	447
35350	4060	903	21	319
35420	3375	969	64	226
35490				
35560	5438	961	4	379
35630	4367	710	7	189
35700	3003	790	25	245
35770	3559	910		152
35840	2884	998		69
35910	3320	956	20	194
35980	1678	1131	15	325
36050	3102	1181	9	121
36120	1575	1271	5	98
36190	1622	1295	15	491
36260	2278	1302	12	116
36330	3037	1309	35	141
36400	2745	1309	86	210
36470	2288	1340	124	196
36540	1251	1294	62	147
36610	1032	1305	91	299
36680	1358	1365	48	391
36750	1411	1327	281	68
36820	2417	1292	307	105
36890	1760	1312	154	534
36960	1921	1329	94	143
37030	1684	1302	293	337
37100	2030	1302	511	26
37170	1551	1352	373	11
37240	1860	1337	390	88
37310	1610	1303	102	82
37380	1881	1251	45	248
37450	2008	1293	216	91
37520	976	1316	24	334
37590	1760	1366	6	144
37660	2193	1322	18	321
37730	1304	1342	27	166
37800	2659	1403	183	244
37870	7333	1304	202	168
37940	4942	1403	295	30
38010	4034	1497	269	174
38080	3159	1490	478	
38150	2582	1486	538	95
38220	3613	1537	495	218
38290	2284	1479	371	124
38360	2900	1426	183	40
38430	2514	1373		103
38500	2514	1381	23	121
38570	2494	1342	134	30
38640	2681	1373	55	119
38710	2123	1405	113	76
38780	1424	1421	154	239
38850	2220	1441	356	32
38920	1797	1393	141	80
38990	2741	1386	94	31
39060	3251	1368		78
39130	2759	1380		98
39200	1298	1405		79
39270	3154	832	7	83
39340	3912	577	10	83
39410	3294	555		229
39480	2977	573	22	192
39550	3643	1100	16	267
39620	3061	1332		137
39690	3689	1354	13	102
39760	2332	1409	38	201
39830	2817	1413	127	403
39900	4269	1138	125	251
39970	3796	930	112	134
40040	4417	804	48	303

distance [µm]	Mg [ug/g]	Sr [ug/g]	Mn [ug/g]	Fe [ug/g]
40110	3598	663	21	158
40180	4986	520	13	124
40250	4300	490	43	391

distance [µm]	Mg [ug/g]	Sr [ug/g]	Mn [ug/g]	Fe [ug/g]
40320	3628	418	65	497
40390	4166	459	32	177

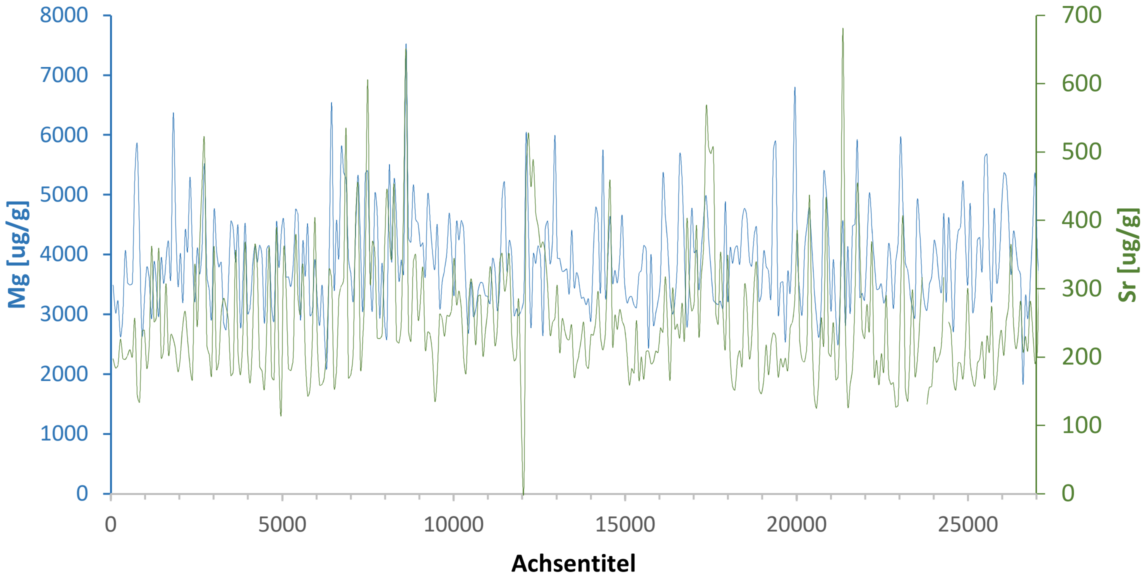

Plotted raw data of Mg and Sr of shell C.

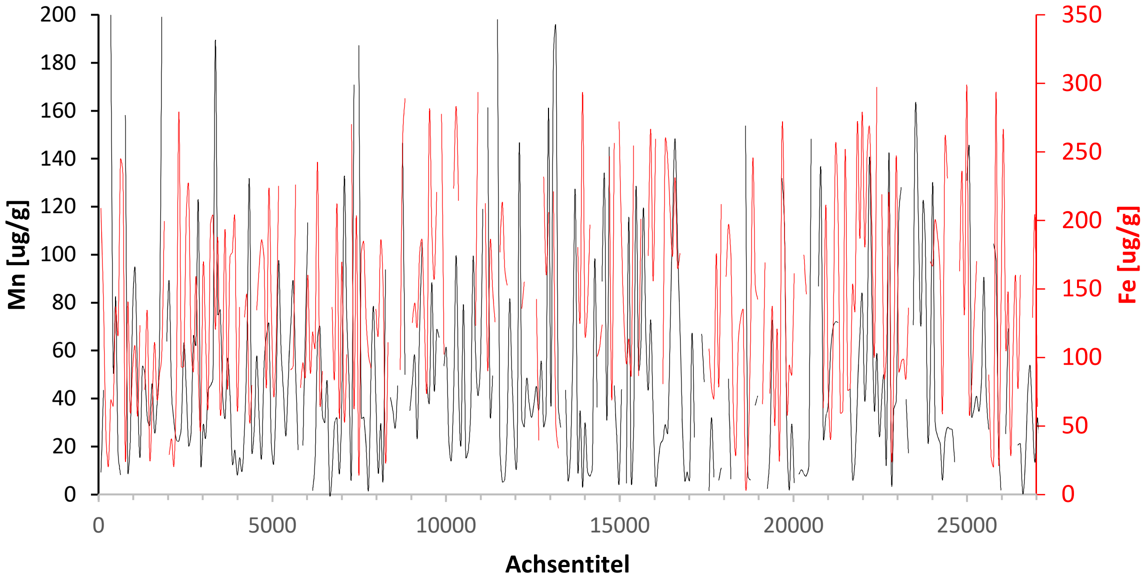

Plotted raw data of Mn and Fe of shell C.

µXRF LINE SCAN RAW DATA OF SHELL FRAGMENT D

distance [µm]	Mg [ug/g]	Sr [ug/g]	Mn [ug/g]	Fe [ug/g]
100	1824	1326	145	16
200	1347	1305	30	20
300	1515	1285	66	28
400	1098	1284	172	15
500	1279	1261	106	37
600	1158	1276	3	78
700	1039	1280		52
800	1767	1290		147
900	2186	1248	112	113
1000	1741	1280	47	142
1100	977	1252	17	206
1200	2020	1275		122
1300	1384	1231	6	95
1400	1132	1249	14	308
1500	1226	1233		19
1600	991	1263	19	135
1700	1025	1273	29	171
1800	1416	1284		59
1900		1302		72
2000		1271		44
2100	997	1241		99
2200	1598	1197		365
2300	1139	1154		350
2400	2077	1103		91
2500	1166	1240		88
2600	1614	1221	6	42
2700	1342	1194	36	39
2800	2913	1191	18	57
2900	3313	1066	26	118
3000	3655	826	42	98
3100	2355	1201	15	53
3200	1708	1290	19	159
3300	1619	1327	27	444
3400	1872	1334	76	38
3500	966	1313	74	69
3600	1674	1287	43	31
3700	1220	1275		29
3800	875	1295	226	139
3900	1663	1274	186	125
4000	3065	1180	29	50
4100	1425	1285	11	28
4200	840	1298	8	61
4300	2317	1230	24	64
4400	1223	1346	10	29
4500	1038	1289	41	192
4600	1893	1282	272	154
4700	3089	1239	157	49
4800	1744	1232	55	58
4900	1883	1271		51
5000	1831	1263		28
5100	2453	1270	43	59
5200	1704	1298	57	196
5300	1833	1231	31	73
5400	2023	1214		116
5500	1697	1202	10	251
5600	1996	1196	164	26
5700	2882	1180	43	153
5800	1710	981		65
5900	2998	803	399	19
6000	2852	808	24	463
6100	2514	659	39	85
6200	3151	565		293
6300	3086	556	107	128
6400	3829	451	16	164
6500	3362	301	43	93
6600	2682	241	83	157
6700	3074	250	68	106
6800	3446	260	64	128
6900	3028	325	51	151
7000	4921	376	48	124
7100	3466	346	118	196
7200	3459	321	116	130
7300	4671	340	26	124
7400	3845	396	97	245
7500	3566	398	69	188
7600	2999	308	47	127
7700	2785	321	52	118
7800				
7900	1729	1348	12	270
8000	2037	1291	25	356
8100	1381	1297	40	186
8200	1182	1314	4	156
8300	998	1343		31
8400		1403	64	135
8500	1251	1357	209	32
8600	1251	1373	349	108
8700	960	1352	188	110
8800	1158	1308	16	65
8900		1336	6	57
9000	976	1323	761	
9100	1312	1317	238	42
9200	1687	1389	12	441

distance [µm]	**Mg** [ug/g]	**Sr** [ug/g]	**Mn** [ug/g]	**Fe** [ug/g]
9300		1262	1	118
9400	1456	1290	143	38
9500	865	1253	114	78
9600	934	1251	99	155
9700	766	1288	782	
9800	1510	1285	45	351
9900		1312	267	1
10000	2256	1321	0	43
10100	1331	1302	53	15
10200	2222	1310	174	31
10300	1015	1266	23	61
10400	1396	1248	158	31
10500	2610	1267	13	80
10600	1405	1303	284	215
10700	1772	1275	73	67
10800	1444	1280	20	51
10900		1273	51	534
11000	1025	1341	115	151
11100	1807	1295	17	35
11200	1680	1352	133	15
11300	1637	1296	131	71
11400	1379	1344	150	107
11500	1066	1344	121	34
11600	1552	1397	11	69
11700	1495	1383	77	44
11800	907	1350	26	23
11900	881	1380	116	94
12000	1678	1416	140	10
12100	1604	1405		18
12200	1181	1416	24	79
12300	984	1380		35
12400	856	1378	49	85
12500	1263	1412	19	66
12600	1234	1392	5	149
12700	907	1378	126	84
12800	1810	1367	379	
12900	1902	1392	4	23
13000	774	1426		2640
13100	1559	1437	43	48
13200	1151	1377	7	109
13300	1183	1352		208
13400	1687	1393		57
13500	1524	1387		69
13600	1158	1380		72
13700	1215	1403	104	39
13800	1292	1328	63	49
13900	1593	1339	48	319
14000	2148	1406		437
14100	1504	1417	2	82
14200	1445	1383	61	57
14300	1488	1383	251	56
14400	1361	1348	726	123
14500	1664	1381	27	93
14600	1190	1414		147
14700	1631	1383	28	81
14800	1510	1392		140
14900	1705	1457	12	111
15000	1133	1454	12	89
15100	1868	1451	21	69
15200	1137	1424	13	17
15300	929	1426	9	83
15400	1712	1371	75	26
15500	2099	1374	20	118
15600	1511	1366	21	664
15700	1547	1376	58	491
15800	1577	1384	34	519
15900	1893	1317	3	157
16000	1943	1351	19	75
16100	1536	1344		121
16200	1048	1336		117
16300	1162	1344		144
16400	797	1348	147	80
16500	763	1366	61	53
16600	2244	1364	38	34
16700	1086	1334	34	26
16800	797	1386		105
16900	1439	1424	81	19
17000	1865	1423	26	81
17100	1765	1348		83
17200	1425	1363	35	37
17300	874	1371	12	311
17400	1703	1313	7	95
17500	1881	1305		52
17600		1357	5	131
17700	1910	1358	2	77
17800	1601	1391	70	155
17900	1191	1343	1	91
18000	1511	1290		50
18100	1698	1280	13	140
18200	1727	1302	98	32
18300	2275	1339	263	22
18400	1856	1324	304	
18500	1238	1352	99	22
18600	2683	1344	55	42
18700	1340	1323	20	75
18800	2044	1293		105

distance [µm]	Mg [ug/g]	Sr [ug/g]	Mn [ug/g]	Fe [ug/g]
18900	1325	1292	36	96
19000		1382	1	74
19100	1081	1357	2	176
19200	1800	1342	73	217
19300	1800	1323	88	219
19400	1039	1317	27	19
19500	1832	1354	28	75
19600	1844	1349	100	82
19700	1501	1374	128	
19800	1087	1351	16	150
19900	1487	1320	40	121
20000				
20100	737	1281	3	52
20200	907	1345	8	52
20300	1557	1363	4	32
20400	1717	1357		121
20500	2050	1360		120
20600	2234	1316	13	315
20700	1641	1369	268	4
20800	1487	1377	102	92
20900	746	1340	17	82
21000	1441	1353		48
21100	2022	1342	9	64
21200	1898	1335	7	13
21300	1730	1330	49	33
21400	2277	1321	516	
21500	1051	1313	88	942
21600	1702	1325	38	112
21700	821	1315	34	36
21800	809	1332		69
21900	1579	1309	6	30
22000	1097	1310	13	77
22100	1206	1321	25	74
22200	915	1335	64	72
22300		1356	40	133
22400	1375	1332	45	57
22500	1222	1322		35
22600	1274	1333		45
22700	755	1337		69
22800	1451	1335	132	86
22900	1811	1265	369	45
23000	1424	1238	20	51
23100	1545	1159	113	59
23200	1156	1135	713	9
23300	1989	1100	17	97
23400	1268	1277		73
23500	1596	1273		147
23600	1177	1281		78
23700	995	1322	12	80
23800	1666	1308		195
23900	1528	1304	33	201
24000		1285	795	
24100	1184	1296	215	18
24200	919	1289	26	55
24300	1958	1286	2	257
24400	1405	1331	205	257
24500	928	1316	261	58
24600	1280	1319	49	41
24700	1198	1354		338
24800	1815	1357		233
24900	1873	1319	6	83
25000	1086	1287	12	125
25100	2031	1300		148
25200	1523	1324		60
25300	763	1337	27	69
25400	1049	1302		235
25500	765	1291		309
25600	3943	1239	90	272
25700	2290	1228	9	174
25800	2327	1246	6	73
25900	1566	1260		64
26000	1381	1235		17
26100	1991	1277	306	
26200	1086	1287	16	32
26300	870	1329		76
26400	1081	1308	11	71
26500	854	1294	38	65
26600	767	1273	24	127
26700	933	1279	45	122
26800	1831	1259		101
26900	1334	1221	64	26
27000	1230	1267	249	196
27100		1260	13	73
27200	1488	1243	36	28
27300	1728	1252	168	191
27400	1741	1248	144	156
27500	2254	1175	177	
27600	2995	1104	36	61
27700	1621	1198	18	92
27800	2227	1232	42	101
27900	1479	1217	139	327
28000	1672	1232	14	257
28100	1567	1228	42	109
28200	1168	1261	306	309
28300	998	1219	57	40
28400		1227	7	44

distance [µm]	Mg [ug/g]	Sr [ug/g]	Mn [ug/g]	Fe [ug/g]
28500	1180	1232	65	15
28600	995	1247	27	162
28700	1259	1224	45	125
28800	953	1272	282	7
28900	1689	1288	95	
29000	1546	1271	6	47
29100	2169	1277	34	53
29200		1254	69	21
29300	2147	1197	143	48
29400	3434	1124	55	131
29500	2274	1120	116	490
29600	1755	1136	24	120
29700	2219	1048		67
29800	1755	1188		79
29900	1322	1201		108
30000	1374	1268	30	177
30100	1062	1212	83	28
30200	772	1241		68
30300	1404	1274	64	12
30400	1521	1240	194	20
30500	1200	1260	22	26
30600	1569	1273	58	11
30700	788	1289	23	38
30800	830	1292	397	11
30900	1079	1250	94	15
31000	841	1289	358	24
31100	2187	1252	115	
31200	2477	1287	141	118
31300	1156	1315	112	174
31400	753	1306	34	77
31500	1163	1268	38	93
31600	2009	1249		91
31700	2201	1297		51
31800		1271	43	218
31900	2226	1237	68	161
32000	1648	1266	14	31
32100	1794	1299	20	49
32200	1477	1276	97	24
32300	1248	1231	3	152
32400	2524	1193		135
32500	1435	1263		119
32600	957	1247	194	70
32700	1065	1294	316	
32800		1317	76	39
32900	1431	1311	197	70
33000	1481	1279	107	30
33100	1131	1314	214	
33200	**1476**	**1336**	**326**	**16**
33300	1132	1298	14	46
33400	1830	1359	26	116
33500	1515	1387	36	145
33600	1609	1322	88	16
33700	1485	1304	222	61
33800	757	1337	61	49
33900	1748	1121	35	32
34000	1737	1188	10	97
34100		1270		170
34200	804	1295		103
34300	1280	1297	0	90
34400	1322	1289	16	113
34500		1310	27	1575
34600	1049	1288	51	54
34700	1097	1259	82	24
34800	1286	1275		47
34900	1021	1284		44
35000	1483	1270		65
35100	1315	1241		14
35200	1583	1260	21	109
35300	856	1270	30	94
35400		1256	11	55
35500		1250	7	402
35600		1225	14	658
35700	2330	1223	73	37
35800	1168	1232	73	25
35900	1121	1220	41	73
36000		1256		194
36100	1118	1309		21
36200		1352		65
36300	1026	1306		15
36400	1041	1255	6	55
36500	1436	1295		93
36600	745	1287	17	133
36700	818	1323	15	40
36800	1420	1385	32	293
36900	976	1387	46	136
37000	1268	1277	368	59
37100	1542	1255	183	63
37200	1513	1272		126
37300	1418	1341		264
37400	1578	1350		597
37500	798	1368	32	483
37600	2478	1310	283	442
37700	805	1355	66	125
37800	819	1301	39	188
37900		1290	85	150
38000	**1221**	**1324**	**324**	

distance [µm]	Mg [ug/g]	Sr [ug/g]	Mn [ug/g]	Fe [ug/g]
38100	1617	1295		104
38200		1280		64
38300	1443	1268	90	92
38400	2047	1269	57	38
38500	1719	1295	145	10
38600	1084	1279	141	17
38700	2047	1287	262	
38800	2112	1332	279	93
38900	1026	1196	50	80
39000	1330	1167	80	132
39100	1232	1255	5	113
39200	1469	1267	4	248
39300	1091	1330		46
39400	1056	1313		99
39500	826	1345		185
39600	1626	1370	2	39
39700	1896	1369	417	
39800	1272	1313	25	49
39900	801	1279		89
40000	1387	1289	740	9
40100		1291	1329	
40200	1660	1336	52	48
40300	1045	1366	6	24
40400	1055	1266		29
40500	1219	1304	24	14
40600	775	1323		42
40700	1844	1326	29	38
40800	1654	1323		169
40900	1702	1324		54
41000	923	1322	22	49
41100	1136	1349	110	114
41200	1432	1350	124	27
41300	1556	1343	62	89
41400	1367	1313	5	356
41500	929	1343	135	125
41600	1523	1340	9	242
41700	2850	1677	38	1096
41800	1610	1902	354	606
41900	1764	1835	254	462
42000	1453	1717	29	258
42100	1772	1598	148	24
42200	1313	1517	18	159
42300	1481	1598	31	267
42400	1411	1520	21	622
42500	1643	1518	15	379
42600	2601	1544	21	457
42700	2868	1495	38	380
42800	2086	1512	14	858
42900	1868	1570	48	341
43000	2686	1599	15	325
43100	1959	1590		504
43200	1678	1594		588
43300	1097	1493		440
43400	1863	1442		274
43500	1790	1364		350
43600	1706	1315	7	328
43700	2034	1403	3	523
43800	1307	1339	2	90
43900	768	1314		435
44000	2382	1359		1414
44100	2034	1395		316
44200	1815	1413	11	532
44300	1864	1431	3	257
44400	1477	1427		23
44500	1693	1401	73	321
44600	2730	1329	167	117
44700		1373	378	527
44800	2274	1385	100	357
44900	1988	1364	83	572
45000	1596	1446	137	646
45100	2099	1451	149	577
45200	1223	1438	5	332
45300	2060	1428	60	435
45400	2087	1476	2	419
45500	4889	1387	13	310
45600	813	1465	269	110
45700				
45800	2536	1384	51	237
45900	919	1323	15	205
46000	804	1320	1	242
46100	1187	1359		227
46200	1226	1345	37	253
46300	1552	1371		222
46400	1134	1432		189
46500	1766	1366	14	245
46600	860	1281	16	150
46700	1557	1364	14	419
46800	1835	1385	15	379
46900	1315	1201	11	216
47000	1670	1348		409
47100	1159	1354		437
47200	874	1452		68
47300	1515	1323		28
47400	1464	1405		65
47500	1783	1247		48
47600		1274	27	59

distance [µm]	Mg [ug/g]	Sr [ug/g]	Mn [ug/g]	Fe [ug/g]
47700	1530	1378	41	143
47800	1381	1461	39	61
47900	1166	1382	46	52
48000	1640	1377	36	61
48100	1919	1384	20	75
48200	1434	1389	4	35
48300	798	1429	8	70
48400	1126	1409	8	27
48500	992	1445	11	51
48600	1768	1383	102	114
48700	1210	1364	420	
48800	1209	1364	20	52
48900	1834	1435	16	63
49000	1401	1421	20	71
49100	893	1432	43	104
49200	895	1431	282	144
49300	1254	1434	189	34
49400	2244	1429	138	21
49500	805	1427	4	30
49600	2168	1360		113
49700	892	1331	873	
49800	1110	1324	881	
49900	1058	1370	604	14
50000	1255	1341	901	
50100	1085	1384	428	10
50200		1368	132	120
50300	1422	1355	207	220
50400	1545	1318	97	46
50500	1646	1397	101	399
50600	1835	1367	114	78
50700	3439	1336	409	182
50800	2343	1335	297	53
50900	787	1330	3	266
51000	1353	1284		55
51100	1593	1242		142
51200	919	1296	21	197
51300	1223	1364	5	42
51400	1022	1320		34
51500	1304	1345		109
51600	1246	1252		54
51700	1164	1369	2	154
51800	1587	1343		52
51900		1285		40
52000	1193	1321		79
52100	1773	1305		21
52200	893	1364	10	90
52300	1088	1326	12	31
52400	1188	1302	29	60
52500	1523	1366	167	25
52600	1307	1310	169	55
52700		1298	2	36
52800	1586	1277	5	27
52900		1331		75
53000	1200	1281		22
53100	1065	1278		30
53200	995	1274		39
53300		1296	8	53
53400	1195	1264	4	37
53500	774	1244	26	51
53600	904	1286	60	41
53700	960	1344	186	10
53800		1249	427	
53900	1497	1298	374	76
54000	1653	1234	563	122
54100	1210	1246	1276	
54200	1311	1248	736	
54300		1245	89	
54400	776	1305		34
54500	1012	1325		51
54600	1048	1324		72
54700	2121	1251		45
54800	987	1320		85
54900	942	1276		112
55000	1007	1230		93
55100	832	1264		64
55200		1247	9	245
55300	1610	1285		55
55400		1275	2	50
55500	1299	1216	101	22
55600		1178	83	215
55700	1930	1015	76	103
55800	2702	1132	9	79
55900	963	1246	25	37
56000	2042	1298	29	49
56100		1306	13	9
56200	838	1286	19	18
56300		1296	27	45
56400	811	1286	11	24
56500	1622	1237		56
56600	999	1214		81
56700	1622	1242		31
56800	898	1271		36
56900		1280		89
57000		1247	9	132
57100	1846	1286	55	83
57200	1408	1250	42	16

distance [µm]	Mg [ug/g]	Sr [ug/g]	Mn [ug/g]	Fe [ug/g]
57300	1219	1223	23	5
57400	1330	1225		11
57500	1735	1231		281
57600		1259		108
57700	1539	1267	4	340
57800		1277	3	125
57900	1135	1245	4	106
58000	933	1282	17	177
58100	753	1263	15	140
58200		1293	33	135
58300	1324	1258	4	69
58400		1231	7	112
58500	1011	1218		112
58600	1256	1201		133
58700	1116	1202		47
58800		1180		75
58900	1215	1139	156	74
59000	1022	1162	18	58
59100	968	1223	55	43
59200	1208	1234	50	46
59300	1103	1206	55	65
59400	2230	1115	24	63
59500	1748	1121	35	29

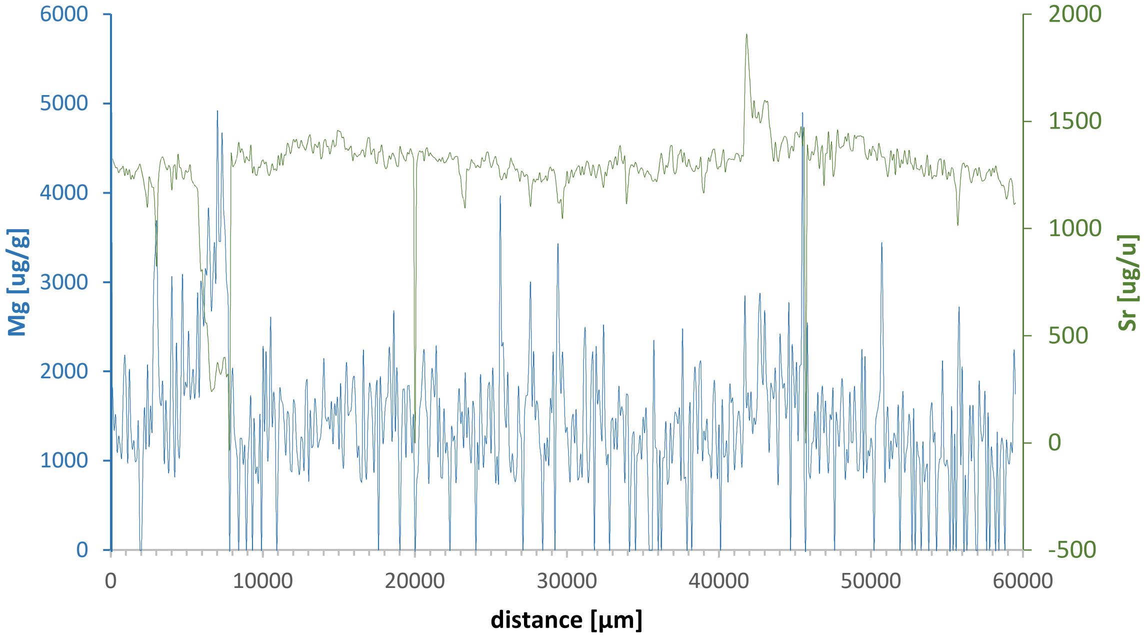

Plotted raw data of Mg and Sr of shell D.

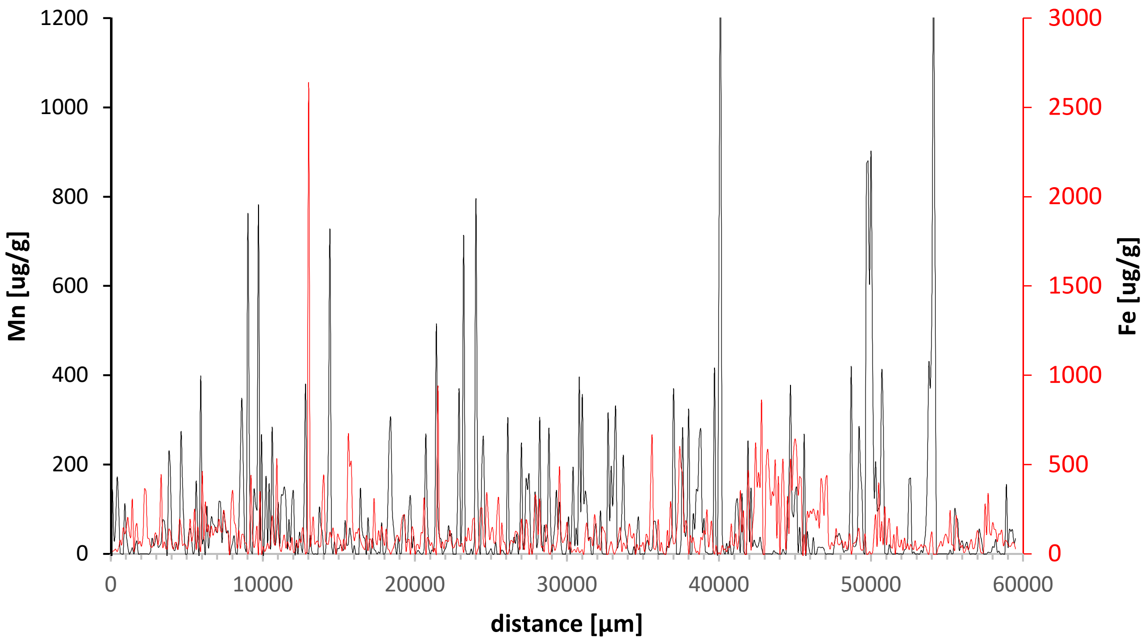

Plotted raw data of Mn and Fe of shell D.

Acknowledgements

The last three years have not always been easy, but in the end, they have been a great experience. Of course, many people were involved in this work, be it through their scientific advice or through encouraging words and gestures. But I would still like to thank a few people in particular:

Dr. Stefan Huck, for the opportunity to write this thesis. Whenever I had questions or problems your door was always open to me. During field trips and conferences, you were a great supervisor and friend. Without you, this thesis wouldn’t have been possible. I would like to especially thank you for your support during the last months.

Prof. Dr. Ulrich Heimhofer, for the chance to work at the Institute of Geology and in your research group. At any given time, you were always around to help with advice, hints, support and encouragement. Your ideas and corrections during the writing of this thesis and its manuscripts, were always helpful and greatly appreciated.

Prof. Dr. Adrian Immenhauser from the Institute of Geology, Mineralogy and Gepophysics (Ruhr-University Bochum), Prof. Dr. Andrea Hampel from the Institute of Geology (Leibniz University Hannover) and Prof. Dr. Francois Holtz from the Institute of Mineralogy (Leibniz University Hannover) are gratefully acknowledged as co-examiners.

Dr. Gianluca Frijia, Dr. Niels de Winter, Dr. Alexis Godet for their collaboration on the manuscripts and/or in the lab. Thank you for your expertise and time.

Christiane Wenske for initiating me into the secrets of the Gasbench and answering every question with great patience.

My colleagues Fanfan, Gang, Katharina, Doris, Janette, Uli M., Fritz, Till and Jörg for their help.

Furthermore, would like to thank: Conny and her Markus, who made the start in Hannover very easy and who were always available for conversations; Lars, as a lovely supporter in challenging personal and academic situations; Nils for the Schnacks in hessian/kölsch dialect during late night shifts; Philipp, for the many analytical and constructive discussions; Schorsch, who always had an open ear; Robert, for semantic lessons, red lines and his precious time. I appreciated all of this.

The gratitude and love I feel for my parents cannot be expressed in words. Thank you for everything you have done. I would like to thank my brother and sister-in-law for their patience, encouragement, help, proof-reading and for giving me the coolest niece in the world! I also thank my best friend HP for being part of my family.

Curriculum Vitae

Personal data

Name:	Katharina Elena Schmitt
Date of birth:	04.12.1986
Place of birth:	Weilburg
Nationality:	German

Education and professional career

July 2007	A-levels (Gymnasium Philippinum Weilburg)
Apr. 2008 - Dec. 2013	Diploma degree in geology (Project title: „effects of different preparation, fixation and dying methods on the isotope signature of carbonate samples“ Johannes Gutenberg - University Mainz)
Aug. 2011	Undergraduate in geology (chemistry, meteorology, mineralogy, general geology)
Apr. 2012 - July 2013	Research assistant at the Department of Applied and Analytical Palaeontology, University Mainz
Apr. 2014 - Oct. 2015	Office employee at ARANO GmbH - Provider for technical documentation
Aug. 2014	Pilot-study for a DFG project in Mexico
Nov. 2015	PhD student (Project title: Early Cretaceous Shoal Water Carbonates from the Central Apennines – Sedimentology, Chemostratigraphy and Sclerochemistry Leibniz Universität Hannover)